Piezoresistive Properties of 2D based Nanocomposites for Strain Sensing Applications

JAMES GARCIA

A THESIS SUBMITTED FOR THE DEGREE OF

DOCTOR OF PHILOSOPHY

IN THE SUBJECT OF

PHYSICS

UNDER THE SUPERVISION OF

PROFESSOR JONATHAN N. COLEMAN

SCHOOL OF PHYSICS

TRINITY COLLEGE DUBLIN

2023

Declaration

I declare that this thesis has not been submitted as an exercise for a degree at this or any other university and it is entirely my own work.

I agree to deposit this thesis in the University's open access institutional repository or allow the Library to do so on my behalf, subject to Irish Copyright Legislation and Trinity College Library conditions of use and acknowledgement.

Elements of this work that have been carried out jointly with other or by collaborators have been duly acknowledged throughout the text.

James Garcia

Piezoresistive Properties of 2D based Nanocomposites for Strain Sensing Applications

Abstract

The superlative piezoresistive properties of nanomaterials and their composites have attracted great interest in the area of strain sensing. The field has grown exponentially over the past decade, benefiting from the maturity of liquid phase processing of layered crystals and other nanomaterials. The development and application of nanomaterial strain sensors face a number of challenges that must be overcome, if they are to proliferate the next generation of technologies. This work looks to address some of the issues around the stability and sensitivity of the resistance-strain response in piezoresistive nanocomposites, hoping to further optimise strain sensor development.

Piezoresistive nanocomposites show exceptional promise due to their robust, stretchable nature coupled with a high strain sensitivity. A caveat is that the electrical properties of nanocomposites are known to suffer from hysteresis effects and a high strain rate dependence. In an effort to suppress these undesirable effects, a highly strain-sensitive nanocomposite known as G-putty was fabricated into nanocomposite thin films through various printing techniques. The thin films show a marked increase ($\times 10^6$) in conductivity compared to the bulk due to a partial phase segregation of the network. Despite this morphological change, the G-putty thin films maintain a high strain sensitivity. In addition, the preparation of thin films on PDMS substrates frustrates the viscoelastic relaxation observed in bulk G-putty, leading to a significant reduction in the resistance hysteresis and strain rate dependence. The properties of the thin films make them promising candidates for integration in strain sensing devices, with a number of use cases demonstrated.

Following on from the work on G-putty thin films it became clear that a strong relationship exists between the piezoresistive and conductive properties of nanocomposites. Surprisingly the mechanisms underlying this behaviour are not well understood and development has been hampered by the absence of physical models that could be used to fit data and optimize sensor performance. To address this, a model was developed relating strain sensitivity to the filler loading and nanocomposite conductivity. The model was used to fit experimental and literature data, which outputs figures a merit to characterise the piezoresistive response. Importantly the model also provides insight into the piezoresistive mechanism, demonstrating that the effect of strain on the filler network structure dictates the resistance response.

While the initial work of this thesis focuses on polymer nanocomposites, the properties of 2D materials offer an opportunity to study mixtures insulating, semiconducting and conducting phases. Such mixtures are much more difficult to obtain in polymer nanocomposites and thus lie relatively unstudied. The piezoresistive properties of nanocomposite films comprised solely of 2 dimensional nanosheets where explored, displaying a wide range of percolative properties on account of the diverse properties offered by 2D materials. This rich set of behaviours leads to a unique set piezoresistive properties depending on the nanocomposite type. In each case, percolation theory was used to develop models for nanocomposite strain sensitivity as a function of both conductor volume fraction and nanocomposite conductivity. This approach yields equations which can be used to fully describe the experimental data. These results open the way to the future design of improved strain sensing systems.

Publication List

1. D. P. O'Driscoll, S. McMahon, J. R. Garcia, S. Biccai, C. Gabbett, A. G. Kelly, S. Barwich, , M. Moebius, C. S. Boland, J. N. Coleman (2021). Printable G-Putty for Frequency- and Rate-Independent, High-Performance Strain Sensors. *Small,* 17, 2006542. 10.1002/smll.202006542
   [Basis For Chapter 5]

2. J. R. Garcia, D. O'Suilleabhain, H. Kaur, and J. N. Coleman (2021). A Simple Model Relating Gauge Factor to Filler Loading in Nanocomposite Strain Sensors, *ACS Applied Nano Materials*, 4(3), 2876-2886. 10.1021/acsanm.1c00040
   [Basis For Chapter 6]

3. J. Liu, L. Mckeon, J. R. Garcia, S. Pinilla, S. Barwich, M. Möbius, P. Stamenov, J. N. Coleman, V. Nicolosi (2022). Additive Manufacturing of Ti3C2-MXene-Functionalized Conductive Polymer Hydrogels for Electromagnetic-Interference Shielding. *Advanced Materials,* 34, 2106253. 10.1002/adma.202106253

4. E. Caffrey, J. R. Garcia, D. O'Suilleabhain, C. Gabbett, T. Carey, and J. N. Coleman (2022). Quantifying the Piezoresistive Mechanism in High-Performance Printed Graphene Strain Sensors, *ACS Applied Materials & Interfaces,* 14(5), 7141-7151. 10.1021/acsami.1c21623

5. J. Maughan, P. J. Gouveiaad, J. G. Gonzaleza, L. M. Leahy, I. Wood, C. O'Connor, T. McGuiread, J. R. Garcia, D. G. O' Shea, S. F. McComish, O. D. Kennedy, Maeve A. Caldwell, A. Dervan, J. N. Coleman, F. J. O'Brien (2022). Collagen/pristine graphene as an electroconductive interface material for neuronal medical device applications, *Applied Materials Today*, 29, 101629. 10.1016/j.apmt.2022.101629

6. T. Carey, O. Cassidy, K. Synnatschke, E. Caffrey, J. R. Garcia, S. Liu, H. Kaur, A. G. Kelly, J. Munuera, C. Gabbett, D. O'Suilleabhain, J. N. Coleman (2023). High Mobility Flexible Transistors with Low Temperature Solution Processed Transition Metal Dichalcogenides, *ACS Nano,* 17, 3, 2912–2922. 10.1021/acsnano.2c11319

7. J. R. Garcia, M. McCrystal, H. Kaur, T. Carey, J. N. Coleman. Tuneable Piezoresistance in Graphene-Based 2D:2D Nanocomposite Networks, *Accepted to Advanced Functional Materials.*
   [Basis For Chapter 7]

Acknowledgments

It goes without saying, that the first thanks must go to Johnny for providing me with the opportunity to be apart of this incredible group. His support and guidance across four years of research (with a pandemic thrown in for good measure) has been invaluable – it is still a source of amazement that he turns even the most dire looking results into new shoots of optimism.

To the fine people of the Coleman group it has been a privilege to share the last four years whether that has been in the lab, pub or park with cans in hand. A special thanks goes to Dan who introduced me to the dark arts of the Fitz and whose stories on his latest diets and mountaineering adventures were never to be missed. To Cian and Adam for their perspectives and willingness to share a wealth of knowledge on all things scientific and pint related. To Eoin, Dom and Tian; two words will suffice – 'Shaka, Shaka'. To the rest of the group past and present; Sonia, JB, Aideen, Conor, Ruiyuan, Domhnall, Yash, Shixin, Mark, Jack, Luke, Kev, Harneet, José, Bharathi, Emmett and Oran. I am deeply grateful to have shared this adventure with you all.

To friends who saw the light and got proper jobs and to those still in the trenches. Thank you for laughs, fond memories and for just generally putting up with me. You were there when I needed reminding there's life beyond a PhD.

Finally to my family, who have been my rock throughout this PhD and beyond. Words cannot adequately express how much I appreciate you all. Your support through the ups and downs always made things easier and this thesis would not have been possible without you.

Table of Contents

Table of Figures

'I think it's much more interesting to live not knowing than to have answers which might be wrong. I have approximate answers and possible beliefs and different degrees of uncertainty about different things, but I am not absolutely sure of anything and there are many things I don't know anything about, such as whether it means anything to ask why we're here. I don't have to know an answer. I don't feel frightened not knowing things, by being lost in a mysterious universe without any purpose, which is the way it really is as far as I can tell.'

- Richard Feynman

'Talking nonsense is the sole privilege mankind possesses over the other organisms. It's by talking nonsense that one gets to the truth! I talk nonsense, therefore I'm human.'

- Fyodor Dostoevsky

Chapter 1

Introduction

Piezoresistive materials transduce mechanical deformations into a change in a materials electrical properties. The discovery of this effect dates back to 1856, with Lord Kelvin's first observation of electrical resistance changes in iron filaments placed under tension.[1] The 20th century saw a rapid proliferation of piezoresistive materials for strain sensing applications, which has led to piezoresistive strain gauges becoming the method of choice for deformation monitoring in industry. For decades the strain gauge market has been dominated by metal foils and semiconductors which are widely employed to monitor the structural health of materials under load or to measure the residual stress that occurs during manufacturing. It is surprising to learn how commonplace strain gauges are, being found in everyday household appliances such as weighing scales (loadcells) and washing machines (vibration sensors).

The ubiquitous use of strain gauges has resulted in a thriving industry worth billions of euros and a market which will continue to expand as new technologies become available. However, the current commercial strain gauges have some significant drawbacks. Semiconducting based strain gauges offer excellent sensitivity, however, they are brittle with a maximum working range of 0.2% strain,[2] while also being expensive to produce and highly sensitive to temperature. Metal foil strain gauges are a cost efficient alternative with a wider working range, however, even here strain measurements are limited to ~ 3% strain and this improvement in working range comes at a cost of a ~98% loss in sensitivity compared to their semiconductor counterparts.

The evolution of the internet of things has brought forth a whole range of potential technologies with which humans can interface. Here, skin-mounted devices have garnered particular interest, which could be utilised for a host of different applications such as biomedical sensing,[3,4] human–computer interfacing,[5] robotics,[6] and virtual reality devices.[7] Thus, a preeminent goal is to achieve functional devices that can transduce deformations of the skin into electrical signals.[8] These wearable sensors have a number of requirements such as, flexibility/stretchability, electrical stability, and high sensitivity, which will enable the monitoring of both minute and large deformations across a wide strain range. The problem here, is that the properties of metal foil and semiconducting technologies do not meet these demands and so there is a clear need to develop new highly sensitive and flexible/stretchable sensors which will be the foundation of the next generation of sensing technologies.

Nanomaterials and their composites offer an attractive solution, where the overlapping of conductive nanomaterials allows current to flow through hopping or tunnelling mechanisms forming conductive nanostructured networks which can be prepared on the surface or embedded within, elastomeric polymers.[9] These networks tend to be highly sensitive to mechanical deformations leading to large changes of resistance upon

straining, making them ideal as strain sensing elements.[10] Furthermore, nanomaterial networks allow sliding and slippage of adjacent particles on account of the relatively weak van der Waals, vdW, forces which bind the networks together. This means that electrical pathways can still be maintained at strains far larger than what is achievable with traditional sensors.[11]

The high sensitivity and stretchability of nanomaterial networks and their composites show immense promise. However, nanocomposites display a number of characteristics which hinder their ability to provide quantitative strain measurements in real world settings. For example, strain sensors should display negligible hysteresis, while it is paramount that identical deformations must in turn give identical responses regardless of the rate or frequency with which they are applied. A possible solution to this is presented in Chapter 6 by forming printed thin films from a bulk nanocomposite. The production of thin films means the mechanics are primarily described by the backing substrate, while the piezoresistive response is subject to the properties of the nanostructured thin film. This allows for the development of highly sensitive and patterned sensor geometries that can be tailored to the requirements of the strain measurements.

The preparation of novel nanomaterial based strain sensors is primarily based on empirical trial and error. This uncertainty is compounded by a lack models that provide analytical evaluation and thus, researchers have been left with little understanding of the physics underlying strain sensor performance. In particular sensor sensitivity remains somewhat of a mystery with networks comprised of similar components displaying vastly varying strain dependence. In Chapter 7, a model is proposed to describe sensitivity performance in terms of the filler loading and conductivity of nanocomposite strain sensors. The aim here is to provide some insight into the primary factors effecting strain sensor performance, with the ultimate goal of optimising nanocomposite sensitivity.

Piezoresistive nanocomposite systems have been widely explored for their potential as strain sensors. Traditionally, these composites are limited to an insulating polymer matrix and conductive nano filler. This requires a sufficient filler loading to ensure a conductive composite and limits the scope of investigations. A new class of nanocomposites comprised solely of 2-dimensional nanosheets are relatively unexplored in terms of their piezoresistive response. The diverse properties offered by 2D materials allows for the exploration of a variety of nanocomposite types, which may yield novel behaviours. Chapter 8 explores several nanocomposites comprised of combinations insulating, semiconducting and conducting 2D nanosheets, with the aim of studying and developing models for the piezoresistive response.

This thesis will conclude with a review of the significant findings and propose a future direction for investigations. It's hoped that the work presented here will add value to the existing literature and facilitate further development and optimisation of piezoresistive nanomaterial devices.

Chapter 2

2D Materials and their Synthesis

Layered crystals are a diverse set of materials with a broad range of electronic, optical and electrochemical properties.[12] Although interesting in the bulk, the true potential of these materials are unlocked once they are exfoliated into 2D sheets.[13-15] The experimental isolation of monolayer graphene[16] marked the dawning of a new age in materials science, with the possibility of purely 2D materials and their remarkable properties realised. This discovery was a catalyst, and the subsequent scramble led to whole host of materials being exfoliated and characterised. By now, over 150 unique layered materials have been

exfoliated and their potential in areas such as electronic devices, energy storage and sensing explored.[17]

2.1. Characteristics of 2D Materials

Layered materials can be readily exfoliated due to the anisotropic nature of their crystal structure. This is characterised by strong covalent intra-layer bonding between atoms yet comparatively weak van der Waals bonds between the stacked planes. The asymmetry in bonding allows for the isolation of monolayer or few-layer sheets which often show vastly different properties to their bulk counter parts. Changes in electronic properties are attributed to the quantum confinement of electrons to a 2D plane altering the electronic band structure, while the removal of layer-layer interactions greatly enhances the mechanical and thermal properties. Furthermore, the surfaces of layered materials are terminated by electron pairs and are free from dangling bonds, which tends to make them stable against chemical reactions.[18] These qualities have made 2D materials attractive to researchers in terms of the new physics they offer as well as their potential applications. All that is needed are methods to delaminate the layers from their parent crystals to yield 2 dimensional sheets.

Exfoliation is by now a loaded term encompassing many, often complex, mechanical, chemical and solvent assisted procedures. However at its core, exfoliation is a simple concept whereby energy is applied to overcome the van der Waals (vdW) bonds between layers, yet leaving the basal plane intact. This is exemplified in the seminal graphene paper by Geim and Novoselov who used adhesive tape to delaminate monolayers of graphene from the parent graphite crystal.[16]

While this method is still relied upon for producing high-quality nanosheets, the low throughput is a glaring drawback, making its use in the scalable production of graphene-

based devices impractical. This stumbling block has plagued other bottom-up synthesis routes which offer high quality 2D material but at low yield and high cost. As such, there was a need to fill the demand for high quality 2D materials, while maintaining a yield that is compatible for scalable manufacturing. Here solution processing offers an attractive alternative with the ability to process layered crystals into monolayer and few-layer nanosheets at scale.

The remainder of this chapter will build on the characteristics and properties of the materials used in this work, while additionally describing how these materials can be processed in a liquid medium to produce 2D nanosheets.

2.1.1. Graphene

Carbon is the building block of life and forms the basis of all organic chemistry. This flexibility in bonding means carbon-based materials can come in many forms, and with an abundance of physical properties. Graphitic structures can be arrived at by first considering graphene which is a 2-dimensional material consisting of carbon atoms arranged in a honeycomb hexagonal structure, as shown in Figure 2.1A. From there, graphene can be rolled, folded or stacked into shapes of different dimensionality such as 0D-fullerenes, 1D-carbon nanotubes and 3D-graphite (Figure 2.1B). While conceptually straightforward the synthesis of these materials has proved somewhat more challenging and it was not until the 90s that fullerenes and nanotubes were isolated.[19,20]

Graphene is most commonly encountered as graphite which consists of stacks of graphene sheets bonded together by van der Waals forces. Graphite and its crystal structure have been a curiosity for more than a century starting with Sir Benjamin Collins Brodie comments on the highly lamellar nature of thermally reduced graphite oxide in 1859.[21] Graphene was also considered in a theoretical context in 1947 by P R Wallace as he endeavoured to develop a theory for the electronic properties of bulk graphite.[22] Despite

the academic interest, free-standing graphene eluded researchers throughout the 20th century and was instead grown epitaxially on monocrystals with matching crystal lattices.[23] In fact, strictly 2D materials were argued not to exist, with Landau and Peierl's demonstrating that thermal fluctuations should lead to atomic displacement on par with interatomic distances, thus rendering 2D materials thermodynamically unstable.[24,25]

The isolation of freestanding monolayer graphene in 2004 demonstrated that the existence of 2-dimensional materials was indeed possible and theory was reconciled by the fact that graphene sheets contain spontaneous ripples in the 3rd dimension which suppresses thermal vibrations.[26] The patterning of hall bars helped elucidate some of graphene's superlative electronic properties which stem from the two dimensional sp^2 hybridised bonding structure.[16] Here the 2s, $2p_x$ and $2p_y$ orbitals mix to form sigma, σ, bonds between carbon atoms separated by 1.42 Å. This leaves the p_z-orbitals, which are orientated perpendicular to the lattice, to bond covalently with neighbouring carbon atoms to form a π-band. These bands are half-filled with delocalised electrons allowing conduction across the basal plane.

The unique band structure at the vertices of the honeycomb lattice, gives rise to the semi-metallic character observed in single- and bi- layer graphene, shown in Figure 2.1C. As electrons interact with the periodic potential of the hexagonal lattice they experience a linear dispersion relation at the Dirac points. A consequence of this linear dispersion is a zero-effective electron mass, which creates an enormous electron/hole mobility across the lattice, such theoretical mobilities have been shown to be achievable experimentally with values as high as 140,000 cm^2/Vs at room temperature and 1,000,000 cm^2/Vs at 1.7K where quasi-ballistic transport occurs over lengths of 15 mm due to minimised phonon scattering.[27]

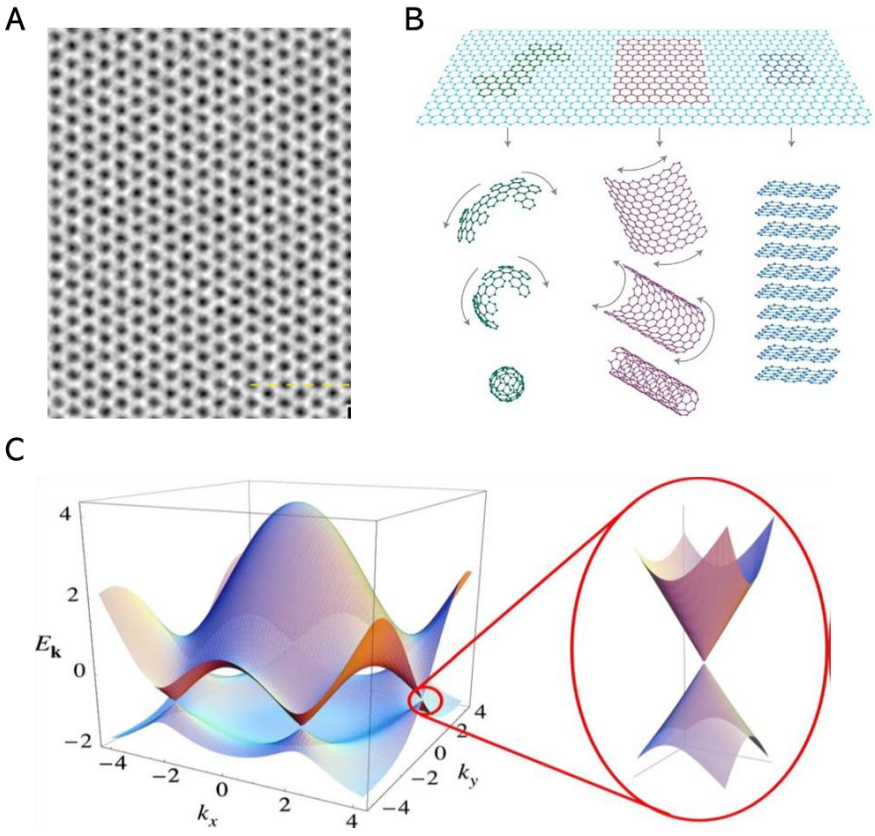

Figure 2.1 – Graphene. A) Direct TEM image of single layer graphene. Image from ref.[28] B) Graphene is a 2D building block for carbon materials of other dimensionalities: 0D – Buckyballs, 1D – Carbon nanotubes, 3D – Graphite. Image from ref.[29] C) Electronic dispersion relation of p-bands. Image from ref.[30]

2.1.2. *Hexagonal Boron Nitride*

While the impressive electron transport and current modulating properties of 2D materials may grab the headlines, to realise fully 2D electronic components, insulating materials are also required. Hexagonal boron nitride (h-BN) has an almost identical crystal structure to graphite, with a layered honeycomb hexagonal structure arranged in alternating atoms of boron and nitrogen, earning it the title of 'white graphite' (Figure 2.2A).

h-BN is characterised by sp^2 hybridised atoms which form strong σ-bonds in the basal plane, while there exists weak covalent bonding of the p_z orbital perpendicular to the

lattice.[31] The similarity in structure with graphene leads to many of the physical properties also being similar, with h-BN displaying impressive mechanical properties and high thermal conductivity.[18,32] However, it is well known that BN has a wide indirect bandgap (~ 6 eV), which is in stark contrast to semi-metallic character of graphene despite the similarity of crystal structure and bonding. This is explained by nitrogen's strong electronegativity which leads to a transfer of electrons from boron to nitrogen.[31] The basal plane therefore comprises of strongly polarised bonds where electrons are essentially 'fixed', resulting in a wide band gap.

h-BN does not occur naturally and in fact there is only one deposit of a naturally occurring BN polymorph discovered to date. Instead, h-BN produced synthetically and has found ubiquitous use in industry with wide ranging commercial applications ranging fillers in cosmetics to advanced cooling systems for aerospace.[33,34] The similar crystallographic structure of h-BN and graphene, meant it was a natural candidate for exfoliation and in the immediate aftermath of the seminal paper on free-standing graphene, the mechanical exfoliation of h-BN nanosheets was demonstrated.[35] Nowadays, boron nitride nanosheets can be produced at scale by a variety of synthesis routes (Figure 2.2B).[36] As with many layered materials the reduction of h-BN thickness to a single layer facilitates a transition from indirect to direct band gap of 6.1 eV (Figure 2.2C).[37] As a consequence, BN nanosheets exhibit a strong UV absorption peak about 215nm, however in the visible range absorption is extremely low and films of h-BN exhibit a high degree of optical transparency, which are promising properties for designing compact UV lasers.[38]

Much of h-BN's success has been achieved when used in conjunction with other nanomaterials. h-BN is chemically inert and atomically flat which makes it ideal as a substrate on top of which devices can be prepared. In fact, adding an additional layer of BN, such that a sandwich structure is created, can dramatically improve the stability of materials such as black phosphorus[39] and $NbSe_2$.[40] Confinement of 2D materials between

BN layers also has implications for the morphology and electrical properties of the active layer which is particularly true in the case of graphene where the lattice mismatch is only 1.7%. Graphene devices prepared on BN show a factor of 3 decrease in roughness compared to the same devices on SiO_2.[18] This has yielded atomically thin multi-layered graphene-BN structures with enormous mobilities of 500,000 cm^2/Vs.[41]

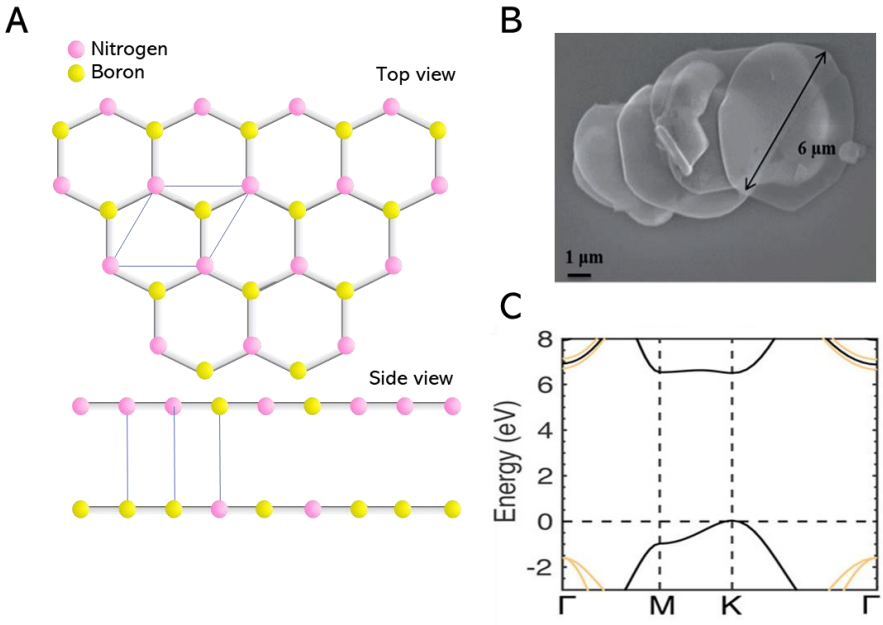

Figure 2.2 – Boron Nitride. A) Atomic structure and layer structure. Image from ref.[14] B) TEM images of exfoliated nanosheets. Image from ref.[36] C) Band structure of single layer Boron Nitride. Image from ref.[31]

2.1.3. Transition Metal Dichalcogenides

Transition metal dichalcogenides (TMDs) are a subclass of 2D layered materials which have seen quite the academic resurgence in recent years due to the novel physical phenomena they display coupled with their suitability towards nanoelectronic[42] and nanophotonic devices.[43] Perhaps the most widely studied of the TMDs is MoS_2, and studies of the material date back to 1920s when the crystal structure and curious

anisotropy was first reported.[44] Since this time, over 60 TMD compounds have been discovered, at least 40 of which have layered structures.[45]

The stoichiometry of TMDs is described as MX_2, where M is a transition metal and X refers to a chalcogen such as sulphur, selenium or tellurium (see Figure 2.3A). TMDs have garnered particular attention through the disparate electronic properties that can be achieved by varying the atomic makeup and structure, from insulators such as HfS_2, semiconductors such as WSe_2 and MoS_2, semi-metals such as WTe_2 and metals such as VSe_2. Each layer of a TMD comprises of three atomic layers with a hexagonally packed plane of transition metal sandwiched between two planes of chalcogens in a X-M-X structure (Figure 2.3B). The tri-plane structure of TMDs layers are thicker (~0.7nm) than graphene and have an interlayer distance of approximately 0.6nm.[46]

The additional complexity in the layer means TMDs can have several structural phases as a result of the differing coordination of the transition metal. The most common thermodynamically stable phases are trigonal prismatic (2H) or octahedral (1T). These phases are known as polymorphs and can be viewed as different stacking orders of the atomic planes. The 2H phase is characterised by an ABA stacking where the chalcogen is in an identical position above and below the transition metal plane. By contrast, the 1T phase corresponds an ABC stacking order such as the one shown in Figure 2.3B. Here, the integer defines the number of individual layers that make up the unit cell. This is important, as a material's phase strongly defines the electronic character. For example, the naturally occurring 2H-MoS_2 is semiconducting (bulk band gap ~ 1.3eV),[47] whereas the 1T phase is metallic. Moreover, phase transitions between the 2H and 1T phases can be induced via intercalation of lithium and other alkali ions.[48]

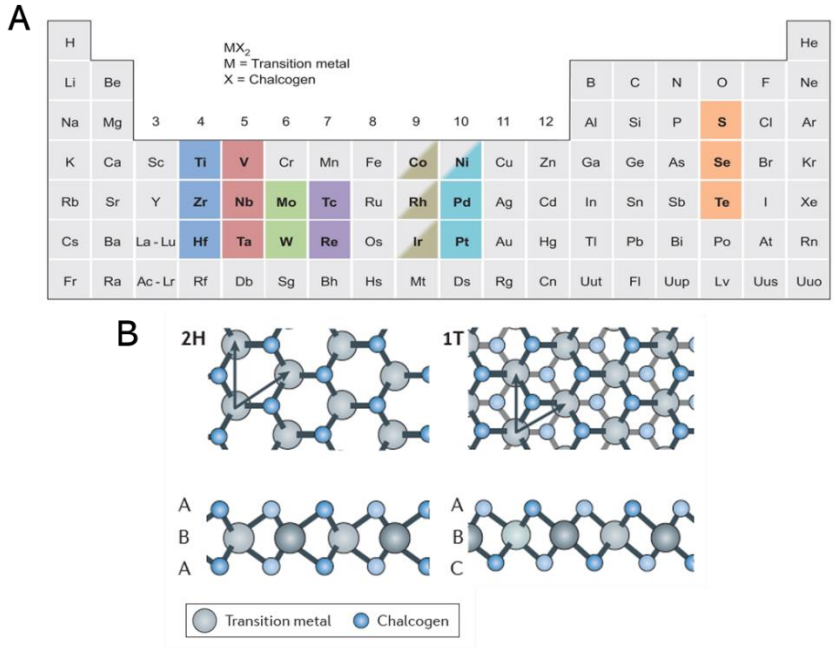

Figure 2.3 – Transition Metal Dichalcogenides. A) Periodic table highlighting the elemental make up of transition metal dichalcogenide crystals. Image from ref.[45] B) Atomic structure of 2H and 1T phases. Image from ref.[48]

Apart from the coordination environment another consideration to the electronic structure of TMDs is the d-electron count. Moving from group 4 to 10 results in a progressive filling of the non-bonding d bands and depending on the filling procedure TMDs can exhibit different electrical characteristics. When orbitals are partially filled , TMDs exhibit metallic conductivity as is the case for 2H-$NbSe_2$. Fully occupied orbitals, such as 1H-HfS_2 give rise to semiconductors, where the fermi level is located between bands (Figure 2.4A).[45]

The transition of bulk TMDs to their 2D counterparts was a topic of curiosity throughout the 20th century with the first reports of ultra-thin MoS_2 obtained using adhesive tape[49] in 1963, while the isolation of free standing MoS_2 monolayer[50] was reported a few decades later in 1986. On the coattails of the graphene 'gold rush' a revival of research in 2D TMDs began in earnest. Of particular promise to electronic and optoelectronic applications are group VI TMDS which display a dramatic change in band gap as the thickness is reduced

to a monolayer (Figure 2.4B), where the monolayer bandgap is typically 50% larger than the bulk counterpart.[51] Interestingly, the bulk and monolayer also differ in the nature of the bandgap. In the bulk TMDs contain an indirect bandgap, however, as the layer number is reduced to a monolayer, a direct bandgap occurs which increases the efficiency of electron-hole recombination. This manifests as an extreme enhancement of photoluminescence, of the order of 10^7.[47,52] These direct bandgaps tend to occur in the visible spectrum which makes them ideal candidates for use in photovoltaics, LEDs and displays.[53]

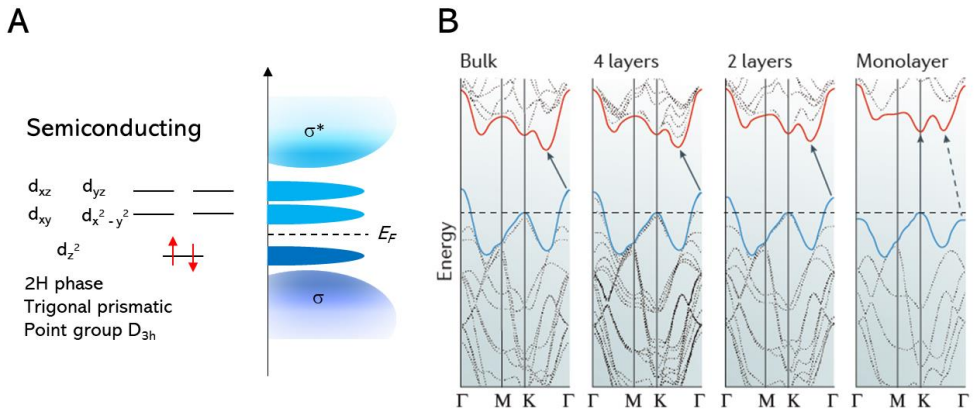

Figure 2.4 – TMD Electronic Structure. A) Orbital filling of group 6 transition metals in trigonal prismatic coordination. Image from ref.[54] B) Transition of indirect to direct bandgap as MoS_2-2H is scaled down from bulk to monolayer thickness. Image from ref.[48]

2.2. Synthesis of 2D materials

2D materials offer an attractive alternative to silicon-based electronics not only in terms of performance but also because of the flexibility they offer. In order for 2D materials to realise commercial success there must be methods to produce high quality 2D nanosheets at scale with fine control of dimensionality and defect level. Furthermore, these methods must be economical so that they can compete with existing technologies.[55] In its current state 2D materials synthesis can be broadly separated into bottom-up and top-down methods.

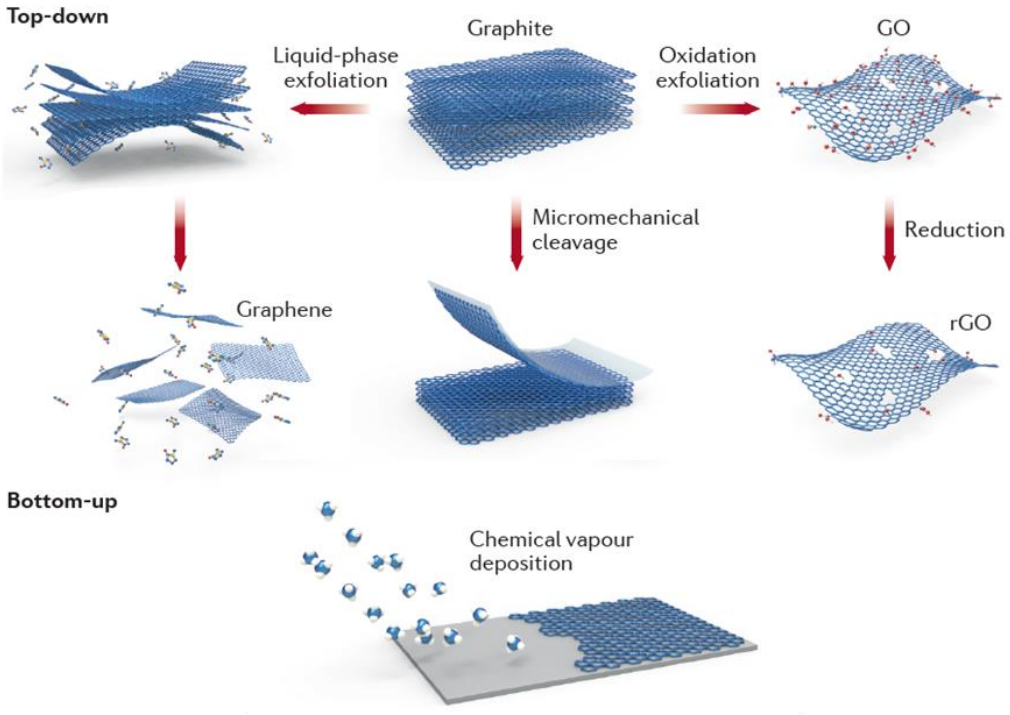

Figure 2.5 – 2D Material Synthesis. Various bottom up and top down synthesis routes for graphene. Image from ref.[56]

As the names suggest, bottom-up methods involve growing atomically thin nanosheets from elemental precursors, common processes for growth are chemical vapour deposition[57] (CVD) and pulsed laser deposition[58] (PLD). In contrast, top-down methods involve the creation of nanosheets through the delamination of bulk parent crystals, and

include techniques such as mechanical[59], chemical[60] and liquid-phase exfoliation.[61] (see Figure 2.6).

To date no one method has proven to be the 'holy grail' of nanosheet production with a trade-off between quality and yield remaining a significant hurdle. This means that processes are interchanged to suit their end applications and so each process is still a topic of research and refinement.

2.2.1. Chemical Vapour Deposition

Chief among the bottom up methods is chemical vapour deposition (CVD) which has shown great promise for high quality monolayer growth. Here powder precursors are sublimated at high temperature to form a vapour which can then be condensed as single-crystal monolayers. For example. MoS_2 can be produced from a MoO_3 precursor which is reduced in the presence of sulphur vapour to form volatile suboxides.[47] These suboxide compounds can diffuse into the substrate and further react with the sulphur to form triangular single layers of MoS_2. This technology has matured rapidly and now offers precise yet wafer-scale growth of layered materials such as graphene,[62] MoS_2,[47] WS_2[63] and WSe_2.[64] CVD also offers good compatibility with current semiconducting manufacturing, which reduces the barrier to entry for commercial scale processing. These features mean CVD shows promise for use in high performance electronics and optical applications. However, there are significant limitations the process. Scalability is subject to furnace and substrate size, while many of the precursors and by-products can be hazardous or toxic.[65] In addition, the process necessitates high temperatures which are energy intensive and limit substrate choice. These drawbacks means CVD is a process for high-end applications where nanosheet quality is paramount, therefore alternatives are needed for large scale, high mass manufacturing.

2.2.2. Micromechanical Exfoliation

The process of mechanical exfoliation is an inherently simple concept whereby adhesive tape is used to peel nanosheets from the parent crystal. Through iterative peeling steps nanosheets down to the monolayer can be isolated.[59] Cheap and effective, this method had much success in producing large and high quality sheets for proof of concept studies elucidating the properties of 2D materials as far back as the 1960s.[49,50] Of course the glaring bottleneck here is the low throughput and tedious nature of the process which inhibits its use in scalable applications. However to this day, mechanical exfoliation remains the best method of obtaining thin high quality layered materials for academic research.[66]

2.2.3. Solution Processing of 2D materials

The methods described above have a common theme. That is, they are capable of producing high quality nanosheets but at high cost and low yield. This limitation means alternative methods are needed for the facile preparation of nanosheets at scale.

Solution processing is an umbrella term which describes the processing and dispersion of 2D materials in a liquid media. Solution processing is a useful technique which allows grams of material containing unfathomable numbers of nanosheets to be processed even in research laboratory environments. Despite the gigantic number of nanosheets to be characterised, a range of robust spectroscopic techniques have now been developed which can the yield information on the ensemble nanosheet dispersion in terms average nanosheet size, thickness and quality.[67] Nanosheet dispersions can be deposited on substrates through a range of well-established techniques such as spin coating,[68] inkjet printing[69] and spray coating,[70] while blending dispersions with polymer dispersions can facilitate the production of homogeneous nanocomposite systems.[71] These characteristics

lend solution processed materials to a myriad of applications in electronics, mechanical reinforcement and energy storage.[72]

Chemical Exfoliation

Intercalative exfoliation involves the insertion of molecules between the layers of the crystal. The presence of molecules induces an expansion in the crystal, weakening the van der Waals forces between adjacent layers. The degree of layer expansion depends on the diameter of the intercalating molecule. The creation of wide interlayer distance lowers the energetic cost to nanosheet delamination and allows for layer exfoliation by either mild sonication or thermal shock, as shown in Figure 2.6.

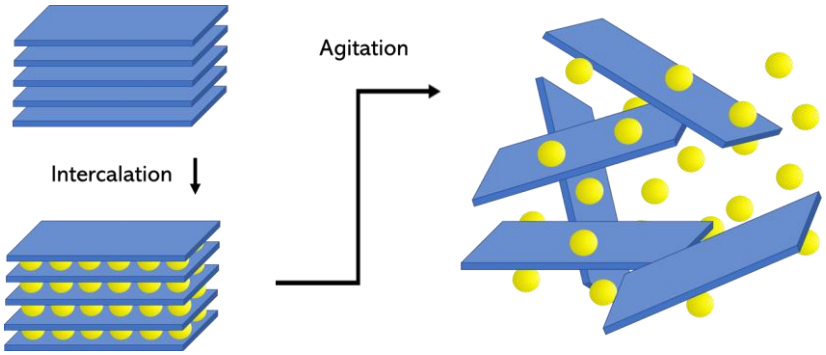

Figure 2.6 – Chemical Exfoliation. Schematic of exfoliation by intercalative methods. Image adapted from ref [14]

The processing of layered crystals has been a chemists playground for more than a century and in 1859 the first synthesis of graphite oxide (GO) was demonstrated.[21] This involved intercalating graphite with concentrated acids before exfoliation with aggressive bases, producing large thin sheets of GO in addition to some less welcome explosive by-products. Thankfully, the less hazardous Hummers method is now common place for graphene oxide production, using a combination of sulphuric acid, sodium nitrate and potassium permanganate to introduce hydroxyl (-OH) and epoxy (-COH) groups to the basal plane.[73] The addition of such groups functionalise the surface of the nanosheets rendering them strongly hydrophilic.[74] This can be advantageous, preventing re-

aggregation and allowing the resulting nanosheets to be dispersed in water and organic solvents. GO is electrically insulating; however, reduction can remove oxygen atoms to yield an electrically active material. While successful at restoring the electrical properties, defects and the presence of residual oxygen means that the superlative properties of graphene cannot be recovered despite extensive efforts.[75]

Beyond GO, chemical exfoliation can be applied to a whole host of other layered materials, including TMDs,[76] black phosphorous,[77] layered double hydroxides[78] and metal chalcogens.[79] These processes utilise intercalants to expand the distance between layers, thus facilitating exfoliation. Some intercalants such n-butyllithium can also charge transfer to the layer, while this facilitates good dispersion of nanosheets in solution, due to electrostatic repulsion, the nanosheet properties tend to be distinct from their pristine counterparts. This occurs in MoS_2, where nanosheets experience a semiconductor to metallic transition through changes in the structural phase.[48]

Recent developments have shown layered hexagonal metal carbides and carbon nitrides can also be chemically exfoliated.[60,80] These materials demonstrate metallic electrical conductivities and display rich chemistries which show promise for energy storage applications.[81] The bulk, also known as MAX phase, takes the form $M_{n+1}AX_n$ where M is an early transition metal, A is a group 13 or 14 element and X is carbon and/or nitrogen. In these structures the $M_{n+1}X_n$ layers are interweaved with layers of A atoms. The layers are bonded together covalently rather than by vdW bonds as is the case in most other layered crystals. However, selective etching of the A layer can be achieved by hydrofluoric acid, resulting in the production of thin single layer sheets of micron sizes. These new exfoliation methods are a testament to the versatility of solution processing.

Liquid-Phase Exfoliation

Clearly, a space exists to isolate nanosheets at high yield through a simple and versatile process that requires limited post-processing steps. Just four years after the mechanical exfoliation of graphene, liquid-phase exfoliation (LPE) was to developed for exfoliating layered crystals.[61] LPE involves the mechanical delamination of sheets from layered crystals through ultrasonic energy or shear forces in a stabilising solvent environment. The stabilisation of the dispersion depends on the solvent minimising energetic effects between neighbouring nanosheets which prevents reaggregation. Thus, stable colloidal dispersions of nanosheets can be produced upon choice of an appropriate solvent.

LPE builds on decades of research in the field of chemical exfoliation, now allowing the production defect-free nanosheets without the requirement for covalently bonding molecules to the basal plane.[82] Crucially, monolayer and few-layer nanosheets produced by LPE have properties distinct from their bulk counterparts. The technique itself is rather versatile and appears to be applicable to any layered material.[14] Recently the approach has even been extended to non-layered materials with the preparation of quasi-2d nanoplatelets.[83] At first glance, these non-layered materials appear to have anisotropic covalent bonding schemes which results in preferential cleavage normal to the weakest bonds, however there are reports of exfoliation of isotropic materials to 2D platelets[84] and research is ongoing to understand this phenomena.

The resulting dispersions tend to be polydisperse in nature with a broad distribution of nanosheet lateral sizes and thicknesses present. This poses a problem as the band gap for materials is highly dependent on thickness, however, these distributions can be narrowed by applying centrifugal forces to dispersions allowing nanosheets of desried dimensions to be preferentially selected.

While the initial studies on LPE where carried out in the solvent N-Methyl-2-pyrrolidone, it was found that by sonicating layered crystals in water with additional salts or polymers, high aspect ratio nanosheets dispersions can similarly be achieved.[85,86] Nanosheets exfoliated in surfactants tend to thinner but of smaller length when compared to exfoliation of the same materials in organic solvents.[87] Upon exfoliation ions or polymers adsorb non-covalently onto the sheet surface, here, they act as stabilisers preventing reaggregation through electrostatic or steric repulsion. While the use of water is clearly preferable to harmful organic solvents, the removal of stabilisers is not straightforward and residuals are likely. Surfactants can be removed by a series of washing steps whereas adsorbed polymers can be decomposed through annealing.[88]

Ultrasonication

Ultrasonication involves the conversion of high frequency mechanical oscillations in acoustic waves (Figure 2.7A). These waves generate cavitation bubbles that collapse into high energy jets and induce intense shear and normal forces to act on the layered crystal, as shown in Figure 2.7B.[89] As numerous bubbles collapse, the sum of the kinetic energies is enough to overcome the VdW bonding leading to exfoliation. The high tensile and shear stresses generated will lead to ruptures in the basal plane, and so fragmentation of nanosheets also occurs.[90,91] Two methods of ultrasonication are generally employed, bath sonication which is a low energy process setting up standing waves in a small tank. The low intensity along with interference and damping of the ultrasonic waves within the tank means reproducibility can be difficult and yield is poor.[92] Sonic probe sonication is an alternative high energy process whereby the probe is inserted directly into the dispersion. This means that the intensity experienced by crystallites is strongly dependent on the distance to the probe, which again means reproducibility can be challenging. However, yields are much improved and simple post centrifugation steps can limit batch to batch variations.

Given the intensity of the mechanical process, one might assume that this is deleterious to the quality of the basal plane, however, studies how found the basal plane to remain relatively pristine with defects confined to the nanosheet edge.[82,93]

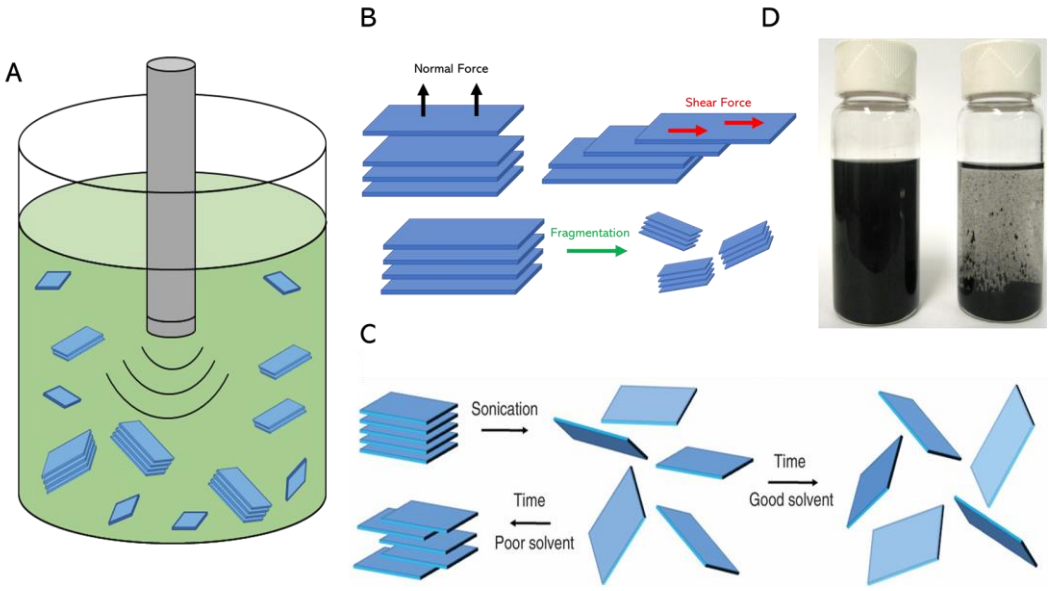

Figure 2.7 – Liquid Phase Exfoliation. A) layered crystals delaminated via probe sonication. B) Exfoliation mechanisms associated with microjets during sonication. Image from ref.[66] C) In 'good' solvents – those with matching surface energies, nanosheets are stabilised against re-aggregation. In 'poor' solvents - those with mismatched surface energies, nanosheets tend toward re-aggregation. Image adapted from ref[14]. D) Examples of stabilised and reaggregated dispositions. Image from ref.[94]

2.2.4. Stabilisation

The success of LPE is contingent on the ability to stabilise dispersions of nanosheets in liquid medium post-exfoliation. This is important not only for characterisation of the nanosheets themselves but in terms of applications where the long-term stability of inks throughout printing or composite preparation processes is vital, particularly in a commercial context. Considerable efforts have gone into understanding and applying theory to nanosheet dispersions allowing suitable solvents, surfactants and polymers to be identified.[95-100]

Solvent stabilisation

The key to liquid-phase exfoliation does not rest solely upon overcoming the interlayer bonding of crystallites, the liquid environment also plays a crucial role by lowering the energetic cost of exfoliation through solvent-nanosheet interactions and stabilising the subsequent dispersion against re-aggregation (Figure 2.7C&D).

Due to their earlier discovery, carbon nanotubes was the initial guinea pig used to tackle solvent-stabilised dispersions, with N-methyl-pyrrolidone (NMP) and dimethyl formamide (DMF) identified as particularly effective at producing stable dispersions.[101] Drawing inspiration from decades of work on polymer stabilisation, this was formalised by Bergin et al.[99] who showed that stable dispersions could be achieved when the surface energies of the solvent and nanotube closely match. This was extended to 2D nanosheets in 2008 with an extensive study showing that solvents with surface energies close to 40 mJ m^{-2} were found to maximise the concentration of dispersed nanosheets, but had unfortunate characteristics such as high boiling points and toxicity.[97]

Thermodynamics tells us the a stable dispersion occur when the free energy of mixing, ΔG_{mix} is negative.[102] The free energy of mixing is given by:

$$\Delta G_{mix} = \Delta H_{mix} - T\Delta S_{mix} \qquad (2.1)$$

Where T is the temperature and ΔH_{mix}, ΔS_{mix} are the enthalpy and entropy of mixing. Due to the dimensionality and high rigidity of nanosheets, ΔS_{mix} is small and hence the goal is to minimise ΔH_{mix} such that a negative value of free energy can be obtained. Strategies to achieve this depend on consideration of the Flory-Huggins interaction parameter[102]

$$\chi = -\frac{z}{2}\frac{(2\varepsilon_{AB} - \varepsilon_{AA} - \varepsilon_{BB})}{kt}$$

(2.2)

Where z is the coordination number between of both solvent and solute, ε represents the strength of the inter-molecule pairwise interaction, and the subscripts A and B represent the solvent and solute, respectively. For stable dispersions solvent-solute interactions must dominate and this is realised when $\chi < 0$. When solute-solute or solvent-solvent dominate $\chi > 0$, which leads to solute aggregation. χ can also be approximately related to the Hildebrand solubility parameters,[103] δ_i which the square root of the cohesive energy density, such that:

$$\chi \approx \frac{v_0}{kT}(\delta_{A,T} - \delta_{B,T})^2 \ , \ \delta_i = \sqrt{E_{T,C}/V}$$

(2.3)

Where $E_{T,C}$ is the total molar cohesive energy and V is the molar volume of the solvent. The enthalpy of mixing can then be given as:

$$\frac{\Delta H_{mix}}{V_{mix}} = \chi\phi(1-\phi)kT / v_0$$

(2.4)

Here V_{mix} is the total volume, ϕ is the solute volume fraction and v_0 is the solvent molecular volume. This equation illustrates that minimising the difference in solubility parameters will yield a smaller value of ΔH_{mix} and so, more favourable mixing.[104] Matching δ_i has been an effective strategy for non-polar systems where the only interactions are dispersive, however, in reality most systems also contain polar and hydrogen bonding interactions. To account for this Hansen expressed the total cohesive energy density in terms of is dispersive, D, polar, P, and hydrogen bonding, H, components[103]

$$E_{C,T} = E_{C,D} + E_{C,P} + E_{C,H} \rightleftharpoons \delta^2{}_T = \delta^2{}_D + \delta^2{}_P + \delta^2{}_H$$

(2.5)

With this in mind equation 2.3 can be re-written as

$$\chi \approx \frac{v_0}{kT}\left[\left(\delta_{D,A} - \delta_{D,B}\right)^2 + \left(\delta_{P,A} - \delta_{P,B}\right)^2 + \left(\delta_{H,A} - \delta_{H,B}\right)^2\right]$$

(2.6)

Thus careful matching of all solubility parameters is required to realise small values of χ.

Surfactant Stabilisation

As an alternative to toxic organic solvents, exfoliation of 2D materials has also been demonstrated in water, however given the high surface energy of water additional surfactants are required to facilitate exfoliation. Surfactants are amphiphilic molecules, that is, they have a hydrophobic tail consisting of a long hydrophobic alkyl chain and a hydrophilic ionic head. The hydrophobic tail adsorbs to the nanosheet basal plane by London dispersion forces, while the ionic head interacts with aqueous environment. An ion becomes dissociated from the hydrophilic head group and acts as a counter ion. These counter ions are subject to Brownian motion but remain electrostatically bound in the vicinity of the tail group, creating an electric double layer (Figure 2.8A). The diffuse nature of the counter ions results in an effective net surface charge around the nanosheet from which similarly charged colloids are repelled by coulomb forces, inhibiting re-aggregation.

The physics of the competing double layer and vdW forces was first studied by Derjaguin and Landau,[105] and independently by Verwey and Overbeek,[106] giving rise to the eponym, DVLO theory. This concept was adapted for two dimensional nanosheets and the overall potential energy as a function of the distance between the sheets, *D*, is given by[85]

$$V_T(D) \approx A\kappa\zeta^2 e^{-\kappa D} - B/D^4$$

(2.7)

Where A & B are constants of the system, κ^{-1} is the Debye screening length (a measure of the double layer thickness) and ζ is the zeta potential. This expression is strictly valid *for* $|\zeta| < 25$ mV, however it serves as an approximation for colloidal behaviour and can provide rough, numerical estimates. It is clear from the equation that two approaching particles will experience a repulsive potential barrier, if the potential is not of sufficient magnitude attractive vdW forces will overcome the repulsive forces leading to coagulation of the particles (Figure 2.8B). The magnitude of the potential barrier and thus effective dispersion stability can be achieved by tuning κ^{-1} and ζ. A zeta potential of $|\zeta| > 30$ mV is considered sufficient to achieve long-term dispersion stability and can be varied by changing surfactant type and concentration.[85]

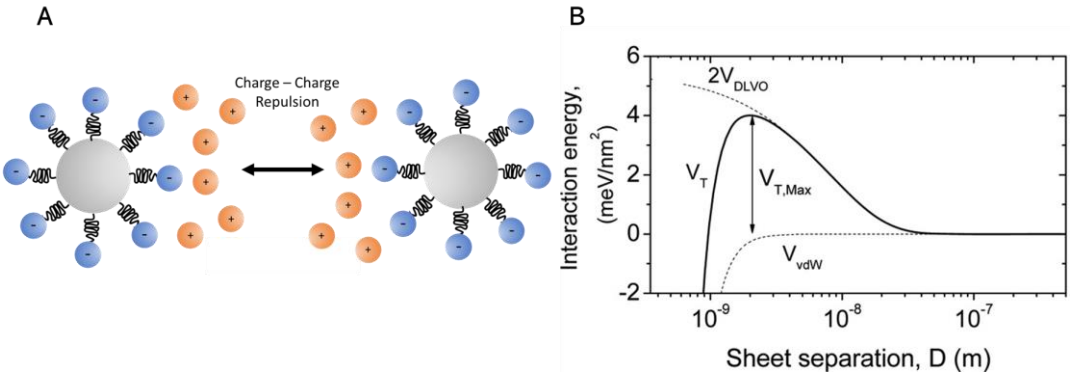

Figure 2.8 – Surfactant Stabilisation. A) Surfactant stabilisation of particles within solution via amphiphilic molecules. Image from ref.[107] B) Interaction energy as a function of nanosheet separation. Contributions due to Coulomb repulsion (V_{DVLO}) and attractive vdW forces (V_{vdW}) are shown as dashed lines. The sum of the interaction (V_T) is a solid line. Adapted from ref.[85]

From an economical and safety perspective exfoliation in water is far more attractive than organic solvents. The glaring obstacle here is the presence of surfactant. Although it has been shown that nanosheet electronic devices can be prepared from water/surfactant

dispersions, the nanosheet-surfactant-nanosheet interface must be detrimental to the transport properties of the network. Furthermore typical printing substrates and techniques are often not compatible with water-based solutions due to the high boiling point, surface energy and viscosity. It is therefore preferable to exchange exfoliated nanosheets into a more suitable solvent for final processing.

Liquid Cascade Centrifugation

Although top-down exfoliation methods effectively delaminate layers from their parent crystal, the manner of delamination is not a precise affair. At the same time, high-energy sonication can also induce scission along the basal plane of already exfoliated layers. This means that the resulting nanosheet dispersions are polydisperse in nature with nanosheets comprising of a broad range of lengths and thicknesses. This can have significant implications in terms of applications. Electronic devices may require well defined band gaps, while larger sheets are optimal for mechanical reinforcement. With this in mind, having a degree of control over the lateral size and thickness of the final dispersion is necessary in order to optimise their application. This has been addressed by implementing centrifugation strategies to narrow the size distribution of nanosheet dispersions.

Two techniques have generally been employed for size selecting of nanosheets: density gradient ultracentrifugation (DGU) and liquid cascade centrifugation (LCC). DGU exploits to subtle differences in nanosheet density, whereby a medium of graded density (DGM) is used to separate out certain sizes of nanosheets when the nanosheet density is equal to that of the surrounding medium.[108]

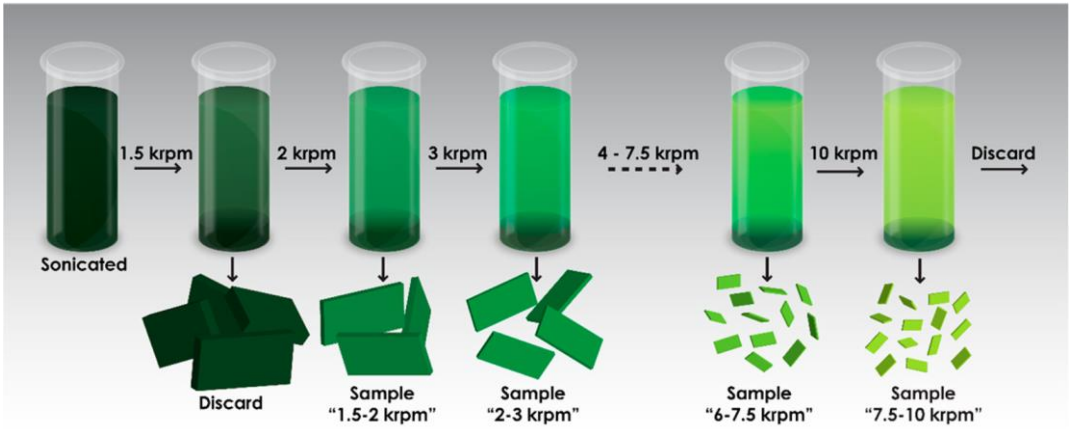

Figure 2.9 – Size Selection of Nanosheets via Liquid Cascade Centrifugation. Nanosheets of specific size distributions can be trapped by centrifuging in iterative steps. Image from ref.[109]

LCC is a sedimentation based approach where nanosheets can be size selected through the application of centrifugal forces. The rate of sedimentation is described by the Svedberg equation

$$s = \frac{m(1-\rho V)}{f} \tag{2.8}$$

Where s is the sedimentation coefficient, m is the mass, ρ is the solvent density, V is the volume a gram of material occupies in the solvent and f is the frictional coefficient. The key here is the mass dependence of the sedimentation where larger and thicker nanosheets will sediment faster than their smaller and thinner counterparts. Centrifugation acts to catalyse this sedimentation process and can be exploited to extract particular size fractions of nanosheets. This is achieved by applying increasing centrifugal forces in iterative steps. Removing the sediment between each step captures a certain size fraction of nanosheets. After a final high speed centrifugation step, the final dispersion is enriched with small monolayer sheets.[109] The sediment from previous steps can be simply be redispersed under mild sonication to yield nanosheet dispersions of discrete sizes (Figure 2.9). The simplicity

and versatility of the technique makes it an attractive post-processing step for nanosheet dispersions however there are some considerations to bear in mind. Primarily, the mechanism of sedimentation results in nanosheet dimensions being intrinsically coupled, that is, nanosheets of large lateral sizes are thicker and contain multiple layers whereas monolayer rich dispersions can only be isolated at lateral sizes less than 50 nm.[110] The inability to obtain large monolayers is a significant drawback of LPE, however, in this work, the isolation of monolayers is not of primary importance and LCC is a useful method to broadly define the distribution of nanosheets present.

Chapter 3

2D Networks and their Composites

With the isolation of 2D materials and their superlative properties now realised, attention has turned towards their utilisation for functional devices and materials.[111] One approach is to isolate single 2D nanosheets and directly stack/arrange the nanosheets on other 2D materials or deposited metal contacts, as shown in Figure 3.1A. This has shown success in preparing heterostructures and single nanosheet devices for applications such as strain sensors,[112] transistors[113] and photovoltaic devices.[114] The drawback here, is that the process is slow and cumbersome, however, a degree of scalability has been achieved in the form of

layer-by-layer growth of heterostructures utilising bottom up processes such as MBE and CVD. This method, broadly termed vdW epitaxy,[111] is still in its infancy and faces critical challenges to implementation in particular, control over layer thickness and a lack of understanding on the mechanisms underlying growth and performance.[115] Furthermore, the previously discussed limitations of bottom-up processes still remain, and so it appears unlikely that vdW epitaxy will be the source of low cost, mass market devices.

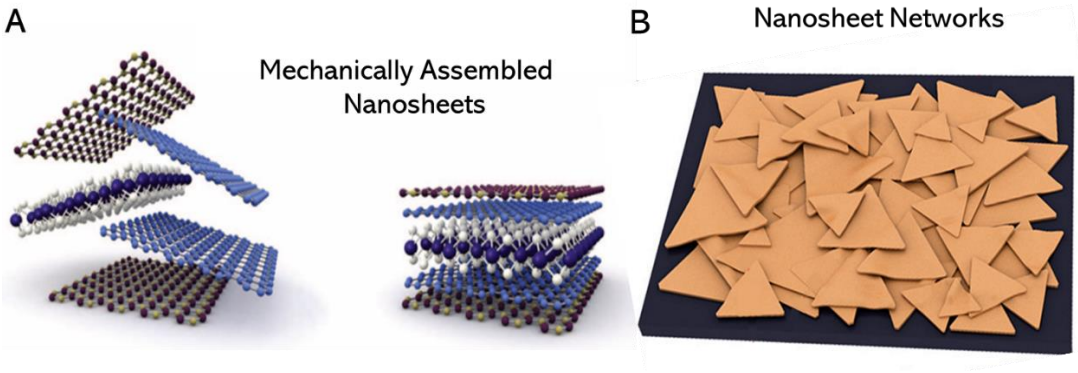

Figure 3.1 – Assembled Nanosheets and Nanosheet Networks. A) Schematic of mechanically stacked nanosheets from which functional heterostructures can be obtained. The process requires precise placement of nanosheets in order to obtain well-defined reproducible devices. Adapted from ref.[111] B) Schematic of networks formed from overlapping of adjacent nanosheets. This type of assembly leads to large area, continuous nanostructured networks. Adapted from ref.[116]

Solution processed nanosheets offer an enticing alternative in terms of both cost and ease of processing. The simplicity lies in the fact that nanosheet dispersions are essentially inks and are compatible with conventional printing methods for large area electronics.[117] The advantage here is that processing temperatures are relatively low which allows for direct deposition on a wide array of substrates, in particular flexible and stretchable polymers. Additionally, nanosheet dispersions can be readily dispersed into polymer solutions for the preparation of functional polymer nanocomposites.[118,119] In comparison to vdW epitaxy, devices from solution processed dispersions are not limited to interactions

between a few nanosheets and their electrical contacts. Instead devices comprise of vast networks of nanosheets (Figure 3.1B) and performance is, more often than not, limited by the presence of vdW junctions between the sheets and by extension the connectivity of the networks.[120] While this may complicate network performance it can also offer an opportunity, as networks can be sensitive to external stimuli, which is realised through the change in electrical properties of the network. This means that networks show exceptional promise in terms of sensing applications. This chapter will briefly discuss some of the common properties of networks comprised both solely of nanosheet networks and nanosheet/polymer blends, before moving to the percolation type behaviour these materials display.

3.1. Low-Dimensional Networks

As the Internet of Things has garnered increasing interest, there is a palpable need to develop technologies which can be seamlessly integrated into everyday life. Conventional silicon technologies are bulky, inflexible and costly, which limit their integration in areas such as health monitoring where devices will be imbedded in clothing or adhered to the skin and comfort is paramount. Here printed networks of nanomaterials (Figure 3.2A,B,C) show much promise owing to their stability, versatility and device performance. 0D, 1D and 2D inks have seen rapid growth and have been adapted to a variety printing techniques. Since each strategy has a distinct set of characteristics, the morphology of nanomaterial films can vary by printing process. However, there are common features in all printed networks which are pertinent to device performance.

A feature of nanomaterial networks is that their conductivities are orders of magnitude lower than the intrinsic conductivity of the constituent material, furthermore, there can be a high dependence on the geometry of the constituent nanoparticles.[121] This points to

some rather complex interactions during network formation. Conductive nanomaterials deposited on a substrate form a disordered array of particles which yield a macroscopic conductive network. Within the network, its constituents are separated by junctions where adjacent particles are in close proximity and are separated by a narrow vdW gap. Although it should be noted that in the case of metallic nanomaterials these gaps are bridged by disordered grain boundaries.[117] This means that electrical conduction through the network typically occurs via hopping or tunnelling of electrons across the junctions. Hopping, denotes the excitation of charge carriers into available, delocalised states. From there electrons can then 'hop' to free states at other conducting sites to transport charge.[88,122] Tunnelling, on the other hand refers to quantum mechanical effects where carriers have a finite probability of tunnelling across an energetic barrier or gap. Regardless of the mechanism the probability of electron transport is exponentially dependent on the distance between two conducting sites and so one can expect the junctions between the network constituents to play an important role in the overall networks properties.

Nanomaterial networks can be thought of as an arrangement of parallel in-series resistances, whereby the resistances experienced by an electron travelling through a particle (R_P) are also accompanied by transit across a junction between two particles, R_J (Figure 3.2D). This means the network resistance is dependent on both R_P and R_J. Junction resistances can vary dramatically, for example conducting nanosheets display rather large junction resistances of the order 10^3 - $10^7 \Omega$.[88] While studies on silver nanowires report junction resistances between 10^0 - $10^4 \Omega$.[123] The broad distribution of junction resistances points to the complex nature of charge transport in nanomaterial networks and further work is required to better understand these mechanisms.[88]

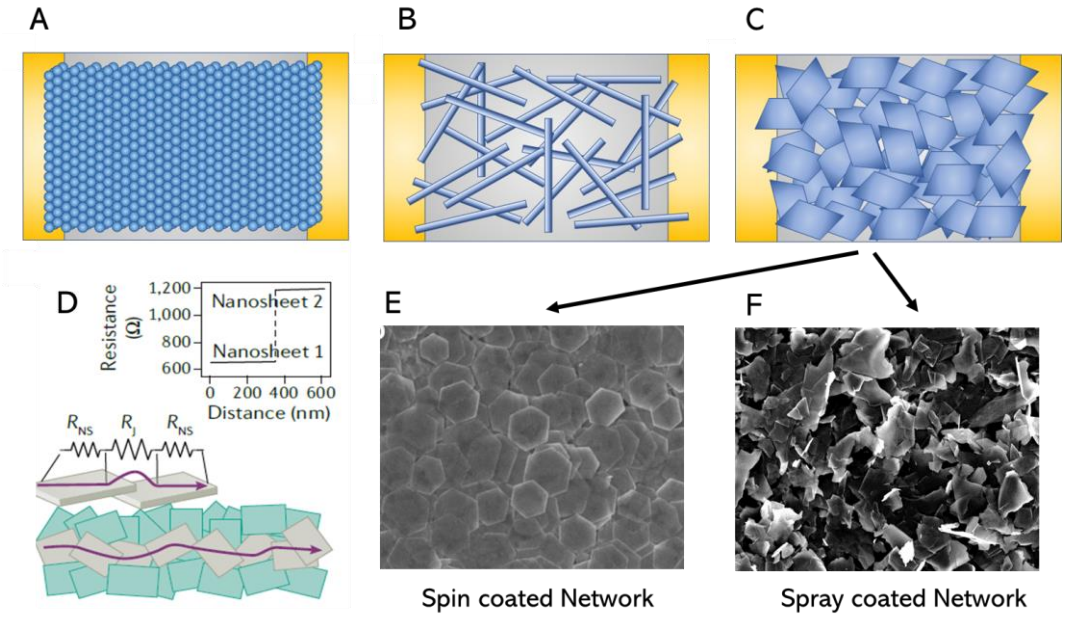

Figure 3.2 – Nanomaterial Networks. Schematic of nanostructured thin films A) zero-dimensional, B) one-dimensional, C) two-dimensional. Images adpted from ref.[124] D) Schematic of a nanosheet network, purple line defines the electron path across grey nanosheets, where it encounters series resistances associated with the resistance of the nanosheet and of inter nanosheet junction. A conductive atomic force microscopy measurement showing a large step as the atomic force microscope tip crosses an inter-sheet junction (inset). Image from ref.[88] SEM images of D) highly aligned spin coated and E) obliquely aligned spray coated nanosheet networks. Image in D) is from ref.[124]

While R_J will depend on the distance between particles, another consideration is the geometry of the nanoparticle and how this will affect the nature of the junction. We can envisage that for 0D particles such as silver nanoparticles, there is little overlap between adjacent particles. The intrinsic nanoscale dimensionality of the particles leads to a high areal density of grain boundaries, ~ 10^5 μm^{-2}. These interfaces tend to be highly disordered arising from bulk lattice termination, surface species and misalignment between randomly oriented particles.[117] This leads to the presence of transport barriers and trapping sites which can severely limit charge transport.[125] This is in contrast to 2D nanosheets or entangled nanotubes where the overlap area between adjacent particles is

far larger, facilitating improved charge transport and thus superior network conductivities. Moreover, it has been demonstrated conductivity scales with aspect ratio (AR) in conductive nanosheet networks, where high aspect nanosheets create large area and conformally contacted junctions.[88,126]

A printed nanomaterial film will contain a certain amount of free volume, otherwise called porosity, which is present regardless of the deposition method used. This arises because of packing considerations and it is well known that geometric objects cannot occupy all the space in a finite volume. For example, solid spheres packed randomly into a cylindrical volume have a packing efficiency of 64% meaning the porosity of the configuration is 36%.[127] This idea of has been extended to ellipsoids of various alignments and aspect ratios. However, even in an optimized case (aligned and high AR), numerical simulations yield porosities of ~30%.[128,129] A drawback of this porosity is that it prevents networks from realising the performance of the intrinsic material, this is particularly relevant for 2D nanosheets where large porosities will hinder conformal overlap of the basal planes, thus limiting charge transport.[130] Depending on the deposition method, the alignment and hence packing efficiency may change drastically. For example, spray coated films tend to be highly porous (~50%) and are aligned obliquely due to the blanket deposition of inks,[131] whereas spin coated films can show a higher degree of basal plane alignment and hence more efficient packing, as shown in Figure 3.2E&F. Recent advancements have shown exceptional basal plane alignment can be achieved through the preparation of ultra-thin high AR nanosheets which form tiled conformal networks with properties approaching that of single flakes.[68]

As indicated above, the average orientation of particles with respect to the direction of current is an important aspect of nanomaterials networks. As a general rule of thumb alignment of nanosheets leads to much higher network conductivities.[132] This is because high basal plane alignment leads to large area conformal junctions, significantly

enhancing charge transfer. Theoretical work on nanosheet orientation appears to be thin on the ground, however, there are reports of anisotropic electrical properties in silver nanosheet networks which is the result of partial alignment of nanosheets during processing.[130] Similar results have been reported for graphene-only networks where in-plane conductivity increases dramatically, and shows a conductivity ratio (in-plane/out-of-plane) of 1000 once alignment is induced.[132] An interesting note here is that composites and thin films containing CNTs show some very different behaviour, as CNTs rotate the number of intersections with other CNTS per unit length varies strongly as a function of average orientation angle. Hence perfectly aligned CNTs will display no network conductivity at all while the highest conductivities are observed when nanotubes are iso-tropically or close to iso-tropically orientated.[133-135]

As a final note, it is important to not only consider the properties and geometries of the constituent nanomaterials but also the environments in which nanomaterials and their networks are formed. Starting powders will inevitably contain some amounts of contaminants which are sure to effect network performance. A common strategy to limit contamination in LPE involves mild sonication of the precursor dispersion before sedimenting out the powder via centrifugation.[93] This serves to remove soluble contaminants, however the total removal of contaminants is a challenging endeavour and therefore careful selection of the starting powders is necessary. Additionally, solvent molecules and surfactant adsorb to the nanomaterial surface, which become trapped within pores of the networks during deposition. Thermal annealing can be used to remove volatiles and decompose additives however substrate choice can limit annealing temperatures and hence the efficiency with which volatiles and additives are removed.[88]

3.2. Composites

For almost the entirety of its history, mankind has made use of composite materials. The earliest examples date back millennia when straw was used to reinforce mud and clays, to improve the performance of structural bricks. This primitive technology has quite literally stood the test of time and even today straw reinforced mud is the primary component of massive structures like the Great Mosque of Djenné in central Mali (Figure 3.3A&B).

Composites are materials which comprise of two or more distinct phases where the final properties differ from those of the original components. The phases of two component composites are described as the matrix and filler. The matrix is the continuous component of the material which binds the filler and defines the material's shape. While the filler component can be thought of as an additive that is incorporated into the continuous matrix phase (Figure 3.3C&D). Composites now encompass many classes of materials, however, traditional matrices include materials such as polymers, ceramics, clays and metals.[136] The filler can imbue the matrix with additional functionality according to the properties of filler and the interaction between the two phases. Various fillers have been used to achieve mechanical reinforcement, conductivity enhancement, gas barrier and sensing capabilities in composite systems.

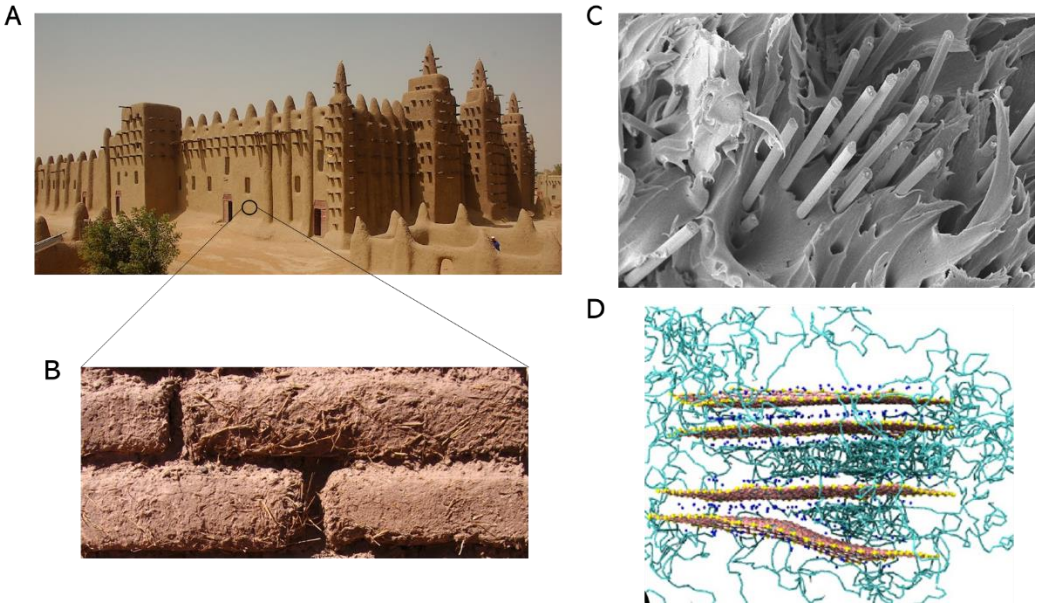

Figure 3.3 – Composite Systems. A) Image of the Great Mosque of Djenné, Mali. B) Mud and straw composites that can be used as structural materials. C) Carbon fibre filler embedded with in a continuous matrix phase. Image from ref.[137] D) Simulation of filler sheets embedded within a polymer matrix comprised of interwoven polymer chains. Image from ref.[138]

The genesis of modern composite technologies began with the development of plastics as an alternative to natural resins derived from plants at the beginning of the 20th century. Strong, flexible and cheap to produce, plastics truly have transformed the world and are now ubiquitous to daily life. The versatility of plastics means they can be found in practically any application and have supported all of the key developments of the last century such as the transition to electrification through insulating wires, the proliferation of computers and cell phones, as well as lifesaving advances in modern medicine. Plastic composites have played a vital role in shaping the modern world, usually in the form of reinforcement of existing materials. In 1936 plastic resins were combined with glass fibres and thus fibreglass composites were born. At the time fibreglass displayed properties far exceeding any available plastic. Stronger than common metals, non-magnetic, insulating

and chemically inert, fibreglass soon found itself being used in a vast array of applications from windows and thermal insulation to circuit boards and anti-slip flooring.

In the late 50s and 60s carbon fibres were introduced as new fillers for composites owing to their high strength, low weight, temperature stability and low thermal expansion.[139] Carbon fibres (CNFs) are graphitic structures in the order of 10s of microns in diameter. While not possessing the high performance properties of carbon nanotubes, their general characteristics are broadly the same and after decades of research they have found applications in a variety of industries where low weight and high strength are paramount, including the wings of passenger planes, wind turbine blades and high performance automotives.

3.2.1. Nanocomposites

Nanocomposites are defined as composite systems where the filler component is a nanomaterial. They offer advantages over traditional composites due to the enhanced properties of nanomaterials compared to the bulk, in addition, the increase in surface area improves the interfacial interaction between the nanomaterial and matrix per unit mass. This means that comparatively smaller amounts of nanomaterials are required, which keeps costs low and decreases the probability of defects.

Mechanical Properties

The impressive mechanical properties of layered 2D nanosheets and 1D nanotubes makes them ideal candidates as reinforcing agents in nanocomposites. The reason for this is the sp^2 sigma bonding and hexagonal lattices which characterise these materials making them resilient to in-plane deformations.[140] Graphene is a standout in this department, with an elastic modulus, $E = 1$ TPa and an intrinsic strength, $\sigma_T = 130$ GPa for individual monolayers.[141] This gives it the grand title of 'the strongest material ever measured'. Due

to these incredible mechanical properties graphene has been intensively studied as a reinforcement filler for composite systems with great success.[142]

The mechanics of materials are generally evaluated via stress-strain curves obtained from tensile measurements. In Figure 3.4A, typical stress-strain curves of polyethylene oxide at various nanosheet loadings are shown. From these curves, measures of several mechanical properties can be obtained and plotted as a function of filler loading (Figure 3.4B) : Elastic modulus, E_c, is the slope of a linear approximation of the stress-strain curve about 0 strain. Tensile strength, σ_T, the maximum stress which the composite can withstand. Tensile toughness, which describes the materials robustness and is a measure of the area under the stress-strain curve.

A simple description of reinforcement by a high-modulus filler (graphene) in a low modulus matrix is given by the 'rule of mixtures'[143]

$$E_c = E_f\phi + E_m(1-\phi) \tag{3.1}$$

Where E_c, E_f, E_m are the elastic modulus of the composite, filler, matrix and ϕ is the filler volume fraction. The rule of mixtures makes a number of assumptions, principally, that the filler is uniformly dispersed within the matrix, there is perfect bonding between the filler and matrix, and that the composite is absent of voids. Realising composites with these properties is not so trivial and it is well known that aggregation of fillers is an issue in nanocomposite systems, resulting from vdW interactions between fillers which can be greater than the filler-polymer affinity. At higher filler contents, aggregation becomes unavoidable leading to degradation of the mechanical properties which not predicted by equation 3.1. Thus, the rule of mixtures is generally only applicable at low filler content.[140]

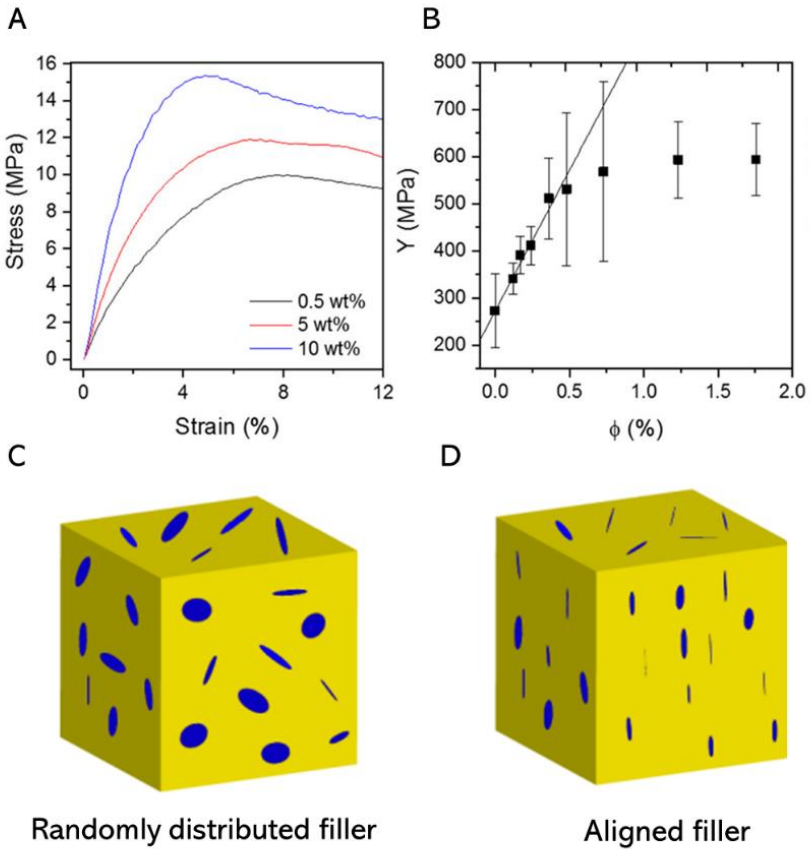

Figure 3.4 – Nanocomposite Reinforcement A) Stress-Strain curves at various filler loadings demonstrating a significant increase in strength and elastic modulus. Data from ref.[144] B) Elastic modulus plotted as a function of filler volume fraction, the solid line is behaviour predicted by the rule of mixtures, which deviates at higher filler loadings. Data from ref.[144] Schematic of C) randomly distributed and D) aligned filler nanocomposites.

While the simplicity of equation 3.1 is attractive, it does not account for the geometry or orientation of the filler particles within the matrix. For this reason a modified version has been proposed:[145]

$$E_c = \eta_f \eta_0 E_f \phi + E_m(1-\phi) \qquad (3.2)$$

Where η_f and η_0 are the filler dependent length and orientation factors. η_0 takes a value of 1 for aligned nanosheets and it has been shown that for randomly orientated nanosheets $\eta_0 = 8/15$.[146] The length factor ($0 \leq \eta_f \leq 1$) encompasses the efficiency of the matrix-filler stress transfer and reflects its dependence on both the shape of the filler and the strength of the filler matrix interface.[145] η_f takes the form:

$$\eta_f = 1 - \frac{\tanh\left(\frac{ns}{2}\right)}{ns}, \qquad n \approx \sqrt{\frac{E_m \phi}{E_f (1+\nu)}} \tag{3.3}$$

Where s is the aspect ratio of the filler and ν is Poisson's ratio. This yields an intuitive understanding that fillers with a high aspect ratio will lead to an improved elastic modulus. A further consideration is that the commercial production of layered 2D materials will likely yield nanosheets of a few layers rather than monolayers. This has implications for the magnitude of the filler modulus, as E_f depends on the nanosheet layer number and will have a smaller modulus compared to the monolayer.[140] Much like a deck of cards, the relatively weak vdW forces between the monolayers will allow graphene sheets to slide in response to an applied shear force. Thus, the overall nanocomposite reinforcement depends on the strength of the vdW bonding between the layers of nanosheets.[147]

The elastic modulus is the most widely studied aspect of nanocomposite reinforcement, however, the addition of filler can have a profound effect on several other mechanical properties. The tensile strength, σ_T, can show significant increase upon the addition of small amounts of filler, however, σ_T tends to be more sensitive to aggregation and improvements saturate at lower loadings than in the case of E_c. Aggregated nanosheets can act as failure points during elongation of a nanocomposite material. This not only results in a deterioration of σ_T but also reduces the ductility of the material and so there is often

a trade-off between nanocomposite strength and ductility.[148] Extending this idea means that the tensile toughness also varies with ϕ and there typically exists an optimised loading for which the maximum toughness can be obtained.

Electrical Properties

Plastics display an abundance of useful properties, this along with their versatility and ease of processing means that there is normally a suitable plastic to meet a desired application. One aspect where plastics struggle is in the fact that they are typically insulating. This can be resolved by the addition of conductive fillers to the polymer matrix to form an electrically conducting nanocomposite. A mechanically robust yet flexible conductive material is extremely attractive and has a wide breadth of possible applications such as electromagnetic interference shielding,[149] flexible electrodes[150] and conductive adhesives.[151] Traditionally, carbon black (CB) has been used to imbue plastic with conductive properties, however, composite conductivities using graphene and CNT fillers can be orders of magnitude higher at the same loading levels and under identical processing conditions.[152] This is attributed to the fact that graphene and CNTs display much higher intrinsic conductivity and aspect ratios (AR) than CB. The higher AR facilitates better overlap of the conducting particles and thus better transport properties. These advantageous features have resulted in graphene and CNTs already being used on a large scale as a substitute for CB in static dissipation.[153]

In terms of their electrical properties nanocomposites can be thought of as almost identical to the nanomaterial networks discussed earlier, where instead of air being present in the pores there is a matrix material such as polymer. The additional consideration here is that instead of a vdW gap between adjacent nanomaterials a thin layer of polymer now exists. This polymer increases the distance between the nanomaterials and hence, the junction resistances tend to be much larger, with reports of

R_J ~ 400 MΩ for MoS_2:Polymer composites.[144] Nonetheless, tunnelling and hopping are still the dominant mechanism for electron transport and junction-junction transport has been directly observed in carbon nanofiber composites, which were investigated using conductive-tip atomic force microscopy.[154] As in the case of nanomaterial networks, changes in composite electrical properties can be induced through the alignment (Figure 3.4C&B) of nanomaterials within the matrix or by increasing the aspect ratio of the filler. These phenomena have been both experimentally and computationally for graphene nanocomposites, which display significant increases in composite conductivity with increasing aspect ratio and nanosheet alignment.[155-158]

3.3. Percolation

In the section above, the electrical characteristics of nanomaterial networks and their composites was discussed. This was a general discussion and paid no heed to the loading of conducting particles within a film or material. Intuitively one can expect some scaling of conductivity with an increase in the number of conducting particles and as we have previously discussed, mechanical reinforcement predicts a linear increase in the Young's modulus with filler volume fraction. However, the electrical properties are not linearly dependent on ϕ and instead extreme, abrupt transitions from insulating to conductive behaviour are observed. This is because the onset of electrical conductivity is related to the connectivity of the conductive particle network rather than the interface between the matrix and the filler.

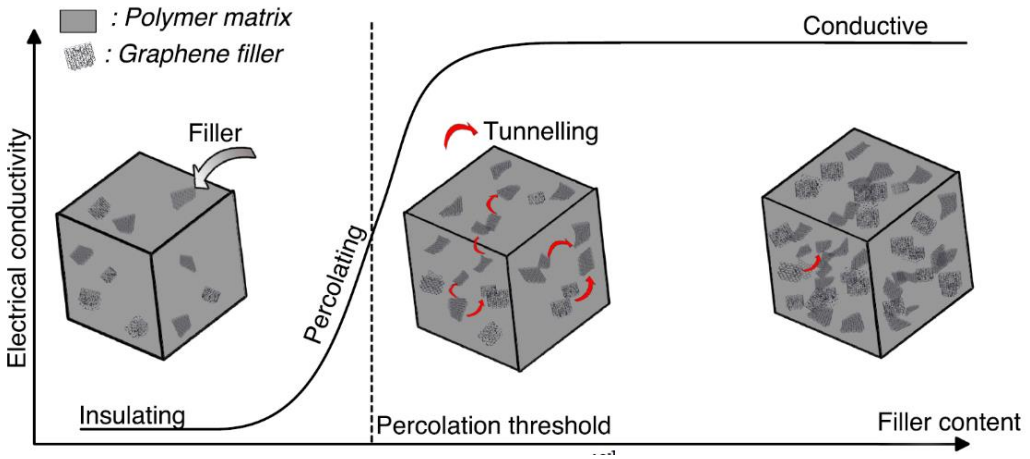

Figure 3.5 – Electrical Percolation in Graphene Nanocomposites. Schematic depicting the variation in conductivity as filler content is increased. This results in a characteristic 'S' shape behaviour which can be modelled by equation 3.4. Image from ref[22].

The effect of introducing a conductive filler into a less conductive matrix has attracted interest for decades and is by now well understood. The model composite comprises of a random distribution of filler inside an insulating matrix. When filler loadings are small, the insulating matrix dominates and isolated conductive particles 'decorate' the matrix. Since there is no long range connectivity across the material the conductivity increases marginally. As progressively more conductive material is added clusters of conductive material form and increase in size, leading to a further increase in conductivity. At a critical point known as the percolation threshold, ϕ_c, the first conductive path is formed and the distance between conductive particles is such that electrons can travel across the entire material by hopping or tunnelling mechanisms through adjacent conductive particles. This transition is characterised by a sharp jump in conductivity. About ϕ_c composite conductivity is highly sensitive to ϕ and will continue to rise as additional connected conductive pathways are established and begin to intersect. As $\phi \rightarrow 1$, conductivity begins to saturate toward some ultimate value (Figure 3.5).

This kind of behaviour is commonly observed in conductive composites regardless of the type of filler or matrix used and is described within the framework of percolation theory.[159] Percolation is a mathematical model which goes back to Flory and Stockmayer,[160] who used it to describe gelation processes in polymers and it is used widely to describe connectivity and transport in complex systems. Originally, site and bond percolation models based on square lattices (large enough to negate boundary conditions) were proposed.[161] The square sites have an occupation probability of p. A small occupation probability results in isolated sites with occasional nearest neighbour pairs bonded together forming a cluster. As p increases the size of the clusters grow, with the mean distance of two points in the same cluster defined as the correlation length. At a critical occupancy, p_c, the correlation length diverges such that it traverses the entire lattice and from this point connectivity increases, reaching a maximum at $p = 1$ (Figure 3.6A).

The similarity between this graphical model and the conductivity behaviour of composites is striking. Percolation like behaviour in composites was first reported on in 1966 when spherical silver particles where added to Bakelite.[162] This discovery fascinated both experimentalists and theoreticians alike, and percolation theory was quickly adapted to explain this phenomenon. [159,161,163-168] Conductivity percolation models are obtained by considering resistor networks from which resistors are removed at random. By assessing the connectivity of these resistor networks general models applicable to many systems can be generated.[163] The utility of this theory lies in the fact that a number of network properties can be obtained from relatively simple algebraic descriptions

$$\sigma = \sigma_c(\phi - \phi_c)^t \tag{3.4}$$

Where σ is the network conductivity, σ_c is a scaling constant and t is the percolation exponent. Moreover, the equation above is not limited by the microstructure of the

composite. This simplifying property means percolation theory is now widely used to describe conductive behaviour in nanocomposite materials comprising of a vast array of fillers, matrices and morphologies.[166]

The classical theory of lattice percolation, discussed earlier, predicts that t is universal and is determined only by the dimensionality of the space and not by factors such as structure or inhomogeneity.[164] Of relevance here is that in 3 dimensions, $t \approx 2$, while in 2 dimensions $t \approx 1.3$.[166] However, this universality was called into question as reports, particularly of polymer composites, found some t values to be far larger than 2, with values as high as $t = 9$ reported.[166,169] The physical reason for this is that continuum percolation systems will contain a distribution of junction resistances, where the distribution is broad and has a larger weighting towards poorer conductors. Due to the distribution of the network, the average resistor value diverges as the percolation threshold is approached which leads to larger divergences in conductivity than would 'normally' be expected and hence larger values of t are observed.[164,166-168] The presence of polymer between conductive particles is highly likely to lead to the scenario described above and thus, non-universal values of t are expected for polymer nanocomposites in general.

The percolation threshold, ϕ_c, has none of the universal constraints associated with the percolation exponent. That is, ϕ_c expected to be dependent on factors such as the geometry, orientation and morphology of the filler within the conducting matrix. Due to the vast number of reports in the literature it is impossible to cover all the possible interacting dependencies of ϕ_c, however some salient points can be extracted.

A computational study of ellipsoids by Garboczi[170], showed that aspect ratio and geometry of the filler has a dramatic effect on the percolation threshold. A value of $\phi_c \sim 29\%$ is predicted for spherical fillers, whereas large aspect ratio ellipsoids, such as LPE nanosheets, ϕ_c is predicted to vary as $1.27(d_s/l)$ where d_s is the sheet thickness and l is the

sheet length. Similarly, for high aspect ratio rods, such as 1D nanotubes $\phi_c = 0.6(r/l)$ where r is the rod radius and l is the length. Common ratios of nanosheets (AR = 50) and nanotubes (AR = 100) give values of $\phi_{c,elipsoid}$ = 2.54% and $\phi_{c,rod}$ = 0.6% respectively. These trends fit well with what is observed experimentally in the case of carbon fillers which display different geometries and dimensionalities. A number of studies show similar decreases in ϕ_c as fillers are changed from CB → Graphene → CNTs, although the actual values can vary from those mentioned above.[171,172]

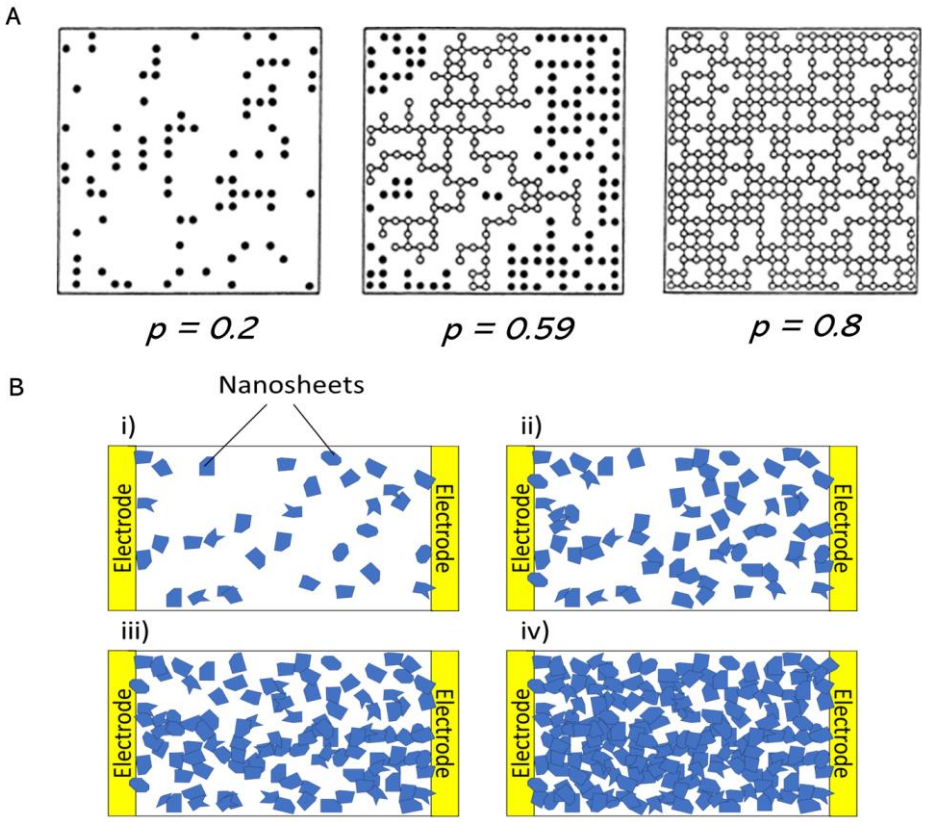

Figure 3.6 – Percolation Networks A) Classical site-bond percolation model, here the black dots denote the site, while connected paths through the lattice are shown as hollow connected dots. p denotes the probability of a random site being occupied. Image from ref.[173] B) Network connectivity in percolating 2D thin film networks. As material is added in iterative steps i) – iv) connected paths of nanosheets form allowing current to flow.

Morphology can also play an important role in determining ϕ_c. Typically the orientation of the filler and degree of aggregation are considered. Several reports both computational and experimental show that alignment of nanosheets leads to a increase of ϕ_c in the direction of alignment.[155,174,175] For example, highly aligned nanosheet networks display percolation thresholds greater than 10 vol%,[131,176] while, homogeneously dispersed graphene/polymer composites display values of $\phi_c \sim 1$ vol%.[122] When considering nanotubes, the lowest percolation thresholds are attained from random orientations and alignment leads to increases in ϕ_c, in fact no percolative behaviour will be observed at moderate CNT loadings for highly aligned nanotubes.[134,135] This is the result of a dramatic reduction in overlap area with increasing CNT alignment.

Aggregation is a common occurrence in nanocomposites and while this may be deleterious to the mechanical properties, it can have the advantage of significantly reducing the percolation threshold. In such instances, rather than being uniformly dispersed within the matrix, conductive particles coalesce into filler rich and filler depleted regions. Since the filler is essentially confined to a smaller volume within the material, ϕ_c values are reduced compared to the homogeneously dispersed case.[177-179] This behaviour is analogous to what is observed in highly porous media or segregated networks where the filler must aggregate in the regions not occupied by voids or large impenetrable solids.[180-182]

Similarly, percolation type behaviour can also be observed in thin films deposited on insulating substrates. Here, one can imagine an ink containing nanosheets, where the ink is deposited in an iterative number of steps through passes of a spray coater or inkjet printer. The build-up of the network over successive passes is shown in Figure 3.6B. After the first pass the network is discontinuous between the electrodes and the substrate is decorated in islands of nanosheets. As more material is deposited there is eventually a

point where a single continuous pathway will form, this is known as the critical thickness, t_c. Above t_c, conductivity scales in a percolative manner according to

$$\sigma \propto (t_{Net} - t_c)^n \tag{3.5}$$

where t_{Net} is the network film thickness and n is a new percolation exponent. Naturally this thickness scaling dependence does not continue indefinitely and conductivity will saturate towards a bulk value, at an approximate thickness of ~300 nm for LPE nanosheets.[183]

3.4. Fabrication and Deposition Methods

The solution phase processing of 2D materials and other nanomaterials opens the door to a multitude of opportunities in printed electronics and functional materials. However, creating stable dispersions is just the beginning, as nanosheets must be assembled as networks or combined with other materials to produce devices. This area has been the subject of intensive efforts as researchers search for the most effective strategies for developing nanomaterials into the next generation of technologies. In the following section, we will consider some fabrication techniques of bulk nanocomposites and printed nanomaterial networks.

3.4.1. Preparation of bulk polymer nanocomposites

Incorporating nanomaterials into polymers is highly advantageous, allowing for improved mechanics and additional functionalisation in the form of electrical and sensing properties. There are several strategies used to insert nanomaterials into polymer matrices. Although each technique is inherently different, they all seek to achieve the same end goal: the homogenous dispersion of nanomaterials within the matrix. This is actually somewhat of a challenge as the high specific-surface area, and strong self-affinity through

vdW forces, means nanomaterials have a tendency to aggregate. The most popular methods for nanocomposite preparation are solution blending, melt blending, and in-situ polymerisation. While recently, some more innovative methods have been proposed, such as infusion of nanosheets by swelling of polymers in nanomaterial dispersions.[184]

3.4.1.1. *In-situ polymerisation*

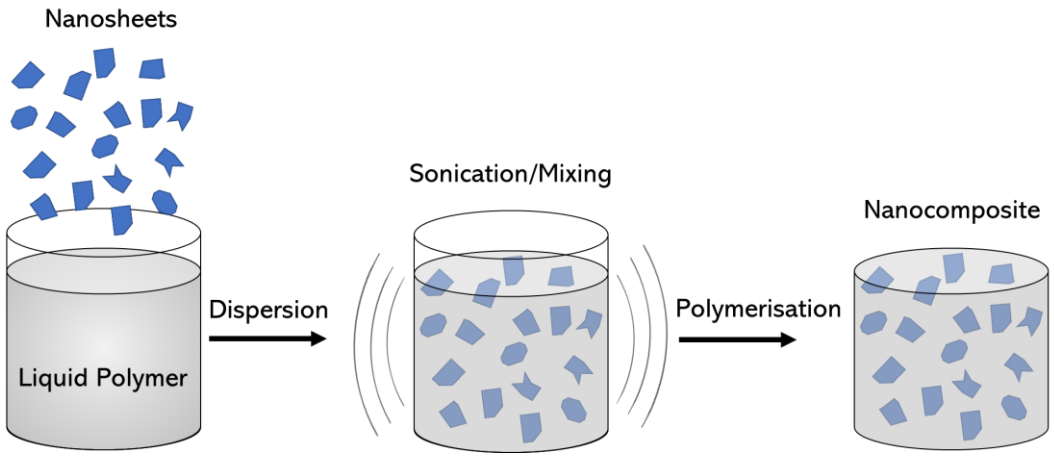

Figure 3.7 – In-situ Polymerisation. Schematic of a nanocomposite formed by in-situ polymerisation. Polymer and nanomaterials are dispersed into a homogenous mixture. Crosslinking is then initiated by a catalyst or curing yielding a nanocomposite. Image from ref.[185]

In-situ polymerisation can be achieved by first introducing nanomaterials into a polymer solution and dispersing via mixing and sonication. Once a homogenous dispersion has been achieved, a curing agent is added, which crosslinks the polymer chains with the filler *in-situ* to form the final composite (Figure 3.7). In-situ polymerisation has proved remarkably successful in forming well-dispersed nanocomposites and was the first method used commercially by Toyota in 1991, where nanoclays were mixed with nylon fibres for the manufacturing of timing belts.[186] The nature of the process creates an improved polymer-nanomaterial interface as covalent bonds are formed between monomers adsorbed to the nanomaterials surface and the matrix.[187] This is highly beneficial for the mechanical properties as a good interface facilitates better stress transfer

between the polymer and nanomaterial.[145] On the other hand, this can hamper the electrical properties, as covalent bonds hinder contact between fillers and reduce the effective aspect ratio.[122]

3.4.1.2. Melt processing

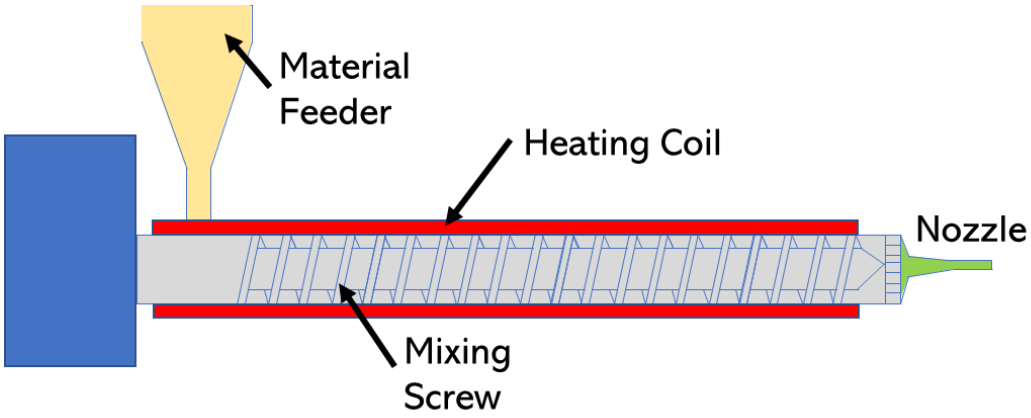

Figure 3.8 – Melt Processing. Schematic of melt compounding process where Nanocomposite and polymer pellets are fed are mixed by a screw under heating creating a viscous liquid mixture. Upon cooling a solid nanocomposite forms. Image taken from ref.[188]

Melt processing is often preferred when large volume fractions of nanomaterials are required. The process offers simplicity and high throughput, which is widely applied in large-scale manufacturing. During the process, polymer pellets are melted into a viscous liquid, and nanomaterials are dispersed into the liquid polymer by shear mixing or extrusion (Figure 3.8). The challenge here, is that adding large quantities of nanomaterials significantly increases the mixture viscosity and can lead to polymer degradation in high-shear environments. This means that empirical optimisation of processing parameters is required, with a new set of parameters needed each time filler loading is changed.[187] Furthermore, homogeneity of small volume fractions of filler is often challenging to achieve, and melt processing nanocomposites typically show higher percolation

thresholds and lower conductivities than nanocomposites fabricated by other methods.[71,122,189]

3.4.1.3. Solution blending

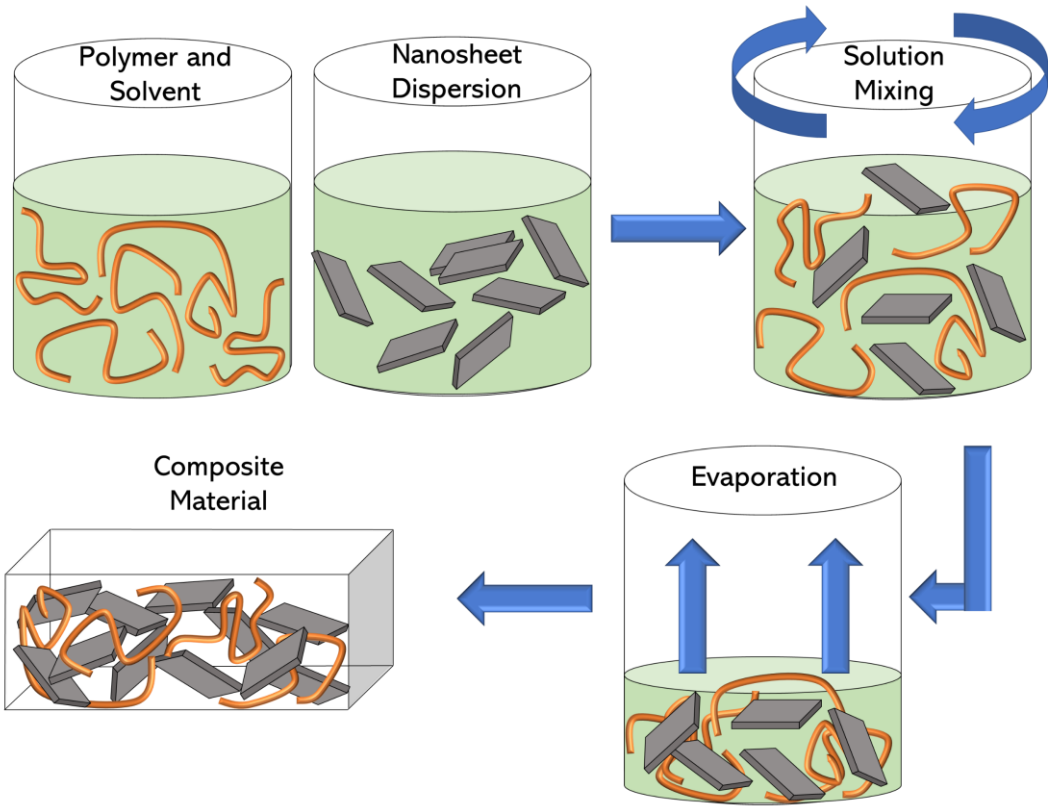

Figure 3.9 – Solution Bending. Schematic of a nanocomposite formed by solution blending. Polymer and nanomaterials are prepared separately in common solvents. They are then mixed by blending and ultrasonication. Finally, the solvent is evaporated to form the final nanocomposite. Image from ref.[190]

Solution blending involves polymer dissolution and dispersion of nanomaterials in a common solvent. Typically the polymer solutions and nanomaterial dispersions are prepared separately before being mixed under a combination of mechanical stirring and ultrasonication. Nanocomposites can then be formed through filtration of solutions onto filter membranes or solvent evaporation under mixing before casting into moulds (Figure 3.9). This method has proven particularly useful since the low viscosity nature of the

solutions facilitates good dispersion of nanomaterials, leading to lower percolation thresholds, compared to other methods, and enhanced nanocomposite performance.[189] One problem which exists is finding solvents that are compatible with both polymer solubility and nanomaterial dispersion. This is particularly true for thermoplastic elastomers, which are typically only soluble in high boiling-point and toxic solvents such as DMF [142,191] and THF.[192]

3.4.2. Deposition Methods

Developing nanomaterials for flexible electronics requires a refinement of deposition techniques, enabling dispersions to be transformed into networks in a low complexity and cost-efficient manner. The relative ease with which the rheological properties of 2D dispersions can be tuned allows for formerly graphical printing techniques, such as inkjet printing, spray coating, and screen printing, to be used as deposition methods for functional inks. This compatibility with mature and well-established techniques has seen the rapid proliferation of printed nanomaterial networks across materials research and industry.

3.4.2.1. Screen Printing

Screen printing is an ancient technique dating back to 200 AD in China, where stencils were used transfer inks onto fabrics. Over the preceding centuries, refinement of the process has allowed the printing of more intricate designs, and deposition on virtually any substrate is now possible. During the 20th century, screen printing evolved from its graphical origins and is now the technique of choice for mass production of printed electronics, photovoltaics, and organic displays. Screen printing is an inherently simple technique that benefits from being easily compatible with a wide array of inks, while continuous films can be deposited in a single pass with proper ink optimisation. In

conjunction with easily integrated roll-to-roll processes, these properties allow screen printing to realise an exceptionally high throughput of 80 m/s.[193]

Generally, a squeegee transfers ink through a patterned mesh onto a substrate. The mesh comprises silk, fibre, or metal threads, with the mesh pore size defined by the thread diameter and the spacing between threads. Mesh size is the primary parameter for determining resolution; however, the rheological properties of the ink also play a role and with proper tuning of these parameters print feature sizes of 100 μm are readily achievable. Patterned stencils are prepared by first coating the screen in a photo-polymerised resin. Masking the desired pattern with a film positive during the curing process, yields the final stencil.

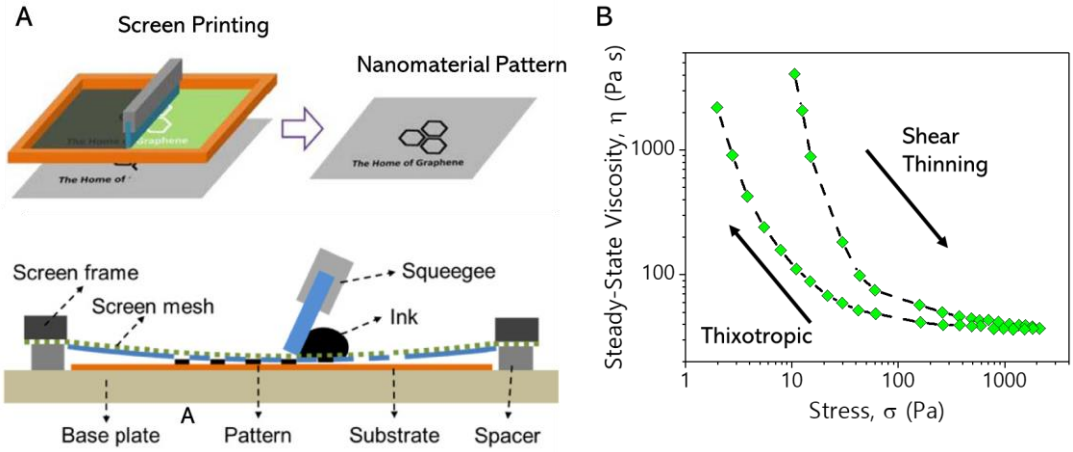

Figure 3.10 – Screen Printing. A) A schematic of the screen printing process used to print viscous nanomaterial ink. The squeegee exerts a shear force which pushes ink through the patterned mesh to deposit on a substrate. A spacer is used to create a gap between the screen and substrate allowing for smoother deposition. Image adapted from ref.[194] B) Desirable properties in screen printing inks which display both shear thinning and thixotropic behaviour. Image from ref.[195]

A schematic of the printing process is shown in Figure 3.10A. As the squeegee applies shear, the ink undergoes a decrease in viscosity and flows through the screen. During the

printing process, the paste experiences a significant variation in strain rate (1 – 100 s^{-1}). At the highest shear rates, the paste is at its most liquid-like and flows easily through the screen to deposit on the substrate. As the shear rate is reduced, the ink approximately recovers its original viscosity and holds the deposited pattern. This means that the rheological behaviour of an ink is essential to its printability, with the key requirement that the ink is thixotropic and shear thinning (Figure 3.10B) in nature.

The screen printing process requires inks that are highly viscous and are usually described as pastes. These pastes have viscosities of 1 – 10 Pa s. This requirement for higher viscosities is not generally suited to as-prepared LPE dispersions, and therefore inks need to be thickened in some way. One route to higher viscosities is increasing the loading of nanomaterials; ink rheology strongly depends on the volume fraction, ϕ, of nanoparticles present within the liquid. Nanoparticles dispersed in a liquid affect their flow field due to energy dissipation from particle-liquid and particle-particle interactions.[196] The number of these interactions increases with ϕ which restricts particles to smaller diffusion domains. The net result is a decrease in the diffusion coefficient according to the Einstein-Stokes relation, $D = (k_B T/6\phi\eta r)$, which links the diffusion coefficient, D, with ϕ taken up by the solid in a liquid medium. Here, T is the absolute temperature, k_B is the Boltzmann constant, η is the liquid viscosity and r is the particle's radius. The Einstein-Stokes relation predicts D for dilute solutions, however developing equations for high concentration pastes have proved far more challenging. Several models[197-199] have been proposed to describe the relationship between ϕ and η. While precise predictions have proved elusive, the salient point here is that ink viscosity diverges with increasing ϕ.[200]

An alternative method to increase ink viscosity is found through the introduction of polymeric binders to ink dispersions. This has the advantage of lowering the mass of conductive material required to make a viscous ink while facilitating greater stability and

printability than nanomaterial and solvent alone.[201] Ethyl-cellulose has proven particularly popular with researchers, owing to its rheology and solvent compatibility being well suited to screen printing processes.[193] However, the presence of polymer between particles can hamper network performance, and high-temperature annealing is generally required to remove polymer species and recover binder-free network properties.[88,202]

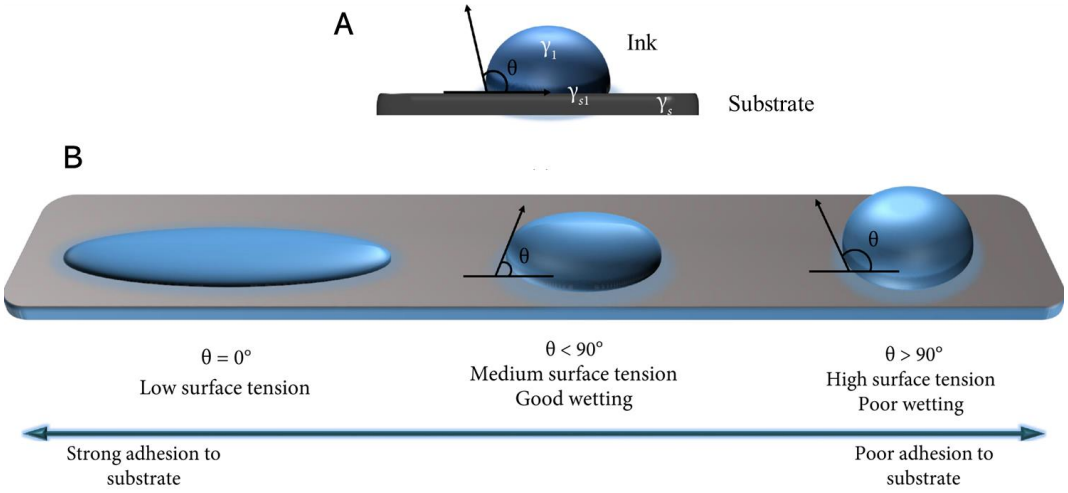

Figure 3.11 – Ink Wettability. A) Schematic of the formed contact angle, q, between ink and substrate. B) As the surface tension of the ink increases relative to the surface energy of the substrate, the contact simultaneously increases which results in poorer wetting. Images taken from ref.[203]

In order to achieve fine resolution and good film quality, there must be appropriate wetting between the ink and the substrate. Poor wetting arises from a mismatching of surface energies between the ink and substrate.[203] This results in the inability of the ink to maintain contact to the surface, forming droplets in order to reduce surface contact. This results in uneven and discontinuous films. In contrast, good wetting arises from well matched surface energies, where the ink spreads across the surface and yields smooth, continuous films. Wetting is defined by Young's equation[204]

$$\gamma_{s-v} = \gamma_{s-i} + \gamma_{v-i} \cos\theta$$

(3.6)

Where $\gamma_{s\text{-}v}$, $\gamma_{s\text{-}i}$ and $\gamma_{s\text{-}v}$ are the interfacial surface tensions between the surface, ink, and vapour, while θ is the formed contact angle. As shown in Figure 3.11, contact angles of < 90° result in favourable wetting, and a general criterion of $\gamma_{s\text{-}i} > \gamma_{v\text{-}i}$ holds to achieve good print quality. Within the print industry, it is accepted that appropriate wetting can be achieved when ink surface tension is about 7 – 10 mN m^{-1} lower than the surface energy of the substrate.[193] This is particularly relevant for printing on polymer substrates which typically display relatively low surface energies of 20 – 50 mN m^{-1} and require a careful choice of solvent for ink formulation. The final solvent choice will also need to take into consideration the solvent boiling point. This is because solvents with low boiling points tend to evaporate quickly, resulting in dried material clogging the screen mesh, which is deleterious to print quality. As a rule, solvents with boiling points above 100 °C are appropriate for screen printing.

3.4.2.2. *Spray Coating*

Aerosol deposition is found in everyday life, with almost every household containing a spray-can of some variety. Aerosol printing techniques are extremely attractive since they are not limited by the rheological constraints of other printing techniques. Spray coating is the simplest form of aerosol printing and has been used for at least 150 years. The key selling point is low cost and scalability, when fine resolution is not required. This is exemplified by the use of airbrush techniques in a wide array of industry settings for the deposition of polymers and pigment inks, where it is favoured for the versatility, and high throughput offered. These properties make airbrushing an useful technique for printed electronics as large area, and highly uniform films are easy to prepare. It is also ideal for studying the fundamental properties of nanomaterial networks since inks generally only

comprise of a nanomaterial and low boiling point solvent, without the need for additional additives, and a vast array of nanomaterials have been studied with this method to date[205-208]

A schematic of the spray coating process is shown in Figure 3.12A&B. The airbrush body is separated into two distinct chambers. The first chamber is filled with compressed N_2. The second contains the ink, which is gravity fed from an external reservoir into the spray nozzle. Engaging the trigger retracts the needle and simultaneously actuates the flow of N_2 and ink. The high-velocity N_2 shears the ink into an aerosol comprised of micron-sized droplets. The spray flume is then directed onto a substrate, which is usually heated to ensure efficient evaporation of the solvent and to avoid coalescing droplets on the substrate surface. Films of different thicknesses can be achieved by controlling the number of deposition passes, while patterned films can be prepared through bonding of shadow masks to the substrate, with a resolution of approximately ~ 50 μm.

Although the mechanism of spray coating is relatively simplistic, the parameter space is rich and leaves plenty of scope for optimisation.[209] Factors such as stand-off distance, flow rate, and nozzle diameter play a role in determining the uniformity and reproducibility of films. However, N_2 back pressure is found to have the most profound effect on final film formation, as higher pressures yield aerosols of smaller droplet size. [210]These smaller droplets allow a more uniform deposition of material on the substrate while the reduced droplet volume significantly reduces evaporation time, leaving less scope for liquid-liquid and surface-liquid interactions, which can hamper film formation.

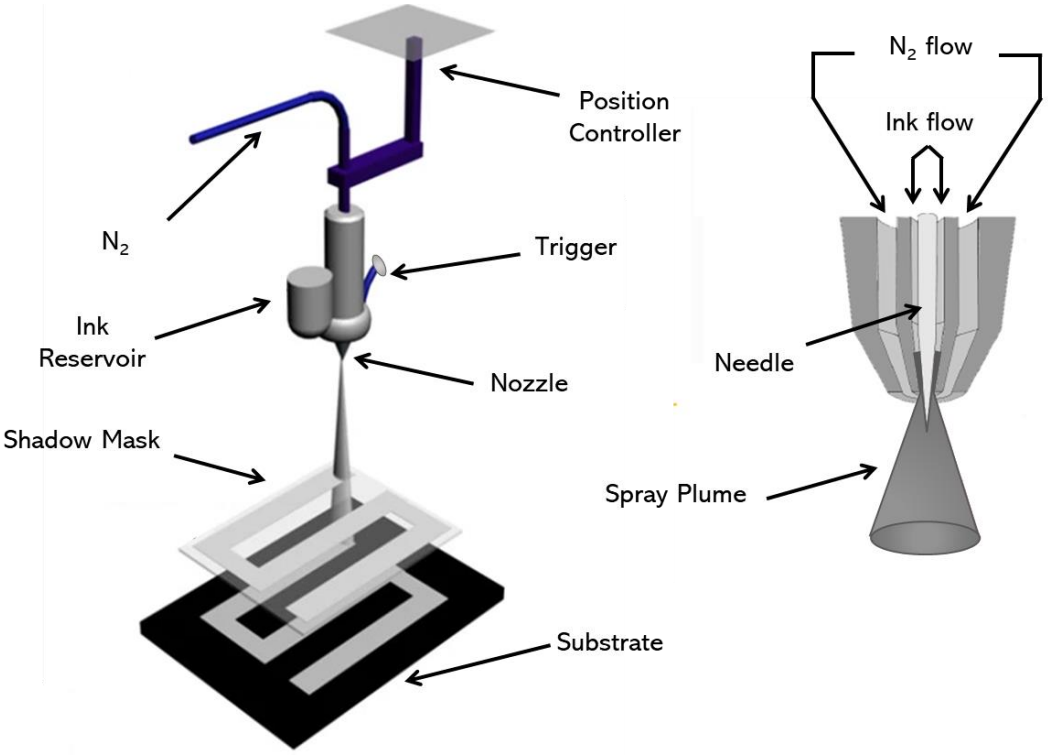

Figure 3.12 – Spray Coating. A) A schematic demonstrating the typical spray coating process using an airbrush. The blanket deposition of ink necessitates the use of shadow masks to define print patterns on the substrate. Image adapted from ref.[211] B) A schematic of the nozzle head in an airbrush system. The trigger actuates the withdrawal of the needle which allows ink and N_2 to mix forming an aerosol.

Perhaps the most attractive aspect of spray coating is the versatility it offers, as it is compatible with a wide array of organic solvents without the need for additives or complex deposition procedures. Generally, the only parameters that need to be tuned are the substrate temperature and ink flow rate, which will depend on the boiling point of the solvent in question and the limitations of the substrate. This means efforts can be focused on producing stable nanomaterial dispersions rather than on the rheological properties of the ink.

3.4.2.3. *Aerosol Jet Printing*

A recent addition to the printing toolbox, Aerosol jet printing (AJP) is a more sophisticated aerosol printing technique that allows ultrafine patterning of functional inks onto substrates. Its compelling capabilities have attracted great interest from the research community on account of the high resolution and ability to interface with both 2D and 3D surfaces. [212]

A nanomaterial ink is first ultrasonically atomised into a fine, dense mist of micron-sized droplets (Figure 3.13A). An inert carrier gas transports the aerosol to the deposition head where a sheath gas collimates the aerosol producing a jet that can be directly deposited onto a substrate (Figure 3.13B). This collimation gives AJP its fine resolution, with feature sizes down to 10 μm readily achievable. Again, the simple description belies the true complexity of the process, and in order to realise uniform and reproducible films, each new nanomaterial ink requires rigorous empirical optimisation. This is partly due to the interplay between the physical processes of atomization and transport with the rheology of the ink (surface tension, viscosity, boiling point, etc.).

AJP offers a high degree of flexibility and typical ink viscosities range between 1 – 10 mPa s, although it is possible to atomise inks of much higher viscosities (~1000 mPa s) with the use of pneumatic atomisers. This contrasts nicely against other direct write methods, such as inkjet printing which are limited to viscosities of 8 - 20 mPa s. Ultrasonically atomised aerosols are achieved by subjecting the ink to MHz frequency ultrasound, generating capillary waves on the ink's surface. At the peak of these waves, the liquid is sheared from the bulk,[213] resulting in the formation of well-defined distributions of aerosolised droplets, typically 2 – 5 μm in diameter. As has been already noted for spray coating, the distribution and size of the droplets are key aspects of film formation and can be optimised

by tuning a number of parameters such as ink viscosity, surface tension, density, and the inputted ultrasonic energy.[214]

Once atomised, the aerosol is transferred to the deposition head via carrier gas flow, where it is focused by N_2 sheath gas into a collimated jet through both a virtual and physical nozzle. There are a myriad of factors that can affect the print formation, such as solvent drying in the N_2 gas or transport losses through gravitational settling. However, it is generally accepted that the most pertinent parameter to print resolution and uniformity is the focusing ratio.[215] In addition to collimating the aerosol, the sheath gas accelerates it into a jet through the deposition nozzle. The focusing ratio defines the relationship between the carrier gas flow, that is, the amount of material carried to the deposition head, and the sheath flow rate, which determines the impinging velocity and deposited line width. Several reports demonstrate that a focusing ratio of 2 gives optimum print resolution and uniformity.

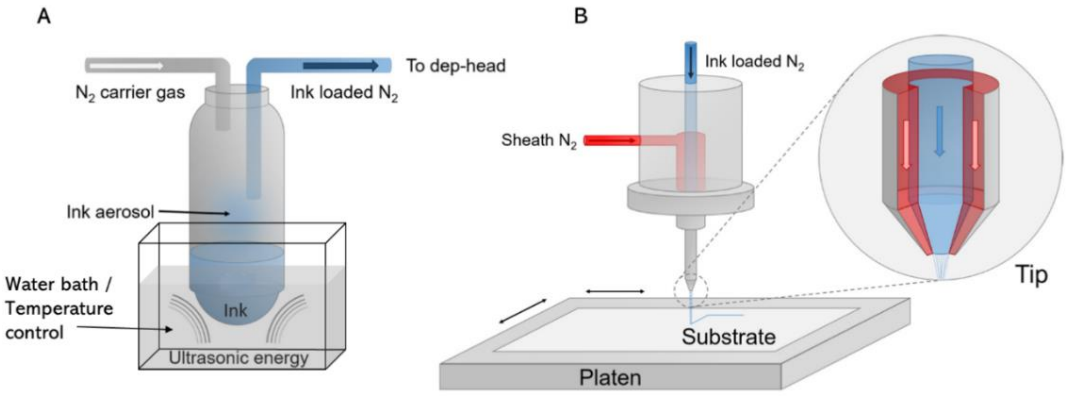

Figure 3.13 – Aerosol Jet Printing. Schematics outlining operating principles of the process. A) Atomisation of ink via ultrasonic energy, the ink is then transferred to the deposition head by N_2 carrier gas. B) Focusing, collimation and deposition of aerosol onto a target substrate. Image adapted from ref.[216]

Finally, aerosol-substrate interactions must be considered. As with spray coating, heating of the substrate is typically used to efficiently evaporate solvent and reduce droplet coalescing. However, due to the deposition velocity, this may not be sufficient, and an additional matching of the surface energies is required to ensure proper wetting of ink droplets to the substrate surface.

Chapter 4

Piezoresistance and Strain Sensing

Strain sensors operate by transducing an externally applied strain into electrical signals. Traditionally, they have been used to measure the structural health of buildings, bridges, and railway lines.[217] However, the Internet of Things (IoT) evolution has generated much interest in developing ubiquitous sensing platforms, and there is now a prescient need to develop flexible and stretchable strain sensors for use in healthcare monitoring and robotics.[218]

Nanomaterials have proven to be highly effective here, where electrically conductive

networks act as active sensing elements for piezoresistive,[219] piezoelectric[220] and capacitive[221] type strain sensors. New strain sensors technologies are not limited to nanomaterials however, with optical,[222] and triboelectric[223] sensors also showing potential. Regardless of the sensing mechanism these newer technologies generally offer superior sensitivity compared to commercial strain gauges that are currently available. Furthermore, it is possible to integrate these new sensor types with elastomeric polymers allowing much wider strain ranges than are currently possible. A materials sensitivity is defined by a metric known as the gauge factor, which is a measure of the linear change in a materials electrical properties about zero strain, for example for piezoresistive materials the gauge factor, G, is defined as $G\varepsilon = \Delta R/R_0$.

In order to give a general overview of the field, this chapter will briefly discuss the different mechanisms for strain sensing mentioned above. However, the primary focus will be on the piezoresistive mechanism as it is the most pertinent to this work.

4.1. Capacitive sensing

Capacitive strain sensors operate by sandwiching a dielectric layer between two conductive electrodes. Under an applied voltage, current cannot flow through the dielectric layer and opposite charges build up on the electrode surfaces forming a capacitor. For a parallel plate capacitor the initial capacitance is given as:

$$C_0 = \varepsilon_0 \varepsilon_r \frac{l_0 w_0}{d_0} \tag{4.1}$$

Where ε_0 and ε_r are the dielectric constants of vacuum and of the dielectric material respectively, while, l_0 is the length, w_0 is the width and d_0 is the distance of the plates. Under stretching the geometry of the plates and the distance between them changes. The

resulting increase in capacitance can be measured as a function of applied strain, yielding a strain sensor. Consider the capacitive sensor shown in Figure 4.1A. Under an applied tensile strain, ε, the sample length changes according to $l = l_0 (\varepsilon + 1)$, while the width and thickness vary according to the Poisson ratio, ν, such that $w = w_0 (1-\varepsilon\nu_{electrode})$ and $d = d_0(1-\varepsilon\nu_{dielectric})$. Assuming that the dielectric and electrode Poisson ratio are approximately equal, the strain dependence capacitance will vary as:

$$C = \varepsilon_0\varepsilon_r \frac{l_0(1+\varepsilon)w_0(1-\varepsilon\nu_{electrode})}{(1-\varepsilon\nu_{dielectric})d_0} = \varepsilon_0\varepsilon_r \frac{(1+\varepsilon)l_0w_0}{d_0} \qquad (4.2)$$

This predicts a simple linear relationship between strain and capacitance, $C/C_0 = (1 + \varepsilon)$. The gauge factor is defined by the relative change in capacitance such that $G\varepsilon = \Delta C/C_0$. This means a gauge factor of 1 is expected for parallel plates of equal area. It is worth noting however, that at large strains the Poisson ratio is no longer constant and hence the linear relationship breaks down.

Clearly the high stiffness and rigidity of conventional capacitors are not suitable for strain sensing applications. Therefore, the tactic here is to use flexible and stretchable polymers, such as polydimethylsiloxane (PDMS), as a dielectric layer with conductive electrodes prepared as nanomaterial thin films encased in an additional PDMS layer (Figure 4.1A). This yields capacitive sensors close to the theoretical limit of parallel plate capacitors ($G = 1$).[11,224-226] An example of this is shown in Figure 4.1B where $\Delta C/C_0$ is plotted as a function of strain, which displays a doubling of capacitance at 100% strain.

While capacitive strain sensors offer an exceptional linear response, the geometrical constraints severely limit their sensitivity compared to what is achievable with piezoresistive sensors. Recently Nur et al.[227] have proposed modifying the electrode geometry via pre-straining. Here a conductive layer is deposited on a pre-strained PDMS

substrate, ripples are induced in the conductive layer on release of the pre-strain breaking the simple parallel plate geometry. This yields a capacitive sensor with a much improved sensitivity of $G \sim 3$, although this is still far below the state-of -the-art of other sensor types.[228] Another approach is to alter the geometry of the sensor such that two electrodes are constructed into a 2D interdigitated electrode pattern[229] (Figure 4.1C), however, regardless of the design gauge factors are limited to less than 2.[230]

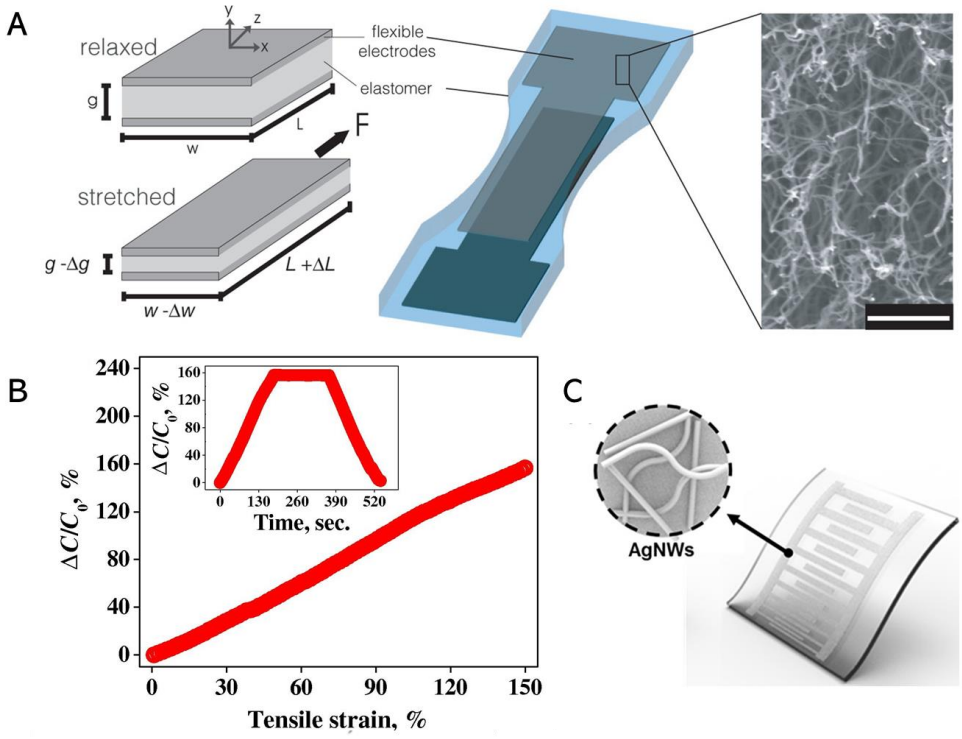

Figure 4.1 – Capacitive Sensing. A) A typical parallel plate capacitor sensor. A dielectric elastomer is sandwich between to conducting CNT electrodes to form the sensor. Straining the material reduces distance between the two electrodes according to the Poisson ratio and an increase in capacitance is observed. Image from ref.[231] B) Typical capacitance – strain response with a gauge factor very close to the theoretical value of 1. Inset – Capacitance plotted as a function of time in response to a 150% applied strain. Graph taken from ref.[232] C) Alternative capacitive senor design based on 2-dimensional interdigitated electrodes. An applied strain increases the distance between each electrode finger leading to a negative capacitive gauge factor. Image taken from ref.[231]

4.2. Piezoelectric Sensing

Piezoelectric materials are those which produce an electric current in response to mechanical deformation or conversely a change in current through the material will result in mechanical deformation. Traditionally these materials were ceramics, which tend to be inflexible and brittle. For this reason, piezoelectric materials were very rarely used as sensors. However, they found great success as actuators, forming the basis of a number of microscopic techniques such as STM,[233] and AFM,[234] where fine control of distances is required.

The discovery of the piezoelectric effect in PVDF (polyvinylidene fluoride), by Kawai in 1969, opened up new opportunities for the preparation of piezoelectric thin films and are now the dominant piezoelectric sensing elements available commercially. Virgin PVDF is found in a randomly orientated crystalline structure without any piezoelectric effect. Under processing a piezoelectric response can be created by augmenting the polymer into a semicrystalline structure which is preferentially orientated in the required sensing direction.[235] Alignment can be induced mechanically through cyclic stretching of the films, and is complimented by application of high electric fields which rotate dipoles in the direction of the field.

The piezoelectric effect arises from induced dipoles on application of strain as shown in Figure 4.2. While the opposite facing poles inside a material cancel each other out, those on the surface remain. This macroscopic polarisation generates an electric field which allows the conversion of mechanical strain to an electrical signal. In response to the electric field, free charge will flow until the polarisation effect is neutralised. This implies that no charge will flow in the steady or unperturbed state. As the force is removed, the polarisation is reversed and so charge will flow in the opposite direction back to its original state. This creates an inherent limitation as piezoelectric strain sensors are only suitable

for dynamic measurements. Furthermore, PDVF is not stretchable and has a large Young's modulus of $E = 2.5\ GPa$. This makes it useful as a pressure sensor but limits its applications in health monitoring where substrates must be soft, stretchable and conform to the skin.

To tackle the challenge of limited sensing range and rigidity, recent attempts have focused on the use of piezoelectric nanomaterials combined with elastomers and textiles.[236] These sensors take the form of nanostructured thin films or composites. PZT (lead zirconate titanate) nanoribbons[237] and ZnO nanowires[238] have been the most heavily investigated, which demonstrate continuous and high precision monitoring of vital signs and speech.

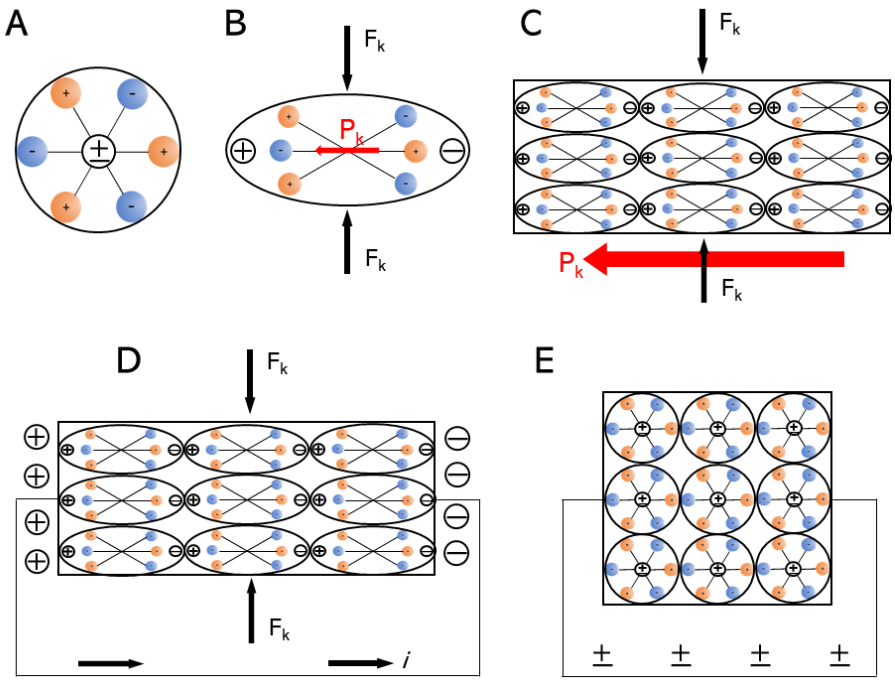

Figure 4.2 – Piezoelectric Mechanism. A) An unperturbed molecule without piezoelectric polarisation, the molecule shown here is neutral but prior polarization can exist. B) The molecule is subjected to a force (F_k) which induces a polarisation of the molecule (P_k). C) Shows the macroscale polarisation of molecules in response to an applied force. D) Opposite charges are neutralised within the body of the materials leaving a net charge on the surface, generating current flow. E) The materials returns to a neutral state when the force is removed. Images adapted from ref.[239]

4.3. Piezoresistive sensing

The oldest of the sensing mechanisms was first discovered by Lord Kelvin in 1856,[1] who reported that the current through an iron wire changed when a weight was applied to its end. Now termed piezoresistance, this describes the resistance change in a material in response to an applied strain. In the case of metals, the change in resistance arises from a narrowing in the cross-sectional area due to the Poisson effect, much like the capacitive sensors discussed earlier. As with all strain sensors, the figure of merit is the gauge factor which describes the relative change in resistance due to strain

$$G\varepsilon = \frac{\Delta R}{R_0} \tag{4.3}$$

Where ΔR is the change in resistance and R_0 is the zero strain resistance of the material. The equation shows a linear relationship between resistance and strain, and as such, is only valid for the linear or low-strain regime.

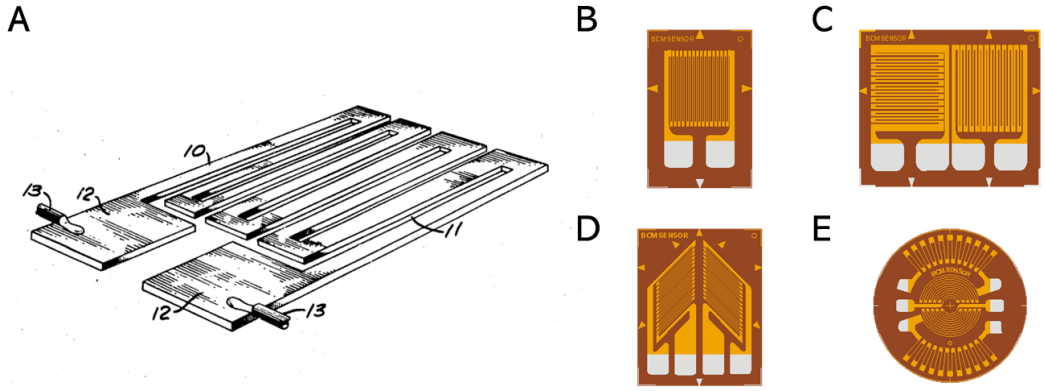

Figure 4.3 – Metal Foil Strain Gauges A) Image from one of the first commercial metal foil strain gauge patent.[240] Modern commercial metal foil strain gauges for measuring tensile strain, with patterned foils for measuring B) Tensile strain, C) Perpendicular tensile strains, D) Shear and E) Pressure.

Following on from Lord Kelvin's discovery a century prior, Simmons patented the metal foil strain sensor in 1946 and a similar design is still used widely today.[241] This comprises of parallel windings of metal foil supported by an insulating polymer backing, such as polyimide, as shown in Figure 4.3A. The popularity of metal foil strain gauges arise from the fact that they can be easily produced at scale and in a cost-effective manner. The metal foil typically consists of a nickel-copper alloy that can be easily integrated with conventional circuitry without the need for complex additional components and are readily adapted to an array of different geometries for measuring tensile strain, shear and pressure (Figure 4.3B-D). However, such gauges do have some inherent limitations: The sensitivity is rather low and is limited to $G \sim 2$ [217] by geometric constraints of the Poisson effect. This results in a small and difficult to measure output in the low strain region particularly if there is system noise.[242] Furthermore, the maximum measurable strain is determined by the yield strain of either the metal foil or polymer substrate which is typically $\varepsilon \sim 4\%$. Above this, gauges will undergo irreversible plastic deformation and can no longer return to the zero-strain resistance. A further consideration, is the relatively high elastic modulus of the polymer substrate, $E_{\text{polyimide}} = 3$ GPa, which requires adhesive bonding to the object of interest hindering the versatility and flexibility of the device.

In 1954, the piezoresistive effect was discovered in semiconductors such as silicon (Si) and germanium (Ge) with the first commercial sensors produced only a few years later. In this instance sensors, do not rely on geometric changes. Instead, an applied strain induces atomic changes which alter the electronic structure and hence the intrinsic conductivity of the material. This local electronic effect is far greater than the global geometric effect and leads to gauge factors as large as $G \sim 175$ in p-type silicon and as low as $G \sim -135$ in n-type silicon.[243] The changes in conductivity are related to variations in the number of free carriers and their mobility, which is induced by lattice deformation. This behaviour

can be strongly influenced by the direction of strain and symmetry of the lattice, as well as type and level of doping.[219]

The exceptional piezoresistive properties of semiconductors enables them to be used as high precision strain sensors. However, they are typically brittle, which restricts their applications to small strain pressure sensing. In order to achieve high sensitivity and reproducible piezoresistive behaviour, the semiconducting material must be mono-crystalline since grain boundaries, impurities and defects can dramatically impact the electronic structure of the material.[244] Manufacturing methods for monocrystalline silicon are energy intensive and expensive and so will not be used for low cost everyday applications. A further note here is that semiconductor electronic properties display a significant temperature dependence, where increasing temperature typically leads to an increase of carrier concentration in the conduction band but a reduction in carrier mobility due to increased phonon scattering. Since the piezoresistive mechanism is also dependent on the electronic structure, temperature changes not only cause variation in conductivity but also in gauge factor and requires sophisticated compensating techniques to increase the sensor operating temperature range.

The discussions above highlight a gap in the market. That is, there is a need for highly sensitive strain sensors with wide working strain ranges, which can be prepared on a range of flexible and stretchable substrates. Such sensors would open the door to a wide range of application particularly in the areas of biomedical sensing, robotics or virtual reality.[245] For example, one can envisage a scenario where humans or robots require artificial skins to manipulate objects, interface with a computer or manually guide a piece of technology. In this instance, an array of tactile sensors will be required to create haptic perception and surface strain distribution mapping.[218] For these technologies to succeed and match the level of human dexterity, sensors must be capable of detecting both minute and large

stresses/strains. Indeed simple detection is not sufficient and quantitative values of stress and strain will ultimately be required.[246]

For these applications nanomaterials have shown particular promise, where they can be integrated into polymer matrices or deposited as patterned thin films to form sensors. As has been discussed previously, the conductivity of these materials is associated with hopping and tunnelling mechanisms between adjacent conductive nanomaterials and thus the electronic properties are determined by connectivity of the junctions. The application of strain alters the structure of the network and is assumed to increase the distance between adjacent particles. Let us consider that tunnelling mechanisms dominate in these materials, in 1963 Simmons put forward an equation to describe quantum mechanical tunnelling between two electrodes separated by an insulating thin film:[247]

$$R_{tunnel} = \frac{V}{A_J J} = \frac{h^2 d}{A_J e^2 \sqrt{2m\lambda}} \exp\left(\frac{4\pi d}{h}\sqrt{2m\lambda}\right) \qquad (4.4)$$

Where V is the potential difference, A_J is the cross sectional area of the junction, J is the tunnelling current density, h is Plank's constant, d is the distance between the nanomaterials, e is the electron charge, m is the electron mass and λ is the height of the potential barrier between the two nanomaterials. The exponential dependence of the resistance on d arises from the fact that the wavefunction of an electron, and therefore the tunnelling probability, decays exponentially across a potential barrier. This results in a piezoresistive network which is highly sensitive to the distance between conductive particles (Figure 4.4A).

A materials resistance can be related to its resistivity, ρ, by

$$R = \frac{\rho l}{A}$$

(4.5)

Where A is the cross sectional area of the sample through which current travels and l is the sample length.

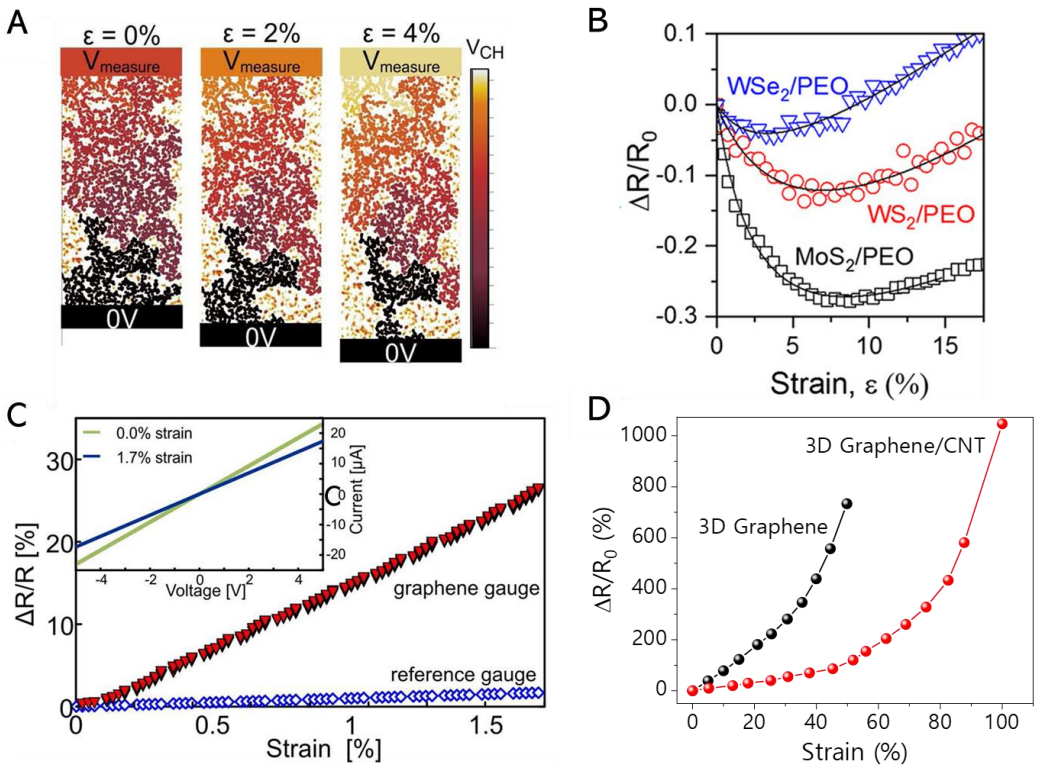

Figure 4.4 – Piezoresistive Sensing A) Graphical representation of the voltage drop across a piezoresistive network at a fixed current at various strain. As the strain increases, the voltage drop in areas of the conductive network get larger leading to higher total network resistances. B) An example of negative piezoresistive behaviour in polymer:semiconducting nanocomposites. Data from ref.[144] C) Resistance-strain response for a graphene thin film network, which displays high sensitivity and linearity at low strain . The response from a commercial strain gauge is also included for comparison. Images taken from ref.[248] D) An example of non-linearity which occurs at higher strains, this is generally characterised by an exponential increase in resistance due to the increase in tunnelling resistances between particles. Image from ref.[249]

If we recall the equation for piezoresistive gauge factor, $G\varepsilon = \Delta R/R_0$, and combing with equation 4.4, in the limit of low strain, G can be related to a materials zero-strain resistivity, ρ_0, or conductivity, σ_0 (See appendix B for full details).

$$G \approx (1+2\nu) + \frac{1}{\rho_0}\frac{d\rho}{d\varepsilon} \approx (1+2\nu) - \frac{1}{\sigma_0}\frac{d\sigma}{d\varepsilon}$$

(4.6)

The first term of the equation is associated with the geometric gauge factor, for example, an incompressible material ($\nu = 0.5$) with a constant resistivity under strain yields a gauge factor of 2. This geometric gauge factor is commonly observed in metal foil strain gauges. However, if the resistivity does vary with strain this means G has scope to vary as is seen in crystalline silicon strain sensors.

For a tensile strain, the strain dependent resistivity ($d\rho/d\varepsilon$) in nanomaterial networks is generally positive, which is explained by adjacent conductive nanomaterials being moved further apart, and thus, increasing the average junction resistance of the network. In fact, the piezoresistive effect can be incredibly large, with gauge factors as high as 500 reported in graphene based nanocomposites.[10] There are however, some examples in the literature of nanomaterials networks whose resistivity decreases with applied tensile strain, such as in MoS_2: polyethylene-oxide (PEO) composites (Figure 4.4B).[144] This counter intuitive behaviour is attributed to a good mechanical interface between the MoS_2 and PEO which allows the nanosheets themselves to be strained. This manifests in a decreasing resistivity with applied tensile strain as MoS_2 has a large intrinsic negative gauge factor ranging from -225 – 50 depending on the nanosheet layer number.[250,251]

The performance of a piezoresistive strain sensor is assessed through the measurement of the materials resistance as a function of strain. The initial resistance response is typically linear, however as strain is increased above a certain point, the fractional resistance change

deviates from linearity (Figure 4.4C&D). This can be due to a various factors such as the initiation of cracks or dislocations in the network,[252-254] this is a major drawback 0D nanoparticle sensors which are particularly sensitive to cracking due to the poor overlap of adjacent particles. For this reason 1D nanotubes or 2D nanosheets are preferred to 0D nanoparticles, as networks constituents can slide over one another allowing a larger strain range before disconnections occur (Figure 4.5A&B).[255]

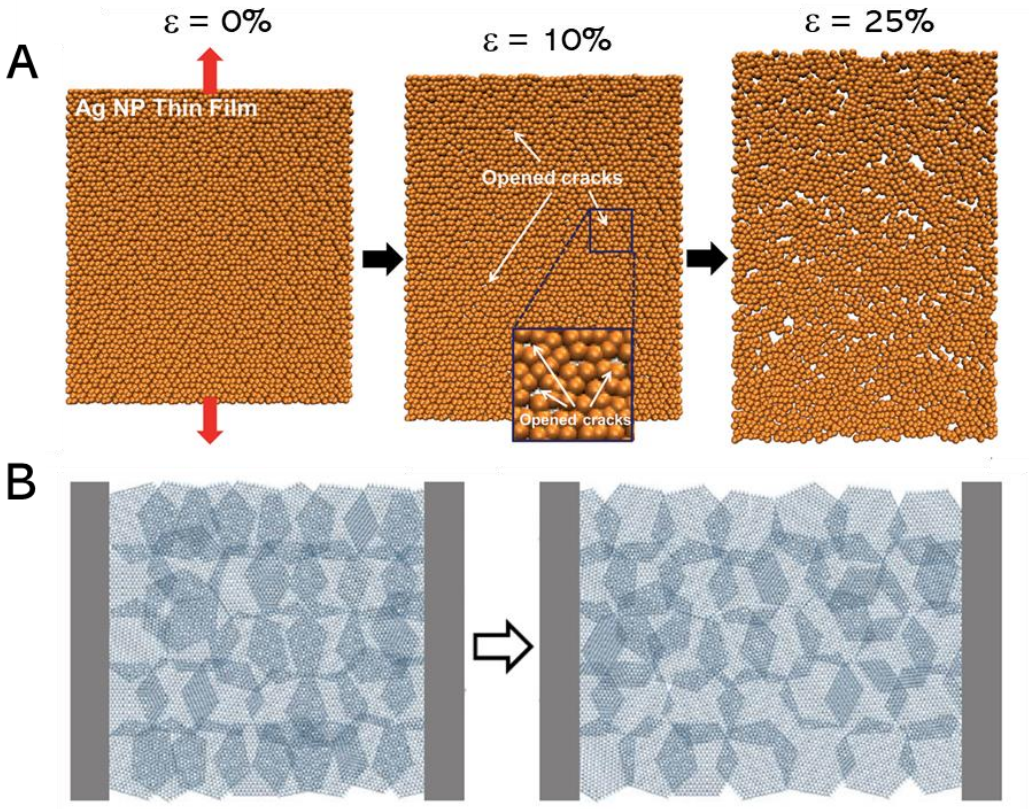

Figure 4.5 – *Evolution of 0D and 2D Networks Under Strain. A) Schematic evolution of 0D film morphology in response to applied strain. Due to particles geometry microcracks quickly propagate throughout the film as strain is applied. Image taken from ref.[253] B) Schematic of well overlapped and aligned nanosheets as strain is applied the overlap area between sheets reduces but the film is free from cracks. Image taken from ref.[117]*

As strain is increased conductive particles are separated by large distances causing an exponential increase in resistance, as predicted by the junction tunnelling resistance, R_{tunnel}. This leads to non-linear resistance behaviour which is at odds with the definition of the gauge factor in equation 4.3. That is, G describes the linear resistance-strain relationship. This particular point has led to inconsistencies in how G is reported and will be elaborated on further in the following section.

4.4. Metrics for Strain Sensing

While nanocomposites and nanomaterial thin films show immense promise for the new age of tactile sensing, there exists a wide variability in the reporting of strain sensing metrics and how strain sensing performance is evaluated. This is an issue that exists across the field and leads to a high degree of ambiguity on what exactly is being reported without looking directly at the data. For transparency we will discuss how the metrics used in this work are interpreted.

Gauge Factor

As Boland has noted,[256] the gauge factor is the most commonly reported metric of strain sensor performance. The manner in which it is reported has been left to the interpretation of researchers, which has led to gauge factors being reported in a variety of different ways. Researchers may:

- Fit a number of linear approximations to a single resistance-strain curve, such that the gauge factor is reported in different strain regimes.
- Fit a single linear approximation of the entire resistance-strain curve, but not accurately capture the resistance behaviour at lower and higher strains
- Plot the gauge factor as a function of strain.

For this reason Boland introduced an additional metric to compliment the gauge factor called the working factor, *W*, this is defined as the strain limit (taken from 0 strain) at which the fractional resistance change is no longer linear. This will give researchers information on both the sensitivity and this sensitivity's strain range for each sensing material. For this reason, the sensors reported in this work will only consider the gauge factor in the linear regime about zero-strain.

Hysteresis

Hysteresis is a phenomenon that refers to the fact that a material's properties are dependent on its previous state. Hysteresis can be found in many physical systems, but of particular relevance to strain sensors are the materials mechanical and electrical hysteresis.

Mechanical hysteresis, describes the energy dissipation which occurs during a strain cycle. During the tensile loading and unloading parts of the cycle, some energy is dissipated in the form of heat or movement of molecules within the material. This can be visualised in a material stress-strain curve, where the unloading cycle follows a lower path back to the zero stress point than during the loading phase (Figure 4.6A). The ideal case is that materials are linearly elastic, that is, they follow Hooke's law. Hookean materials are those which follow an identical linear path in both loading and unloading. In reality no material is perfectly elastic as even elastomers and extremely stiff materials display minimal hysteresis in their elastic regimes. Viscoelastic materials can show extremely large hysteretic behaviour on account of stress relaxation and are generally separated into two forms: viscoelastic solids and viscoelastic liquids. Consider a step strain which is applied to a viscoelastic material where the strain is held constant for a period of time, *t*. In a viscoelastic solid, stress relaxation effects will occur and the stress will relax to a finite non-zero value as $t \rightarrow \infty$. By contrast, in a viscoelastic liquid the stress will relax to zero as $t \rightarrow$

∞. These time dependent effects can result in materials undergoing permanent or quasi-permanent deformations depending on the strain and strain-rate applied.[257] Hysteresis is quantified in a dimensionless number and is a measure of the area of the hysteresis loop divided by the area under the loading part of the curve.

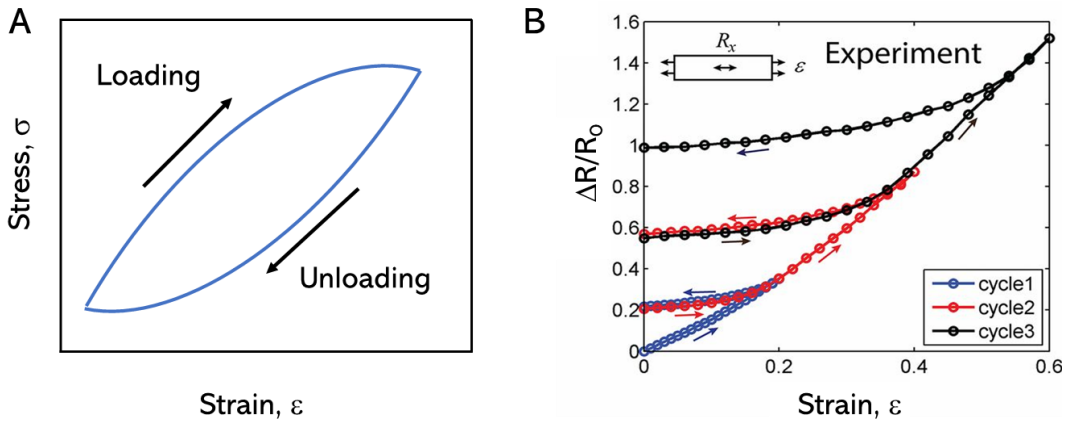

Figure 4.6 – Hysteresis in Strain Sensors. A) A schematic of mechanical hysteresis in a materials. The degree of hysteresis is defined by the area of the enclosed loop. B) An example of large electrical hysteresis in conductive CNT nanocomposites. The goal of researchers is to minimise the hysteresis loop while maintaining a high degree of linearity. Image taken from ref.[258]

Similar to mechanical hysteresis, the electrical hysteresis is a measure of how the resistance path varies during a loading and unloading cycle. In order to reliably match resistance values to an unknown strain, the resistance strain curve should follow the same path in both the loading and unloading directions, resulting in the desirable outcome of no electrical hysteresis. This metric is of great practical importance in realising commercial applications of sensors, however it is often overlooked when reporting strain sensing performance and seldom quantified. Although this area of strain sensing is less explored, some general comments can be made about the electrical hysteresis present in nanomaterial thin films and composites. The electrical hysteresis (Figure 4.6B) will be a function of both the displacement of the conductive network and the mechanical hysteresis of the polymer. The contribution of these effects are more easily observed in

nanomaterial thin films, where thickness differences between thin film (~100's nm) and substrate (~100s μm) means the mechanical hysteresis is dependent on the substrate material, while the piezoresistive performance is determined by the thin film. However, for composite systems it is far more complex as the polymer-nanomaterial interface must also be considered.[259]

Strain Rate and Frequency dependence

In order to capture the dynamic movements of the human body it is essential that the resistance response for the same strain is identical regardless of how quickly the strain is applied. One can imagine trying to capture the movements of an athlete, this will require the capturing of movements which are both fast and slow or may occur with different frequencies. This means the stability of the resistance response under varying strain rates and cycling frequencies is of critical importance. Unfortunately this too is under-reported in the field of strain sensing. When reported, nanocomposites tend to display a high degree of strain rate dependence,[260,261] whereas, nanomaterial thin films display a comparatively small rate dependence.[89,262]

A common feature of strain sensors under dynamic repeated cycling, is that the peak to peak values of resistance tend to decay in a power law like manner, before eventually reaching a steady state, as shown in Figure 4.7. One train of thought is that this is related to the conductive network being in a non-equilibrium position when first deposited, as the network is subjected to small deformations this allows a gradual reconfiguration of the network to a more optimised state and thus the resistance of the network falls.[263] Another interpretation is that resistance decay is related to mechanical effects of the polymer matrix.[264]

The Mullins effect describes stress-softening that occurs in elastomeric materials under repeated cycling, this manifests as a power law decrease in the maximum material stress

known as Basquin's law (Figure 4.7B).[265] The degree of softening is strongly related to the applied strain with higher strains leading to more pronounced softening. This effect has been attributed to a number of mechanisms but broadly appears to be related to internal friction between the polymer chains. This sliding of adjacent chains leads to increased temperatures, chain breakage and other structural changes.[264,266-268] The Mullins effect also leads to a phenomenon known as permanent set which refers to an extension in the length of a sample at zero stress following a stretch and release.[266]

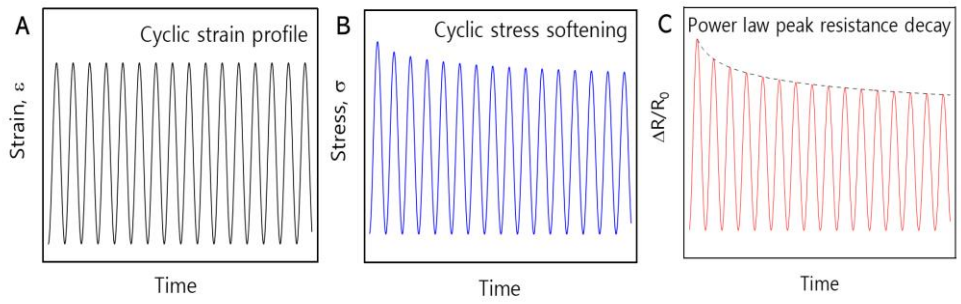

Figure 4.7– Cycling Dependence of Strain Sensors A) Sensor under goes a cyclic straining test. B) The maximum stress decreases according to Basquin's law, with the behaviour occurring as a consequence of the Mullin's effect. C) The relative resistance response from the sensor, the maximum relative resistance is seen decrease in a Basquin-like fashion showing equivalence between the mechanical and electrical response.

Both the Mullins effect and permanent set are reversible to a certain degree, however, this tends to be on timescales ranging from 100 – 10^6 s.[266] Recently, the equivalence between the Mullins effect and the peak-peak resistance decay in piezoresistive nanocomposites has been shown,[264] with the effect being attributed to a Mullins-like restructuring of the conductive network during cycling (Figure 4.7C).

An important note here, is that the mechanical hysteresis and Mullins effects discussed above occur in both neat polymers and in filled polymer nanocomposites, however the presence of filler tends to exacerbate these effects.[266,267,269] This leaves researchers with an

issue, on one hand sensors should have low resistances that meet the requirements for modern circuitry. As has been seen from percolation theory, this will require a non-trivial amount of filler. On the other hand, large quantities of fillers may compromise the sensing performance, though interfacial effects between the filler and matrix. This problem has yet to be solved but suggests that the best way forward might be to prepare piezoresistive thin films supported by neat polymer substrates allowing these effects to be mitigated.

Overview

Table 4-1: General characteristics of various sensor classers and types.

Sensor Type	Linear strain range	Gauge Factor	Hysteresis	Dynamic Sensing	Steady - state Sensing	Strain rate dependence
Capacitive	100%	~1	Small	Yes	Yes	No
Piezoelectric	0.1%	~20	Large	Yes	No	Yes
Metal Foil (Piezoresistive)	3%	~2	Small	Yes	Yes	No
Semiconducting (Piezoresistive)	0.3%	~200	Small	Yes	Yes	No
Nanocomposite (Piezoresistive)	Up to 20%	~500	Large	Yes	Yes	Yes

An overview of strain sensing characteristics for the various sensor classes and types is given, Table 4-1. While the list of compared properties is not exhaustive, it serves to show that at present a trade-off usually exists depending on the choice of sensor. For example capacitive sensors offer an excellent linear strain range, hysteresis and cycling performance but have a poor sensitivity, in contrast piezoresistive semiconducting strain gauges offer high sensitivity but a small linear strain range. Ultimately the choice of sensor will depend on the target application however, there exists a gap in the market for a general purpose sensor which can measure both small and large strains with good sensitivity, here

piezoresistive nanocomposites offer the most viable solution if methods can be found to mitigate hysteresis and strain rate effects.

Chapter 5

Bulk to 2D Sensing

Nanocomposites show exceptional promise as strain sensors owing to their large working strains and sensitivity, which far outperform the standard commercial strain gauges available today.[270] The development and optimisation of these new strain sensing technologies is essential if the promise of technologies such as unobtrusive, constant health monitoring or seamless interfacing between humans and robotics are to be realised.

A graphene and siloxane based nanocomposite named G-putty was reported in 2016, which was a viscoelastic liquid in nature and showed exceptional sensitivity, reporting gauge factors as large as 500.[10] G-putty's viscoelasticity allows graphene nanosheets to be extremely mobile within the polymer matrix and a clear link has been demonstrated

between G-putty's piezoresistive properties and viscosity.[271] Furthermore, flake mobility leads to two distinct resistance behaviours in response to strain. Initially the material deforms in an elastic manner which leads to the characteristic increase in resistance. At higher strains, or indeed at constant strain the material undergoes stress relaxation. Two mechanisms are present here, the first is that the hydrogen bonds that exist between -OH groups of the siloxane chains break and reform over time scales of ~1s, the second is entanglement of polymer chains. On the application of strain, polymer chains begin to re-align and then slide relative to one another in the direction of the applied strain leading to stress relaxation. This stress relaxation can be investigated by applying a step strain to G-putty and monitoring the exponential decay of the stress with time. The onset of this relaxation is generally associated with a dramatic decrease in the materials resistance

The precise mechanisms behind the reduction in resistance have not been definitively shown, however the simplest explanation is that nanosheets can move via diffusion in viscous medium where nanosheets that become disconnected from the conductive network due to strain can move back together diffusively to reconnect with neighbouring nanosheets. Such a mechanism can explain network reformation at reasonably long timescales (~100s), however it cannot explain the reduction in resistance under straining. It is therefore suggested that under strain nanosheets become disconnected from the conductive network but are sufficiently close enough to interact by vdW and electrostatic forces. This interaction between nanosheets allows neighbouring nanosheets to move back together, reforming inter-nanosheet junctions and thus lowering the network resistance.[10] Such interaction-induced network formation has been previously observed with CNTs dispersed in liquids.[272] It seems plausible that a similar mechanism should occur in G-putty although at a slower rate due to the matrix viscosity.

Despite G-putty's impressive conductivity, like many other nanocomposites, G-putty suffers from a number of pitfalls which leave it wanting in other strain sensing metrics:

Nanocomposites display low conductivities typically less than 10 S/m,[122] while the presence of filler also introduces viscoelastic effects into the material which can lead to a large electrical hysteresis,[259] and a gauge factor which is highly strain rate dependent.[261,273] This is a significant issue for strain sensors where minimal hysteresis and stable gauge factors are required to accurately match resistance values to strain. G-putty is prime example of these difficulties due to its extreme softness resulting in viscoplastic relaxation on straining, this means that G-putty can undergo permanent, non-recoverable deformations due to viscous flow. This combination of factors, means that despite G-putty's high strain sensitivity it is impractical for use as a real world strain sensor.

It is proposed that some of these issues could be addressed by preparing thin films of G-putty on elastomeric substrates. The idea here is that the physical pinning of G-putty to a standard elastomer may frustrate some of the viscoplastic behaviour observed in bulk G-putty. This combination of pinning and reduction of a 3D bulk composite to a quasi-2D thin film is likely to reduce flake mobility, thus reducing electrical hysteresis and strain rate effects. This presents an interesting case, particularly as it is possible to compare thin film performance to the bulk nanocomposite and will give insight into how nanocomposite strain sensors may be optimised.

5.1. Experimental Methods

First, graphite powder (Branwell, graphite grade RFL 99.5) was dispersed in NMP at a concentration of 100 mg/ml. Graphene was prepared by ultrasonic probe sonicating (Hielscher UP200S, 200 W, 24 kHz) the initial dispersion for 72hrs at an amplitude of 50%. The process temperature was maintained at 7 °C using a chiller to avoid overheating of the probe. The resulting dispersion underwent mild centrifugation using a Hettich Mikro 220R centrifuge (fixed angle rotor) at 1,500 rpm for 1.5 hrs to remove unexfoliated

material and large aggregates. The supernatant was then filtered onto a 0.1 μm nylon membrane forming a solid disk of reaggregated graphene nanosheets. The disk was milled by mortar and pestle into a fine powder before being ultrasonically redispersed in chloroform for 2 hrs at a concentration of 10 mg/ml to form a stock dispersion.

G-putty is a viscoelastic siloxane based graphene nanocomposite described in previous works.[10,271] First silicone oil was partially crosslinked with the use of boric acid to form a gum like substance similar to silly putty. 2ml of silicone oil (VWR, 350 cSt) was added to a 28ml glass vial. Boric acid (Sigma-Aldrich 99.999% trace metal basis) was ground by mortar and pestle until a fine powder was formed, before being added at a concentration of 400 mg/ml to the silicone oil and magnetically stirred until a homogenous and opaque mixture formed. An oil bath was preheated to 175 °C (IKA C-MAG HS 7 hot plate with the temperature controlled and monitored using an ETS-D5 thermometer). Glass vials were added 6 at a time to a custom built aluminium holder which was submerged in the bath, the temperature of the bath was then increased to 225 °C. The mixture was cured under continuous magnetic stirring for 2.5 hrs, after which the vials were removed from the holder and allowed to cool, the resulting material was a viscoelastic gum which was removed from the glass vials with a spatula.

0.5 g of viscoelastic gum and the appropriate volume of graphene dispersion where then to a beaker, eg. Adding 43 mls of stock dispersion will yield a composite of 15 vol%. The gum is soluble in chloroform which means a homogenous mixture can be achieved under stirring. Once fully dissolved the mixture was heated to 50 °C and the solvent was allowed to evaporate. Once the mixture becomes extremely viscous the heat was removed and the remaining solvent was left to evaporate at room temperature overnight. The resulting nanocomposite was then removed from the beaker and folded over itself multiple times to ensure homogeneity. Printing inks could then be formed by dispersing G-putty in

appropriate solvents. The concentration and solvent used was dependent on printing process, with both chloroform and butanol used in this work.

Spray coating inks were prepared by dispersing in chloroform at a concentration of 10 mg/ml via bath sonication for 1 hr. Spray coating of the resulting ink was carried out with a Harder and Steenbeck Infinity Airbrush (0.6mm nozzle) attached to a Janome JR2300N mobile gantry, at a stand-off distance of 100mm and a nitrogen gas backpressure of 4bar. Pre -cut elastomeric substrates were used as the bases for these coatings, each typically 0.5mm thick. These were produced by mixing a silicone based polymer with a curing agent in a ratio of 10:1 (PDMS, Dow Corning Sylgard 184), the mixture was then cured for 90 mins at 120 °C.

Screen printing inks were prepared by adding butan-1-ol to G-Putty at a solvent to solids ratio of 1 g/ml. Due to the small amounts of solvent involved the vials were then sonicated for 30mins to soften the G-putty. The mixture was then hand mixed with a spatula until a smooth homogeneous paste formed. The ink was printed on both Ecoflex (0.3 mm) and sylgard 184 (0.5mm) PDMS substrates, using a homemade manual screen printing setup. This includes a Saatilene Hitech 100.40Y Mesh, rubber squeegee and screen/substrate offset distance of approximately 5mm. 2 deposition passes ensured a continuous film formed.

Aerosol jet printing was carried out using a Optomec AJP300 (150 mm nozzle), these inks used here are identical to those used for spray coating. The water bath was set to 10 °C with the atomiser current set to ~0.45 A. and the platen to 90 °C. The carrier and sheath flow rates were set in the range 10-14 sccm and 65-75 sccm respectively. To stabilise the

ink while printing N_2 was passed through a chloroform filled bubbler. All printing was performed at a platen speed and temperature of 1mm/s and 90 °C respectively.*

Resistance measurements were carried out using a Keithley KE2601 source meter in a 2-probe mode, controlled by LabView software. Electromechanical tests are carried out in conjunction with a Zwick Z0.5 ProLine Tensile Tester (100 N Load Cell). G-putty samples where moulded into a cylindrical shape approximately 1 mm in diameter and with a gauge length of 9 mm. Printed G-putty thin films have a width of 5.5 mm and a gauge length of 20 mm, films are contacted with silver paint at each end. Tensile measurements were carried out at a strain rate of 1.85%/s unless otherwise stated. At each filler volume fraction a total of 4-6 resistance-strain measurements were carried out and an average value of G was obtained. The error bars contained within the plotted data is the standard error of the average value. This is calculated as the standard deviation divided by the square root of the number of samples.*

* AJP deposition was performed by Dr. Adam Kelly

* Mechanical and electrical step strain, hysteresis and strain rate measurements of bulk G-putty were performed by Dr. Daniel O'Driscoll

5.2. Results and Discussion

5.2.1. Materials Characterisation

Dispersions of liquid exfoliated nanosheets can be inspected by TEM to assess the nanosheet charcteristics. Figure 5.1A&B shows thin nanosheets of various lengths are present within the dispersion. The polydispersity of nanosheet lengths is an intrinsic property of LPE exfoliated nanosheets.[110] The histogram of nanosheet lengths shown in Figure 5.1B was obtained from 100 counts of individual nanosheets, giving an average of, $\langle L \rangle = 430 \pm 20$ nm.

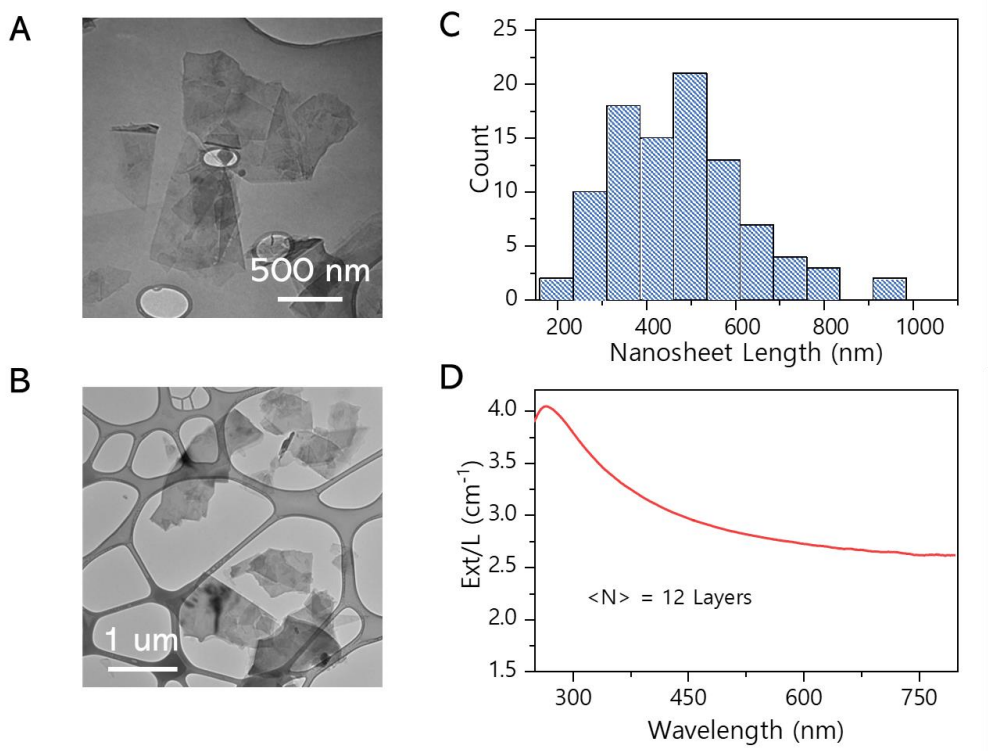

Figure 5.1 – Graphene Characterisation. A) – B) TEM images of graphene nanosheets, showing thin nanosheets of various lateral sizes. C) Lateral size distribution obtained from TEM images. Distribution comprises of 100 counts of individual nanosheets. D) Extinction spectra of graphene.

Optical spectra of nanosheet dispersions provide a wealth of information on the average nanosheet of a distribution and is a well-established method of obtaining dimensional estimates of nanosheets.[93] The nanosheets prepared here can be analysed according to methods outlined by Backes et al.[67] Optical spectra are interpreted through the Beer-Lambert Law, $Ext = \varepsilon_{ext} Cl$, where Ext is the extinction (Absorbance plus scattering), ε_{ext} is the extinction coefficient, C is the nanosheet concentration and l is the path length. The extinction spectrum of graphene is shown in Figure 5.1C. The spectrum is typical of previous observations, which is broad and featureless except for a single π - π^* peak, observed at approximately 270 nm. The exact position and intensity of the peak is sensitive to the dimensionality of the nanosheets, whereas the features at the high wavelength plateau (>550 nm) are relatively size/thickness independent. This has allowed for the proposal of an empirical formula which relates the extinction ratio between the peak, ε_{max}, and at 550 nm, ε_{550}, to the average nanosheets thickness, ⟨N⟩.

$$\langle N \rangle = 25 \times \varepsilon_{550} / \varepsilon_{max} - 4.2 \qquad (5.1)$$

Applying this to the graphene spectrum in Figure 5.1C, yields a mean layer number, ⟨N⟩ ~ 12 monolayers.

While NMP is preferred for exfoliation, its boiling point (270 °C) makes it impractical for composite formation due to the high processing temperatures needed to evaporate the solvent. Instead lower boiling point solvents such as chloroform and IPA are preferred. For this reason the exfoliated graphene is transferred into chloroform producing a stock dispersion for composite formation. The G-putty bulk composite is prepared through the simple mixing of the graphene dispersion and a homemade viscoelastic gum. The solvent is removed from the mixture by evaporation to yield a viscoelastic graphene

nanocomposite (Figure 5.2A). This material's mechanical and electrical properties have been comprehensively studied in previous works.[10,271]

Composite inks can be formulated by ultrasonically dispersing G-putty in various solvents such as butanol and chloroform (Figure 5.2B&C). The ink viscosity can be tailored by varying the ratio of solids and solvents, with a 3 order magnitude change in viscosity readily achievable. Figure 5.2D shows the viscosity profile as a function of shear rate for various concentrations of G-putty dispersed in butanol. Increasing the G-putty concentration leads to a dramatic increase in ink viscosity, furthermore, the most concentrated inks display clear shear thinning or pseudo plastic behaviour. As the concentration is reduced the inks begin to approximate a Newtonian fluid, as is the case for pure butanol solvent, this is attributed to a reduction in the number interactions between the dispersed particles.

The addition of large amounts of solvent yields low viscosity liquid like inks, while the addition of relatively small amounts of solvent results in a nanocomposite paste where the polymer acts similarly to a binder in traditional inks. Access to such a wide range of viscosities means the inks can be tailored to suit a number of different printing techniques. For example, screen printing requires high viscosity pastes (1-10 Pa s) and shear thinning behaviour, while spray coating requires low viscosity inks (1-30 mPa s).

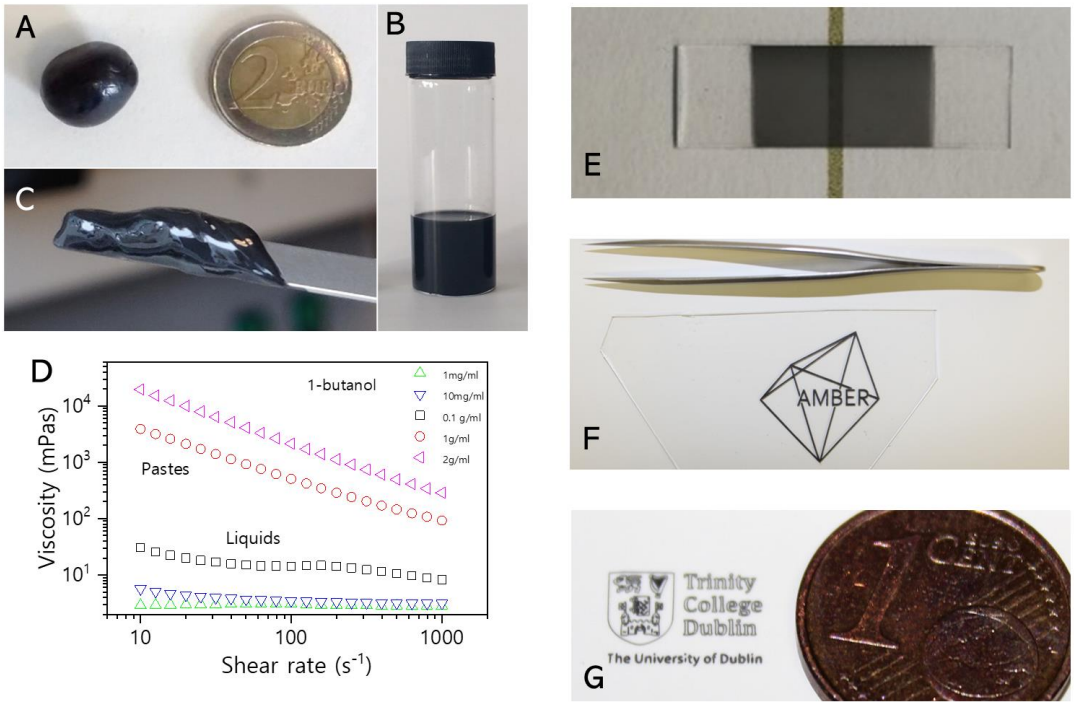

Figure 5.2 – Ink Characterisation. A) – C) G-putty in various forms A) Bulk composite. B) Ink. C) Viscous paste. D) Rheological properties of G-putty ink, at various concentrations. As the concentration increases the inks become more paste like displaying shear thinning behaviour. E) – G) Printed G-putty thin films. E) Spray coated. F) Screen printed. G) Aerosol jet printed.

To demonstrate the versatility of G-putty inks, thin films were deposited via spray coating, aerosol jet printing (AJP) and screen printing techniques (Figure 5.2E-G). Spray coated films were deposited on pre-cut elastomeric substrates, with the shape of the substrate defining the dimensions of the G-putty film. Importantly screen and aerosol jet printing allow patterning of films during deposition through, stencilling in the case of screen printing, or digitally controlled deposition in the case of AJP. A low viscosity chloroform based ink was employed for spray coating and AJP, while a viscous butanol based paste was used for screen printing. The choice of solvent depends on the requirements of the printing technique. Chloroform was chosen for the aerosol based processes as fast solvent evaporation on contact with the substrate leads fewer film inhomogeneities.[70] However, chloroform is too volatile to be used in screen printing, where solvent evaporation can

lead to clogging of the screen mesh and poor print quality. Screen printing solvents ideally sit in a specific range, with a relatively high boiling point, allowing a stable ink consistency, yet an evaporation rate that is fast enough so that deposited film do not require annealing post deposition. Furthermore, the PDMS elastomers used here have exceptionally low surface energies (21 mN m^{-1}),[274] ideally the solvent surface tension should lie 7-10 mN m^{-1} below the surface energy of the substrate, however an appropriate solvent with this criteria could not be found. As an alternative, butanol was chosen due to its low surface tension (23 mN m^{-1}),[193] this coupled with the high viscosity of the paste allows the formation of continuous patterned films.

All films appear visually uniform and undergo further characterisation to assess the composition and morphology of the final films. Thermogravimetric analysis (TGA) was performed in a nitrogen atmosphere on both bulk G-putty loaded with 15 wt% graphene and samples of the preprepared thin films reclaimed from both spray coated and drop cast depositions. The TGA in Figure 5.3A appears almost identical between the bulk and thin film samples suggesting there are no material compositional changes as a result of ink formulation or printing. Note that the majority of the weight loss occurs in the 300 – 500 °C temperature range, corresponding to the decomposition of the polymer matrix. Additional mass loss occurs about 700 °C and is associated with the decomposition of graphene in atmosphere.[275] From the percentage weight loss, the graphene loading in the sample can be inferred, with all samples displaying the expected 15% mass loss.

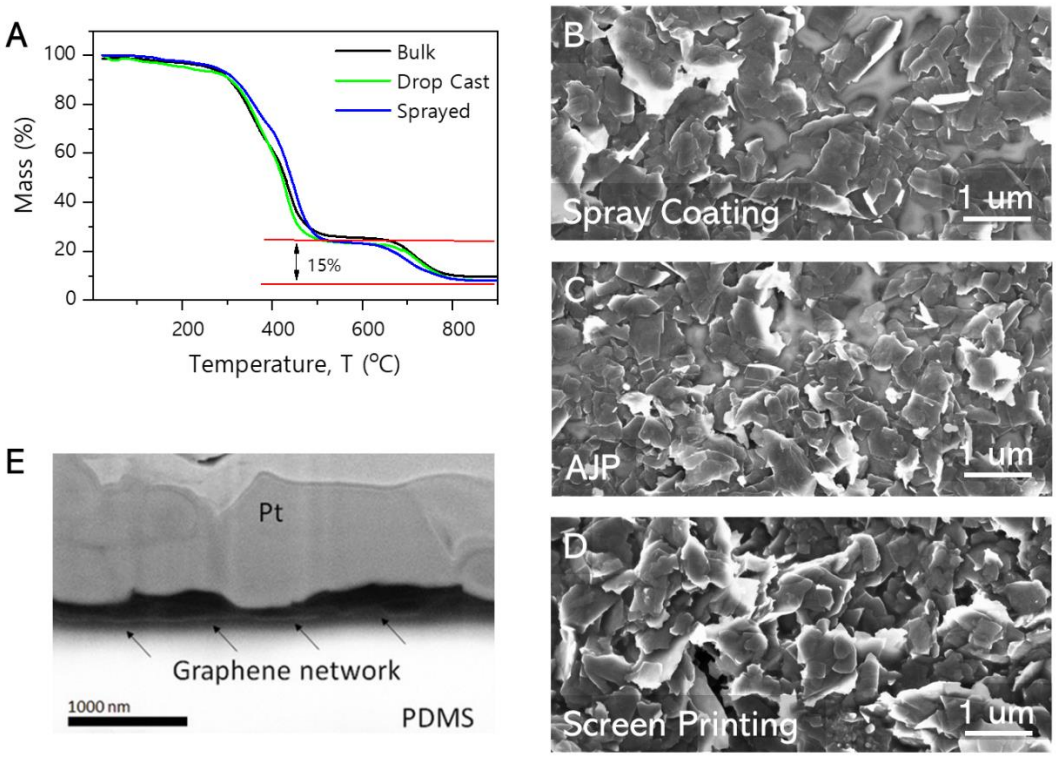

Figure 5.3 – Thin Film Characterisation. A) TGA of bulk, spray coated and drop cast films. Almost identical curves are observed in each instance. B) - D) SEM images of B) Spray coated. C) Aerosol Jet Printed and D) Screen printed thin films. E) SEM cross section prepared by focused ion beam milling, showing a distinct phase separation between graphene and PDMS. The top Pt layer is deposited as part of the imaging to prevent sample damage.

SEM was used to image the surfaces of printed films. The film surfaces are rich in graphene nanosheets with relatively small amounts of polymer acting as binder. This is surprising given amount of graphene present in the original composite (15 wt%) and previous TGA results. Although the film surface appears to be relatively uniform in each sample, the morphology of the films is not consistent and depends on the printing method used. The spray coated film surface (Figure 5.3B) consists of 90-95% nanosheets, interspersed with graphene free regions which can be as large as 1- 2 μm in size. AJP thin films (Figure 5.3C) have a similar nanosheet coverage, and while the nanosheet free regions still exist they tend to be on a smaller length scale ~0.5 μm. The screen printed film surface (Figure 5.3D)

appears to be rougher and somewhat porous compared to films prepared by aerosol methods, while no nanosheet free regions are evident. The length scale of the nanosheet free regions gives an estimate of the associated network non-uniformities. Assuming these non-uniformities are holes with an average diameter of 1.5 μm which contribute to 5 – 10% of the network area. Then each hole is associated with a network area of 5 μm × 5 μm. This implies that networks of larger areas than this are relatively uniform, as is the case with our samples.

The finding of graphene rich surfaces leaves a question about the distribution of polymer and graphene throughout the thin film. To investigate this, SEM was performed on a cross section of a spray coated film prepared by focused ion beam milling. As shown in Figure 5.3E, the process involves a capping of the film with platinum to protect the sample. Directly under the Pt, a well-defined graphene rich surface network is observed, at increasing sample depth the graphene gives way to almost pure polymer. This is evidence for partial vertical phase-segregation of graphene and polymer during deposition. This effect is likely the result of the relative stability of graphene and PDMS in the spraying solvent. As the solvent evaporates from the substrate surface the solids concentration within the solvent increases, the graphene and the PDMS likely become thermodynamically unstable at different concentrations thus driving composite phase-segregation.

Probing the nature of the interface between the G-putty thin film and elastomeric substrate is rather difficult due the extreme softness of the thin films, in practice the interface could be probed via peel tests, where the input energy, U, can be related to the adhesive fracture toughness, U_A, and the plastic work in behind the peel arm, U_p, such that: $U_A = U - U_p$, where the input energy is given $U = N_p/w(1-\cos\theta)$. Here N_p is the force acting on the peeling film, w is the film width and θ is the peel angle i.e. the angle between the

substrate and the peeling film. Such a measurement would necessitate complete film removal from the substrate surface, however this is not a certainty given the vertical phase segregated nature of the film.

5.2.2. Electromechanical Characterisation

Electrical measurements were performed on bulk G-putty and corresponding sprayed coated films with a range of different graphene loadings. The film thickness was kept constant at ~ 1 μm, this value was chosen as it is well above the thickness percolation regime and the films should therefore be free of any thickness dependent effects.[89,130,131,183] The conductivity of each sample was plotted against the graphene volume fraction, ϕ, in Figure 5.4A. The behaviour of both data sets is consistent with percolation theory which describes the ϕ - dependence on composite conductivity, σ, according to the percolation equation:

$$\sigma_0 = \sigma_c(\phi - \phi_c)^t \qquad (5.2)$$

where σ_c is a scaling factor and t is the percolation exponent. Comparing the parameters obtained from fitting the bulk and thin film data (Figure 5.4A) shows a large decrease in the percolation exponent, where $t_{Bulk} = 4.6$, while $t_{film} = 1.4$. The percolation exponent behaviour is consistent with a narrowing of the junction resistance distribution. In addition, σ_0 is seen to dramatically increase going from bulk to thin film and a 6 order of magnitude increase in conductivity is observed for comparable graphene loadings. A maximum thin film conductivity, σ_0 = 300 S/m, is considerably higher than what is achievable in most nanocomposites.[122]

The thin film electrical properties lend credence to the earlier claim that a partial phase segregation is occurring within the thin film. Firstly, the percolation exponent is reduced,

suggesting a narrowing of the distribution of junction resistances.[168] This is likely the result of induced alignment of the graphene flakes during deposition, especially when considering that the thickness of the thin film (< 1 μm) is similar to that of the graphene nanosheet length (430 nm). The confining of nanosheets to a quasi 2 dimensional space should intuitively limit the number of point-like nanosheet junctions within the composite and lead to preferential overlap of neighbouring nanosheets thus reducing the distribution of junction resistances.

The increase in conductivity is a result of a reduction in the tunnelling resistance between nanosheets as the composite moves from bulk to thin film, while the magnitude of the increase indicates that the tunnelling distance between nanosheets has decreased. Such as scenario would arise in the presence of phase segregation where less polymer should be present between adjacent nanosheets. This transition from 3D to 2D like percolation is not unprecedented and has been observed in previous reports on phase segregated nanocomposites.[276,277]

The electromechanical response of the bulk and thin films were investigated by monitoring the resistance of the material in response to an applied strain. Shown in Figure 5.4B is the resistance response of a 15 wt% sprayed thin film. As is typical in nanocomposites, the resistance is seen to increase with increasing strain. The film shows excellent sensitivity and robustness in addition to a wide a sensing range of 55% strain. Below ~20% strain the relative resistance change $\Delta R/R_0$ is approximately linear. A well-defined linear resistance-strain response is important for practical sensing applications, this large linear strain region far surpasses what is achievable with graphene only thin films[89] and is competitive with state-of-the-art nanocomposites.[256]

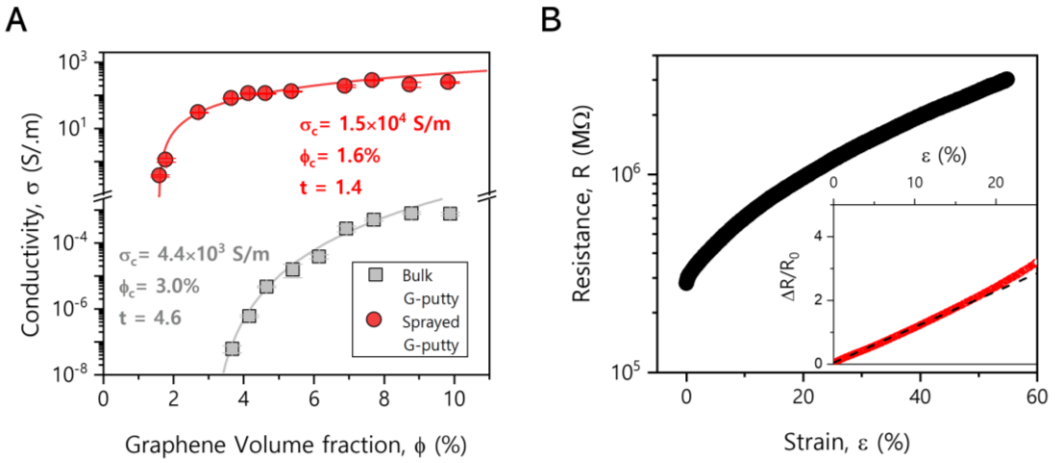

Figure 5.4 – Electrical and Electromechanical Characterisation. A) Bulk and thin film conductivity plotted as a function of composite volume fraction. Solid lines are fits to percolation theory. B) Thin film resistance plotted as a function of tensile strain. Inset shows a quasi-linear response in the relative resistance change up to ~20% strain

In order to probe the strain sensitivity of these thin films more deeply, a range of samples at different graphene loadings were prepared, in each instance the piezoresistive response was measured and $\Delta R/R_0$ was plotted as a function of strain. A representative subset of the responses are shown in Figure 5.5A, showing that as the loading of graphene is reduced the samples become more sensitive to the applied strain. This results in an increase in the gauge factor, G, which is defined as $G\varepsilon = \Delta R/R_0$ in the linear $\Delta R/R_0$ region. In Figure 5.5B, the average gauge factor is plotted as a function of ϕ, displaying a monotonic increase in G as ϕ is reduced. A maximum gauge factor, $G \sim 110$, is achieved for graphene loadings below 5 wt%. Similar monotonic behaviour is observed in bulk G-putty and is common to many nanocomposite strain sensors.[278,279]

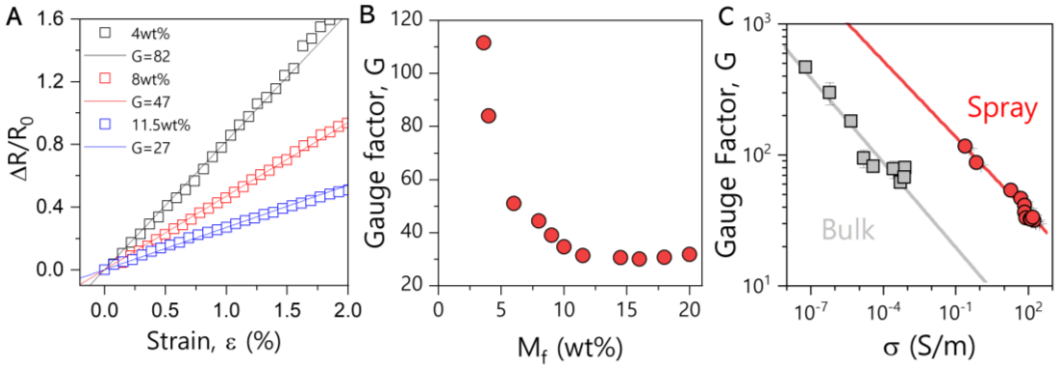

Figure 5.5 – Gauge Factor Response. A) Representative curves showing the relative resistance change as a function of strain. Thin film gauge factor is calculated from the slope of the linear fits. B) Gauge factor shows a strong dependence on graphene mass fraction, with the lowest graphene loadings leading to the most sensitive films. C) Gauge factor for both bulk and thin films G-putty plotted as a function of conductivity, showing lower law like behaviour.

The relationship between G and ϕ suggests that a negative correlation should exist between G and σ_0. Plotting G as a function of conductivity for both G-putty thin films and bulk G-putty (Figure 5.5C) demonstrates a clear inverse power law trend between the two quantities. The graph also highlights the differences between the two networks, where a given G can be achieved at much higher conductivities in the thin film. This is important, as low sheet resistance sensors are preferable for sensing due to the low power requirement of wearable electronics. This comes from the simple $V = IR$ relationship where larger resistance sensors will require higher voltages to maintain the same current, thus increasing the power requirement.

One caveat of the printed sensors is that the accessible range of G is limited somewhat when compared to the bulk case. It's hypothesised that the forming of a partially phase segregated network restricts flake mobility thus reducing network sensitivity. This is not unexpected as previous work shows flake mobility to be an important factor in G-putty sensitivity[271] however the decline in sensitivity is more than compensated by the increase in composite conductivity.

5.2.3. Hysteresis, Strain rate and Frequency Dependence

As discussed earlier the issue with G-putty as a practical strain sensor is its large viscoelastic relaxation which allows rapid reforming of the graphene network. This relaxation of the graphene network can be visualised in Figure 5.6 where strain is applied in stepwise increments of 0.5% with a 900s hold between each step. Instead of the resistance remaining relatively constant at each step height (creating a staircase), as would be the case for a perfectly elastic material, the resistance decays exponentially the graphene network reforms in the soft polymer matrix. The response of the printed G-putty thin films contrasts well against this backdrop, showing a much more staircase-like behaviour. Note there are some short term relaxation effects at the step edges however these are short lived, with the resistance becoming relatively constant after 5 seconds of hold. We suggest that this decrease in resistance is a remnant of the mechanisms found in G-putty and is associated with a partial network reformation as nanosheets recombine under wdV and electrostatic forces in the viscous network, however this network reformation is clearly not as extreme as in the case for bulk G-putty.

It is proposed that the suppression of the relaxation is ultimately due to the thinness of the samples. At the interface between film and substrate the composite is pinned allowing very little relaxation of the film. It's suggested that relaxation is a function distance from the interface so that for very thick films relaxation could occur far away from the substrate surface, as film thickness is reduced the mechanics of the G-putty approach that of the underlying substrate, producing a quasi-elastic resistance response.

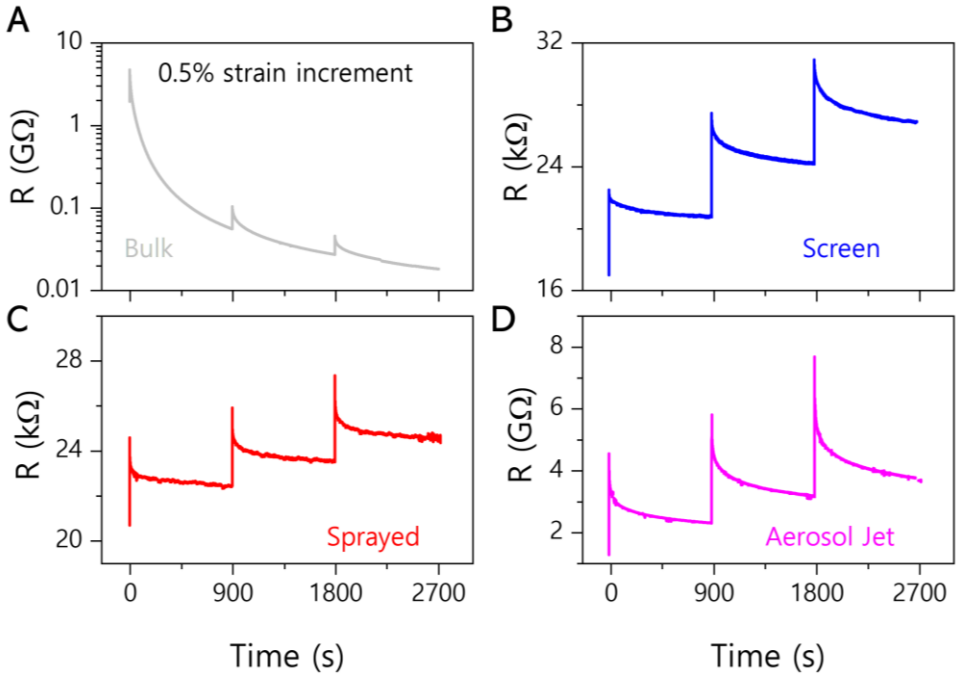

Figure 5.6 – Step Strain Response. A) Bulk, B) Screen printed, C) Spray coated and D) AJP thin films strained in 0.5% increments followed by a 900s hold. Resistance is monitored over time.

This mechanics of the bulk and printed films can be visualised in Figure 5.7A, here the bulk composite shows extreme visco-plastic mechanical hysteresis, while the thin film mounted on a substrate shows minimal hysteresis, approaching that of a characteristic elastomeric response. The corresponding resistance-strain response is shown in Figure 5.7B where the extreme relaxation of the graphene network in G-putty is evident. Initially G-putty deforms elastically, resulting in an increase in the materials resistance. However, as stress relaxation occurs the graphene nanosheets become highly mobile within the matrix allowing the network to reform,. This is evident from a decrease in the observed resistance. The mobility is so extreme that the resistance quickly drops below the initial zero-strain value and continues to decline during the unloading cycle. Although the spray coated films, certainly do display hysteresis it is much reduced and in stark contrast to the bulk, as the resistance returns close to its original value during the unloading phase.

The resistance hysteresis is defined as the area of the hysteresis loop divided by the area under the R-strain curve associated with the loading cycle. The hysteresis for the bulk and printed films is plotted as a function of strain rate in Figure 5.7C. Bulk G-putty shows a very large and strain rate dependent hysteresis with values ranging between -1 – 0.25, here the negative sign indicates that the resistance of the unloading cycle is higher than the resistance during the loading cycle. Printed films show a much smaller hysteresis (~0.15) and are virtually independent of strain rate.

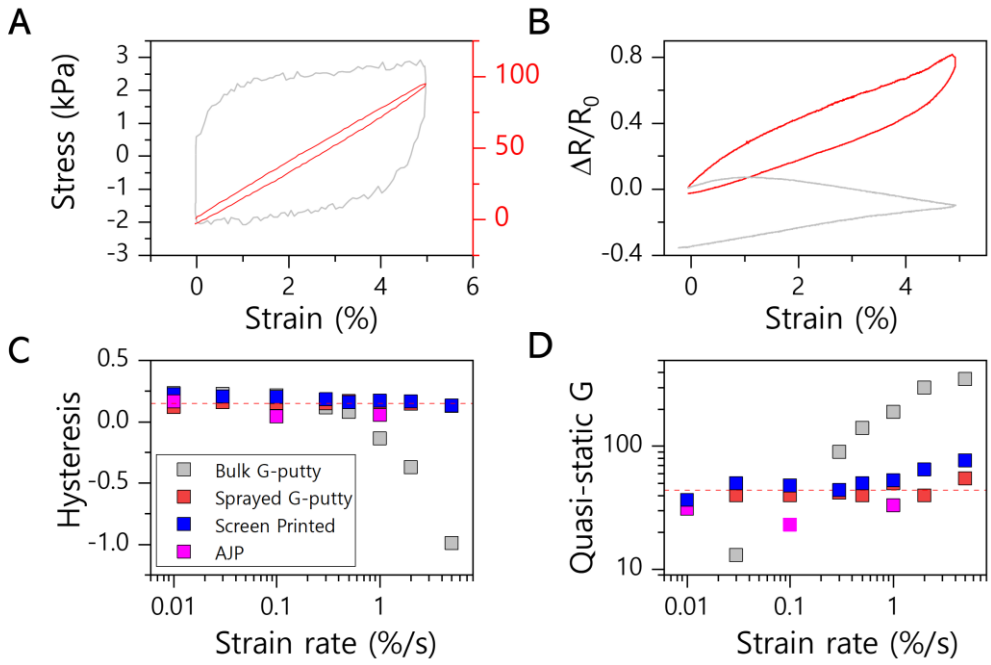

Figure 5.7 – Strain Rate and Hysteresis. A) Mechanical hysteresis of bulk G-putty (grey) and spray coated (red) samples backed by a sylgard-180 pdms substrate. B) Electrical hysteresis for bulk and spray coated samples. C) - D) Strain rate dependence of the C) electrical hysteresis D) quasi-static gauge factor of bulk and thin films.

The strain rate invariance of the resistance response can also be seen in measuring quasi-static gauge factor. Quasi-static is used here to qualify that a single resistance-strain

measurement yields a different gauge factor when compared to resistance-strain measurements under constant cycling (the reason for this is discussed below). Similar to the hysteresis response, the quasi-static gauge factor of bulk G-putty is highly dependent on the strain rate used, while, the printed films are found to be almost completely independent of the strain rate applied (Figure 5.7D). Low hysteresis and strain rate independence are exceptionally important for real world sensing where the relationship between resistance and strain should ideally be the same under all conditions, yielding accurate quantitative information from strain sensors.

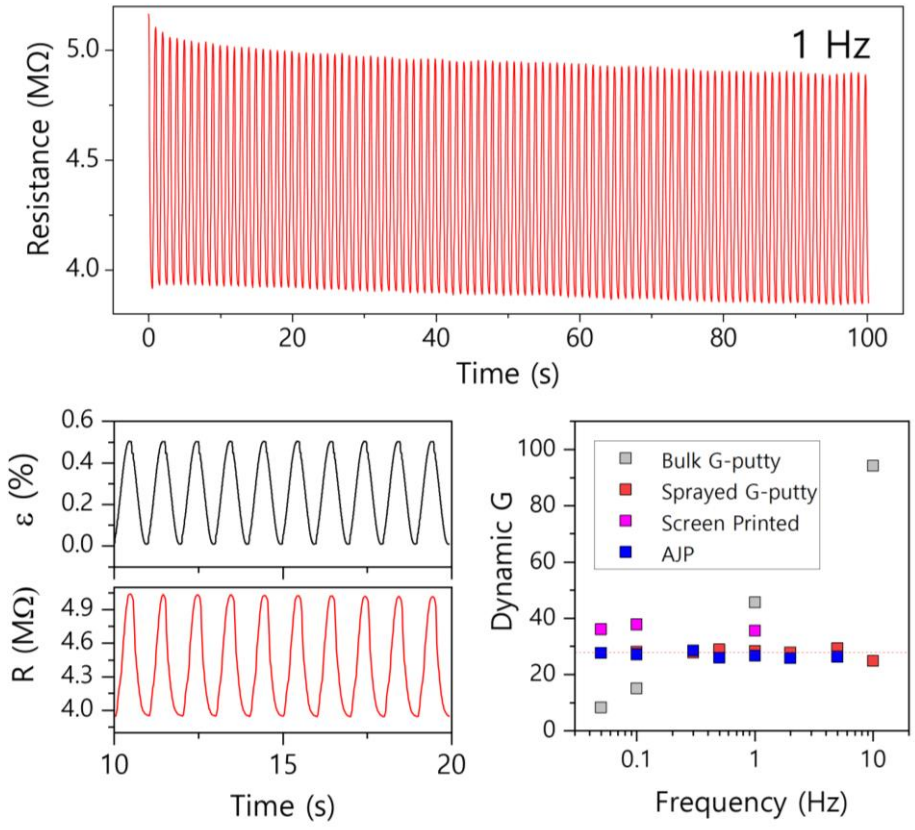

Figure 5.8 – Oscillatory Resistance-Strain Response. A) Resistance changing as a function of time in response to an applied sinusoidal strain. The response attains a quasi-stable state after an initial sharp decrease in resistance. B) A magnified version of the resistance response. C) The dynamic gauge factor (Relative change in resistance from peak to peak plotted as a function for frequency.

The strain rate independence of the resistance response suggests that oscillatory measurements should be similarly independent of the oscillating frequency. To test this, printed films were oscillated in a sinusoidal manner between 0 – 0.5% strain. After an initial decrease in peak resistance the response becomes relatively stable as shown in Figure 5.8A&B. The behaviour is reminiscent of the Mullin's effect which describes the decrease in a materials peak stress when cycled. The resistance response is probably a combination of this stress relaxation in the substrate and some mobility of the graphene network. This has implications for the gauge factor and indicates that different values will be found when comparing single static strain measurements (Quasi-static G) and the relative resistance change (in the steady state) between oscillatory peaks, defined as the dynamic gauge factor. The dynamic gauge factor is plotted as a function of oscillating frequency in Figure 5.8C. Again it can be seen that while the bulk composite is highly frequency dependent, the printed films are almost perfectly independent of frequency. The eagle eyed will also note that the average dynamic gauge factor (G ~ 30) is lower than the quasi-static gauge factor (G ~ 42) as discussed above.

5.2.4. Strain Sensor Applications

The properties of the prepared thin films make them ideal candidates as electro-mechanical sensors. In order to explore their viability for real world sensing, the sensors were deployed for various applications. For devices to be capable of measuring bodily vital signs such as pulse, sensors must deform simultaneously with the skin. This requires sensors to be thin so that they can adhere and conform to the epidermis, while at the same time being very soft, such that they are comfortable to wear and mimic skin deformation.[3,177,270] This means that the mechanical properties of skin sets the limit of appropriate materials, with a Young's modulus less than 300 kPa accepted as being appropriate for unimpeded monitoring.[280]

Screen printed G-putty thin films on an ultra-soft PDMS elastomer called Ecoflex (elastic modulus ~ 150 kPa), were mounted on a subject's wrist. The thin soft substrate adheres to the skin without the need for adhesive and is capable of measuring the pulse at the radial artery with the corresponding waveform (Figure 5.9A-D) matching well with what is expected. The pressure exerted by the artery is small ~ 5 kPa[281] and demonstrates the minute strain detection afforded by the sensors. The versatility of the G-putty inks and printing techniques is demonstrated in Figure 5.9E&F. In this instance a commercial band-aid is used in place of the elastomeric substrates. Even with this unoptimised substrate, deformation in the skin due to variation in blood pressure can still be resolved. The ability to produce thin films on a range of soft substrates is a distinct advantage of our G-putty ink system, this is in contrast to commercial strain gauges which must be fabricated on stiff polymer substrates and so are unable to resolve mechanical deformations of the skin.

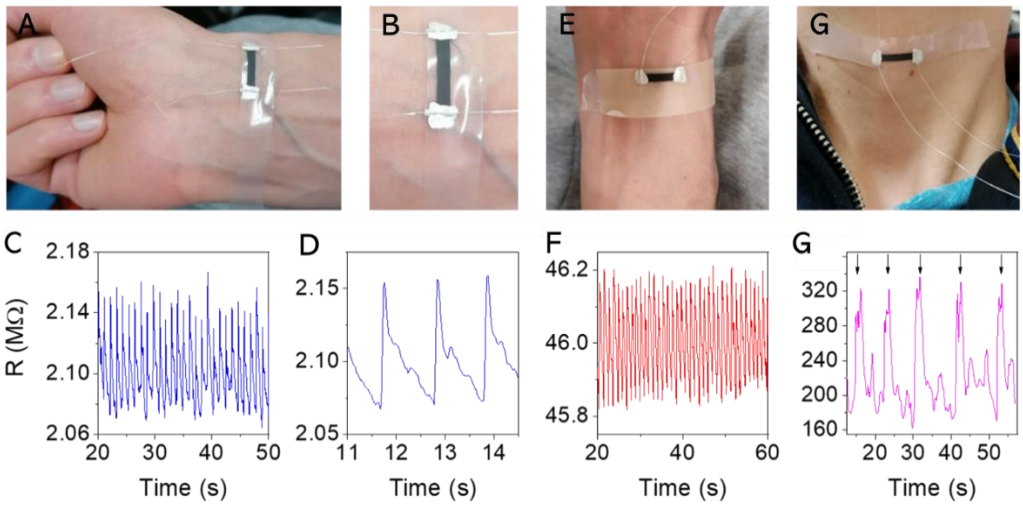

Figure 5.9 – Biomedical Sensing. A) – B) images of wrist mounted sensors. C) – D) Corresponding resistance output showing pulse at the radial artery. E) – F) Pulse measurements carried out with a commercial band aid substrate. G) – H) Sensor mounted on Adams apple to monitor swallowing. Arrows denote swallowing events.

Further applications of the sensors can be shown in the area of diagnostics. Dysphagia is a medical condition which describes swallowing difficulties in patients arising from a range of factors. A typical diagnosis of dysphagia requires an invasive examination carried out by a specialist. Instead we suggest mounting printed G-putty sensors on the patients laryngeal prominence, allowing swallowing to be measured quantitively and crucially non-invasively (Figure 5.9G-H) which opens the path to novel diagnostic applications.

5.3. Conclusions

In conclusion, the ability to formulate G-putty thin films from printable inks has been demonstrated. This is achieved with simple dilution of the inks, where varying the solids to solvent ratio allows inks of various viscosities to be utilised for printing. The resulting patterned films are of high conductivity and strain sensitivity, while also demonstrating low hysteresis and independence of both the applied strain rate and frequency. These properties are in stark contrast to the bulk behaviour which despite its high sensitivity shows poor performance across the other metrics. The behaviour is attributed to two mechanisms: One is the pinning of the thin film at the composite-substrate interface, which should restrict flake mobility somewhat. The second is a partial phase segregation of the composite which brings the graphene nanosheets closer together dramatically increasing the conductivity. The thin film properties are ideal for tactile sensing which is demonstrated by utilising the films for vital sign and bodily motion monitoring.

Chapter 6

Relating Piezoresistance to Percolation Scaling

Piezoresistive nanocomposites generally consist of a conductive nanofiller embedded within a polymer matrix. Traditionally carbon nanotubes[135,179,282,283] and graphene[122,142,252,284] have been explored as fillers, however, piezoresistive behaviour has been observed with a whole host of nanofillers such as silver nanoparticles,[253,285] 2D semiconductors,[144] carbon black,[226,286] conducting polymers,[287,288] and MXenes.[289,290] The changes in nanocomposite electrical conductivity by introducing filler to an insulating matrix have been the subject of intense experimental and theoretical work for decades and are now well understood.[134,162,163,168,181,291,292] As a result, one might assume that the

piezoresistive properties of these composites are also well understood, however this is not the case. The general consensus is that nanocomposite piezoresistivity arises solely from increased tunnelling distance upon applying strain.[293-297] If this is the case, an exponential increase in resistance should be expected. However, many reports demonstrate that the resistance is approximately linear, particularly at low strain.[256]

To date, understanding of the piezoresistive response has relied on empirical evaluation; however, the fabrication process and resistance-strain measurements are time-consuming and generally yield only small insights towards sensor optimisation.[180] In addition to experimental trials, several numerical studies have been used to model the piezoresistive response in nanocomposites.[296,298,299] More recently, these numerical models have turned to the response of different network geometries with segregated, structured multilayer, and homogenous nanocomposites investigated.[180] The problem here is that numerical models are filler specific and cannot be universally applied. Furthermore, simple analytical models are not currently available.

Straightforward models are needed, yielding simple equations describing how the gauge factor, G, varies with filler volume fraction, ϕ, or composite conductivity, σ. Such models would allow the fitting of experimental data and give an insight into the nanocomposite properties that determine the gauge factor. Ultimately, this will enable the development of nanocomposites with enhanced values of G. In this study, percolation theory is used to develop a simple model relating the gauge factor of nanocomposite piezoresistive materials to both the filler volume fraction and the zero-strain conductivity, σ_0. This model's accuracy is tested against various composites with different conductive fillers and is supported by a detailed study of how percolation parameters vary with applied strain.

6.1. Experimental Methods

Graphene was prepared by ultrasonic tip sonication (Hielscher UP200S, 200 W, 24 kHz) of graphite (Branwell, graphite grade RFL 99.5) in 1-methyl-2-pyrrolidone (NMP) (Sigma-Aldrich, HPLC grade) at a concentration of 100 mg/mL for 72 h and an amplitude of 60%. The resulting dispersion was centrifuged at 1500 rpm for 90 mins to remove unexfoliated graphite and aggregates. The supernatant was filtered through a 0.1 μm nylon membrane, forming a thick disk of re-aggregated nanosheets. The nanosheet disk was ground into a fine powder and was added to separate solvents of chloroform and IPA at concentrations of 10 mg/ml and 1 mg/ml respectively. Stock nanosheet dispersions were prepared by sonication for 90 mins at a 40% amplitude.

Bulk G-putty was produced from chloroform/graphene dispersions and a homemade viscoelastic putty, a detailed description of the procedure is described in Chapter 6. While G-putty is an ultra-sensitive nanocomposite, its viscoelastic properties are novel and standard piezoresistive nanocomposites are made from elastomers. As a comparison a piezoresistive nanocomposite was produced from a commercial elastomer using graphene as a filler. A 0.4 g sample of Sylgard 170 (Dow Corning) Part A and Part B was added to a beaker containing 10 mL of the IPA/graphene dispersion and stirred under magnetic stirring for 2 min. An additional volume of graphene dispersion was then added depending on the required graphene loading. The mixture was gently heated to 40 °C, and the solvent was allowed to evaporate under continuous stirring. Once almost all of the solvent had evaporated, the mixture was transferred into Teflon moulds (35 × 35 mm). The mixture was left to stand for 12 h to ensure complete solvent evaporation and then cured at 100 °C for 1 h in an oven. The final composite has a thickness ~ 600 μm and was cut into parallel strips 3.5 mm in width for electromechanical characterisation, the resulting composite is termed G-sylgard.

DC resistance measurements were carried out using a Keithley KE2601 source meter in 2-probe mode, the current was fixed at 1 μA while the current and resistance where allowed to vary. The instrument was controlled using LabView software. Electromechanical tests are carried out in conjunction with a Zwick Z0.5 ProLine Tensile Tester (100 N Load Cell). G-putty samples were moulded into cylindrical shapes approximately 1mm in diameter. For both G-putty and G-sylgard samples a 9 mm gauge length is used. The error bars contained within the plotted data is the standard error of the average value. At each filler volume fraction a total of 4-6 resistance-strain measurements were carried out and an average value of *G* was obtained. The error bars contained within the plotted data is the standard error of the average value. This is calculated as the standard deviation divided by the square root of the number of samples.

A JEOL JEM-2100 LaB_6 transmission electron microscope operating at 200 kV was used to provide images of individual nanosheets. The dispersion was diluted to low concentrations and drop-cast onto an ultrathin carbon film TEM grid provided by Ted Pella, Inc. The TEM grid was placed on a piece of filter paper in order to wick away any excess solvent and then dried overnight in a vacuum oven. The images were used to obtain a statistical analysis of the nanosheet lengths, here defined as the longest axis of each nanosheet.

UV–visible spectroscopy was performed using a Perkin Elmer UV-Vis Spectrophotometer to optically characterise the exfoliated nanosheet dispersion. The wavelength was scanned between 800 and 200 nm, and a 4 mm path length-reduced volume quartz cuvette was used for the measurement.

6.2. Results and Discussion

6.2.1. Literature Trends

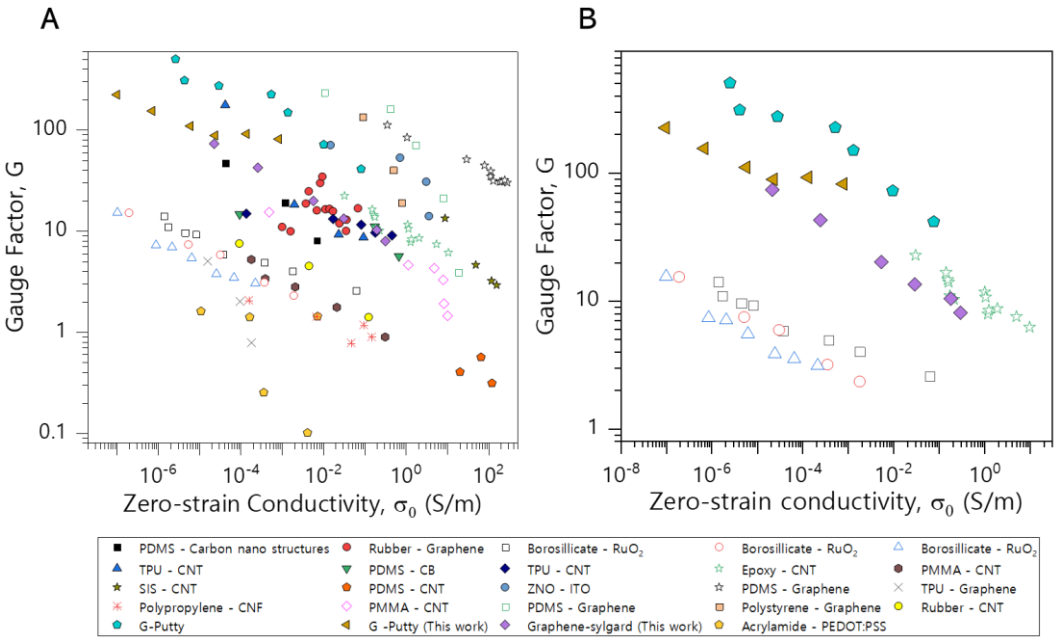

Figure 6.1 – Review of Literature Data. A) Gauge factor plotted as a function of zero-strain conductivity for a range of literature composites,[10,184,191,260,273,278,279,300-310] showing a general decline in gauge factor with increasing conductivity. B) A paired back version of A) where only the most extensive data sets are shown.[10,278,298]

Before developing a model, it is important to assess the trends in the literature since any model must be consistent with experimental data and display certain general features. The primary method of changing piezoresistive sensitivity is through variations in loading of conductive filler, with the gauge factor increasing rapidly as the filler volume fraction moved towards percolation threshold from above.[10,203,298] The reason for this can be demonstrated by considering a network at the percolation threshold, where only one connected path is present. In such an instance, the conductive network will be highly sensitive to any perturbation to the path, such as strain. For a network with many connected parallel pathways the resistance of the conductive network is determined by the

most well connected paths and is therefore less sensitive to perturbations. While increasing the filler volume fraction decreases the gauge factor, according to percolation theory, it should simultaneously increase nanocomposite conductivity. As expected, an increase in gauge factor is often accompanied by a reduction in conductivity throughout the literature.[10,177,184,191,260,273,278,279,298,300-311]

A review of the literature identifies various papers which report both nanocomposite conductivity (at zero-strain) and gauge factor each measured at various different filler loadings, as shown in Figure 6.1A. The data demonstrates the expected negative correlation between gauge factor and conductivity with the most extensive datasets (Figure 6.1B) suggesting a roughly power-law relationship between σ_0 and G. Any successful gauge factor model must be capable of describing the dependence of *G* on both ϕ and σ_0 in a way which is consistent with the above findings and is applicable across a broad range of sensing materials.

6.2.2. Model Development

When a piezoresistive material is strained the resistance changes for two reasons. First, there is a relatively small change due to the geometric changes that occur under strain, such an effect is dominant in metal foil strain gauges. Second, the resistance can change due to variations in a materials conductivity under strain.[217] This effect can be positive[10,184] or negative[144] and has the possibility of being very large in some systems, including nanocomposites.[219]

These effects are quantified in a simple equation[217]

$$G \approx 2 - \frac{1}{\sigma_0}\left(\frac{d\sigma}{d\varepsilon}\right)_0 \qquad (6.1)$$

Where the '2' is associated with the geometric gauge factor of an incompressible material. The subscript zero indicates that the quantity should be taken in the limit of zero strain, which arises from approximations in the derivation that are only valid at low strain. This equation can be applied to percolative systems by differentiating the standard percolation equation

$$\sigma_0 = \sigma_c(\phi - \phi_c)^t \tag{6.2}$$

with respect to strain, assuming that σ_c, ϕ_c and t, are all strain dependent. Thus the differentiation takes the form

$$\frac{d\sigma}{d\varepsilon} = \frac{d\sigma}{d\sigma_c}\frac{d\sigma_c}{d\varepsilon} + \frac{d\sigma}{d\phi_c}\frac{d\phi_c}{d\varepsilon} + \frac{d\sigma}{dt}\frac{dt}{d\varepsilon} \tag{6.3}$$

Carrying out the differentiation yields

$$\frac{d\sigma}{d\varepsilon} = \sigma_c(\phi - \phi_c)^t\left[\frac{1}{\sigma_c}\frac{d\sigma_c}{d\varepsilon} + \ln(\phi - \phi_c)\frac{dt}{d\varepsilon} - \frac{t}{\phi - \phi_c}\frac{d\phi_c}{d\varepsilon}\right] \tag{6.4}$$

This equation can be combined with equation 6.1 by taking all the parameters in their low strain limits. Implying that $\sigma \cong \sigma_0$ and by extension $\sigma_c \cong \sigma_{c,0}$, $\phi_c \cong \phi_{c,0}$, $t \cong t_0$. This yields an equation relating G to the percolative parameters of the composite

$$G \approx \left[2 - \frac{1}{\sigma_{c,0}}\left(\frac{d\sigma_c}{d\varepsilon}\right)_0\right] - \left[\ln(\phi - \phi_{c,0})\left(\frac{dt}{d\varepsilon}\right)_0\right] + \left[\frac{t_0}{\phi - \phi_{c,0}}\left(\frac{d\phi_c}{d\varepsilon}\right)_0\right] \tag{6.5}$$

An important feature of this equation is the prediction that G scales inversely with $\phi - \phi_{c,0}$, which implies a divergence as $\phi \to \phi_{c,0}$ and explains the experimental observation that G increases sharply as the percolation threshold is approached from above. For practical purposes the first square bracket can be re-written in terms of $\ln\sigma_c$

$$G \approx \left[2 - \left(\frac{d\ln\sigma_c}{d\varepsilon}\right)_0\right] - \left[\ln(\phi - \phi_{c,0})\left(\frac{dt}{d\varepsilon}\right)_0\right] + \left[\frac{t_0}{\phi - \phi_{c,0}}\left(\frac{d\phi_c}{d\varepsilon}\right)_0\right] \tag{6.6}$$

Using equation 6.2, equation 6.6 can instead be described in terms of the zero-strain composite conductivity, σ_0.

$$G \approx \left[2 - \left(\frac{d\ln\sigma_c}{d\varepsilon}\right)_0\right] - \left[\frac{\ln\left(\sigma_{c,0}/\sigma_0\right)}{t_0}\left(\frac{dt}{d\varepsilon}\right)_0\right] + \left[t_0\left(\frac{\sigma_{c,0}}{\sigma_0}\right)^{1/t_0}\left(\frac{d\phi_c}{d\varepsilon}\right)_0\right] \tag{6.7}$$

The equations are written with bracketed terms to differentiate the contributions from each term which will facilitate the discussion below.

6.2.3. Factors Contributing to the Gauge Factor

The advantage of this approach is that knowledge of electrical percolation can be used to understand nanocomposite piezoresistivity. As has been outlined in Chapter 3, a number of factors influence the percolation parameters $\sigma_{c,0}$, $\phi_{c,0}$ and t_0. Clearly changes to these parameters will similarly have implications for the gauge factor via equations 6.6 and 6.7. For example, the dispersion state of the filler will affect $\phi_{c,0}$, with the alignment of the filler[131] leading to higher $\phi_{c,0}$ compared to randomly orientated[142] systems. According to equation 6.6, this will lead to a reduction in G for a given ϕ. The matrix will also play an important role, for example, polymer crystallisation on the filler surface has been shown

to increase interparticle resistance thus decreasing $\sigma_{c,0}$.[312] Such crystallisation should lead to a reduction in G according to equation 6.7. While the percolation parameters are well known, less well known are the strain dependent derivatives. Here, some time will be taken to consider the physical interpretation of these parameters.

First consider the term $(d\ln\sigma_c/d\varepsilon)_0$. To understand this term, note that most polymer-based nanocomposites contain highly conductive fillers, therefore, σ_c is limited by the junction resistance (R_J) between adjacent filler particles such that $\sigma_c \propto 1/R_J$.[312] Whether intersheet transport occurs by hopping or tunnelling mechanisms,[10,313] it's expected that $R_J \propto e^{kd}$, where d is the interparticle separation at a given strain and k is a positive constant. Assuming that d scales with the applied strain then $\varepsilon = (d - d_0)/ d_0$, where d_0 is the zero strain interparticle separation. Combining these ideas gives $d\ln\sigma_c/d\varepsilon \propto -kd_0$, which means $(d\ln\sigma_c/d\varepsilon)_0$ should be negative. This negative sign is in line with many studies showing composites to become more resistive upon tensile deformation.[10,184,296,298,314] This is significant as it means the first bracketed term of equations 6.6 and 6.7 must be positive.

Thus, the first term in equations 6.6 and 6.7 is predominantly associated with interparticle transport and describes the mechanism traditionally used to describe the piezoresistive response in nanocomposites.[295-298] However, the existence of the two other terms in equation 6.6 and 6.7 show that this is not the only contribution to G.

The second term of equation 6.6 and 6.7 is controlled by the strain dependence of the percolation exponent, $(dt/d\varepsilon)_0$. The percolation exponent has been shown to vary from universality based on the width of the distribution of junction resistances, with a wider distribution leading to larger values of t_0.[164,166,168,169] The application of strain will most likely increase the separation between adjacent sheets according to $d = d_0(\varepsilon + 1)$, therefore broadening the distribution and increasing t_0. On the other hand, strain should align the nanosheets somewhat so that the network becomes more 2D like than 3D, this in turn will

lower t_0.[295] It's therefore expected that $(dt/d\varepsilon)_0$ is controlled by a combination of junction and network properties, each driving $(dt/d\varepsilon)_0$ in different directions. Previous, theoretical calculations have suggested that $(dt/d\varepsilon)_0$ and $(dln\sigma_c/d\varepsilon)_0$ should have the same sign.[169] If this is true then $(dt/d\varepsilon)_0$ is generally negative and further implies that the second bracketed term in equation 6.6 and 6.7 are also negative. This has important implications which will be discussed below.

The final bracketed term of equation 6.6 and 6.7 is controlled by the strain dependence of the percolation threshold $(d\phi_c/d\varepsilon)_0$. The application of strain is likely to alter the structure of the network such that the percolation threshold is modified in some way. As an example, consider a network at the percolation threshold so that there is a single connected path of nanosheets through which current can pass. Applying tensile strain to such a network is unlikely to result in new paths forming, instead it is much more likely that the current path will break. This modification to the network structure should shift the percolation threshold to higher filler volume fraction. Thus, it's expected that $(d\phi_c/d\varepsilon)_0$ will always be positive, which is consistent with studies considering how conductivity varies with nanotube alignment in CNT networks. Alignment can act as a proxy for tensile strain, these studies show that as nanotubes become more aligned the percolation threshold similarly increases.[134,315]

Thus, in addition to the effect of strain on interparticle transport, which is generally considered as the mechanism controlling piezoresistive properties in networks, it's proposed that there are other factor related to both the junction and network properties which contribute to the piezoresistivity and hence *G*. Later on in this chapter the magnitude of these effects will be considered, however first, it's necessary to demonstrate that the equations above can describe experimental data.

6.2.4. Fitting Experimental Data

While equations 6.6 and 6.7 provide a theoretical description of the gauge factor dependence on both ϕ and σ_0 respectively, they cannot be used to fit experimental data in their current form. This is simply due to the fact that there are five unique parameters to be fit, which would inevitably lead to overfitting. However, considering the contributions of the individual bracketed term allows for some simplification. Noticing that $ln(\phi - \phi_{c,0})$ is a slowly varying function compared to $(\phi - \phi_{c,0})^{-1}$ as $\phi \to \phi_{c,0}$, it is likely that the second term of equations 6.6 and 6.7 is also slowly varying compared to the third. This allows us to consider the second term constant for fitting purposes, providing that $(dt/d\varepsilon)_0$ is not far larger than $t_0(d\phi_c/d\varepsilon)_0$ (this will be justified below). Applying this approximation yields a new form of equations, such that:

$$G \approx G_{0,\phi} + \frac{G_1}{\phi - \phi_{c,0}} \tag{6.8}$$

$$G \approx G_{0,\sigma} + (\sigma_1 / \sigma_0)^{1/t_0} \tag{6.9}$$

Where $\phi_{c,0}$, $G_{0,\phi}$, G_1, $G_{0,\sigma}$ and σ_1 are (near) constants. Note that this model implies that G has a near power law relationship with σ_0 which is consistent with the observations in Figure 6.1.

Testing the model

To test these models, two siloxane based graphene-polymer nanocomposites were prepared. One is a homemade viscoelastic polymer produced from crosslinking silicone oil with boric acid called G-putty (Figure 6.2A), as described in Chapter 5. The other is a

commercially available elastomer called syglard-170, which is chemically crosslinked through curing. The resulting graphene-elastomer composite is named G-sylgard (Figure 6.2B).

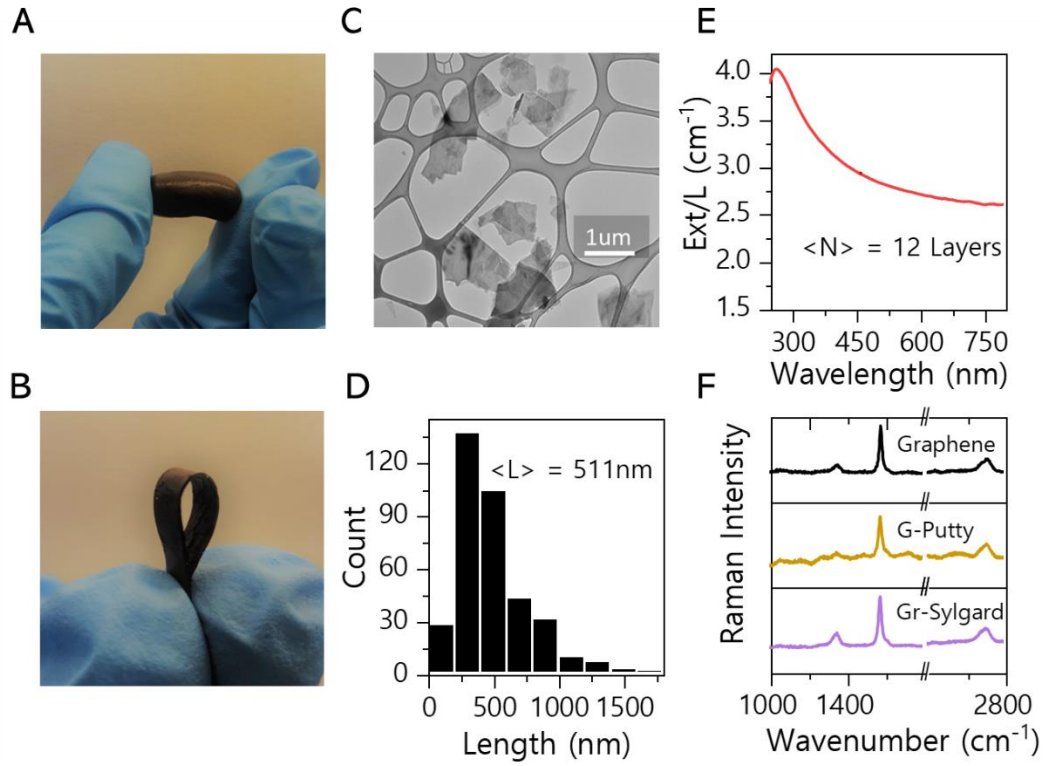

Figure 6.2 – Composite Characterisation. A) Image of G-putty nanocomposite. B) Image of G-sylgard nanocomposite. C) Representative TEM images of graphene nanosheets. D) Nanosheet length statistics determined from TEM images. Nanosheets have an average lateral size of 511 nm. E) UV-Vis extinction spectra of the graphene dispersion from which nanosheet layer number can be determined.[67] Raman spectra for graphene, G-putty and G-sylgard. Graphene peaks are present in each sample, showing graphene maintains its chemical composition when embedded in the polymer matrix.

The graphene nanosheets for these composites were prepared by liquid phase exfoliation. TEM (Figure 6.2C&D) shows these nanosheets to have an average lateral size of $\langle L \rangle$ = 511nm, while the average layer number $\langle N \rangle$ = 12 was determined from UV-vis spectroscopy (Figure 6.2E) using previously published metrics.[67] Both nanocomposites were formed by simple mixing of the polymer and nanosheet dispersions, followed by

evaporation of the solvent. Raman spectra of the graphene nanosheets and resulting nanocomposites are shown in Figure 6.2F . All spectra comprise of the D,G and 2D bands associated with graphene. The low intensity of the D band indicates that the graphene is relatively defect free while the contour of the 2D band suggests that the graphene is comprised of few layers.

For each composite, a range of different graphene volume fractions are prepared and are characterised in terms of their zero-strain conductivity, σ_0 and their sensitivity to strain, G, via resistance-strain measurements. Figure 6.3A shows the expected percolation like scaling of σ_0 with increasing ϕ. The solid lines are fits to percolation theory (Equation (6.2)) and linearised versions of the plots are shown in Figure 6.3B. The conductivities of both nanocomposites vary rather differently across the volume fraction range, which points to the important role played by the matrix in determining final composite properties. Here a maximum graphene volume fraction of ~9.5 vol% and ~ 8.5 vol% is used for G-putty and G-sylgard respectively. In G-putty it is found that composite quality begins to significantly deteriorate at high graphene loadings, as nanosheets tend to reaggregate, which is a common problem in composites.[122] In the G-sylgard case, at higher loadings graphene inhibits the in-situ polymerisation of the PDMS, which again leads to a significant deterioration in composite quality. As such ~9.5 vol% and ~ 8.5 vol% are chosen as cut-off points for this study as composites maintain good dispersion and mechanical robustness at these loadings.

The percolation thresholds are $\phi_{c,0}$ = 3.4 vol% and $\phi_{c,0}$ = 5.5 vol% for G-putty and G-sylgard respectively. These percolation thresholds are relatively large for graphene-polymer nanocomposites with a review from Marsden et al.[122] showing values ranging between 0.005 – 5%. A number of studies show that the in-situ polymerisation process used to prepare G-sylgard typically leads to larger percolation thresholds. The results are

consistent with another report on an in-situ polymerised siloxane graphene nanocomposite which yielded $\phi_{c,0}$ = 8.1 vol%.[191] Values of $\sigma_{c,0}$ are rather different for G-putty ($\sigma_{c,0}$ = 3.3 kS/m) and G-sylgard ($\sigma_{c,0}$ = 44 MS/m), however a wide discrepancy between values of $\sigma_{c,0}$ is not uncommon and $\sigma_{c,0}$ is observed to vary over many orders of magnitude depending on the processing and nanocomposite composition.[122] The reason for the large discrepancy in $\sigma_{c,0}$ is not entirely clear, one possibility is that each composite is formed by slightly different processing methods. The PDMS polymer in G-putty is first crosslinked before the addition of graphene while for G-sylgard the polymer is crosslinked with graphene *in-situ*. These variations in processing can lead to differences in the polymer/graphene interface as well as homogeneity of graphene dispersion within the polymer.[316] The percolation exponents are 5.4 and 5.1 for G-putty and G-sylgard. These values are far above the 3D universal value of t_{un} = 2, which is common in polymer nanocomposites and indicates a wide distribution of junction resistances.[166]

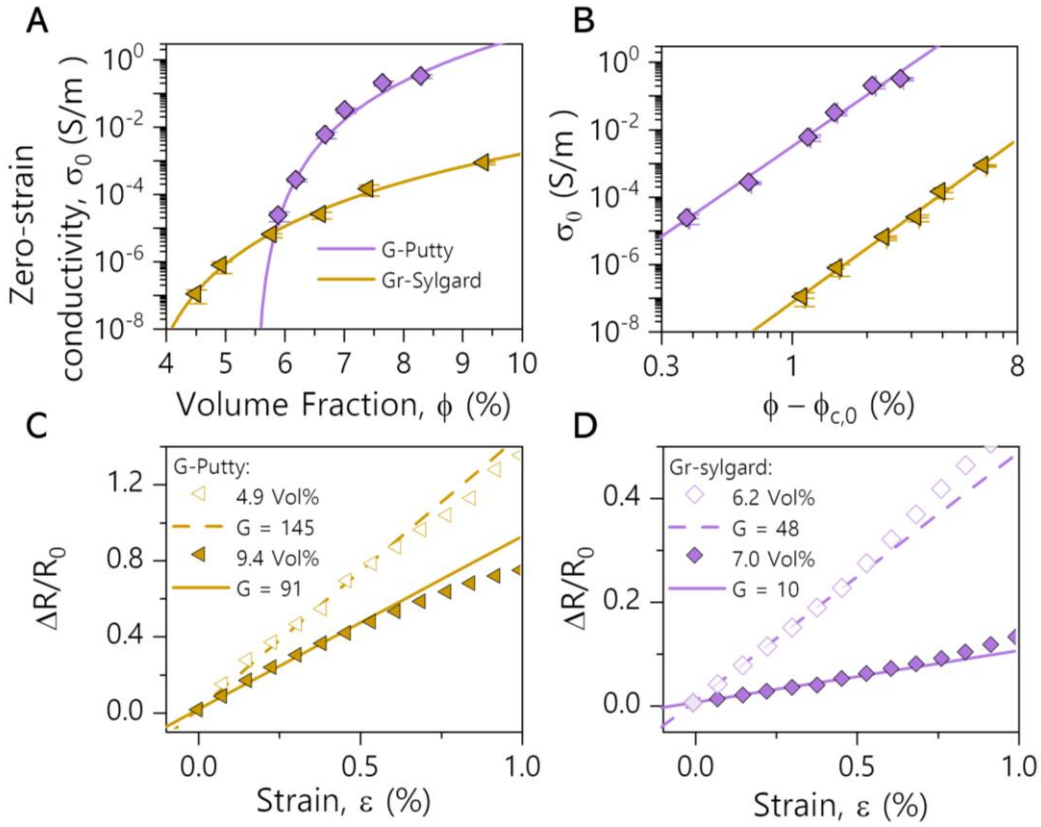

Figure 6.3 – Electrical and Electromechanical Characterisation. A) Zero strain conductivity plotted as a function of filler volume fraction. The solid lines are fits to equation 6.2. B) Linearised log-log form of A). C) Representative electromechanical response of G-putty at two different filler volume fractions. D) Representative electromechanical response of G-sylgard at two different filler volume fractions.

The electromechanical properties of the nanocomposites are probed by tracking the variation in resistance as a function of strain (Figure 6.3C&D). As is almost always observed, the resistance is seen to increase with applied strain. The fractional resistance change is seen to increase linearly with strain up to approximately ~0.75%, with the gauge factor extracted from the slope of the straight line for each volume fraction.

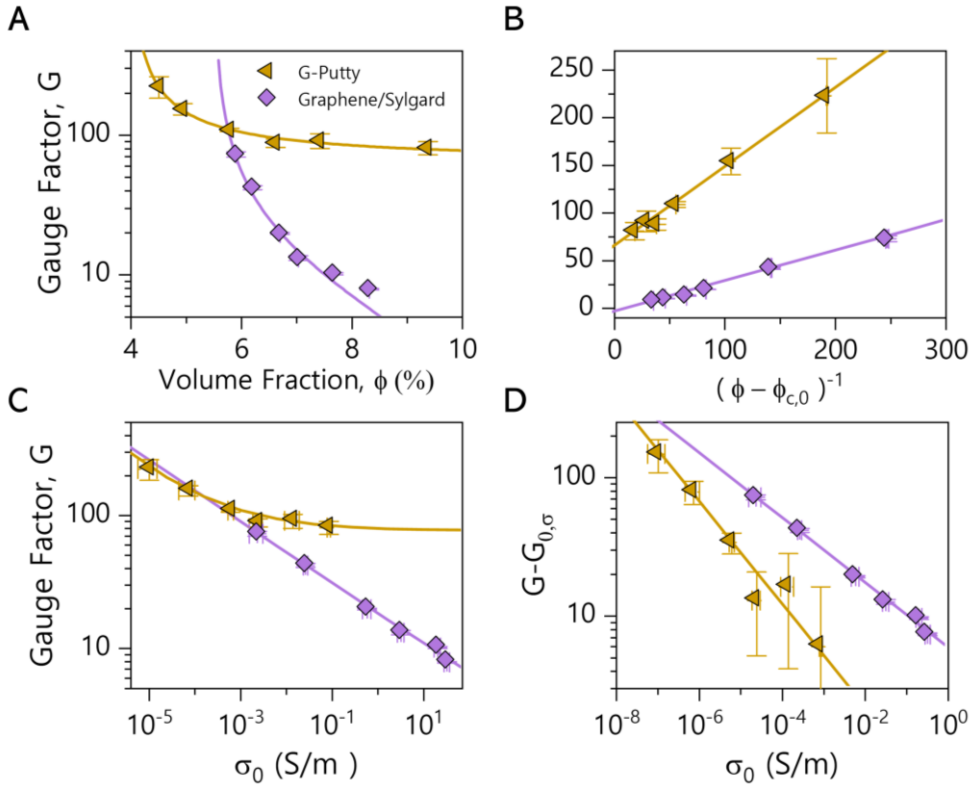

Figure 6.4 – Gauge Factor Characteristics. A) Gauge factor plotted as a function of filler volume fraction. The solid lines are fits to equation 6.8. B) A linearised form of A), showing fidelity of the equation. C) Gauge factor plotted as a function of the zero-strain conductivity. The solid lines are fits to equation 6.9. D) A linearised form of C), demonstrating the near power law relationship.

The resultant gauge factor is plotted as a function of ϕ for each composite with a linearised version shown in Figure 6.4A&B . As predicted by equation 6.8, G is seen to diverge as $\phi_{c,0}$ is approached from above. The complementary conductivity-gauge factor plot is shown in Figure 6.4C&D. Again, this data can be plotted in a linearized fashion to confirm the fidelity of the model, equation 6.9. The fit parameters for the models can be found in Table 6.1.

Table 6-1 - Various parameters obtained from linearized fits of data to Equations 6.2 (σ_0 vs. ϕ), 6.8 (G vs. ϕ) and 6.9 (G vs. σ_0).

	G- sylgard	G-putty		G-sylgard	G-putty		G- sylgard	G-putty
From fitting σ_0 vs. ϕ			From fitting G vs. ϕ			From fitting G vs. σ_0		
$\ln(\sigma_{c,0})$	18 ± 1	8.1 ± 0.6	$G_{0,\phi}$	-5 ± 1	63 ± 3	$G_{0,\sigma}$	0.5 ± 0.1	75 ± 5
$\phi_{c,0}$	5.5 ± 0.1%	3.4 ± 0.1%	G_1	0.32 ± 0.01	0.83 ± 0.03	σ_1 (S/m)	2220 ± 110	0.08 ± 0.04
t_0	5.1 ± 0.2	5.4 ± 0.3	$\phi_{c,0}$	5.5 ± 0.1%	4.0 ± 0.1%	t_0	4.3 ± 0.20	2.9 ± 0.3

Fit Parameters

As described above, standard strain sensor measurements can lead to three distinct datasets, (σ_0 vs ϕ, G vs ϕ, G vs σ_0) which can be fit with equations. This approach yields 9 different fit parameters. It is worth noting that there is some redundancy here, for example, $\phi_{c,0}$ can be extracted from both equations 6.8 and 6.9, while inspection of $G_{0,\phi}$ and $G_{0,\sigma}$ shows that they are actually identical. Therefore in reality, only two of the three equations will be required to extract all the percolative parameters.

To further demonstrate the power of these models, they have been applied number to of datasets from the literature, in addition to the composites above. In each case the data was fit using equations 6.2, 6.8 and 6.9 and the fit parameters are extracted (see Appendix B for complete composite characterisation). The percolation threshold is extracted from fitting σ_0 vs ϕ and G vs ϕ (Figure 6.5A), the extracted parameters agree very well with almost identical values found in each case as shown by the solid line (y = x). Fitting σ_0 vs ϕ and G vs σ_0, yields estimates for the percolation exponent (Figure 6.5B). The data lies in the vicinity of the y = x line. Although there are some non-trivial deviations, by and large the agreement is reasonable. Shown in Figure 6.5C, is the data for $G_{0,\phi}$ obtained by fitting G vs. ϕ using equation 6.8, which is plotted versus $G_{0,\sigma}$ obtained by fitting G vs. σ_0 using

equation 6.9. While these parameters should be equal as described above, they also have the greatest scope for deviation. This is because accurate values of these parameters require good data for G at high values of ϕ (and so σ_0). However, most papers do not report such data, while aggregation effects can cause significant errors. Despite this, reasonable agreement is found between these parameters with only two samples, both graphene-based giving significant deviation. Altogether the results give confidence that the developed models can accurately describe the data.

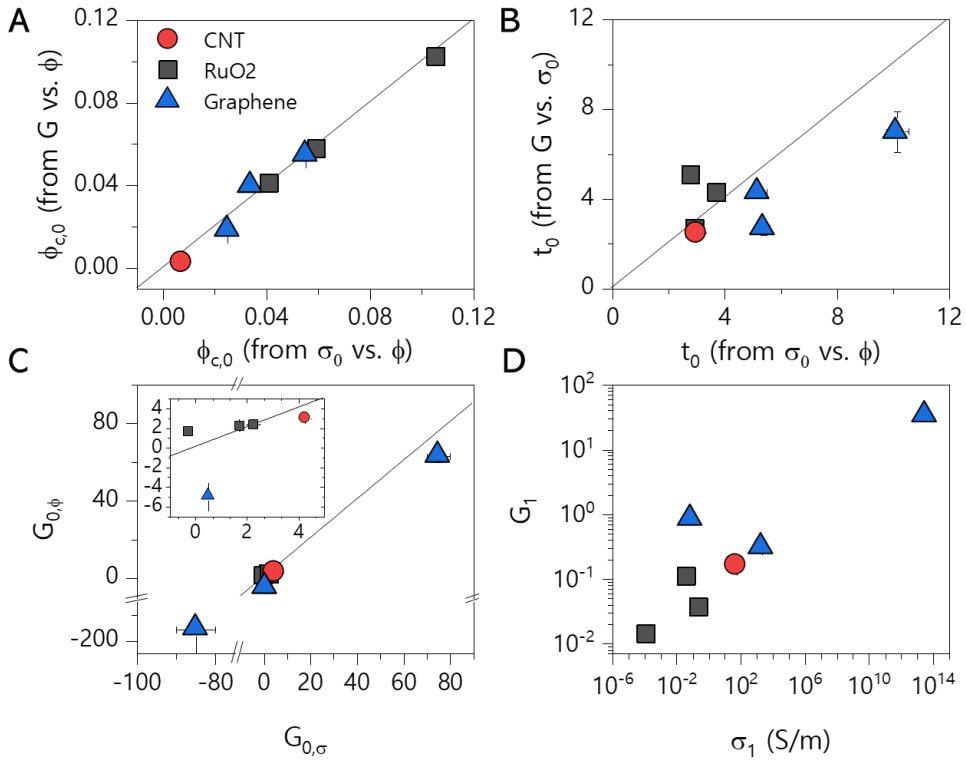

Figure 6.5 – Fitting Literature Data. A) Comparison of the percolation threshold obtained from fitting σ_0 vs ϕ and G vs ϕ. B) Comparison of the percolation exponent obtained from fitting σ_0 vs ϕ and G vs σ_0. C) Comparison of the gauge factor constant $G_{0,\phi}$ and $G_{0,\sigma}$ obtained from fitting G vs ϕ and G vs σ_0. D) Comparison of the gauge factor scaling factors G_1 and σ_1.

Assuming the model is indeed accurate, it is worth considering what values are obtained for G_1 and σ_1. These parameters are plotted in Figure 6.5D and tend to scale with each

other as is expected from inspection of equation 6.8 and 6.9. Both parameters span a broad range, with G_1 varying from ~0.01 to ~30 and σ_1 varying from 10^{-4} to 10^{13} S/m. It is clear that large values of G_1 and σ_1 are required in order to achieve high gauge factors. Interestingly, RuO_2 composites display the smallest values of G_1 and σ_1 while graphene and CNT based composites tend to display much higher values. Furthermore, it should be noted that even composites with the same composition such as graphene and siloxane polymer can show very different values of G_1 and σ_1. This latter point suggests that additional factors such as composite morphology also play an important role in piezoresistive performance. This is not surprising since it is well know that morphology also plays a crucial role in the electrical percolation parameters, for example in some instances filler aggregation can lead to a lower percolation threshold and larger composite conductivities. In this case we expect the piezoresistive response to be smaller than in an equivalent well dispersed composite, this is because the conductive network is less susceptible to strain as nanosheets will be better connected within the smaller volume they are confined to.

Strain Dependence of Percolation Parameters

While the methods described above are useful for extracting percolative parameters, they do not directly yield values of the strain dependence. It would ultimately be more useful to determine how accurately equation 6.6 and 6.7, explain experimental data, as it these equations which contain the underlying physics of the piezoresistive process. Given the zero-strain percolative parameters of the composites are already known, testing these equations will require values of the strain dependent terms $(dln\sigma_c/d\varepsilon)_0$, $(dt/d\varepsilon)_0$ and $(d\phi_c/d\varepsilon)_0$. To obtain these parameters, resistance-strain measurements (at 0.2% strain increments) are recorded for various volume fractions and converted to resistance versus volume fraction data sets, each at various strains (limiting ourselves to strains from 0 to

2%). Assuming a constant material volume, resistance can be converted to conductivity, yielding the strain dependent conductivity via:

$$\sigma = R\frac{L_0}{A_0}(\varepsilon+1)^2 \tag{6.10}$$

Where A_0 and L_0 are the zero-strain sample length and cross-sectional area. This procedure yields a set of conductivity versus volume fraction, each at different strain. Examples of this are shown in Figure 6.6, which show a reduction in conductivity with strain at all volume fractions. These curves are then fit using equation 6.2 which yields values of $ln\sigma_c$, ϕ_c and t as a function of strain. By plotting the percolation parameters versus strain values for $(dln\sigma_c/d\varepsilon)_0$, $(dt/d\varepsilon)_0$ and $(d\phi_c/d\varepsilon)_0$ can be obtained. While literature data on these parameters is thin on the ground, there are a few papers against which the results can be compared.

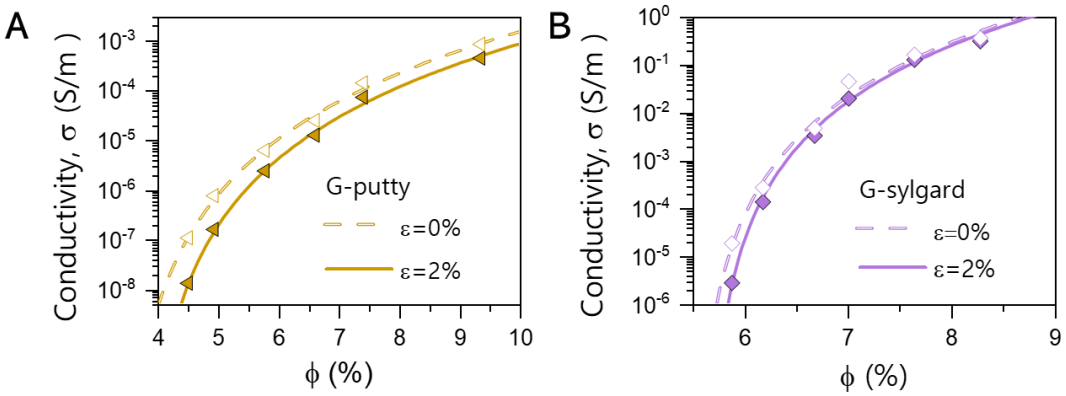

Figure 6.6 – Strain Dependent Percolation. Conductivity percolation plots at 0% and 2% strain. By fitting these plots at various increments of strain the strain dependence of $ln\sigma_c$, ϕ_c and t can be obtained for A) G-putty and B) G-sylgard.

The data in Figure 6.7A&B demonstrates a clear increase in the percolation threshold with strain which yields values of $(d\phi_c/d\varepsilon)_0 = 0.07$ and $(d\phi_c/d\varepsilon)_0 = 0.5$ for G-sylgard and G-putty

respectively. The positive slopes are expected, as outlined in the earlier discussion, and agree with previous studies which demonstrate an increase in the percolation threshold under strain and under alignment. For example Zhang et al. have measured $(d\phi_c/d\varepsilon)_0 =$ 0.004 in polymer-nanotube composites.[181]

As shown in Figure 6.7C&D, $ln\sigma_c$ is found to decrease under strain, although the change is small compared to the error bars. Notwithstanding the error, values of $(dln\sigma_c/d\varepsilon)_0$ are found to be -4.4 and -120 for G-sylgard and G-putty respectively. A value of $(dln\sigma_c/d\varepsilon)_0$ ~ -30 was extracted from ref [295] for comparison. Importantly the negative sign of the term matches the physical understanding of the network as described earlier. It is expected that $(dln\sigma_c/d\varepsilon)$ should vary with interparticle distance, d_0 such that $(dln\sigma_c/d\varepsilon) - kd_0$. If a nontrivial amount of interparticle charge transport is to occur, the value of d_0 must lie in a relatively narrow range (d_0 can never be less than the van der Waals distance while values greater than a few nanometres will result in negligible tunnelling current). This means that much of this large difference is probably associated with variations in k between composites. As k is presumably controlled by the details of the interparticle potential barrier, this shows that the nature of the junction can have a significant impact on the gauge factor.

Both composites also show a reduction in t with increasing strain (Figure 6.7D&E). As before, the error bars are large compared to the variation, yet a well-defined trend exists. The low strain values are found to be $(dt/d\varepsilon)_0 =$ -4.2 and $(dt/d\varepsilon)_0 =$ -33 for G-sylgard and G-putty respectively. A previous work also found $(dt/d\varepsilon)_0$ to be negative, with a value of -8 found for polyurethane-MWCNT in this case.[295] It should be further noted the signs of $(dt/d\varepsilon)_0$ are the same as those found $(dln\sigma_c/d\varepsilon)_0$ which is consistent with results from previous studies.[169,295]

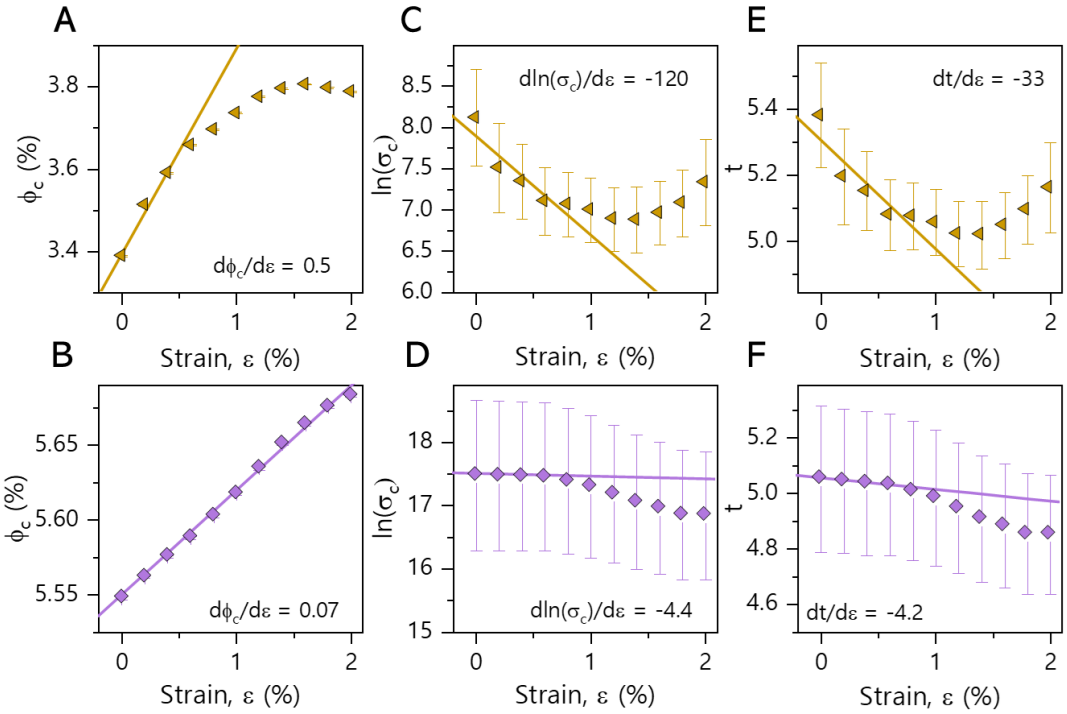

Figure 6.7 – Strain Dependence of Percolation Parameters. A) – B) ϕ_c , C) – D) $ln\sigma_c$, E) – F) t , plotted as a function of strain for G-putty (top) and G-sylgard (bottom). The parameters show well defined trends with the linear region of the data at low strain used to obtain $(d\phi_c/d\varepsilon)_0$, $(dln\sigma_c/d\varepsilon)_0$ and $(dt/d\varepsilon)_0$.

The strain dependent parameters are summarised in the table below:

Table 6-2 - Parameter values obtained from linear fits at low strain to the percolation data presented in Figure 6.7 (A-F).

	$\left(d\ln\sigma_c/d\varepsilon\right)_0$	$\left(dt/d\varepsilon\right)_0$	$\left(d\phi_c/d\varepsilon\right)_0$
Expected sign	-ve	+ve	-ve
G-Sylgard value	-4.4	-4.2	0.07
G-putty value	-120	-33	0.5

Now that all the quantities of equations 6.6 and 6.7 have been determined, numerical curves of G as a function of ϕ_0 and σ_0 can be generated. The parameters from Table 6.2 and the relevant percolation values obtained from fitting equation 6.2 are substituted into

equations 6.6 and 6.7. This yields the black curves found in Figure 6.8, which match the experimental data extremely well, illustrating the validity of the approach.

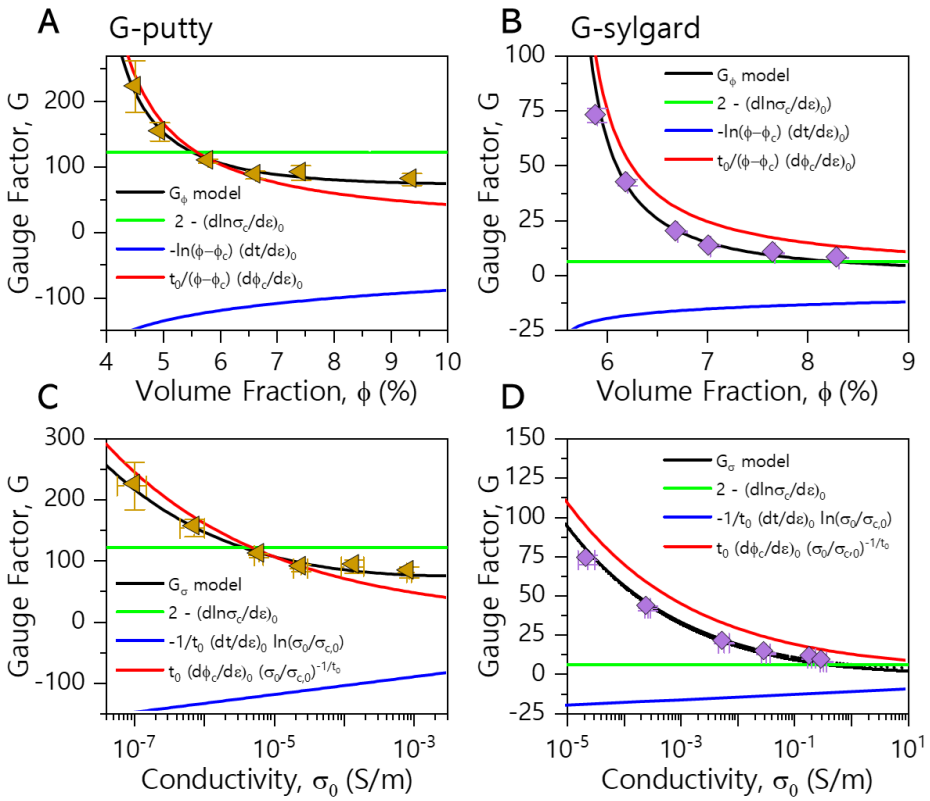

Figure 6.8 – Model Predictions. Experimental gauge factor data plotted versus graphene volume fraction (A-B) and zero-strain conductivity (C-D) for G-putty (A,C) and G-sylgard (B,D) composites. In each panel, the black lines are obtained by plotting either equation 6.6 (A-B) or 6.7 (C-D). The other lines correspond to the individual contributions of the bracketed terms in equation 6.6 and 6.7.

The magnitude of each of the bracketed terms in equations 6.6 and 6.7 is assessed by plotting the contribution from each term separately. The primary thing to note here is the similarity between the third bracketed term (red line) and the total equation (black line) which indicates that this term dominates. This result justifies the earlier assertion that the second bracketed term can be treated as a constant, owing to its weaker dependence on ϕ and σ_0. In addition, the first and second term are of similar magnitude, which means they

somewhat cancel out. Depending on the degree of cancellation this can result in small or negative values of $G_{0,\phi}$ and $G_{0,\sigma}$, limiting the contribution from the first two terms to the gauge factor. This further supports the proposal that the third term is particularly important, especially when accounting for variations in G close to the percolation threshold.

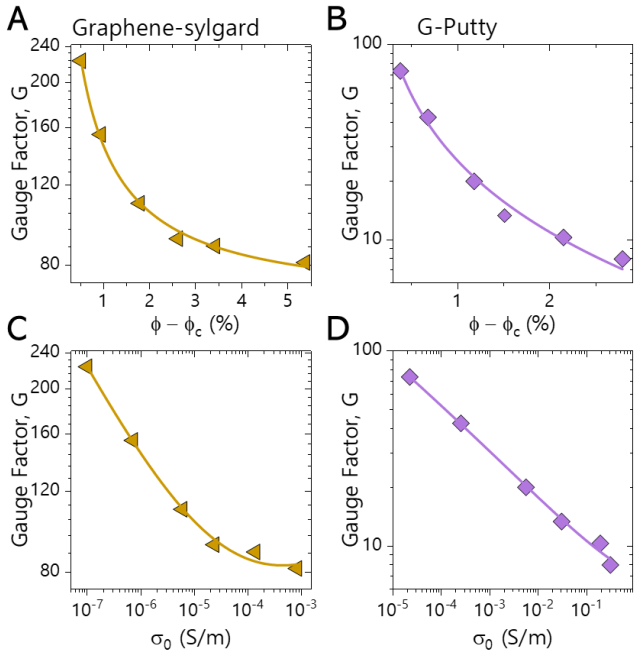

Composite	G-sylgard	G-putty
Expected Values		
$(d\ln\sigma_c/d\varepsilon)_0$	-4.4	-120
$(d\phi_c/d\varepsilon)_0$	0.07	0.5
$(dt/d\varepsilon)_0$	-4.2	-33
From fitting G vs. ϕ		
$(d\ln\sigma_c/d\varepsilon)_0$	0 ± 19	-66 ± 16
$(d\phi_c/d\varepsilon)_0$	0.06 ± 0.01	0.16 ± 0.01
$(dt/d\varepsilon)_0$	2 ± 5	-2 ± 5
From fitting G vs. σ_0		
$(d\ln\sigma_c/d\varepsilon)_0$	-16 ± 7	-205 ± 25
$(d\phi_c/d\varepsilon)_0$	0.068 ± 0.003	0.64 ± 0.04
$(dt/d\varepsilon)_0$	-6.3 ± 1.9	65 ± 9

Figure 6.9 – Fitting the Strain Dependent Derivatives. A) – B) Gauge factor versus volume fraction, the solid lines are fits to equation 6.6 for G-putty and G-sylgard. C) – D) Gauge factor versus conductivity, the solid lines are fits to equation 6.7 for G-putty and G-sylgard. Fit parameters can be found in the corresponding table.

Given the accuracy with which equations 6.6 and 6.7 describe experimental data, one might ask if the simplification of equations to 6.8 and 6.9 is necessary. Note that instead of fitting the percolation parameters ($\sigma_{c,0}$, $\phi_{c,0}$ and t_0), fixed values of the same quantities, obtained from fitting equation 6.2 could instead be used. Therefore, only $(d\ln\sigma_c/d\varepsilon)_0$, $(dt/d\varepsilon)_0$ and $(d\phi_c/d\varepsilon)_0$ need be found. This fitting was attempted, however, some mixed results were obtained, yielding some reasonable values, while some results were far from

expected or had large errors (Figure 6.9). It's believed the main problem here is associated with the limited number of data points per data set (six in this case). Although such data sets are standard or even extensive compared to the literature, they are clearly not reliable enough to extract the derivatives. However, this might be addressed in the future, simply by fabricating larger sample sets with more filler volume fractions, leading to more data points per data set.

6.2.5. Optimising the Gauge Factor

Now that it seems reasonably clear that equations 6.6 and 6.7 can be used to quantitively used to describe experimental data. It is worth considering how the gauge factor might be maximised. Focusing on equation 6.6, the first two terms would ideally be large and positive. Given the findings above and from literature[169] that $(dln\sigma_c/d\varepsilon)_0 \propto (dt/d\varepsilon)_0$, this will inevitably lead to some cancellation. If it is possible to engineer these parameters in some way, the preferable scenario is one where $(dln\sigma_c/d\varepsilon)_0$ is large yet $(dt/d\varepsilon)_0$ is minimised. A complication here is that t_0 should be large in order to maximise the third term. Therefore, the most pragmatic solution is to maximise both $(dln\sigma_c/d\varepsilon)_0$ and t_0 while hoping $(dt/d\varepsilon)_0$ is not too large to negatively affect *G*. $(dln\sigma_c/d\varepsilon)_0$ could be maximised through optimising kd_0 as previously mentioned. Doing so would require knowledge of the interparticle transport mechanism and therefore *k*. For example, Simmon's tunnelling suggests that k could be maximised by increasing the height of the interparticle tunnelling barrier.[297,298] This may be possible by coating filler particles in a wide-band gap insulator, however this is likely to be deleterious to the conductive properties of the network.

The third term of equation 6.6 is less ambiguous. This term will always be positive and will be maximised for large values of t_0 and $(d\phi_c/d\varepsilon)_0$. As discussed previously, t_0 is associated with the width of the distribution of the interparticle junction resistances and

is a parameter that might be engineered in some way. The nature of $(d\phi_c/d\varepsilon)_0$ is less clear. However, if t_0 is known, then $(d\phi_c/d\varepsilon)_0$ can be obtained from equation 6.8. To give some insight into $(d\phi_c/d\varepsilon)_0$, the G_1 values obtained from fitting equation 6.8 are combined with t_0 values obtained from fitting ϕ vs σ and σ vs G (an average value is used) to obtain $(d\phi_c/d\varepsilon)_0$. Plotting the resultant values of t_0 and $(d\phi_c/d\varepsilon)_0$ shows a well-defined relationship with larger values of t_0 leading to increased values of $(d\phi_c/d\varepsilon)_0$, as shown in Figure 6.10.

A physical understanding of this behaviour can be obtained by considering a composite with a large t_0 very close to the percolation threshold, such that there is a wide distribution of interparticle junction resistance. Under these circumstances only one complete current path exists which will have at least one bottle neck. The larger the value of t_0, the higher the probability that the limiting interparticle junction is one of high resistance. Since large junction resistances are likely to be associated with a large interparticle separation $(R_J \propto e^{kd})$ and therefore more likely to be broken under an applied strain. Such a breakage would shift the percolation threshold to higher filler volume fractions thus increasing $(d\phi_c/d\varepsilon)_0$ and illustrating the connection with t_0.

The discussion above illustrates the importance of t_0 and the compounding influence of t_0 on the third term of equation. A reduction in the negative contribution of the second term can also be achieved by increasing t_0. Therefore its suggested the soundest approach to increasing G is to find ways to engineer composites with high t_0 values.

Given that the measurements here only consider network effects in the axis of strain it is worth taking some time to consider, the effect of uniaxial strain on a conductive composite network perpendicular to the strain direction. Due to the Poisson effect the materials thickness and width undergo compression, recalling that $R = L/\sigma A$, the dimensional contraction in channel length and width should cancel out leading to a decrease in resistance which is linearly proportional to strain. It can then be shown that in the limit of

low strain the transverse geometric gauge factor should be -1. However it is likely that the effect of strain on the particle network is far more prominent than the simple geometric effect. Since contraction is taking place perpendicular to the applied strain it is likely that the average distance between particles in the current direction is on average decreasing (as long as the particle orientation does not change too much under strain), this again will lead to a decrease in resistance in the transverse direction so while G is expected to be positive in the direction of tensile strain we can expect the transverse gauge factor to be negative.

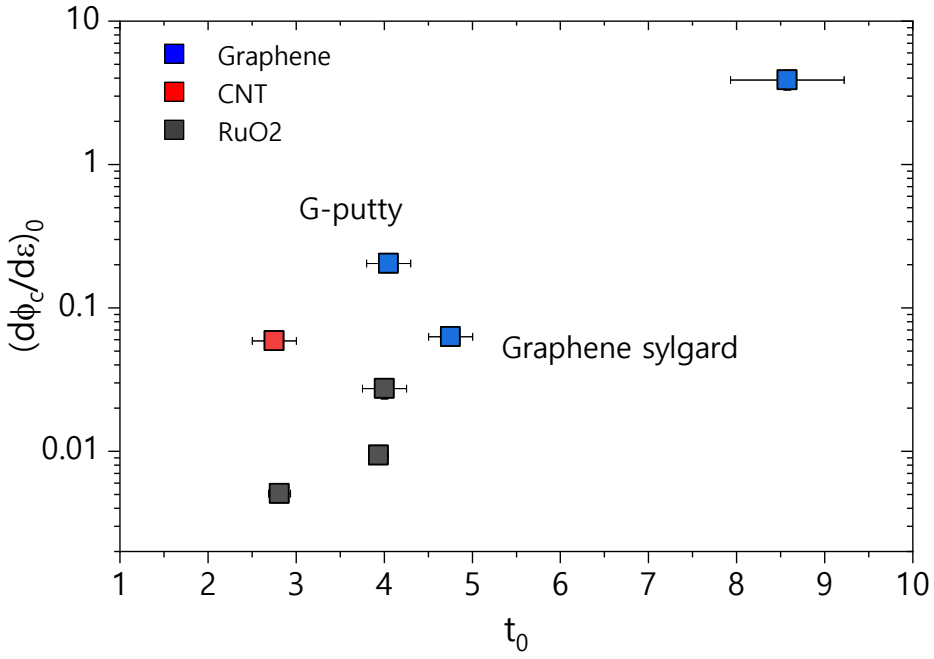

Figure 6.10 – Optimising the Gauge Factor. A demonstration of the positive relationship between $(d\phi_c/d\varepsilon)_0$ and t_0. This indicates that engineering higher values of t_0 may be a viable path to accessing very large gauge factors.

6.3. Conclusions

This work has used percolation theory to develop a model relating the nanocomposite gauge factor (sensitivity) to the filler volume fraction in piezoresistive sensors. This model predicts the gauge factor to diverge as the filler volume fraction approaches the percolation threshold from above, a key feature observed experimentally for nanocomposite sensors. In addition, alongside the widely considered contribution from the interparticle resistance, the model shows the gauge factor to depend strongly on effects associated with the network of filler particles.

The model is in good agreement with experimental data, both measured here and extracted from the literature. In addition, once the percolation fit parameters and their strain derivatives were independently obtained from experimental data and inserted into the model, gauge factors could be predicted to a good degree of accuracy.

These results are important for two reasons. First, the equations can be used to fit the experimental data, yielding figures of merit for piezoresistive performance. This allows the comparison of strain sensors both with each other and with the literature. More importantly, this work shows the response of composite strain sensors to be more complex than previously thought and shows the effect of strain on the particle network to be at least as important as the effect of strain on the interparticle resistance.

Chapter 7

Piezoresistive Properties of 2D:2D nanocomposites

Piezoresistive nanocomposites are an important class of materials which allow for the fabrication of highly sensitive strain sensors. Typically, these nanocomposites are comprised of a polymer matrix with a conducting filler, as has been discussed in previous chapters. However, strain sensors need not be limited to traditional nanocomposites, and can also be comprised solely of nanomaterial based thin films supported by polymer substrates. The particular attraction of these thin film systems is that the mechanical properties of the sensor depend on the mechanics of the substrate, while the electrical and piezoresistive properties are determined by the particle network.[177,248]

Despite their attraction, the understanding underlying thin film sensor performance is rather nebulous, and this has led to a lack of control over sensor strain sensitivity. To date, the only reliable control of nanomaterial thin film sensitivity and conductivity is achieved through exploiting thickness percolation effects, where very thin films close to the thickness percolation threshold show an exceptionally high piezoresistive response and the magnitude of the response gradually decreases as the bulk regime is approached.[89,317,318] Thus, it would be useful if other methods could be exploited to control the piezoresistive response, opening the door to novel types of sensor design as well as giving some insight into the mechanisms underlying piezoresistive networks. Based on the results of previous chapters, it's proposed that combining different nanomaterials to form nano:nano composites is a promising strategy to yield printable, high performance piezoresistive materials with tuneable sensitivity. Nano:nano composites are distinct from polymer nanocomposites or single nanomaterial networks. This is because the interaction between the disparate components and diversity of nanomaterial properties can dramatically affect nano:nano composite conductivity.[249,255,290,319-323] However, the piezoresistive properties of these systems are relatively unexplored, particularly the gauge factor dependence on filler volume fraction and nanocomposite conductivity.

The aim of this work is to investigate the conductive and piezoresistive properties of various combinations of 2D nanosheets. These combinations comprise of two-phase mixtures of conducting, semiconducting and insulating 2D materials. The conductive behaviour of these nanocomposites should be described by percolation theory with the ultimate goal of relating the piezoresistive and percolative network properties. This information will guide future progress towards high performance strain sensors.

7.1. Experimental Methods

Nanosheet dispersions of graphene, Gr (Asbury, Grade 3763), boron nitride, BN (Sigma Aldrich, >98.5 %), tungsten diselenide, WSe_2 (Alfa Aesar, 99.8 %) and tungsten disulphide, WS_2 (Alfa Aesar, 99.8 %) were prepared in the same way. Firstly, powders (30 mg ml^{-1}) were immersed in a 80ml solution of DI water and Sodium Cholate Hydrate, NaC, 6 mg ml^{-1}). The dispersion was probe sonicated using a Sonics Vibra-Cell VCX-750 ultrasonic processor at 50 % amplitude and 6:2 on:off ratio for 1 h. The process was maintained at 7°C to prevent overheating and minimise solvent evaporation. The resulting dispersion was centrifuged (Hettich Mikro 220R centrifuge) for 1 h at 3824 g, the supernatant was discarded and the sediment was redispersed in 80 ml DI water and NaC (2 mg ml^{-1}) via bath sonication. The dispersions were then sonicated for 8 h at 50% amplitude and 4:4 on:off ratio. Unexfoliated and large nanosheets were removed by centrifuging the dispersions at 106 g for 2 h and discarding the sediment. The supernatant was then centrifuged at 3824 g for 2 h, discarding the supernatant and redispersing the sediment in 80ml DI water and NaC (2 mg ml^{-1}) to obtain stock dispersions of nanosheet inks. The nanosheet concentration was determined via vacuum filtration of a fixed dispersion volume onto an alumina membrane and measuring the change in mass.

To remove excess the NaC, the graphene stock dispersion was centrifuged at 3824 g for 2 h, the supernatant discarded and sediment redispersed in DI waster. Silver nanosheets, AgNS (Tokusen USA N300) are commercially sourced and delivered as a viscous paste. Upon dilution with DI water workable inks can be obtained. Ink concentration was determined via vacuum filtration of a fixed ink volume onto an alumina membrane and measuring the change in mass. Composite inks of different concentrations were achieved by mixing AgNS and graphene inks in various ratios. Note the selected mass fractions where chosen according to data in previous works, which show that the percolation

threshold for 2D:2D composites lies between 5wt% - 20wt%.[131,176] The ink concentration was tailored so that the solids volume content was the same in all inks. In this case the starting AgNS ink had a concentration of 2 mg ml^{-1} and graphene ink had a concentration of 0.43 mg ml^{-1}. Transfer of stock dispersions to IPA was achieved by centrifuging at 3824 g for 2 h. The sediment was then redispersed in IPA. This was repeated three times to remove a residual water and surfactant. Nanocomposite inks were then achieved by the same methods as those described above. Extinction spectra were recorded for each dispersion using a Varian Cary 50 UV-Vis spectrophotometer in 0.5 nm increments with a 10 mm quartz cuvette.

Nanocomposite inks were deposited into networks via spray-coating using a Harder and Steenbeck Infinity Airbrush, in tandem with a Janome JR23000N mobile gantry. A platen was used to heat the substrates to 70 °C. A N_2 back pressure of 4 psi, nozzle diameter of 400 μm and stand-off distance of 10 cm were also used. Single line patterns of 15 mm × 1 mm were achieved by spray-coating of IPA based inks through a patterned steel mask onto polyimide substrates supplied by DuPont (35 mm × 5 mm × 0.125 mm). The water based inks were sprayed in the same fashion however in this instance the substrates were alumina-coated PET (NM-TP-3GU100 A4) from Mitsubishi Paper Mills. A Bruker Dektak Profilometer was used to establish thin film thickness with a stylus tip of 12.5 μm and stylus force of 9.8 μN. Film thickness was measured on films sprayed on glass substrates, and were found to be between 600-1000 nm thick, well above the thickness percolation thresholds of LPE nanosheet networks.[89,130,183]

The electrical properties of the films were probed using a Keithley KE2601 source meter in a 2-probe mode, controlled by LabView software. Electromechanical tests are carried out in conjunction with a Zwick Z0.5 ProLine Tensile Tester (100 N Load Cell). All samples had a gauge length, L_0 = 25 mm. Tensile measurements were carried out at a strain

rate of 1 %/s. At each filler volume fraction a total of 4-6 resistance-strain measurements were carried out and an average value of *G* was obtained. The error bars contained within the plotted data is the standard error of the average value. This is calculated as the standard deviation divided by the square root of the number of samples.

Raman spectra were acquired with Horiba Jobin Yvon set up using a laser line of 532 nm. A 10X objective was used with a neutral density filter to avoid heating of sample. The samples for the Raman measurements were prepared by drop casting the dispersion (~0.5 mg/ml) onto the heated silicon wafer coated with 300 nm of silicon dioxide. SEM images of 2D:2D nanocomposite thin films were captured using a Zeiss Ultra scanning electron microscope with accelerating voltages of 2 – 5 keV. A JEOL JEM-2100 LaB_6 transmission electron microscope operating at 200 keV was used to provide images of individual nanosheets. The dispersion was diluted to low concentrations and drop-cast onto an ultrathin carbon film TEM grids provided by Ted Pella, Inc. The TEM grid was placed on a piece of filter paper in order to wick away any excess solvent and then dried overnight in a vacuum oven. The images were used to obtain a statistical analysis of the nanosheet lengths, here defined as the longest axis of each nanosheet.

7.2. Results and Discussion

7.2.1. Nanomaterial characterisation

To study the piezoresistive properties of nano:nano composites,[324] thin films were prepared from mixtures of various types of conducting (silver and graphene nanosheets), semiconducting (WSe_2 and WS_2 nanosheets) and insulating (BN nanosheets) 2D materials. The first step toward film formation is to prepare inks of each material. Inks of graphene, WSe_2, WS_2 and BN nanosheets were produced by liquid phase exfoliation in water and surfactant.[13,93] Silver nanosheets (AgNS) are commercially sourced and are

delivered as highly concentrated water-based pastes, workable inks are then prepared through simple dilution in DI water.

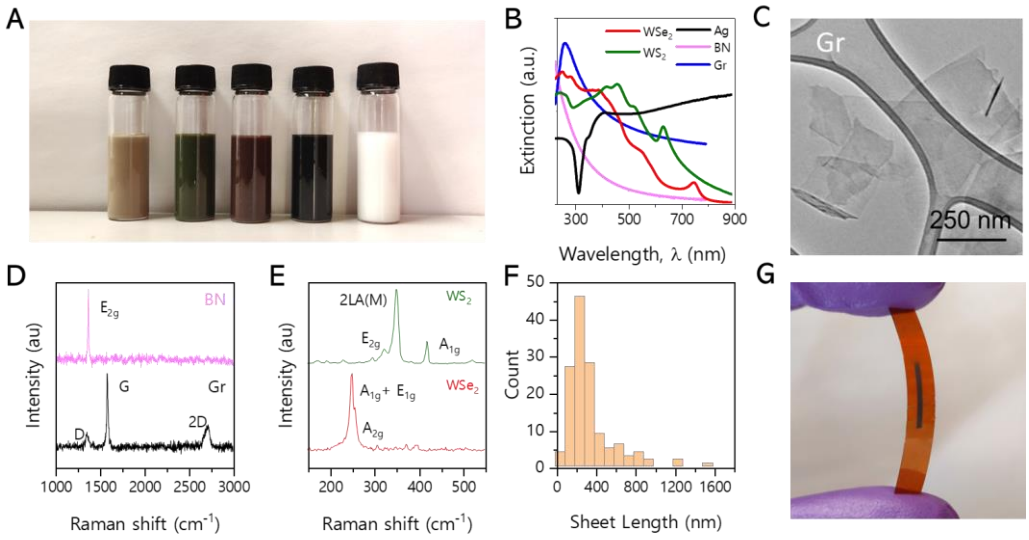

Figure 7.1 – Nanosheet Characterisation A) Image of nanosheet dispersions: Ag, WS_2, WSe_2, Gr, BN. B) UV-Vis extinction spectra of all nanosheet dispersions. C) Typical TEM images of nanosheets: Ag, B N, WS_2, WSe_2 D) Histogram of graphene nanosheet length <L> = 348 nm. Inset: Typical TEM image. E) Raman spectra measured on networks of WS_2, WSe_2, BN, Gr. F) Image of a spray coated 2D:2D nanocomposite network.

An image of the various nanosheet inks is shown in Figure 7.1A. Optical extinction spectra of each dispersion are presented in Figure 7.1B, with each spectrum showing the appropriate features. The characteristic high frequency plateau and π-π* peak are observed for graphene,[67] while BN displays the expected broad scattering background.[325] Both WS_2 and WSe_2 display their main spectral features, namely A excitons at 640 nm[87,326] for WS_2, and 755 nm[87] for WSe_2. The AgNS spectra contains features at 350 nm and 400 nm respectively, which are typically observed in spectra of silver nano-plates[327], -bars[328], -particles[329] and -wires[330], and have previously been attributed to surface plasmon resonances (although the exact location of the features depends on the dimensionality of

the silver). From the extinction spectrum an estimate for graphene layer number can be obtained as discussed previously, utilising the empirical equation proposed by Backes et al.[67] yields, $\langle N \rangle \sim 7$.

Transmission Electron Microscopy (TEM) (Figure 7.1C) confirms the presence of well exfoliated 2D sheets in the prepared graphene dispersions with no non-2D objects observed. Raman spectra, measured on drop cast-films (Figure 7.1D&E), showed all the expected features consistent with literature reports on 2D nanosheets of graphene,[67] WS_2,[331] WSe_2,[332] and BN[325]. Nanosheet length statistics can be extracted from TEM images, as demonstrated in Figure 7.1F with the average graphene nanosheets length, $\langle L_{Gr} \rangle = 348$ nm. An example of a nanosheet film is shown in Figure 7.1G.

The average nanosheet length can b" ext'acted for the other nanosheet dispersions (Figure 7.2A-D), $\langle L_{BN} \rangle = 327$ nm, $\langle L_{WS_2} \rangle = 197$ nm, $\langle L_{WSe_2} \rangle = 161$ nm and $\langle L_{Ag} \rangle = 251$ nm. The LPE nanosheets appear relatively transparent to the electron beam while the AgNS are opaque indicating a thickness difference. The individual inks were mixed to produce nano:nano composite inks of various mass fractions with the following compositions: BN:Gr, WSe_2:Gr, WS_2:Gr, Ag:Gr. The composite inks were prepared as thin films by spray coating the inks onto polyimide substrates.

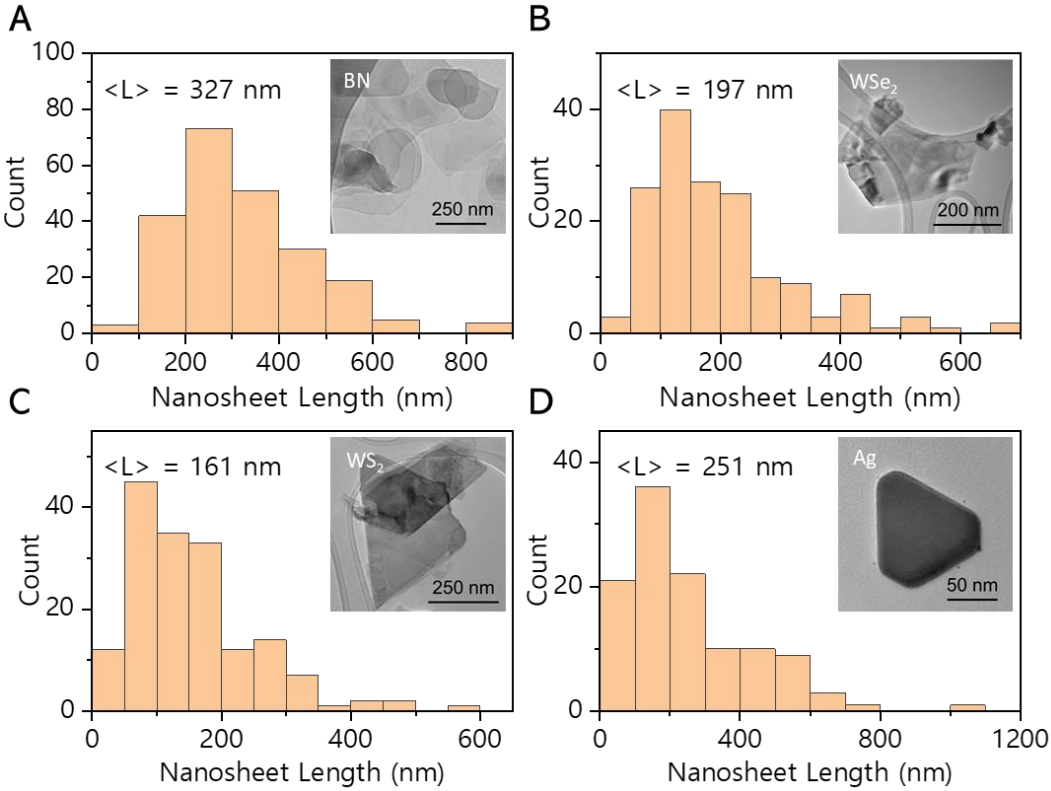

Figure 7.2 – Nanosheet Imaging. TEM Length statistics and images for A) BN, B) WSe_2, C) WS_2 and D) Ag nanosheets. Each distribution comprises of a minimum of 110 individual counts.

7.2.2. Network Morphology

The surface of the final composite films were studied by scanning electron microscope, SEM (Figure 7.3 A-D) showing disordered, porous networks. The films appear uniform over large length scales with graphene nanosheets (dark) mixed homogenously with BN, WSe_2, WS_2, Ag (lighter) nanosheets. Proper analysis of the nanocomposites requires conversion of the inks from mass fraction to volume fraction. In general, graphene is the filler however AgNS is denoted as the filler in the Ag:Gr composites due to its higher conductivity relative to graphene.

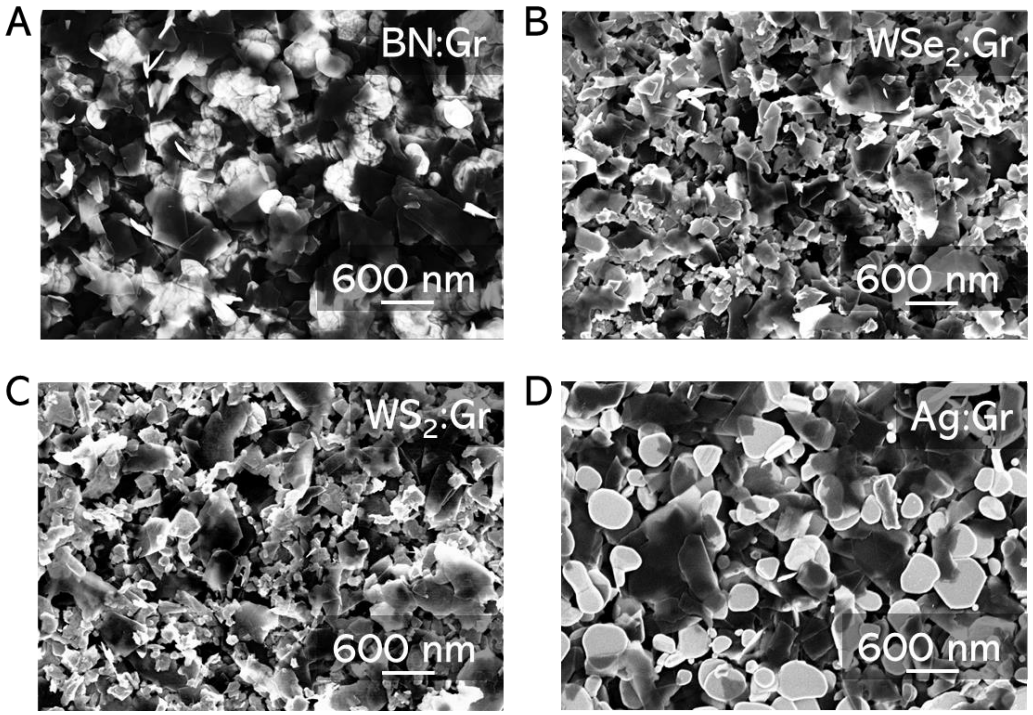

Figure 7.3 – 2D:2D Nanocomposite SEM Characterisation A-D) Representative SEM of nanocomposite networks for A) BN:Gr, B) WSe_2:Gr, C) WS_2:Gr, D) Ag:Gr.

For generality, filler volume fraction is labelled as ϕ although in specific cases, ϕ_{Gr} or ϕ_{Ag} is used. In polymer-based nanocomposites, the filler is embedded in a continuous matrix. However, nano:nano composites consist of a mixture of filler particles, matrix particles and pores, with no continuous phase. Due to imperfect packing of the nanosheets, 2D networks are inherently porous systems. The porosity depends on the deposition method,[88] with spray coated networks displaying porosities (ϕ_p) between 40-60%.[333] ϕ is therefore defined as the volume of filler particles divided by the total film volume. Taking the porosity into account, ϕ can be related to M_f via:[324]

$$\phi = \frac{1-\phi_p}{1+\frac{\rho_f}{\rho_m}\frac{(1-M_f)}{M_f}} \tag{7.1}$$

where ρ_f and ρ_m are the densities of the filler and matrix particles. To convert M_f to ϕ, the following values are assumed: ρ_{Gr} = 2200 kg m^{-3}, ρ_{BN}= 2100 kg m^{-3}, ρ_{WSe_2} = 7500 kg m^{-3}, ρ_{WS_2} = 9300 kg m^{-3}, ρ_{Ag} = 10500 kg m^{-3} and in all cases assume ϕ_p = 0.5.

7.2.3. Percolative Conductivity

The in-plane DC conductivity of each composite type was measured as a function of filler volume fraction (i.e. ϕ_{Gr} or ϕ_{Ag}) as shown in Figure 7.4A-D. The effect of introducing a conductive filler into a less conductive matrix has attracted interest for decades and is by now well understood within the framework of percolation theory.[159] As the filler loading (ϕ) is increased, the composite conductivity first increases slowly, but as a critical volume fraction, the percolation threshold (ϕ_c), is reached a sharp increase in conductivity is observed as the first continuous paths of the filler are established. As progressively more filler is added the conductivity continues to increases steadily towards an ultimate value.[159]

Theoretically, percolative behaviour is generally divided into three separate regimes. Most well-studied is the region above the percolation threshold ($\phi > \phi_c$) wherein the conductivity is described by the percolation equation 7.2:

$$\sigma = \sigma_c \left(\frac{\phi - \phi_c}{1 - \phi_c} \right)^t \tag{7.2}$$

Here, σ_c is a proportionality constant associated with the properties of the filler and t is a percolation exponent.

Equation 7.2 is applicable when considering systems where the matrix is insulating, for example a polymer and conductive filler. This equation should be equally applicable to our BN:Gr nanocomposites, where BN is the insulating phase and graphene is the

conductive filler (Figure 7.4A). The variation of conductivity in BN:Gr nanocomposites with increasing graphene loading is consistent with percolation type behaviour, with a sharp transition from an insulating to a conducting network at $\phi = 0.12$. The conductivity subsequently increases strongly with ϕ_{Gr}, reaching a value of 4000 S/m for the all-graphene network (i.e. that with ϕ_{Gr} =0.5 due to the presence of pores), which is consistent with previously reported values of LPE graphene.[334,335]

By fitting the conductivity data to equation 7.2, the percolative parameters of the network can be extracted (fit parameters are available in Table 7.1). Here the percolation exponent is, t = 2.6, which is reasonably close to the predicted universal value of 2 and agrees well with a report on BN:Graphite powder composites.[159,336] Values of t slightly larger than 2 are commonly associated with a broadening of the junction resistance distribution of the filler particles.[164,336] The percolation threshold obtained for our BN:Gr nanocomposites, ϕ_c = 0.11 is in the range of previous reports.[131,176]

The analysis above follows the most commonly used procedure where conductivity data only exists above the percolation threshold. The data for WSe_2:Gr and WS_2:Gr composites in Figure 7.4B&C shows the typical percolation threshold and region of increasing conductivity for $\phi > \phi_c$. Additionally, the data also shows non-zero conductivities for pristine networks of WSe_2 (7×10^{-3} S/m) and WS_2 (4×10^{-4} S/m) for composites at low filler loadings. Thus, analysis will require models beyond equation 7.2. Note that due to the large channel resistance and low film thickness these networks are limited by the resistance of the network rather than by contact effects between the network and electrode and therefore display ohmic behaviour.[337]

Conductivity data below ϕ_c in insulating matrix composites is rarely reported due to difficulties in measuring exceptionally low conductivities associated with these systems.

Matrices with appreciable conductivities present an interesting case, as composite conductivity should be measurable across the entire volume fraction range. Below ϕ_c, there are no continuous filler paths present and instead filler particles exist as islands or clusters within the matrix. Conductivity in these composites is expected to dominated by the paths of least resistance where conductive paths contain portions traversing both filler and matrix. The conductivity can be modelled by the following equation:[338]

$$\sigma = \sigma_i \left(\frac{\phi_c - \phi}{\phi_c} \right)^{-s} \tag{7.3}$$

Here σ_i is a proportionality constant which can be thought of as the conductivity of a matrix-only film and s is a second percolation exponent. While it would be possible to use equations 7.2 and 7.3 to fit different ϕ-ranges in each of Figure 7.4B&D, this is unsatisfactory as these equations do not agree on the conductivity when $\phi = \phi_c$. This means a third 'cross over' region exists when $\phi \cong \phi_c$ [165]. To avoid the need to perform multiple fitting over various regimes, McLachlan et al[292] developed a functional equation that allows the entire percolation region to be modelled:

$$(1-\phi)\frac{\sigma_i^{1/s} - \sigma^{1/s}}{\sigma_i^{1/s} + A\sigma^{1/s}} + \phi\frac{\sigma_c^{1/t} - \sigma^{1/t}}{\sigma_c^{1/t} + A\sigma^{1/t}} = 0, \qquad A = (1-\phi_c)/\phi_c \tag{7.4}$$

Importantly equation (7.4 reduces to equation (7.2 as $\sigma_c \to \infty$ or equation 7.3 as $\sigma_i \to \infty$. Practically speaking, the simplest way to use equation (7.4 is to fit data for ϕ as a function of σ, rather than vice versa as would usually occur.

Figure 7.4B&C shows conductivity versus volume fraction for WSe_2:Gr and WS_2:Gr networks, with the corresponding fits to equation (7.4 (Full list of fit parameters can be found in Table 7.1). The percolation exponents were observed to be $t = 2.6$ and $t = 3.0$ for WSe_2:Gr and WS_2:Gr nanocomposites, with almost identical t-values are reported in other works on 2D:2D networks such as MoS_2:Gr[131] and WS_2:Gr.[176] Additionally, the second percolation exponent gives $s = 0.5, 0.6$ for both composite pairs. This value is somewhat lower that the reported universal value of $s = 0.87$,[159] however, it is consistent with values of $s = 0.40 - 1.06$ found in powder based composites.[336,338] It should be noted that much larger values of $s = 5.4, 7.6$ have been previously observed in 2D:2D composites.[131,339] From the fits to equation 7.4 the percolation threshold is extracted for each nanocomposite, finding $\phi_{c,Gr} = 0.13$ and $\phi_{c,Gr} = 0.10$ for WSe_2:Gr and WS_2:Gr respectively. These values are in line with the previous value of $\phi_{c,Gr} = 0.11$ for BN:Gr nanocomposites.

The Ag:Gr conductivity data in Figure 7.4D presents some rather surprising behaviour. There is a region of sharply increasing conductivity ($\phi_{Ag} > 0.2$), where σ increases in a well-defined manner, before reaching 1.1×10^6 S/m for an all-silver network ($\phi_{Ag} = 0.5$). Such behaviour is consistent with normal above-percolation behaviour. However, the region below the apparent percolation threshold ($\phi_{c,Ag} < 0.2$) shows a conductivity which falls off with increasing silver volume fraction. This divergence from monotonic behaviour is in contrast to what one might intuitively expect and cannot be modelled by equation 7.4.

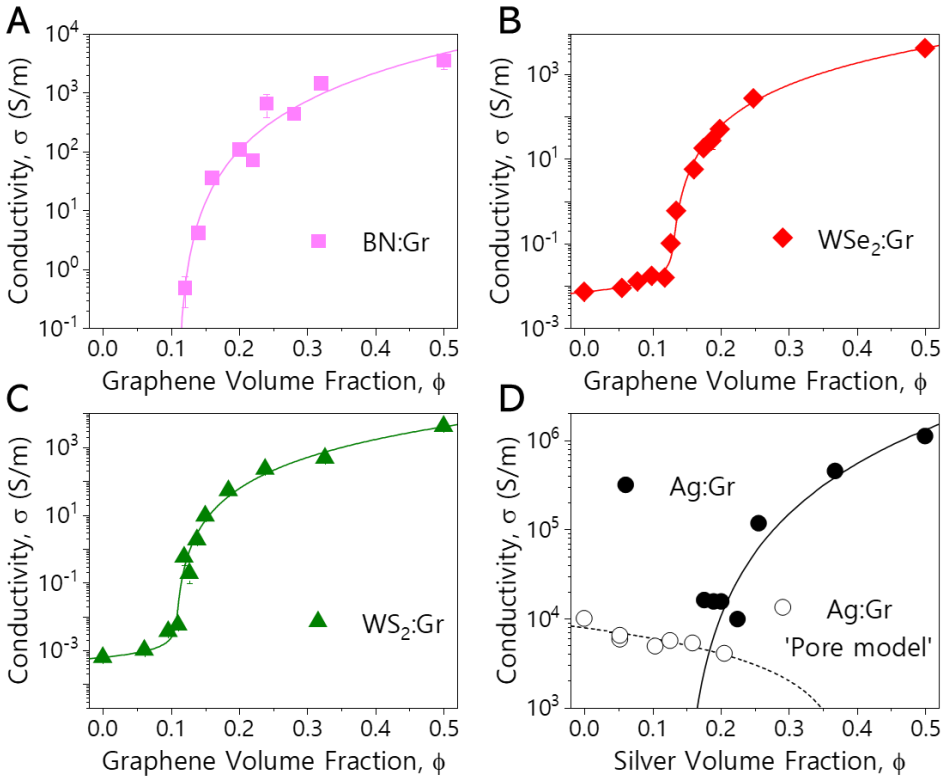

Figure 7.4 – Nanocomposite Electrical Properties. Conductivity, σ, plotted as a function of filler volume fraction, ϕ for A) BN:Gr, B) WSe_2:Gr, C) WS_2:Gr, D) Ag:Gr. The solid and dashed lines are fits to various models discussed in the text.

The region where $\phi > 0.2$ (filled circles) is first analysed before turning to the anomalous behaviour at lower ϕ. Fitting the $\phi > 0.2$ region with equation 7.2, yields $t = 2.5$. This result is consistent with the other nanocomposite data discussed above. However, in this instance $\phi_{c,Ag} = 0.16$, which is larger than the previously obtained values for BN, WSe_2, WS_2 nanocomposites. This difference is attributed to the relatively low aspect ratio of AgNS, $k = \langle L_{NS}/t_{NS} \rangle$, of ≈13.5,[130] compared to graphene which has a much higher ratio k ≈ 150. Previous work shows the percolation threshold depends on the geometry of the filler particles.[170] In fact, in the case of disk like ellipsoids, ϕ_c can vary with the aspect ratio, where large aspect ratios lead to lower values of ϕ_c, as seen here.[170]

The anomalous behaviour for ϕ<0.2 is attributed to the effect of poor interparticle charge transfer between graphene nanosheets and silver nanosheets (possibly arising from large junction resistances between the two particles). This means that below ϕ_{Ag}, where the first all-AgNS conductive path forms, the AgNS do not contribute to conduction at all. However, the AgNS do take up space, reducing the volume of the network of graphene nanosheets which can conduct current and essentially act like additional pores. Considering this "pore effect", the conductivity of the graphene network (below the silver percolation threshold) can be described in terms of graphene volume fraction, as in equation 7.2. This is achieved by noting the total film volume comprises of graphene, silver and pores such that $1 = \phi_{Gr} + \phi_{Ag} + \phi_p$. As hypothesised above, when ϕ_{Ag}<0.2, the silver does not contribute to conduction due to charge transfer limitations. In this range conductivity increases with increasing ϕ_{Gr} and so decreases with increasing ϕ_{Ag}. Applying equation 7.2 but writing the graphene volume fraction in terms of the silver volume fraction: $\phi_{Gr} = 1 - \phi_{Ag} - \phi_p$. A nominal percolation threshold is assumed and termed $\phi_{c_p,Gr}$ (which can be related to a nominal silver volume fraction $\phi_{c_p,Ag}$) above which, there is so much non-conducting silver and pores that a conducting graphene network does not exist: $\phi_{c,Gr} = 1 - \phi_{c,Ag} - \phi_p$. Therefore, below the percolation threshold:

$$\sigma = \sigma_c \left(\frac{\phi_{c_p,Ag} - \phi_{Ag}}{\phi_{c_p,Ag} + \phi_p} \right)^{t_p} \tag{7.5}$$

It is important to note that $\phi_{c_p,Ag}$ is a nominal value which is different from the percolation threshold associated with the formation of a percolating network of AgNS described above. Here t is re-written as t_p to demonstrate that the exponent is also distinct to that in equation 7.2.

Table 7-1 – *Fitting parameters obtained from fitting σ_0 vs ϕ data in Figure 7.4A-D*

	Log(σ_i)	Log(σ_ϵ)	*s*	*t*	ϕ_c	Model
BN:Gr	-	4.6 ± 0.4	-	2.6 ± 0.5	0.109 ± 0.001	Eq. 8.2
WSe_2:Gr	-2.15 ± 0.02	4.6 ± 0.1	0.5 ± 0.1	2.6 ± 0.2	0.13 ± 0.01	Eq. 8.4
WS_2:Gr	-3.22 ± 0.04	4.7 ± 0.2	0.6 ± 0.3	3.0 ± 0.3	0.10 ± 0.01	Eq. 8.4
Gr:Ag	-	7.1 ± 0.4	-	2.5 ± 0.4	0.160 ± 0.001	Eq. 8.2
Gr:Ag (Pore Model)	-	4.2 ± 0.1	-	0.9 ± 0.3	0.39*	Eq. 8.5
* Fixed value						

To facilitate fitting, an estimated value for $\phi_{c_p,Ag}$ is used, by assuming $\phi_{c_p,Gr}$ ~ 0.11, similar to the percolation threshold obtained for BN:Gr, as it is a similar network where BN does not contribute to conduction ($\phi_{c,Gr}$ ~ 0.11). Approximating ϕ_p ~ 0.5 gives $\phi_{c_p,Ag}$ = 0.39. Fitting the data then yields t_p = 0.9, this is notably smaller than the values for *t* observed earlier in this work. However previous work by Barwich et al.[132] has shown that the percolation exponent of porosity dependent conductivity in graphene nanosheet films is ~1,[132] which is similar to the value for the 'pore effect' found here. A summary of all percolative fit parameters is given in Table 7.1.

7.2.4. Piezoresistive Properties of Nano:Nano Composites

The piezoresistive response of each composite film was characterised at low strain by measuring the relative resistance change $\Delta R/R_0$ as a function of applied strain up to ε=1% (Figure 7.5A-D). The gauge factor, G, is defined by $\Delta R/R_0 = G\varepsilon$ and can be extracted from

the low-strain slope of these curves. For all composite types, the gauge factor is highly dependent on the filler loading.

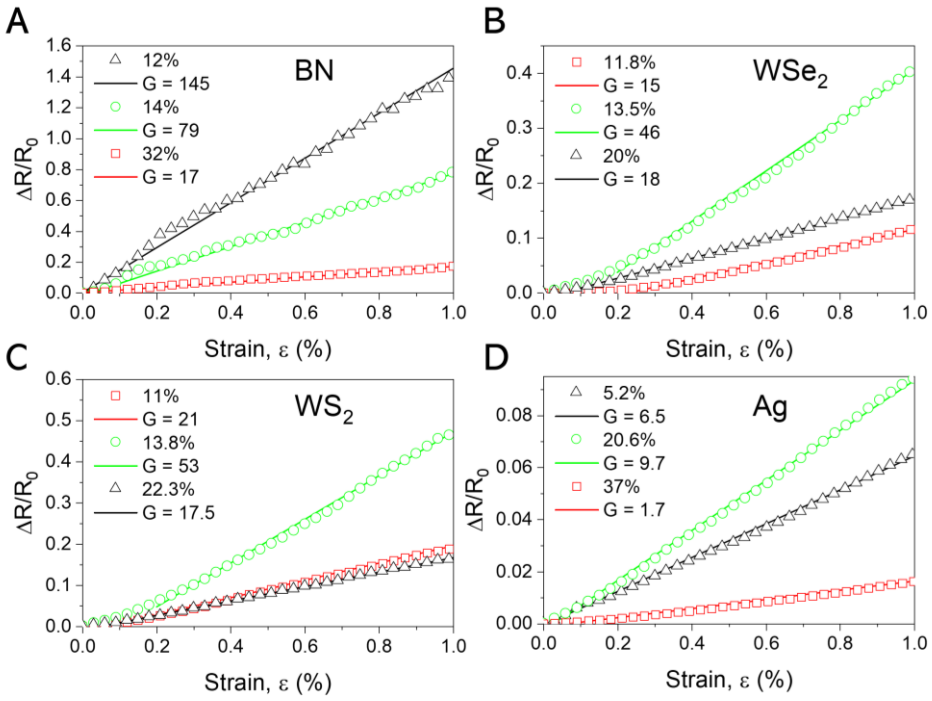

Figure 7.5 – Resistance-Strain Response. A-D) Fractional resistance change plotted as a function of applied strain to the nanocomposite network, each plot is a representative curve which demonstrates the change in piezoresistive behaviour resulting from a variation in filler loading. A) BN:Gr, B) WSe2:Gr, C) WS2:Gr, D) Ag:Gr.

The average gauge factor was plotted as a function of filler volume fraction as shown In Figure 7.6A-D. In each case, well defined trends are observed. For all four composite types, the gauge factor increases as the filler volume fraction is decreased from $\phi = 0.5$, increasing rapidly as ϕ is reduced toward the percolation threshold. Similar behaviour has previously been observed for polymer nanocomposites, where G diverges as ϕ_c is approached from above.[340]

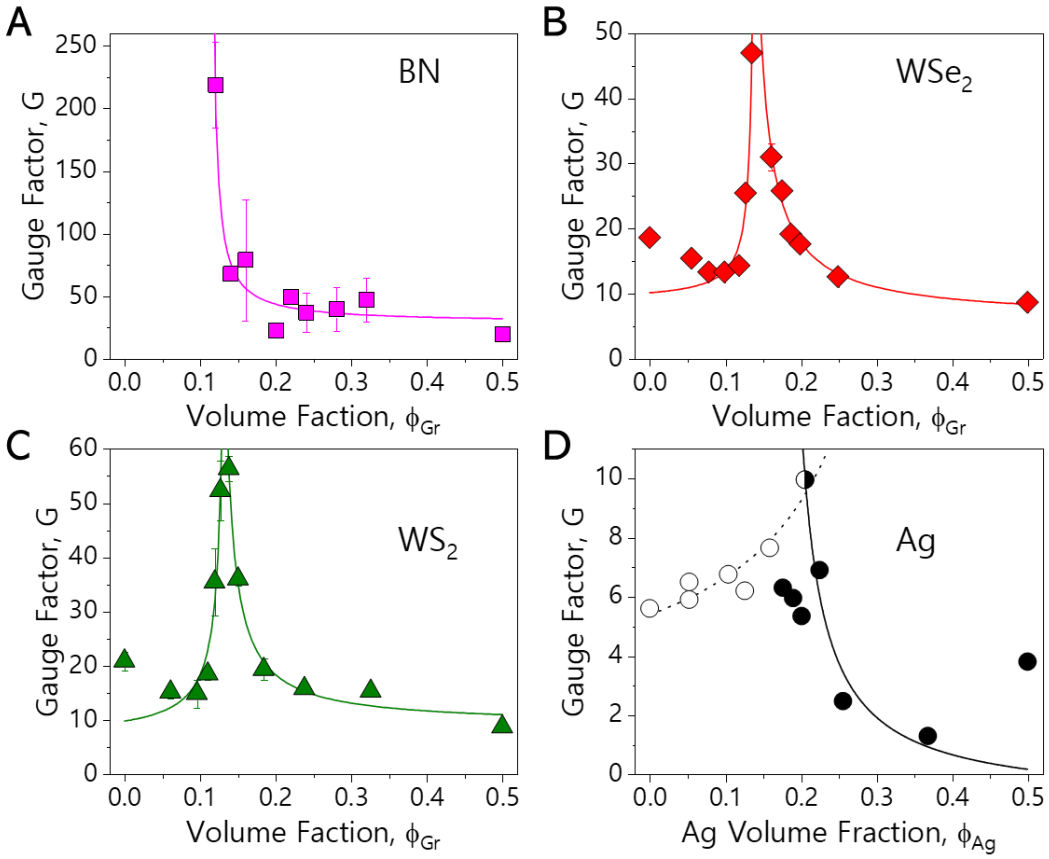

Figure 7.6 – Gauge factor as a Function of Nanocomposite Volume Fraction. A-D) Gauge factor plotted as a function volume fraction for each nanocomposite pair. The solid and dashed lines are fits to various models discussed in the text, fit parameters can be found in Table 7.2. A) BN:Gr, B) WSe2:Gr, C) WS2:Gr, D) Ag:Gr.

In the case of the Gr:BN composites, no gauge factor data exists below the percolation threshold due to the unmeasurably low conductivities for these composites. This means that, like polymer nanocomposites, only the behaviour described above is observed. However, for the WS_2:Gr, WSe_2:Gr and Ag:Gr composites, non-zero conductivities exist below the percolation threshold. |As the filler volume fraction reaches the percolation threshold, the gauge factor peaks and then falls off very sharply as ϕ is reduced further. This behaviour appears to be a feature of composites with non-insulating matrices. The maximum observed values of G were 220, 58, 46 and 10 for BN:Gr, WS_2:Gr WSe_2:Gr, and

Ag:Gr composites, implying that large values of *G* are obtained when lower conductivity matrices are used.

It is noted that pristine WSe_2, WS_2 and Ag networks show slightly higher gauge factors than their respective nanocomposites at the lowest loadings of graphene, the reason for this is unclear but it's speculated this is due to subtle morphological changes in the composite on addition of filler to the pristine network.

7.2.5. Modelling 2D:2D Nanocomposite Piezoresistance

It's believed the unusual properties observed in Figure 7.6A-D are related to the network conductivity and can be explained via percolation theory. Here, simple models are derived to describe the dependence of gauge factor on filler volume fraction.

In the limit of low strain, it can be shown that,[219]

$$G \approx 2 - \frac{1}{\sigma_0}\left(\frac{d\sigma}{d\varepsilon}\right)_0 = 2 - \left(\frac{d\ln\sigma}{d\varepsilon}\right)_0 \tag{7.6}$$

The subscript zero defines that the quantity should be taken in the limit of low strain. This demonstrates that upon straining a material, the resistance changes for two reasons. Firstly, there is a small change due the effect of strain on sample dimensions, for an incompressible material ($\nu = 0.5$) the contribution to the gauge factor is ~2. Secondly, there are resistance variations due to changes in material conductivity, this effect is often quite large and can be both positive[184,299,300,341] and negative.[144,219]

Chapter 5 showed that equation 7.6 can be used to obtain an equation for the gauge factor in polymer nanocomposites.[340] This is achieved in a relatively simple manner, by substituting equation 7.2 into equation 7.6 to yield equation 7.7

$$G \approx \left[2 - \frac{1}{\sigma_c}\left(\frac{d\sigma_c}{d\varepsilon}\right)_0\right] - \left[\ln\left(\frac{\phi-\phi_c}{1-\phi_c}\right)\left(\frac{dt}{d\varepsilon}\right)_0\right] + \left[\left(\frac{t}{\phi-\phi_c} - \frac{t}{1-\phi_c}\right)\left(\frac{d\phi_c}{d\varepsilon}\right)_0\right]$$

(7.7)

As has been discussed previously, $(d\phi_c/d\varepsilon)_0$ is expected to be the dominant term in this equation allowing a simplified form to be used

$$G \approx G_{t,0} + \frac{t}{\phi-\phi_c}\left(\frac{d\phi_c}{d\varepsilon}\right)_0$$

(7.8)

Where $G_{t,0}$ is a composite constant related to other percolation parameters (see Appendix B for full derivation) and $(d\phi_c/d\varepsilon)_0$ is the percolation threshold strain dependence (the subscript *t* on the former quantity is to indicate that this equation is related to equation 7.2). The model has been used to fit the data in Figure 7.6A-D in the region above the electrical percolation threshold (the fit parameters are listed in Table 7.2). Fitting shows that $G_{t,0}$ takes values between -1 and 28.9, with the lowest value being associated with the Ag:Gr nanocomposite while the largest value is associated with the BN:Gr nanocomposite. Fitting the data also yields a value for $t(d\phi_c/d\varepsilon)_0$, however, since *t* is already known from fitting ϕ vs σ, $(d\phi_c/d\varepsilon)_0$ can be extracted for each composite.

$(d\phi_c/d\varepsilon)_0$ can be understood intuitively by considering a composite at the percolation threshold so that there is a single connected path of nanosheets through which current can pass. Applying tensile strain to such a system is unlikely to result in new paths forming, instead it is much more likely that the current path will break and lead to an increase in the percolation threshold. Thus, $(d\phi_c/d\varepsilon)_0$ is expected to be positive and indeed is positive in all cases, with values ranging between $0.15 \leq (d\phi_c/d\varepsilon)_0 \leq 0.68$. In polymer nanocomposites $(d\phi_c/d\varepsilon)_0$ can vary by several orders of magnitude, for example Zhang et

al. have reported $(d\phi_c/d\varepsilon)_0$ = 0.004 in polyurethane–nanotube composites,[295] while the previous chapter shows $(d\phi_c/d\varepsilon)_0$ can be as large as 3. Additionally, equation (7.8 gives an alternative method for determining ϕ_c, which is compared to the ϕ_c values obtained from fits to equation 7.2, finding relatively good agreement in all cases.

The method of combing equation 7.6 with an equation for network conductivity is a very useful one which can be used in various circumstances. For example, in standard composites, this method can be applied apply to the volume fraction range below the percolation by combining equation 7.3 and 7.6 to yield:

$$G \approx \left[2 - \frac{1}{\sigma_i}\left(\frac{d\sigma_i}{d\varepsilon}\right)_0\right] + \left[\ln\left(\frac{\phi_c - \phi}{\phi_c}\right)\left(\frac{ds}{d\varepsilon}\right)_0\right] + \left[\left(\frac{s}{\phi_c - \phi} - \frac{s}{\phi_c}\right)\left(\frac{d\phi_c}{d\varepsilon}\right)_0\right] \tag{7.9}$$

With the simplified version given as

$$G \approx G_{s,0} + \frac{s}{\phi_c - \phi}\left(\frac{d\phi_c}{d\varepsilon}\right)_0 \tag{7.10}$$

where $G_{s,0}$ is a composite constant related to other percolation parameters (see Appendix B for full derivation), the subscript s indicates the relation to equation 7.3. Note that this is equation is very similar to equation 7.8 with one important difference being that the denominator in equation 7.10 is (ϕ_c - ϕ) rather than (ϕ - ϕ_c). Therefore, equation 7.10 predicts an increase in G with increasing ϕ (for ($\phi < \phi_c$), exactly what is found in the experimental data. This means that, nanocomposites with a measurable conductivity below ϕ_c display a peak in gauge factor centred roughly at the percolation threshold.

The model is used to fit the data for WSe_2:Gr and WS_2:Gr composites in Figure 7.6B&C, finding good agreement (the fit parameters are listed in Table 7.2). The obtained values

are $G_{s,0}$ = 8.8, 6.7 while $(d\phi_c/d\varepsilon)_0$ = 0.28, 0.68 for WSe_2:Gr and WS_2:Gr respectively. Similar to equation 7.7, equation 7.8 also yields values for ϕ_c. Fitting the data to equation 7.10 gives slightly higher values of $\phi_{c,Gr}$ = 0.139, 0.136 when compared to values obtained from equation 7.8, $\phi_{c,Gr}$ = 0.128, 0.123. However,the values of ϕ_c obtained from fitting σ_0 vs ϕ as well as both forms of G vs ϕ broadly agree, supporting the validity of the models.

Equations 7.8 and 7.10 have been used to fit G versus ϕ for both WSe_2:Gr and WS_2:Gr data separately above and below the percolation threshold. Of course, it would have been preferrable to derive a model using equation 7.4 to describe the entire percolative range, however, this was not possible due to the complicated mathematical form.

Equation 7.10 describes the G versus ϕ data in standard composites where $\phi < \phi_c$. This equation cannot be applied to the Ag:Gr composites because of the non-standard behaviour: due to junction resistance issues, the AgNSs act as extra pores, not contributing to conduction below the percolation threshold. However, an equation can be derived for the gauge factor in this situation by combining equations 7.5 and 7.6 to give:

$$G \approx \left[2 - \frac{1}{\sigma_c}\left(\frac{d\sigma_c}{d\varepsilon}\right)_0\right] - \left[\ln\left(\frac{\phi_{c_p,Ag} - \phi_{Ag}}{\phi_{c_p,Ag} + \phi_p}\right)\left(\frac{dt_p}{d\varepsilon}\right)_0\right] + \left[\left(\frac{t_p}{\phi_{c_p,Ag} - \phi_{Ag}} - \frac{t_p}{\phi_{c_p,Ag} + \phi_p}\right)\left(\frac{d\phi_{c_p,Ag}}{d\varepsilon}\right)_0\right] \tag{7.11}$$

With the simplified version given as

$$G \approx G_{p,0} + \frac{t_p}{\phi_{c_p,Ag} - \phi_{Ag}}\left(\frac{d\phi_{c_p,Ag}}{d\varepsilon}\right)_0 \tag{7.12}$$

where $G_{p,0}$ is a composite constant related to other percolation parameters (see Appendix B) and the subscript p is to indicate the relation to equation 7.5. Again, this equation is

similar in form to equations 7.8 and 7.10 but, like equation 7.10, predicts an increase in G with increasing ϕ_{Ag} (for $\phi_{Ag} < \phi_{c_p,Ag}$), as is found in the experimental data. The model is used to fit the data (open circles) for Ag:Gr composites in Figure 7.6D, finding good agreement. Here, $G_{p,0} = 1.8$ and $(d\phi_{c_p,Ag}/d\varepsilon)_0 = 1.6$, while $\phi_{c_p,Ag}$ is a fixed value of 0.39 as described earlier when fitting σ vs ϕ for the same system.

It is worth noting that equations 7.8, 7.10 and 7.12 are all very similar in form and imply that G should be maximised by keeping ϕ as close as possible to ϕ_c. In addition, they all depend on the product of the relevant percolation exponent (i.e. t, s, t_p) and the rate of change of percolation threshold with strain ($(d\phi_c/d\varepsilon)_0$ or $(d\phi_{c_p,Ag}/d\varepsilon)_0$). This highlights that these parameters are key to maximising piezoresistive sensitivity in percolative strain sensors. Noting that large values of the exponent are associated with broad distributions of inter-nanosheet junction resistance, a property that might in some way be engineered. Furthermore, it's proposed that $(d\phi_c/d\varepsilon)_0$ is linked to the structure and morphology of the nanosheet network. again, this is something that might in future be engineered, perhaps by controlling the network deposition method.

Table 7-2–- Fitting parameters obtained from fitting G vs ϕ data in Figure 7.6

	$G_{x,0}$	$(d\phi_c/d\varepsilon)_0$	ϕ_c	Model
BN:Gr	28.9 ± 5.6	0.50 ± 0.08	0.113 ± 0.001	Eq. 8.7
WSe_2:Gr (Above ϕ_c)	6.1 ± 1.0	0.32 ± 0.02	0.128 ± 0.001	Eq. 8.7
WSe_2:Gr (Below ϕ_c)	11.1 ± 1.4	0.28 ± 0.04	0.139 ± 0.001	Eq. 8.8
WS_2:Gr (Above ϕ_c)	9.1 ± 1.1	0.24 ± 0.02	0.123 ± 0.001	Eq. 8.7
WS_2:Gr (Below ϕ_c)	6.7 ± 3.2	0.68 ± 0.09	0.136 ± 0.001	Eq. 8.8
Gr:Ag	-1 ± 1	0.15 ± 0.02	0.172 ± 0.001	Eq. 8.7
Gr:Ag (Pore Model)	1.8 ± 0.9	1.6 ± 0.4	0.390*	Eq. 8.9
x can take the subscript t,s or p depending on the model type				

7.2.6. Relationship Between Gauge Factor and Conductivity

From the discussion above, it is clear that both conductivity and gauge factor are intimately linked to the filler volume fraction of each network. This is demonstrated in Figure 7.7A&B which uses data for WSe_2:Gr, to show that the gauge factor peak occurs very close to the conductivity percolation threshold of the nanocomposites. That both *G* and σ depend on volume fraction implies the presence of a mutual relationship between them. To investigate this, the gauge factor of each nanocomposite pair is plotted as a function of conductivity in Figure 7.8A-D. Here, individual *G* and σ values are plotted instead of averaging as was done for previous volume fraction figures.

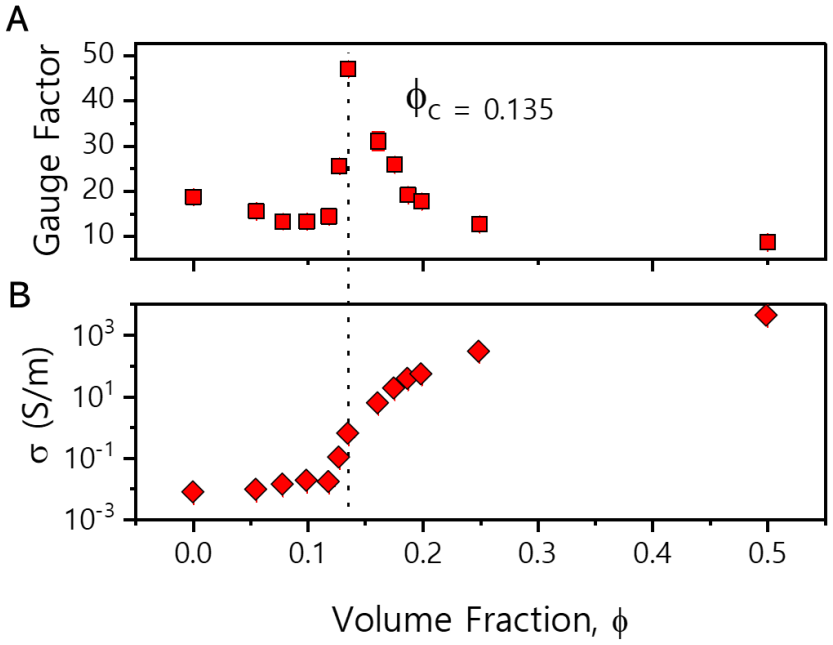

Figure 7.7 – Percolative Behaviour. A) – B) Conductivity and gauge factor plotted as a function of nanocomposite volume fraction for WSe_2 data set. The dashed indicates that a peak in the gauge factor can be observed at the percolation threshold.

G versus σ behaviour is modelled by re-writing the previous gauge factor models in terms of conductivity rather than volume fraction. First consider the situation where the networks are above the percolation threshold. This is the most general scenario and will apply to most composites. Combining equation 7.8 with equation 7.2, yields equation 7.13, which expresses the gauge factor in terms of the zero-strain conductivity:

$$G \approx G_{t,0} + \frac{t}{1-\phi_c}\left(\frac{\sigma}{\sigma_c}\right)^{-1/t}\left(\frac{d\phi_c}{d\varepsilon}\right)_0 \tag{7.13}$$

Here, $G_{t,0}$ is a constant identical to that in equation 7.8. The model predicts that above the percolation threshold, the gauge factor should increase monotonically with decreasing

conductivity, as observed in the data. Furthermore, the model suggests this effect is highly dependent on the percolation exponent *t*.

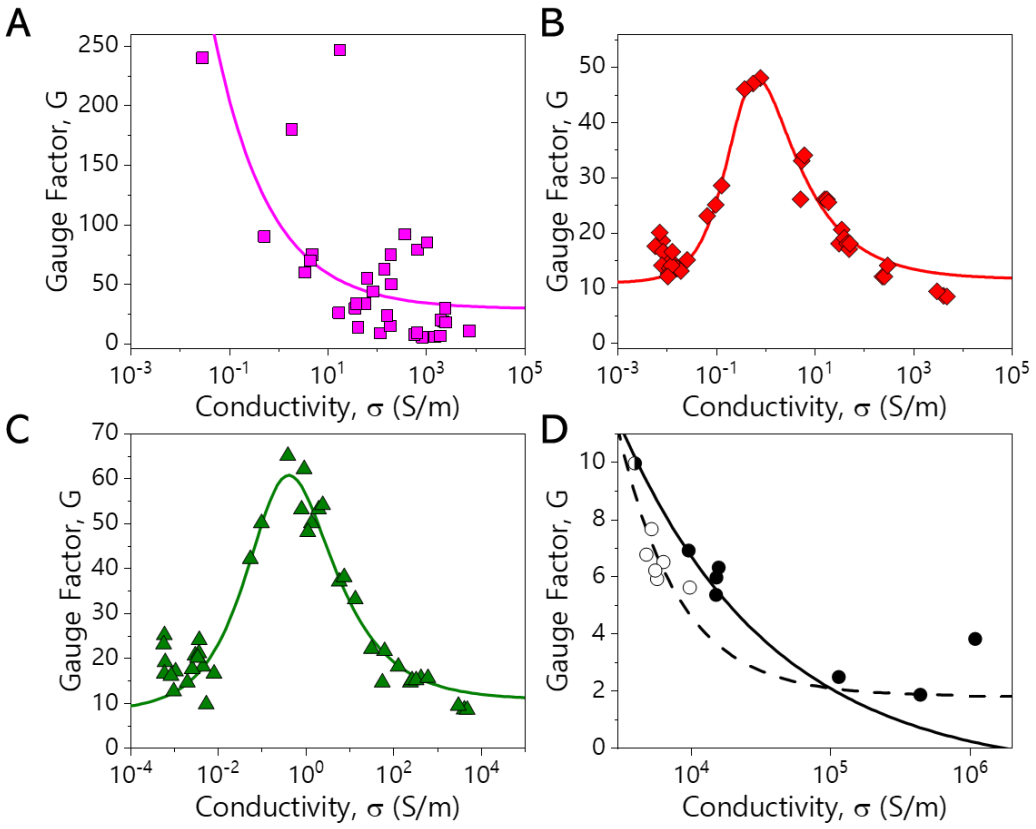

Figure 7.8 – Gauge factor as a Function of Nanocomposite Conductivity. A) BN:Gr, B) WSe_2:Gr, C) WS_2:Gr, D) Ag:Gr. The solid and dashed lines are various models discussed in the text, fit parameters can be found in Table 7.3.

Recalling the previously fitted models, it becomes clear that all the components of equation 7.13 have already been determined. The parameters σ_c, ϕ_c and t are found from equation 7.2, while a second estimate of ϕ_c and the new terms $G_{t,0}$, $(d\phi_c/d\varepsilon)_0$ are found from equation 7.8. Thus, the parameter values may be substituted into equation 7.13 to generate a predictive model for σ vs G, to compare against the experimental data.

Figure 7.8A shows G vs σ for BN:Gr in the region above the electrical percolation threshold whereby G increases as σ decreases across several orders of magnitude. In

addition, the predictive model is plotted using equation 7.13 (See Table 7.3 for parameter values). Notwithstanding the significant degree of scatter, the model captures the overall shape of the BN:Gr very well. This is important as it demonstrates that these models need not only be used for fitting purposes but can instead be used to predict piezoresistive properties of percolative networks once good estimates of the percolation parameters can be obtained.

A similar model can also be obtained for composite systems which display measurable conductivities below the percolation threshold such as WSe_2:Gr and WS_2:Gr networks. This can be achieved by simply combining equation 7.10 with equation 7.3, which yields:

$$G \approx G_{s,0} + \frac{s}{\phi_c}\left(\frac{\sigma}{\sigma_i}\right)^{1/s}\left(\frac{d\phi_c}{d\varepsilon}\right)_0 \tag{7.14}$$

Where $G_{s,0}$ is a constant identical to that in equation (7.10.

The WSe_2:Gr and WS_2:Gr data for σ *vs* G can be divided into two regimes, above and below ϕ_c, and fit to equation 7.13 and equation 7.14 respectively. However, as mentioned above, it is preferrable to obtain a model which describes the entire data range (both above and below ϕ_c). Although equation 7.4, allows conductivity to be described across the whole ϕ-range, its form does not allow G to be written in terms of ϕ. However, it is possible to obtain an equation for G in terms of σ. This can be achieved, by differentiating equation 7.4 with respect to strain and combining the result with equation 7.6. The derivation is described briefly here with further details in Appendix B.

Equation 7.4 is re-written such that:

$$(1-\phi)\frac{\sigma_i^{1/s}-\sigma^{1/s}}{\sigma_i^{1/s}+A\sigma^{1/s}}=-\phi\frac{\sigma_c^{1/t}-\sigma^{1/t}}{\sigma_c^{1/t}+A\sigma^{1/t}}$$

(7.15)

Taking the log of both sides and using the fact that, $(1/\sigma)(d\sigma/d\varepsilon) = d\ ln\sigma/d\varepsilon$.

$$\frac{\left[\frac{d}{d\varepsilon}\sigma_i^{1/s}-\frac{d}{d\varepsilon}\sigma^{1/s}\right]}{\sigma_i^{1/s}-\sigma^{1/s}}-\frac{\left[\frac{d}{d\varepsilon}\sigma_i^{1/s}+\frac{d}{d\varepsilon}(A\sigma^{1/s})\right]}{(\sigma_i^{1/s}+A\sigma^{1/s})}=\frac{\left[\frac{d}{d\varepsilon}\sigma_c^{1/t}-\frac{d}{d\varepsilon}\sigma^{1/t}\right]}{(\sigma_c^{1/t}-\sigma^{1/t})}-\frac{\left[\frac{d}{d\varepsilon}\sigma_c^{1/t}+\frac{d}{d\varepsilon}(A\sigma^{1/t})\right]}{(\sigma_c^{1/t}+A\sigma^{1/t})}$$

(7.16)

The work in chapter 6 demonstrated that the strain dependence of ϕ_c was the dominant mechanism for predicting *G*. Its expected that the same situation should apply here. For simplicity only ϕ_c and σ will be considered as strain dependent. The contribution from other terms *($dt/d\varepsilon$, $ds/d\varepsilon$, $d\sigma_i/d\varepsilon$* and *$d\sigma_c/d\varepsilon$)* are assumed to be approximately constant and will be explicitly added at the end of the derivation. Performing the differentiation under these assumptions yields:

$$\frac{d\ln\sigma}{d\varepsilon}=\frac{dA}{d\varepsilon}\frac{\left[\frac{\sigma^{1/s}}{(\sigma_i^{1/s}+A\sigma^{1/s})}-\frac{\sigma^{1/t}}{(\sigma_c^{1/t}+A\sigma^{1/t})}\right]}{\left[\frac{\sigma^{1/t}/t}{\sigma_c^{1/t}-\sigma^{1/t}}-\frac{\sigma^{1/s}/s}{\sigma_i^{1/s}-\sigma^{1/s}}-\frac{A\sigma^{1/s}/s}{\sigma_i^{1/s}+A\sigma^{1/s}}+\frac{A\sigma^{1/t}/t}{\sigma_c^{1/t}+A\sigma^{1/t}}\right]}$$

(7.17)

Recalling that $A = (1-\phi_c)/\phi_c$ and introducing the approximate constant, $G_{\sigma,o}$, as discussed above yields a final equation describing the gauge factor across the entire percolative range.

$$G \approx G_{\sigma,0} + \frac{1}{\phi_c^{\,2}}\left(\frac{d\phi_c}{d\varepsilon}\right)_0 \frac{\left[\dfrac{1}{\sigma_i^{1/s}/\sigma^{1/s}+A} - \dfrac{1}{\sigma_c^{1/t}/\sigma^{1/t}+A}\right]}{\left[\dfrac{1/t}{\sigma_c^{1/t}/\sigma^{1/t}-1} - \dfrac{1/s}{\sigma_i^{1/s}/\sigma^{1/s}-1} - \dfrac{A/s}{\sigma_i^{1/s}/\sigma^{1/s}+A} + \dfrac{A/t}{\sigma_c^{1/t}/\sigma^{1/t}+A}\right]} \tag{7.18}$$

It must be noted that the, $G_{\sigma,0}$, approximation will only be strictly valid when the gauge factor of the both the matrix ($\phi = 0$) and filler ($\phi = 1\text{-}\phi_p$) components are approximately equal (i.e. G_{WSe_2},G_{WS_2} ~ G_{Gr}), as is the case here. Importantly, in the limiting cases of $\sigma_c \to \infty$ or $\sigma_i \to 0$, equations 7.13 and 7.14 can be recovered from equation 7.18.

The G versus σ data for WSe_2:Gr, and WS_2:Gr composites in Figure 7.8B&C is different from the BN:Gr composites data (Figure 7.8) and indeed most polymer-based nanocomposites. In addition to the increase in G with decreasing σ above the percolation threshold, this data shows a peak in gauge factor such that gauge factors begin to decrease as composite conductivity falls below ~1 S/m. This low-conductivity behaviour is contrary to what is usually observed for polymer-based composites and is an unexpected result. For example, in the previous chapter a monotonic increase in G with decreasing σ was universal to all composites.

The peak in gauge factor occurs at the electrical percolation threshold for each nanocomposite, is in line with the results of Figure 7.7. Ideally, the data would be modelled using equation 7.15 by substitution of parameters as was done for equation 7.13. However, given the large number of parameters to be substituted, an appropriate prediction was not found. Instead, the data has been fit allowing a comparison of the output parameters to the previous models. To facilitate this, some parameters have been fixed (σ_c, σ_i, ϕ_c) using values obtained from earlier models. Therefore, the percolative parameters under study

here are $G_{\sigma,0}$, $(d\phi_c/d\varepsilon)_0$, t and s. The resultant fit describes the data extremely well, with the peak in gauge factor at σ~1 S/m well captured, the corresponding parameters can be found in Table 7.3. From the fitting, $G_{\sigma,0}$ = 11.3, 11.9 and $(d\phi_c/d\varepsilon)_0$ = 0.14, 0.24 for WSe_2:Gr and WS_2:Gr respectively. Although they are of the same magnitude, the values of $(d\phi_c/d\varepsilon)_0$ are somewhat smaller than the values obtained from fitting G versus ϕ data. The obtained values for t (2.19, 2.36) show excellent agreement with σ vs ϕ data. The s values (0.85,1.80) are somewhat larger than the values reported earlier, however overall the same trends are observed with values of t found to be higher than s as is expected from both theory[159] and experiment.[336]

As discussed previously, equation 7.14 describes the ϕ versus G data in standard composites where $\phi > \phi_c$. However for Ag:Gr composites, the variation in conductivity below the percolation threshold is dependent on the fact that AgNSs act as extra pores and do not contribute to conduction. This means a separate equation is required to describe the variation of G with conductivity. Equation 7.12 is re-written in terms of composite conductivity by utilising equation 7.5, to give:

$$G \approx G_{p,0} + \frac{t_p}{\phi_{c_p,Ag} + \phi_p}\left(\frac{\sigma}{\sigma_c}\right)^{-1/t_p}\left(\frac{d\phi_{c_p,Ag}}{d\varepsilon}\right)_0 \qquad (7.19)$$

Where $G_{p,0}$ is identical to that in equation . Similarly to equation 7.13, equation 7.19 can be used as a predictive model. In this instance σ_c, $\phi_{cp,Ag}$ and t_p can be obtained from fitting equation 7.5, while a second estimate of $\phi_{c_p,Ag}$ and the new terms $G_{p,o}$, $(d\phi_c/d\varepsilon)_0$ can be obtained from fitting equation 7.12.

Figure 7.8D shows σ vs G for Ag:Gr data. As before the data contains two regions arising from the differing percolative mechanisms. In both cases the gauge factor increases with decreasing conductivity, meeting in a shared data point (G = 10, σ = 4000 S/m). The data in the region above the percolation threshold is denoted by filled circles with the solid line being the predictive model determined from equation 7.13. The data below the electrical percolation threshold is denoted by open circles, with the dashed line being the predictive model determined from equation 7.16 (See Table 7.3 for parameter values). The experimental data follows the predictive models extremely closely in both cases.

Table 7-3 - Fitting parameters obtained from fitting G vs σ to the data in Figure 7.8, parameters without errors are fixed values for modelling purposes.

	$G_{x,0}$	Log(σ_i)	s	Log(σ_i)	t	ϕ_c	$(d\phi_c/d\varepsilon)_0$	Model
BN:Gr	28.9	-	-	4.6	2.6	0.11	0.5	Eq. 10
WSe_2:Gr	-1	-2.2	0.95 ± 0.07	4.6	2.2 ± 0.2	0.130	0.14 ± 0.04	Eq. 10
WS_2:Gr	11.9 ± 0.7	-3.2	1.80 ± 0.3	4.7	1.80 ± 0.3	0.134	0.24 ± 0.08	Eq. 12
Gr:Ag	11.3 ± 1.5	-	-	7.1	2.5	0.16	0.15	Eq. 12
Gr:Ag (Pore Model)	1.8	-	-	4.2	0.9	0.39	1.6	Eq. 13
x can take the subscript t, σ or p depending on the model type								

In order to frame this work in a wider context σ vs G is plotted, for a range of bulk and thin film percolative nanocomposites from this work and literature (Figure 7.9).[10,89,278,298] To date researchers have typically considered nanocomposites which lie above the percolation threshold, ϕ_c. In such instances the same behaviour is nearly always observed, that is, a monotonic increase in G with decreasing conductivity. This trend is consistent

regardless of the type of filler or matrix used, and would suggest a universality in the piezoresistive response. Uniquely, this work shows it is possible to achieve nanocomposites that have increasing gauge factors with increasing conductivity. In order to achieve such a scenario, its demonstrated that the nanocomposite filler loading must lie in the region below ϕ_c.

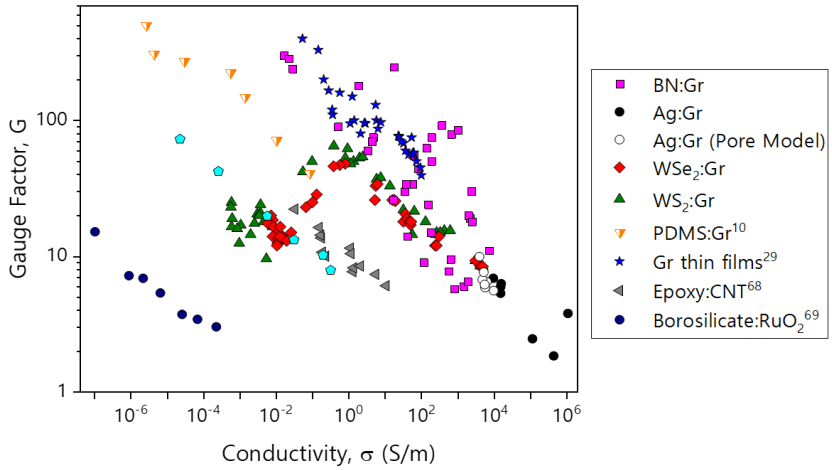

Figure 7.9 – A Wider Context. Gauge factor, G plotted as a function of nanocomposite conductivity, σ. The data here includes nanocomposite networks from this work as well as composites from literature.[10,89,278,298]

7.3. Conclusions

In summary, a study has been conducted on the electrical and piezoresistive properties of 2D:2D nano:nano composites produced from mixtures of silver, graphene, WSe_2, WS_2 and BN nanosheets. The electrical conductivity of each composite appears to vary rather differently with increasing filler volume fraction. However, it was demonstrated that the behaviour of each system can be explained by various percolative mechanisms and can be modelled simple percolation equations.

In addition, the piezoresistive properties of these networks are characterised, by measuring the gauge factor as a function of filler loading for each composite type. As with conductivity, there is a different dependence of the gauge factor on filler volume fraction for each composite type. In all cases percolation theory is used to develop simple models describing the piezoresistive behaviour, with the equations describing the data extremely well in each case.

An important outcome of this work is the observation that gauge factor does not always scale monotonically with filler volume fraction or composite conductivity as was previously thought. In fact, for composites fabricated using matrices with nonzero conductivity, the gauge factor displays a peak when plotted against either filler value fraction or conductivity. Naturally this should be extendable to conductive polymer matrices and fillers, however a comprehensive volume fraction study on such systems has yet to be shown. This percolation type behaviour peak limits the maximum gauge factor obtainable. Alternatively, when composites are produced from mixtures of different types of conducting nanosheet, nonmonotonic conductivity versus filler volume fraction behaviour is observed. These composites display a peak when gauge factor is plotted versus filler volume fraction but monotonic behaviour when gauge factor is plotted versus conductivity. In all cases these surprising and unusual results can be explained using percolation theory and all arise from the differences in percolation behaviour above and below the percolation threshold.

Finally, our analysis shows that for all composite types the gauge factor depends strongly on both the percolation exponent and the rate of change of percolation threshold with strain.

Chapter 8

Conclusions and Future Work

The fervour generated by the rise of modern nanoscience means that the silicon industry finally has a challenger to its monopoly on electronic devices. Although still in relative infancy, the versatility and flexibility of nanomaterials show immense promise in addressing some of the drawbacks to silicon-based devices. There is no better example of this than piezoresistive strain sensors, where the discovery of graphene and carbon

nanotubes has led the way to new strain sensor designs, reinvigorating a field that has remained relatively unchanged for decades. This work aimed to address some of the challenges faced by the field while shedding some light on the mechanisms underlying piezoresistive performance.

The majority of nanocomposites considered to date are prepared as bulk composites rather than thin films or other architectures. Although bulk nanocomposites display excellent piezoresistive performance, they suffer in other strain sensing metrics, which is almost certainly a result of interactions between the filler and matrix. This poses a real challenge, as properties such as minimal hysteresis and strain rate dependence are critical to functional strain sensors. Chapter 5 showed that success in addressing these issues could be found by fabricating nanocomposite thin films (~1μm thick) on neat polymer substrates. The nanocomposite thin films have a high conductivity of ~ 300 S/m, which is many orders of magnitude above the conductivity of the bulk. This behaviour is attributed to partial phase segregation of the nanocomposite. The thin nature of the nanocomposite allows pinning between the film and substrate to occur and a reduction in nanosheet mobility, significantly reducing the large hysteresis and strain rate effects that are found in the bulk nanocomposite. Such properties make the thin films promising candidates as strain sensors with use cases and qualitative measurements demonstrated.

It is well known that by lowering the filler loading in nanocomposite systems, high gauge factors can be achieved. This implies an intrinsic link between gauge factor and conductivity since current pathways through a nanocomposite are determined by percolation effects. Chapter 6 formalises this phenomenon through an analytical model, demonstrating that piezoresistive behaviour of nanocomposite systems can be described by percolation theory. Through the study of experimental data, an insight into the mechanisms underlying piezoresistive performance are obtained, finding that the strain

dependence of the network structure, in addition to the strain dependence on interparticle resistance, plays a considerable role in determining the composite gauge factor. The developed model also gives us a perspective on how the gauge factor might be optimised, indicating that variation of the percolation exponent should allow the gauge factor to be similarly altered even if the nanocomposite components are identical.

Piezoresistive nanocomposites typically comprise an insulating polymer matrix and conductive filler, leading to standard percolation type behaviour. Chapter 7 proposes an alternative type of piezoresistive nanocomposite comprised of mixtures of 2D insulating, semiconducting, and conducting nanosheets. The nanosheet mixtures display distinct electrical properties depending on the nanocomposite components. Insulating:conducting and semiconducting:conducting nanocomposites show a monotonic increase in conductivity with increasing conductor loading. Surprisingly, conducting:conducting nanosheets display non-monotonic behaviour where poor charge transfer results in a minimisation of conductivity below the percolation threshold. However, regardless of the mechanism, all conductive behaviour can described by different percolation models. The piezoresistive properties of these systems show a set of rich behaviours which go beyond what is normally observed in polymer nanocomposites. Importantly, percolation theory shows that the relationship between the piezoresistive properties, nanocomposite conductivity, and filler loading can be fully described. This demonstrates the intimate link between the percolative parameters and sensing performance.

8.1. Engineering the Piezoresistive Performance of Nanocomposites

The work presented in Chapters 6 and 7 demonstrates that the gauge factor and hence the piezoresistive response of nanocomposites depend strongly on nanocomposite

conductivity and filler loading. Following investigations of the experimental data, simplified two-term equations can be obtained. An example of one of these equations is found below

$$G \approx G_{t,0} + \frac{t}{\phi - \phi_c}\left(\frac{d\phi_c}{d\varepsilon}\right)_0$$

While the equation shows that G diverges as $\phi \to \phi_c$, it may not be desirable to fabricate nanocomposites close to the percolation threshold where poor connectivity of the filler leads to low nanocomposite conductivities. Instead, it is worth considering the other two parameters t and $(d\phi_c/d\varepsilon)_0$. While a precise method of altering $(d\phi_c/d\varepsilon)_0$ remains unclear at present, it was illustrated that t and $(d\phi_c/d\varepsilon)_0$ are linked with larger values of t leading to larger values of $(d\phi_c/d\varepsilon)_0$. Thus suggesting, the most practical method for maximising the gauge factor is to increase the percolation exponent, t. Increasing t necessitates a broadening of the junction resistances within a nanocomposite and it is worth considering the scope of the distribution. The vdW gap between nanosheets limits the narrowest junction, while the upper bound of the junction is limited by the exponential increase in resistance with tunnelling or hopping distance. With this understanding, the best way to broaden the junction resistance distribution is to increase the physical distance between neighbouring nanosheets, this could be achieved by varying the molecular weight of the polymer matrix. For example, introducing a certain percentage of high molecular weight polymers to a nanocomposite formulation may allow for more separation between nanosheets thus broadening the distribution and hence t. Naturally, increasing the distance between nanosheets will decrease the composite conductivity, however careful optimisation may allow enhanced nanocomposite gauges factors with only a minimal decline in conductivity.

8.2. Enhancing the Linearity

The primary focus of this work has been the sensitivity of the piezoresistive response in nanocomposite systems. This is done by characterising the response at low strain $\varepsilon \sim 1\%$, where the resistance variation is linear. Of course, if these sensors are to be used in real-world stretchable applications, strains greater than 1% will need to be realised. The problem here is that above low-strain, the increase in tunnelling distance between adjacent conductive particles dominates and leads to an exponential increase in the resistance and a loss of linearity. The lack of an extensive linear range is a limitation of the sensors proposed here and of nanocomposite strain sensors generally.[256,287,342,343] This is particularly relevant when considering sensors that are conformed to human skin since a degree of pre-strain will occur during installation. This means that the initial condition of the strain sensor will generally be offset from zero strain. Furthermore, the amount of pre-strain conferred to the sensor will depend on the location of installation. For example, installing a sensor at a joint will confer a higher degree of pre-strain as opposed to installation on a relatively flat part of the skin. These considerations demonstrate the need for linearity across a wide sensing range and create a significant hurdle for nanomaterials-based sensors to overcome.

Here, inspiration might be drawn from work that enhances the stretchability and conformability of electrical interconnects made from metal foils. These interconnects have a minimal elastic yield strain of approximately 0.3%, prohibiting their integration into stretchable electronics. To overcome this limitation, several works have proposed curved serpentine geometries of interconnects embedded or bonded to supporting substrates,[344-347] as shown in Figure 8.1. This significantly enhances the stretchability of the interconnects, whereby the entire structure can be elastically strained in excess of $\varepsilon \sim 100\%$ while the strain experienced by any single component of the structure is limited to $\varepsilon \sim$

0.3%. While this method is traditionally used to limit changes in resistance of the interconnects, a recent report has shown that selectively depositing metal foil where the tensile strain is maximised, enables the fabrication of metal foil strain gauges which show a linear relative resistance change up to $\varepsilon \sim 50\%$.[348] The drawback here is that the inherent low gauge factor of the foil, coupled with the deformation mechanics of the serpentine limits the gauge factor of the overall system to $G < 1$.[89] Here nanocomposites may present a distinct advantage. These serpentine strategies, coupled with the linear resistance-strain response at low strain, could be exploited to achieve highly linear nanocomposite strain sensors across a wide strain range. The critical point here is that the large piezoresistivity offered by nanocomposites should allow strain gauges with much higher gauge factors, far surpassing what has been demonstrated with metal foils.

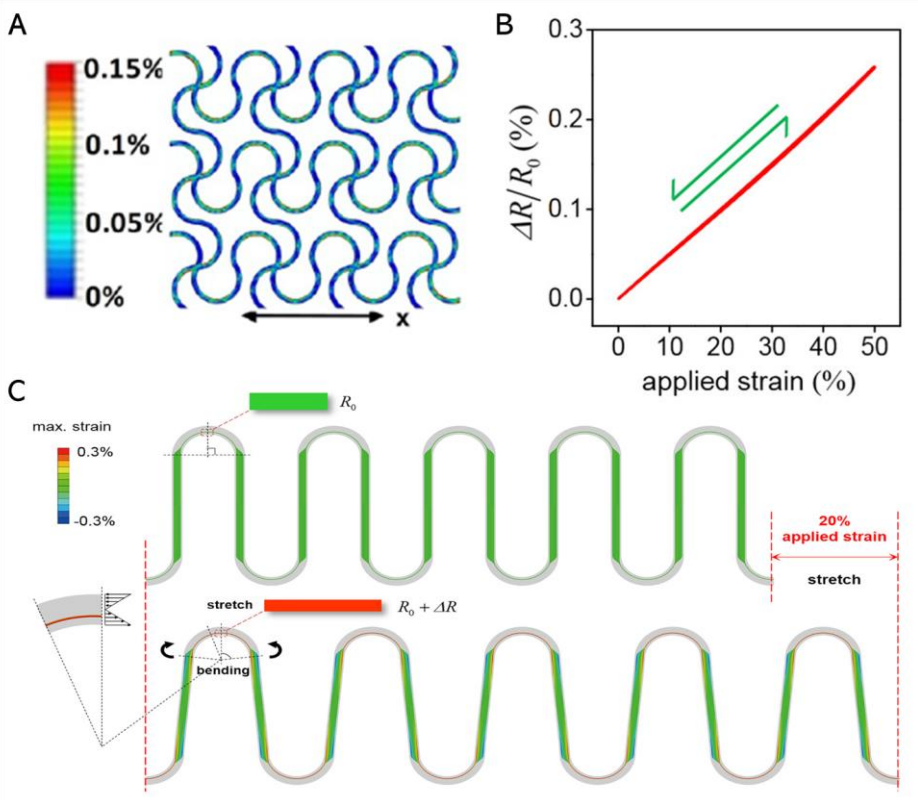

Figure 8.1 – Enhancing the Linearity. A) A design for metal foil interconnects, which allow systems to achieve much higher strains than the strain applied to

any individual component of the system. Image from ref.[346] B) Linear response of metal foil gauge where the foil is selectively deposited on the area of the arch under maximum tensile strain. C) Schematic illustration of sensing mechanism. Images from ref.[348]

An alternative to improving sensor linearity may be found when considering the junction resistance, R_J between two conducting particles. Recall that according to Simmons,[247] R_J is inversely proportional to the areal overlap of the particles, A_J, and is exponentially dependent on the distance between the particles, d, such that $R_J \propto e^{kd}/A_J$. Furthermore, for highly conductive nanosheets such as graphene, the resistance of the network is proportional to the junction resistance.[88] Therefore, in a scenario where strain induces a change in A_J, but keeps d constant we expect the network's resistance to vary linearly.

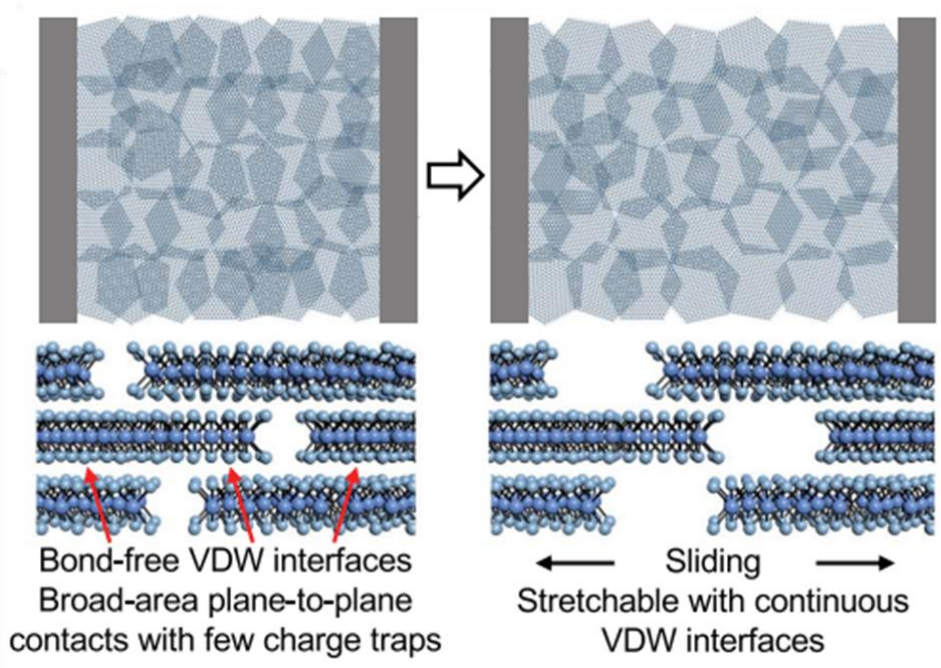

Figure 8.2 – Highly Overlapped Networks. Surface and cross sectional schematics illustrating the junction variation in response to strain for highly overlapped conformal nanosheets. Image from ref.[3]

Following this line of thinking small aspect ratio nanosheets (as in this work), will have a limited linear resistance-strain range. However, if the nanosheets have a large aspect ratio

we can expect a high degree of areal overlap and conformal junctions between the sheets (Figure 8.2), resulting in a much increased linear resistance-strain response.

Preparing thin nanosheets with large lateral size (in sufficient quantities) has been a challenge to the field, however recent progress has demonstrated this is possible via electrochemical exfoliation, with the production of conformal nanosheet networks.[68] The networks produced from high aspect nanosheets show an exceptional ability to withstand strain due to the large areal overlap of the nanosheets. In this case, the network's sensitivity to strain appears to be rather low.[3] However, one can imagine preparing networks of conformal nanosheets close to the percolation threshold, here the nanosheet networks should be far more sensitive to strain yet the overlap of the nanosheets could provide a much improved linear resistance range.

As a final remark, the application of strain sensors in other modes is considered. The focus of this work has been on tensile strain however piezoresistive nanocomposites are equally suitable for pressure sensing applications. This can be achieved be directly applying pressure to a polymer nanocomposite inducing a compressive strain in the material. This usually results in a reduction in a materials resistance in the direction of compression, which is likely a consequence of neighbouring conductive particles being brought into closer proximity and therefore a lowering of the junction resistance. An alternative to this, is the use of very thin nanosheet films backed by comparatively thicker polymer substrates. In this instance compressive or tensile strains can then be induced in the film by bending the substrate. A simple relationship exists between the strain experienced at the substrate surface and the curvature radius of the bend: $\varepsilon = y/r$. Where y is the distance between the neutral axis and surface of the substrate, while r is the radius of the curvature. This will in turn lead to a change in the resistance of the thin film, which will be determined by the compressive or tensile gauge factor (depending on the bending mode)

and the radius of curvature can therefore be inferred. It is important to note that the models developed in this thesis relating the gauge factor to the networks percolative properties could be equally used to study the compressive gauge factor. In fact, it would be interesting to see if the $(d\phi_c/d\varepsilon)_0$ term dominates in compressive strains as it does in tensile strains. Intuitively this would appear to be the case, where the application of compressive strain is likely to bring particles closer together, allowing new conductive paths to form and thus lowering the percolation threshold. This would lead to a negative value for $(d\phi_c/d\varepsilon)_0$ compared to the positive value found in the tensile direction suggesting negative gauge factors should be observed.

Appendix

A. Ancillary Techniques

This appendix will be used to outline the fundamental aspects of primary characterisation techniques which supported device fabrication in this work.

A.1. Uv-Vis Spectroscopy

Optical spectroscopy is one of the principle techniques for the characterisation of nanomaterials dispersed within a liquid media. As light passes through the liquid medium, photons interact with the dispersed matter resulting in absorption and scattering effects. Absorption, *Abs*, occurs through the excitement of electronic transitions within the dispersed material, this means that appreciable absorption will only be observed in semiconducting or insulating materials for energies above the band-gap. For materials with significant lateral sizes, such as nanosheets, there is also an appreciable amount of scattering, *Sc*, of the incident light, which must also be considered.[93] The sum of these effects are described by a quantity known as extinction, *Ext*.

$$Ext = Abs + Sc \tag{A.1}$$

The extinction can be measured in a simple way by monitoring the change in irradiance as light of various wavelengths, λ, passes through a dispersion. Interaction between light and the dispersed materials will attenuate the intensity of light passing through a sample, *I*, relative to the reference, I_0 and can be related to extinction via the Beer-Lambert law

$$Ext = \ln \frac{I}{I_0} = -\ln T \tag{A.2}$$

where *T* is the transmittance. Naturally, the extinction will depend on the number of particles present within a sample and the distance which the light travels. The extinction shows a linear dependence on both the particle concentration, C, and path length, l. A further term known as the extinction coefficient, δ, encompasses the material specific properties, giving the standard equation

$$Ext = \delta Cl$$

(A.3)

Here, δ encompasses both the absorption, α, and scattering, β, components:

$$\delta(\lambda) = \alpha(\lambda) + \beta(\lambda)$$

(A.4)

Measurement of these optical properties is achieved using a dual beam UV-Vis spectrometer, with a schematic of the measurement process shown in Figure A.1. A halogen lamp and deuterium arc source are used to generate near-infrared, visible and ultra-violet light.[349] The light is separated into discrete wavelengths utilising a monochromator comprised of a series of slits, mirrors and diffraction gratings.

The beam is the split, allowing both the sample and a reference to be probed simultaneously, enabling higher accuracy measurements through the removal of scattering and absorption by the solvent and cuvette. The light is then detected by an InGaAs photodiode, with a chopper used to alternate between the sample and reference.

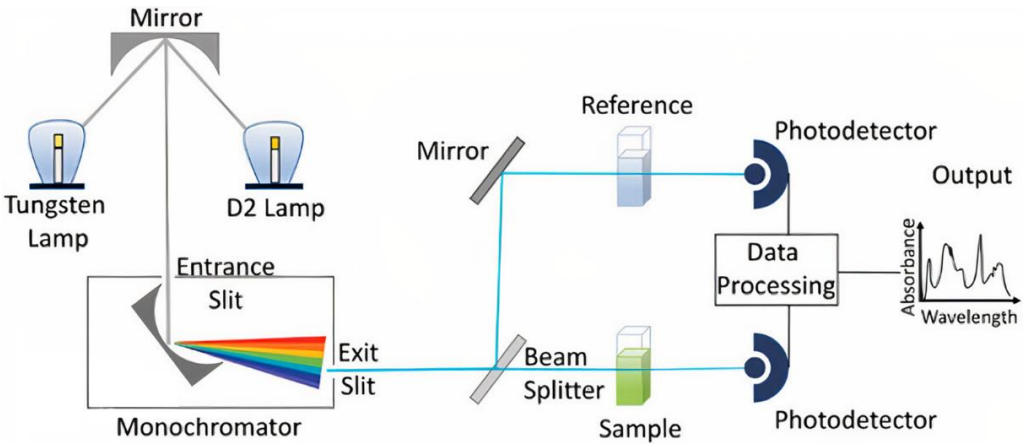

Figure A.1 - UV-Vis Spectrometer. Schematic of a dual-beam UV-Vis spectrometer. Image from ref.[350]

A.2. Raman Spectroscopy

Raman spectroscopy exploits the inelastic scattering of light, where a monochromatic light source is used to probe lattice vibrations in the form of optical phonons. The displaced atoms can be modelled as a harmonic oscillator with vibrations occurring in quantised states as a result of transitions between two discrete energy level. The frequency of the scattered light is shifted to that of the incident monochromatic light, these variations are used to construct a Raman spectrum which can reveal a variety of information about the sample such as; chemical identification, chemical bonding and environmental effects.[351]

Scattering occurs via a two-photon process. Incident light induces a dipole moment in the materials electron cloud forming a higher energy state, where the strength of the interaction is defined by the material polarizability.[352] This formation can be considered a short lived 'virtual' state at the dipole almost simultaneously relaxes through a second photon emission.[353] The majority of scattering is perfectly elastic, where both incident and scattered photons have equivalent energies. This is known as Rayleigh scattering. However, in a very small percentage of cases photons may be scattered at shifted energies as a result of interactions with the materials lattice. Photons may induce vibrations through the creation of an optical phonon in the lattice, this leads to a red shift in the emitted photon and is known as Stokes scattering. However, if the lattice is already in an excited state, the scattered photon may absorb a phonon as the lattice relaxes to a lower vibrational states. In this process the emitted photon is blue shifted and is said to be anti-Stokes scattered. A schematic of the various mechanisms is shown in Figure A.2.

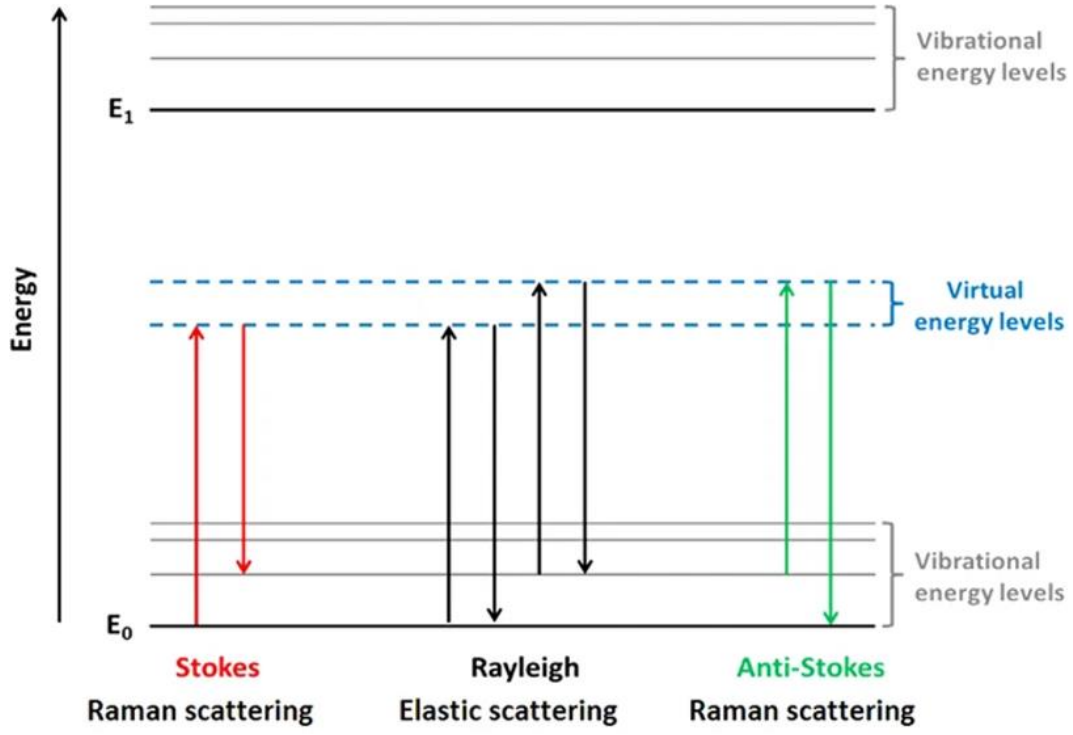

Figure A.2 – Various Raman Processes. Image from ref.[354]

The frequency change of the scattered photon relative to the incident photon is measured as a Raman shift and the intensity distribution of these shifts is used to generate a characteristic Raman fingerprint for a material. Raman spectroscopy is now an integral part of nanosheets characterisation, as in addition to providing a chemical description of a material, it can also be used to analyse nanosheet defects, doping, interlayer coupling, and stress.[355,356]

Raman data in this work was acqyured with a Horiba Jobin Yvon set up using a laser line of 532 nm. Thanks is given to Dr. Harneet Kaur, Dr. Tian Carey and Dr. Victor Vega who acquired the data.

A.3. Transmission Electron Microscopy

Electron microscopy is a useful technique that is widely used for overcoming the resolution limitations of optical characterisation methods (~200 nm). The power of the technique arises from the ability to modulate electron velocity in the presence of an applied electric field. The relationship between a electrons velocity and wavelength is simply described as $\lambda = h/mv$, where h is Planck's constant, v is the electron velocity and m its mass. This can in turn be related to the accelerating voltage, V, such that:

$$\lambda = \frac{h}{\sqrt{2meV}} \tag{A.5}$$

This means that with typical accelerating voltages used in TEM systems, ~200 kV, a theoretical resolution of ~3 picometers can be obtained. In practise such high resolutions are not realisable due to aberrations in the source and lensing column. Despite techniques being put in place to correct these aberrations, TEM resolution is limited to 0.2 nm in conventional systems.[357]

The high energy electrons can penetrate 100s of nm into a sample or, in the case, of nanosheets pass completely through. This has proved particularly useful for imaging 2D nanosheets. As electrons pass through the sample they can interact elastically or inelastically with the attenuation of the electron signal forming the basis of TEM imagery. The images are a result of spatial variation of the scattering, and are dependent on a number of factors such as, thickness, mass, atomic number and grain boundaries. The transmitted electrons are collected by the imaging system, where the scattering contrast allows the rendering of a 2D image of a 3D sample.

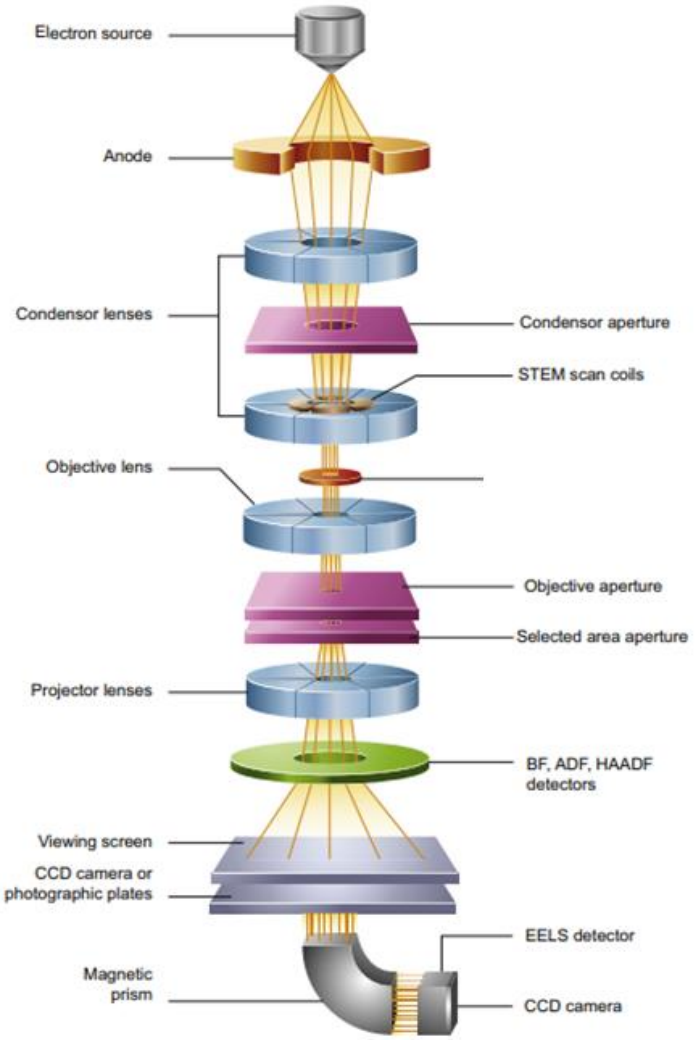

Figure A.3 – Schematic representation of a TEM column. Adapted from ref.[358]

A schematic of the TEM column is shown in Figure A.3. The column can be divided into three sections. First an electron probe is generated by the illumination system, the electron source in a typical system is a thermionic LaB_6 or tungsten filament. The electron beam is then focused onto the sample with a series of condensing lenses. As the beam passes through the sample, electrons may pass through unimpeded or they may be subject to scattering effects. The emergent beam is collected by the imaging system and a series of lenses determine the magnification and spatial resolution of the image. An initial image is formed by the post-specimen objective lens before being magnified into the detection system, generally a cooled CCD.

The TEM imaging in this work was carried out on a Jeol JEM-2100 LaB_6 TEM system operating with a 200 keV accelerating voltage, with thanks given to Dr. Domhnall O'Suilleabháin, Dr. Harneet Kaur and Mark McCrystal who performed the imaging.

A.4. Scanning Electron Microscopy

Following the development of TEM, scanning electron microscopy (SEM) was developed to allow high resolution imaging of materials surfaces. An SEM operates in a similar manner to a TEM, where electrons are focused through electromagnetic lenses onto a sample surface. These electrons are incident under much lower accelerating voltages (0.1 – 30 keV), lowering the penetration depth of the electrons and offering a higher degree of surface sensitivity. Once focused the electron beam is rastered across the surface of the sample utilising xy-scan coil, where the probe-sample interaction at each point is recorded and mapped onto a surface image.

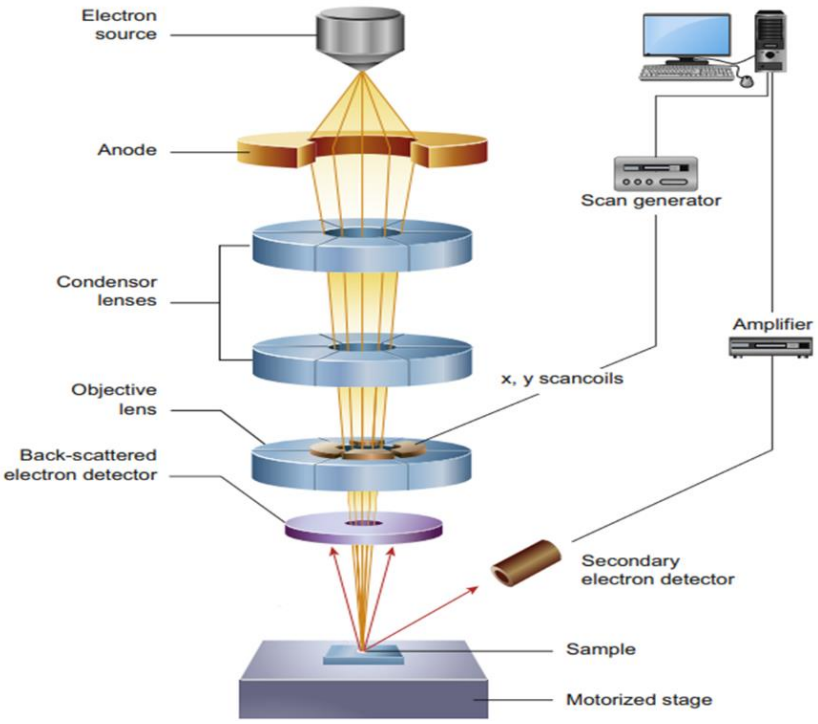

Figure A.4 – Schematic of a SEM column. Adapted from ref.[358]

Rather than rendering an image from transmitted electrons, SEM images are a composite of various electron interactions that occur within a tear-drop shaped volume at the sample surface. The primary contributions come from secondary and back scattered electrons. Secondary electrons are generated via inelastic scattering mechanisms with the atoms within the sample. Here, the incident probe electron ionises the specimen atoms, the emitted electrons from this ionisation are known as secondary electrons. As secondary electrons are of low energy, typically 3 – 5 eV they can only escape from the region within a few nanometres of the specimen surface. Secondary electrons therefore provide spatial resolution and surface information from which topographical maps of the specimen can be rendered.

Backscattered electrons have undergone a single or multiple scattering events upon collision with the specimen surface. These electrons arise from elastic scattering events between the source electrons and the atomic nuclei of the specimen, therefore, the intensity of backscattered electrons is a function of atomic number. Thus, elements in a sample can be distinguished by there relative brightness. Back scattered electrons are of higher energy relative to secondary electrons and so probe a deeper interaction volume of the sample and hence offer a lower resolution.

B. Derivations and Fitting

B.1. Relating the Gauge Factor to Material Conductivity

The conductivity of a material, σ, can be related to the gauge factor, G, by first considering the definition of the resistance

$$R = \frac{L}{A\rho} = \frac{L\sigma}{A} \tag{B.1}$$

Where ρ, is the materials resistivity, L is the length and A is the cross-sectional area of the sample. Combining the definition of the gauge factor, $G\varepsilon = \Delta R/R_0$, allows a relationship between the conductivity and strain dependent resistivity to be obtained.

Assuming that the volume remains constant at low strain, $AL = A_0L_0$. Then resistance can be written as

$$R = \frac{L^2}{\sigma A_0 L_0} \tag{B.2}$$

Taking the strain derivative of the resistance yields

$$\frac{dR}{d\varepsilon} = \frac{1}{A_0 L_0}\left[2L\frac{1}{\sigma}\frac{dL}{d\varepsilon} - \frac{L^2}{\sigma^2}\frac{d\sigma}{d\varepsilon}\right] \tag{B.3}$$

This can be related to the definition of the gauge factor by dividing through by the zero-strain resistance, $R_0 = L_0/A_0\sigma_0$

$$\frac{1}{R_0}\frac{dR}{d\varepsilon} = \frac{\sigma_0}{L_0^{\,2}}\left[2L\frac{1}{\sigma}\frac{dL}{d\varepsilon} - \frac{L^2}{\sigma^2}\frac{d\sigma}{d\varepsilon}\right]$$

(B.4)

Here, an approximation is made that in the low strain limit, $L \approx L_0$ and $\sigma \approx \sigma_0$. Which allows equation B.4 to be re-written as

$$\frac{1}{R_0}\frac{dR}{d\varepsilon} = \left[2\frac{dL/L_0}{d\varepsilon} - \frac{1}{\sigma_0}\frac{d\sigma}{d\varepsilon}\right]$$

(B.5)

Using the definition for strain, $\varepsilon = (L - L_0)/L_0$, the resulting equation gives a smiple relationship between gauge factor and conductivtiy

$$\frac{1}{R_0}\frac{dR}{d\varepsilon} = G = 2 - \frac{1}{\sigma_0}\left(\frac{d\sigma}{d\varepsilon}\right)_0 = 2 - \left(\frac{d\ln\sigma}{d\varepsilon}\right)_0$$

(B.6)

where the bracketed derivative, clarifies that this equation is only valid at low strain.

B.2. Fitting the Gauge Factor Model

In chapter 6, three models are described from which the percolative parameters of a composite can be obtained. The first is the well known conductivity dependence on filler volume fraction. The other two models were developed in this work, and relate the gauge factor to the filler volume fraction and composite conductivity.

$$\sigma = \sigma_c(\phi - \phi_c)^t$$

(B.7)

$$G \approx G_{0,\phi} + \frac{G_1}{\phi - \phi_{c,0}} \tag{B.8}$$

$$G \approx G_{0,\sigma} + (\sigma_1 / \sigma_0)^{1/t_0} \tag{B.9}$$

In order to show the fidelity of the models to describe real data. A number of datasets where obtained from the literature[10,278,298] and fit using the equations above. The complete fitting of this data is shown below in Figures B.1 – B.5

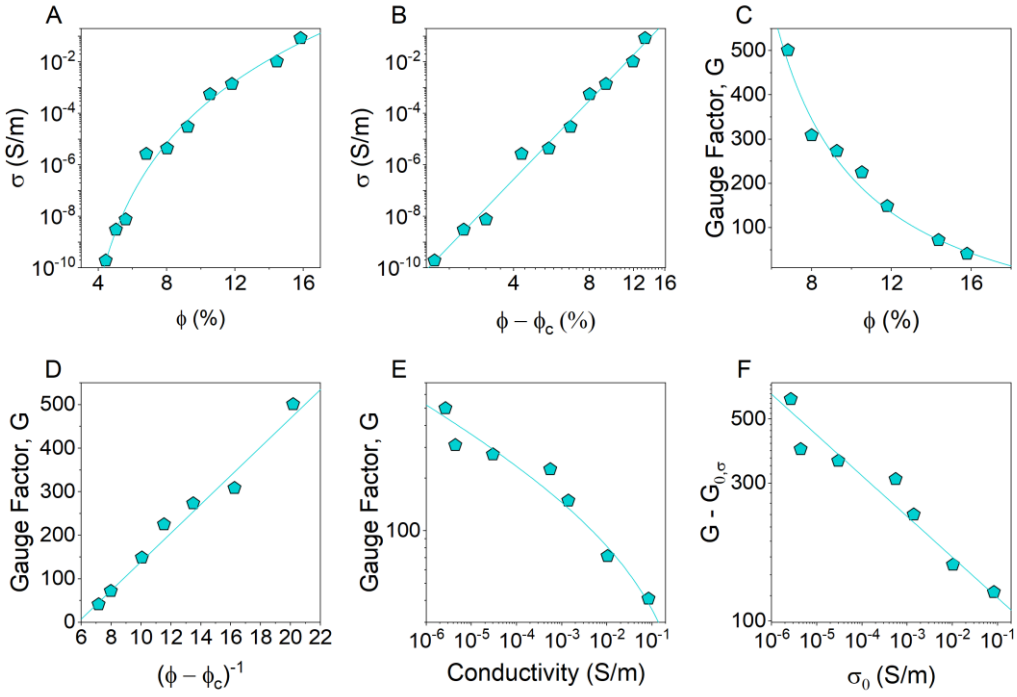

Figure B1: Fits to literature data, Boland et al.[10] The composite is comprised of a siloxane-based polymer matrix and graphene filler (G-putty). A-B) Zero-strain conductivity plotted as a function of A) Graphene volume fraction, ϕ, and B) zero-strain reduced volume fraction, ϕ-$\phi_{c,0}$. The solid lines are fits to the percolation scaling law, equation B.7 . $\sigma_{c,0}$ = 4.3 × 10^7 S/m, $\phi_{c,0}$ = 2.50% and t_0 = 10.2 C-D) Gauge factor plotted versus C) graphene volume fraction, ϕ,

and D) inverse of zero-strain reduced volume fraction, $(\phi-\phi_{c,0})^{-1}$. The solid lines are fits to equation B.8.$\phi_{c,0}$ = 1.86% , G_1 = 33, $G_{0,\phi}$ = -190 E-F) Gauge factor versus conductivity data plotted as G vs. σ_0 (E) and G-$G_{0,\sigma}$ vs. σ_0 (F). The solid line is a fit to equation B.9 t_0 = 7.1, σ_1 = 87 S/m, $G_{0,\sigma}$ = -85

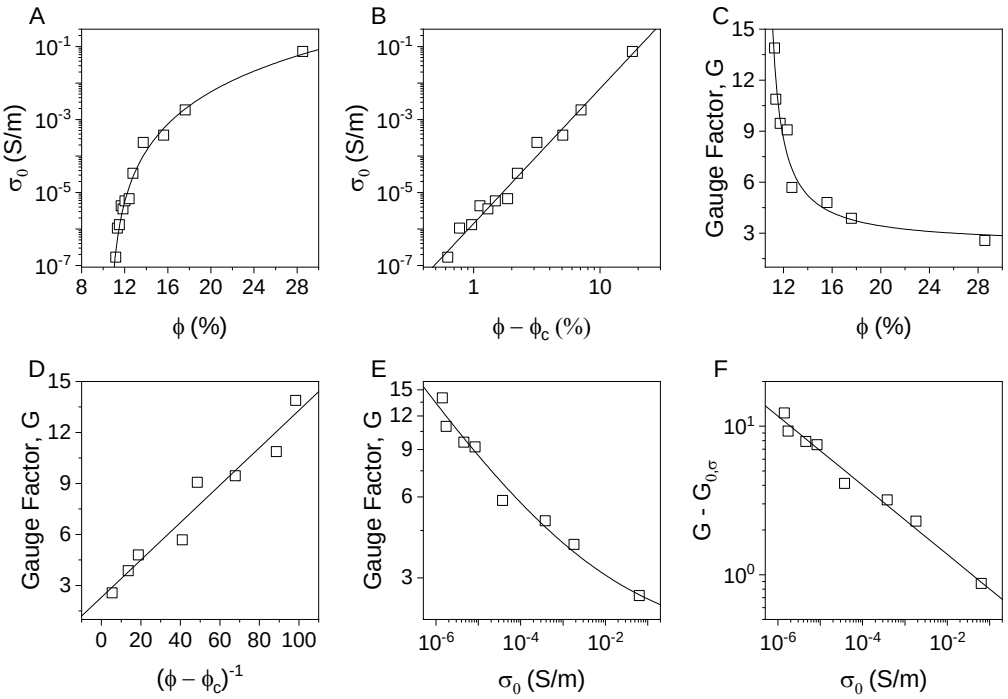

Figure B2: Fits to literature data, Carcia et al.[278] The composite is comprised of a borosilicate glass matrix and RuO_2 filler (Surface area 5 m^2/g). A-B) Zero-strain conductivity plotted as a function of A) RuO_2 volume fraction, ϕ, and B) zero-strain reduced volume fraction, $\phi-\phi_{c,0}$. The solid lines are fits to the percolation scaling law, Eq.1 (main text). $\sigma_{c,0}$ = 34 S/m, $\phi_{c,0}$ = 10.55% and t_0 = 3.7 C-D) Gauge factor plotted versus C) graphene volume fraction, ϕ, and D) inverse of zero-strain reduced volume fraction, $(\phi-\phi_{c,0})^{-1}$. The solid lines are fits to equation B.8 (main text). $\phi_{c,0}$ = 10.24% , G_1 = 0.11, $G_{0,\phi}$ = 2.3 E-F) Gauge factor versus conductivity data plotted as G vs. σ_0 (E) and G-$G_{0,\sigma}$ vs. σ_0 (F). The solid line is a fit to equation B.9 (main text). t_0 = 4.3, σ_1 = 0.47 S/m, $G_{0,\sigma}$ = 1.7

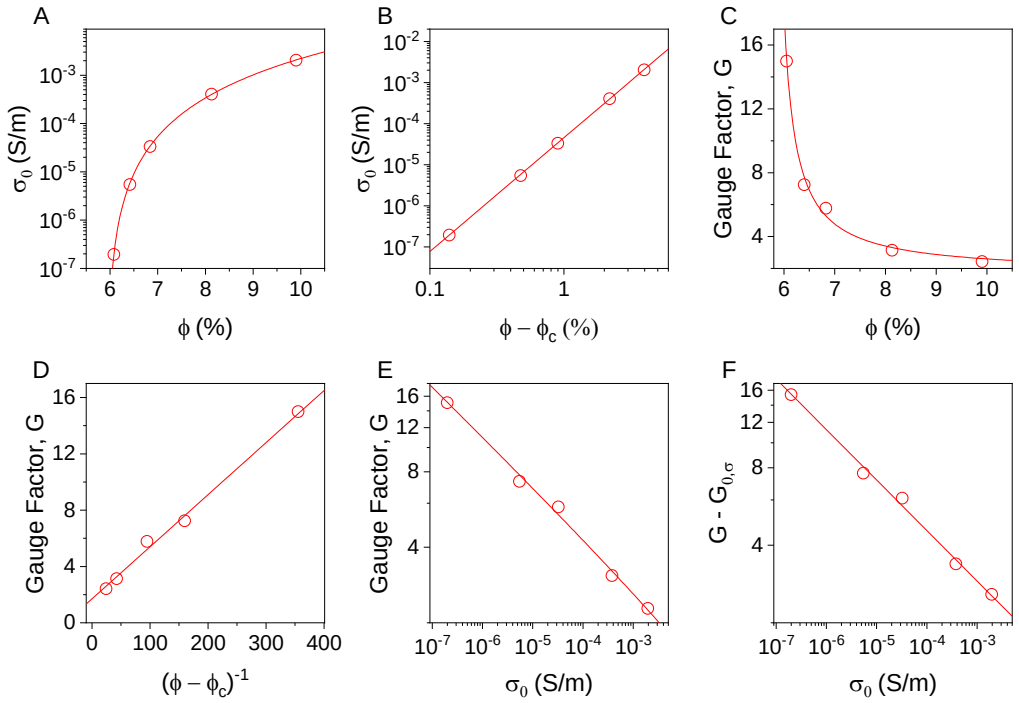

Figure B3: Fits to literature data, Carcia et al.[278] The composite is comprised of a borosilicate glass matrix and RuO_2 filler (Surface area 13 m^2/g). A-B) Zero-strain conductivity plotted as a function of A) RuO_2 volume fraction, ϕ, and B) zero-strain reduced volume fraction, ϕ-$\phi_{c,0}$. The solid lines are fits to the percolation scaling law, equation B.7. $\sigma_{c,0}$ = 16 S/m, $\phi_{c,0}$ = 5.94% and t_0 = 2.77 C-D) Gauge factor plotted versus C) graphene volume fraction, ϕ, and D) inverse of zero-strain reduced volume fraction, $(\phi-\phi_{c,0})^{-1}$. The solid lines are fits to equation B.8. $\phi_{c,0}$ = 5.77% , G_1 = 0.038, $G_{0,\phi}$ = 1.7 E-F) Gauge factor versus conductivity data plotted as G vs. σ_0 (E) and G-$G_{0,\sigma}$ vs. σ_0 (F). The solid line is a fit to equation B.9. t_0 = 5.1, σ_1 = 0.75 S/m, $G_{0,\sigma}$ = -0.3

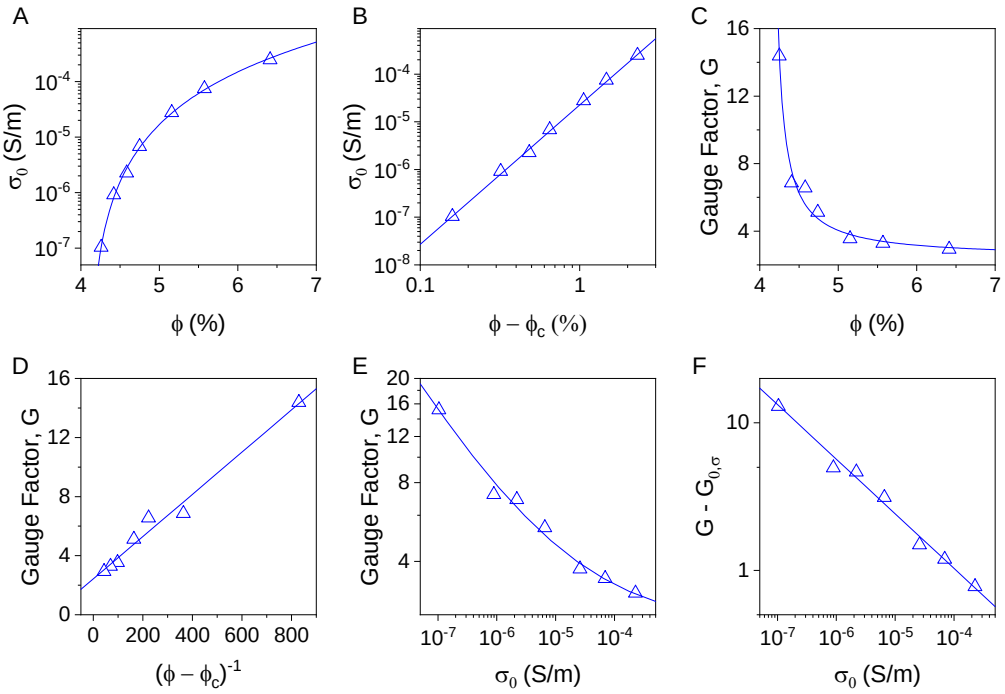

Figure B4: Fits to literature data, Carcia et al.[278] The composite is comprised of a borosilicate glass matrix and RuO_2 filler (Surface area 67 m^2/g). A-B) Zero-strain conductivity plotted as a function of of A) RuO_2 volume fraction, ϕ, and B) zero-strain reduced volume fraction, ϕ-$\phi_{c,0}$. The solid lines are fits to the percolation scaling law, equation B.7. $\sigma_{c,0}$ = 16 S/m, $\phi_{c,0}$ = 4.10% and t_0 = 2.92 C-D) Gauge factor plotted versus C) graphene volume fraction, ϕ, and D) inverse of zero-strain reduced volume fraction, $(\phi-\phi_{c,0})^{-1}$. The solid lines are fits to equation B.8. $\phi_{c,0}$ = 4.13% , G_1 = 0.014, $G_{0,\phi}$ = 2.4 E-F) Gauge factor versus conductivity data plotted as G vs. σ_0 (E) and G-$G_{0,\sigma}$ vs. σ_0 (F). The solid line is a fit to equation B.9. t_0 = 2.71, σ_1 = 0.034 S/m, $G_{0,\sigma}$ = 2.25

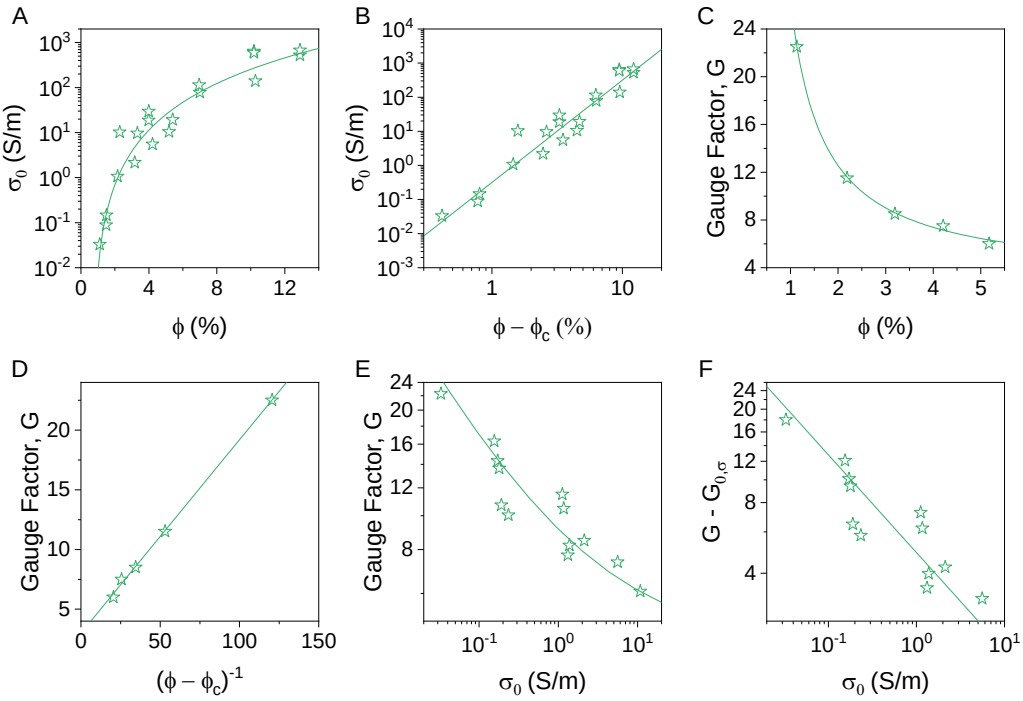

Figure B5: Fits to literature data, Hu et al.[298] The composite is comprised of an epoxy polymer matrix and carbon nanotube (CNT) filler. A-B) Zero-strain conductivity plotted as a function of A) CNT volume fraction, ϕ, and B) zero-strain reduced volume fraction, ϕ-$\phi_{c,0}$. The solid lines are fits to the percolation scaling law, equation B.7. $\sigma_{c,0} = 3.2 \times 10^5$ S/m, $\phi_{c,0} = 0.70\%$ and $t_0 = 3.0$ C-D) Gauge factor plotted versus C) graphene volume fraction, ϕ, and D) inverse of zero-strain reduced volume fraction, $(\phi-\phi_{c,0})^{-1}$. The solid lines are fits to equation B.8. $\phi_{c,0} = 0.31\%$, $G_1 = 0.16$, $G_{0,\phi} = 3.0$ E-F) Gauge factor versus conductivity data plotted as G vs. σ_0 (E) and G-$G_{0,\sigma}$ vs. σ_0 (F). The solid line is a fit to equation B.9. $t_0 = 2.50$, $\sigma_1 = 4.9$ S/m, $G_{0,\sigma} = 4.2$

B.3. Gauge Factor Response in 2D:2D Nanocomposites

Volume Fraction Considerations

The scaling of conductivity, σ, with increasing volume fraction, ϕ, is generally parsed into two separate regimes. The first regime lies below the percolation threshold, ϕ_c, where there are no complete conductive paths through the material. Instead, areas of conductive filler exist as disparate islands throughout the matrix so that an electrons path traverses a combination of low resistance filler and higher resistance matrix. This behaviour is modelled using the following percolation equation[338]

$$\sigma = \sigma_i \left(\frac{\phi_c - \phi}{\phi_c} \right)^{-s} \tag{B.10}$$

Where σ_i is a scaling constant associated with conductivity of the matrix and s is a percolation exponent. Recalling the definition of the gauge factor in terms of composite conductivity

$$G \approx 2 - \frac{1}{\sigma_0} \left(\frac{d\sigma}{d\varepsilon} \right)_0 \tag{B.11}$$

The gauge factor can then be described in terms of the percolative parameters in equation B.10

$$\frac{d\sigma}{d\varepsilon} = \frac{d\sigma}{d\sigma_i}\frac{d\sigma_i}{d\varepsilon} + \frac{d\sigma}{ds}\frac{ds}{d\varepsilon} + \frac{d\sigma}{d\phi}\frac{d\phi}{d\varepsilon} + \frac{d\sigma}{d\phi_c}\frac{d\phi_c}{d\varepsilon} \tag{B.12}$$

Which leads to

$$G \approx \left[2 - \frac{1}{\sigma_i}\left(\frac{d\sigma_i}{d\varepsilon}\right)_0\right] + \left[\ln\left(\frac{\phi_c - \phi}{\phi_c}\right)\left(\frac{ds}{d\varepsilon}\right)_0\right] + \left[\left(\frac{s}{\phi_c - \phi} - \frac{s}{\phi_c}\right)\left(\frac{d\phi_c}{d\varepsilon}\right)_0\right]$$

(B.13)

In chapter 6, it was shown that $(d\phi_c/d\varepsilon)_0$ is the dominant contribution to the gauge factor in bulk polymer nanocomposites and therefore, the other bracketed terms can be considered as quasi-constant. It's expected the same approximation will be valid in the region below ϕ_c, such that

$$G \approx G_{s,0} + \frac{s}{\phi_c - \phi}\left(\frac{d\phi_c}{d\varepsilon}\right)_0$$

(B.14)

Where the constant, $G_{s,0}$, comprising of

$$G_{s,0} = \left[2 - \frac{1}{\sigma_i}\left(\frac{d\sigma_i}{d\varepsilon}\right)_0\right] + \left[\ln\left(\frac{\phi_c - \phi}{\phi_c}\right)\left(\frac{ds}{d\varepsilon}\right)_0\right] - \left[\left(\frac{s}{\phi_c}\right)\left(\frac{d\phi_c}{d\varepsilon}\right)_0\right]$$

(B.15)

The second conductivity scaling regime is qualified as the region above ϕ_c. The percolation threshold marks the filler loading at which the first connected filler path if formed. Above ϕ_c, the conductivity continues to increase in a power law like manner as additional conductive filler is added. This behaviour is traditionally modelled by a separate percolation equation

$$\sigma = \sigma_c \left(\frac{\phi - \phi_c}{1 - \phi_c} \right)^t$$

(B.16)

Where σ_c is a scaling constant associated with conductivity of the filler and t is a percolation exponent. Using the same process as described above the percolative parameters of B.16 can be related to the gauge factor as

$$G \approx G_{t,0} + \frac{t}{\phi - \phi_c} \left(\frac{d\phi_c}{d\varepsilon} \right)_0$$

(B.17)

Where

$$G_{t,\phi} = \left[2 - \frac{1}{\sigma_c} \left(\frac{d\sigma_c}{d\varepsilon} \right)_0 \right] - \left[\ln \left(\frac{\phi - \phi_c}{1 - \phi_c} \right) \left(\frac{dt}{d\varepsilon} \right)_0 \right] - \left[\frac{t}{1 - \phi_c} \left(\frac{d\phi_c}{d\varepsilon} \right)_0 \right]$$

(B.18)

In addition to the standard percolation models, a third model proposed describing the non-monotonic behaviour observed in Ag:Gr nanocomposites. Above the percolation threshold, $\phi_{Ag,c}$, the composite displays typical behaviour with the conductivity increasing according to equation B.16. Below $\phi_{Ag,c}$, some rather surprising behaviour is obersevd. Here, the conductivity is seen to decrease with increasing silver content. This behaviour is attributed to poor charge transfer between the graphene and silver, leading to the silver nanosheets acting as pores within a conductive graphene network. This mechanism is modelled by the following equation

$$\sigma = \sigma_c \left(\frac{\phi_{c_p,Ag} - \phi_{Ag}}{\phi_{c_p,Ag} + \phi_p} \right)^{t_p}$$

(B.19)

where $\phi_{c_p,Ag}$ is the percolation threshold and t_p is the percolation exponent associated with a porosity dependent network. While, ϕ_p is the free volume of the printed nanocomposite.

Again here, equation B.19 is combined with equation B.11 to yield the a description of the gauge factor in terms of the porosity percolation parameters

$$G \approx G_{p,0} + \frac{t_p}{\phi_{c_p,Ag} - \phi_{Ag}} \left(\frac{d\phi_{c_p,Ag}}{d\varepsilon} \right)_0$$

(B.20)

Where

$$G_{p,0} = \left[2 - \frac{1}{\sigma_c} \left(\frac{d\sigma_c}{d\varepsilon} \right)_0 \right] - \left[\ln \left(\frac{\phi_{c_p,Ag} - \phi_{Ag}}{\phi_{c_p,Ag} + \phi_p} \right) \left(\frac{dt_p}{d\varepsilon} \right)_0 \right] - \left[\left(\frac{t_p}{\phi_{c_p,Ag} + \phi_p} \right) \left(\frac{d\phi_c}{d\varepsilon} \right)_0 \right]$$

(B.21)

Conductivity Considerations

While equations B.10 and B.16 are generally suitable for describing percolation behaviour above and below ϕ_c. The two equations do not agree in the 'cross over' region that exists when $\phi \cong \phi_c$, as shown in Figure B6. To remedy this McLachlan et al.[336] has developed a functional equation that allows the entire percolation range to be modelled

$$(1-\phi)\frac{\sigma_i^{1/s}-\sigma^{1/s}}{\sigma_i^{1/s}+A\sigma^{1/s}}+\phi\frac{\sigma_c^{1/t}-\sigma^{1/t}}{\sigma_c^{1/t}+A\sigma^{1/t}}=0\ , \qquad A=(1-\phi_c)/\phi_c$$

(B.22)

While the form of this equation does not allow G to be found in terms of composite volume fraction, G can be written in terms of composite conductivity. A detailed description of this procedure is given below.

$$(1-\phi)\frac{\sigma_i^{1/s}-\sigma^{1/s}}{\sigma_i^{1/s}+A\sigma^{1/s}}=-\phi\frac{\sigma_c^{1/t}-\sigma^{1/t}}{\sigma_c^{1/t}+A\sigma^{1/t}}$$

(B.23)

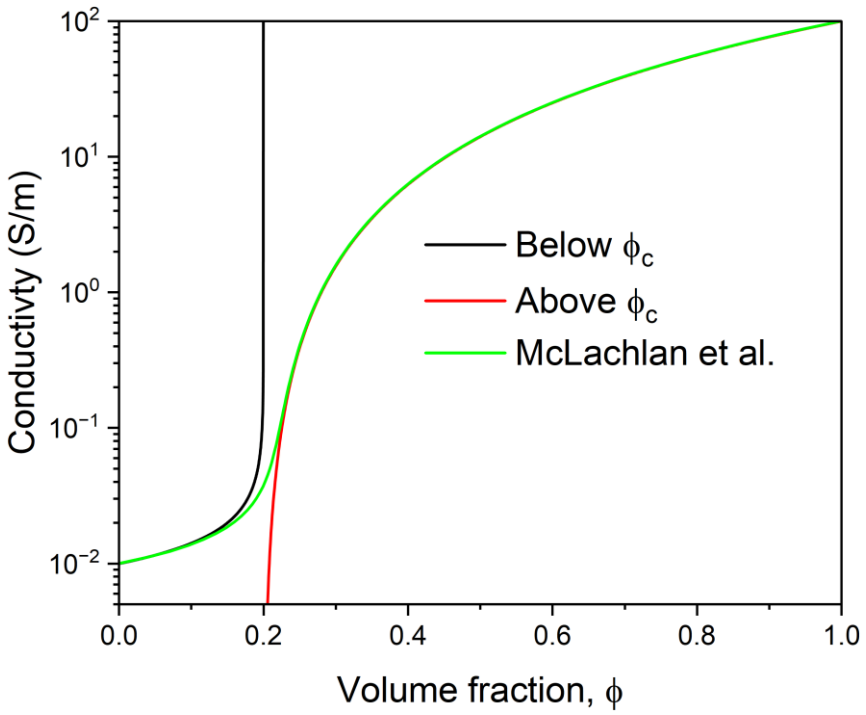

Figure B6 – Percolative scaling. A comparison of equation B.22 developed by McLachlan et al. to model the entire percolative range. Equations B.10 and B.16 demonstrate the predicted behaviour when conductivity above and below ϕ_c are modelled separately.

Taking the log of both sides then gives

$$\ln(1-\phi)+\ln(\sigma_i^{1/s}-\sigma^{1/s})-\ln(\sigma_i^{1/s}+A\sigma^{1/s})=\ln(-\phi)+\ln(\sigma_c^{1/t}-\sigma^{1/t})-\ln(\sigma_c^{1/t}+A\sigma^{1/t})$$

(B.24)

Now using the fact that

$$\frac{1}{\sigma}\frac{d\sigma}{d\varepsilon}=\frac{d\ln\sigma}{d\varepsilon}$$

(B.25)

Equation B.24 can be re-written as

$$\frac{1}{\sigma_i^{1/s}-\sigma^{1/s}}\frac{d}{d\varepsilon}(\sigma_i^{1/s}-\sigma^{1/s})-\frac{1}{(\sigma_i^{1/s}+A\sigma^{1/s})}\frac{d}{d\varepsilon}(\sigma_i^{1/s}+A\sigma^{1/s})$$

$$=\frac{1}{(\sigma_c^{1/t}-\sigma^{1/t})}\frac{d}{d\varepsilon}(\sigma_c^{1/t}-\sigma^{1/t})-\frac{1}{(\sigma_c^{1/t}+A\sigma^{1/t})}\frac{d}{d\varepsilon}(\sigma_c^{1/t}+A\sigma^{1/t})$$

(B.26)

Re-arranging gives

$$\frac{\left[\frac{d}{d\varepsilon}\sigma_i^{1/s}-\frac{d}{d\varepsilon}\sigma^{1/s}\right]}{\sigma_i^{1/s}-\sigma^{1/s}}-\frac{\left[\frac{d}{d\varepsilon}\sigma_i^{1/s}+\frac{d}{d\varepsilon}(A\sigma^{1/s})\right]}{(\sigma_i^{1/s}+A\sigma^{1/s})}$$

$$=\frac{\left[\frac{d}{d\varepsilon}\sigma_c^{1/t}-\frac{d}{d\varepsilon}\sigma^{1/t}\right]}{(\sigma_c^{1/t}-\sigma^{1/t})}-\frac{\left[\frac{d}{d\varepsilon}\sigma_c^{1/t}+\frac{d}{d\varepsilon}(A\sigma^{1/t})\right]}{(\sigma_c^{1/t}+A\sigma^{1/t})}$$

(B.27)

If all the percolation parameters are considered to be strain dependent this equation is going to be too complicated to model effectively, and thus some simplification is required.

As discussed earlier, we expect ϕ_c and the composite conductivity, σ, to be more sensitive to strain than the other percolation parameters. Thus for simplicity only ϕ_c and σ are considered as strain dependent. The contribution from other terms *($dt/d\varepsilon$, $ds/d\varepsilon$, $d\sigma_i/d\varepsilon$* and *$d\sigma_c/d\varepsilon$)* will be accounted for in a constant which will be explicitly added at the end of the derivation.

$$\frac{\left[\frac{d}{d\varepsilon}\sigma^{1/s}\right]}{\sigma_i^{1/s}-\sigma^{1/s}}+\frac{\left[\frac{d}{d\varepsilon}(A\sigma^{1/s})\right]}{(\sigma_i^{1/s}+A\sigma^{1/s})}=\frac{\left[\frac{d}{d\varepsilon}\sigma^{1/t}\right]}{(\sigma_c^{1/t}-\sigma^{1/t})}+\frac{\left[\frac{d}{d\varepsilon}(A\sigma^{1/t})\right]}{(\sigma_c^{1/t}+A\sigma^{1/t})} \tag{B.28}$$

Performing the differentiation gives

$$\frac{\left[\frac{\sigma^{1/s}}{s\sigma}\frac{d}{d\varepsilon}\sigma\right]}{\sigma_i^{1/s}-\sigma^{1/s}}+\frac{\left[\frac{A\sigma^{1/s}}{s\sigma}\frac{d}{d\varepsilon}\sigma+\sigma^{1/s}\frac{d}{d\varepsilon}A\right]}{\sigma_i^{1/s}+A\sigma^{1/s}}=\frac{\left[\frac{\sigma^{1/t}}{t\sigma}\frac{d}{d\varepsilon}\sigma\right]}{\sigma_c^{1/t}-\sigma^{1/t}}+\frac{\left[\frac{A\sigma^{1/t}}{t\sigma}\frac{d}{d\varepsilon}\sigma+\sigma^{1/t}\frac{d}{d\varepsilon}A\right]}{\sigma_c^{1/t}+A\sigma^{1/t}} \tag{B.29}$$

Using equation B.25 we can re-write equation B.28 as

$$\frac{\left[\frac{\sigma^{1/s}}{s}\frac{d\ln\sigma}{d\varepsilon}\right]}{\sigma_i^{1/s}-\sigma^{1/s}}+\frac{\left[\frac{A\sigma^{1/s}}{s}\frac{d\ln\sigma}{d\varepsilon}+\sigma^{1/s}\frac{dA}{d\varepsilon}\right]}{\sigma_i^{1/s}+A\sigma^{1/s}}=\frac{\left[\frac{\sigma^{1/t}}{t}\frac{d\ln\sigma}{d\varepsilon}\right]}{\sigma_c^{1/t}-\sigma^{1/t}}+\frac{\left[\frac{A\sigma^{1/t}}{t}\frac{d\ln\sigma}{d\varepsilon}+\sigma^{1/t}\frac{dA}{d\varepsilon}\right]}{\sigma_c^{1/t}+A\sigma^{1/t}} \tag{B.30}$$

Collecting terms yields

$$\frac{d\ln\sigma}{d\varepsilon}\left[\frac{\sigma^{1/s}/s}{\sigma_i^{1/s}-\sigma^{1/s}}+\frac{A\sigma^{1/s}/s}{\sigma_i^{1/s}-A\sigma^{1/s}}-\frac{\sigma^{1/t}/t}{\sigma_c^{1/t}-\sigma^{1/t}}-\frac{A\sigma^{1/t}/t}{\sigma_c^{1/t}-A\sigma^{1/t}}\right]$$

$$=\frac{dA}{d\varepsilon}\left[\frac{\sigma^{1/t}}{\sigma_c^{1/t}-A\sigma^{1/t}}-\frac{\sigma^{1/s}}{\sigma_i^{1/s}-A\sigma^{1/s}}\right]$$

(B.31)

With some further rearranging

$$\frac{d\ln\sigma}{d\varepsilon}=\frac{dA}{d\varepsilon}\frac{\left[\dfrac{\sigma^{1/s}}{(\sigma_i^{1/s}+A\sigma^{1/s})}-\dfrac{\sigma^{1/t}}{(\sigma_c^{1/t}+A\sigma^{1/t})}\right]}{\left[\dfrac{\sigma^{1/t}/t}{\sigma_c^{1/t}-\sigma^{1/t}}-\dfrac{\sigma^{1/s}/s}{\sigma_i^{1/s}-\sigma^{1/s}}-\dfrac{A\sigma^{1/s}/s}{\sigma_i^{1/s}+A\sigma^{1/s}}+\dfrac{A\sigma^{1/t}/t}{\sigma_c^{1/t}+A\sigma^{1/t}}\right]}$$

(B.32)

Since $A = (1-\phi_c)/\phi_c$, $dA/d\varepsilon$ can be written in terms of ϕ_c

$$\frac{dA}{d\varepsilon}=-\frac{1}{\phi_c^{\,2}}\frac{d\phi_c}{d\varepsilon}$$

(B.33)

Which finally yields

$$\frac{d\ln\sigma}{d\varepsilon}=-\frac{1}{\phi_c^{\,2}}\frac{d\phi_c}{d\varepsilon}\frac{\left[\dfrac{\sigma^{1/s}}{(\sigma_i^{1/s}+A\sigma^{1/s})}-\dfrac{\sigma^{1/t}}{(\sigma_c^{1/t}+A\sigma^{1/t})}\right]}{\left[\dfrac{\sigma^{1/t}/t}{\sigma_c^{1/t}-\sigma^{1/t}}-\dfrac{\sigma^{1/s}/s}{\sigma_i^{1/s}-\sigma^{1/s}}-\dfrac{A\sigma^{1/s}/s}{\sigma_i^{1/s}+A\sigma^{1/s}}+\dfrac{A\sigma^{1/t}/t}{\sigma_c^{1/t}+A\sigma^{1/t}}\right]}$$

(B.34)

Substituting B.34 into B.6 and introducing the constant, $G_{\sigma,0}$ discussed earlier gives us the gauge factor equation

$$G\approx G_{\sigma,0}+\frac{1}{\phi_c^{\,2}}\left(\frac{d\phi_c}{d\varepsilon}\right)_0\frac{\left[\dfrac{1}{\sigma_i^{1/s}/\sigma^{1/s}+A}-\dfrac{1}{\sigma_c^{1/t}/\sigma^{1/t}+A}\right]}{\left[\dfrac{1/t}{\sigma_c^{1/t}/\sigma^{1/t}-1}-\dfrac{1/s}{\sigma_i^{1/s}/\sigma^{1/s}-1}-\dfrac{A/s}{\sigma_i^{1/s}/\sigma^{1/s}+A}+\dfrac{A/t}{\sigma_c^{1/t}/\sigma^{1/t}+A}\right]}$$

(B.35)

References

1 Thomson, W. XXXI. The Bakerian lecture.-On the electro-dynamic qualities of metals. *Philosophical Transactions of the Royal Society of London*, 649-751 (1856).

2 Sensor, B. *Semiconductor Strain Gauge Datasheet*, <https://www.bcmsensor.com/wp-content/uploads/2015/09/210705_Semiconductor_Strain_Gauges.pdf> (2022).

3 Yan, Z. *et al.* Highly stretchable van der Waals thin films for adaptable and breathable electronic membranes. *Science* **375**, 852-859, doi:10.1126/science.abl8941 (2022).

4 Ray, T. R. *et al.* Bio-Integrated Wearable Systems: A Comprehensive Review. *Chemical Reviews* **119**, 5461-5533, doi:10.1021/acs.chemrev.8b00573 (2019).

5 Liu, X. The more and less of electronic-skin sensors. *Science* **370**, 910-911, doi:10.1126/science.abe7366 (2020).

6 Won, P. *et al.* Transparent Soft Actuators/Sensors and Camouflage Skins for Imperceptible Soft Robotics. *Advanced Materials* **33**, 2002397, doi:https://doi.org/10.1002/adma.202002397 (2021).

7 Sundaram, S. *et al.* Learning the signatures of the human grasp using a scalable tactile glove. *Nature* **569**, 698-702, doi:10.1038/s41586-019-1234-z (2019).

8 Ershad, F. *et al.* Ultra-conformal drawn-on-skin electronics for multifunctional motion artifact-free sensing and point-of-care treatment. *Nature communications* **11**, 3823, doi:10.1038/s41467-020-17619-1 (2020).

9 Pang, Y., Yang, Z., Yang, Y. & Ren, T.-L. Wearable Electronics Based on 2D Materials for Human Physiological Information Detection. *Small* **16**, 1901124, doi:https://doi.org/10.1002/smll.201901124 (2020).

10 Boland, C. S. *et al.* Sensitive electromechanical sensors using viscoelastic graphene-polymer nanocomposites. *Science* **354**, 1257-1260, doi:10.1126/science.aag2879 (2016).

11 Lipomi, D. J. *et al.* Skin-like pressure and strain sensors based on transparent elastic films of carbon nanotubes. *Nature Nanotechnology* **6**, 788-792, doi:10.1038/nnano.2011.184 (2011).

12 Tan, C. *et al.* Recent Advances in Ultrathin Two-Dimensional Nanomaterials. *Chemical Reviews* **117**, 6225-6331, doi:10.1021/acs.chemrev.6b00558 (2017).

13 Coleman Jonathan, N. *et al.* Two-Dimensional Nanosheets Produced by Liquid Exfoliation of Layered Materials. *Science* **331**, 568-571, doi:10.1126/science.1194975 (2011).

14 Nicolosi, V., Chhowalla, M., Kanatzidis Mercouri, G., Strano Michael, S. & Coleman Jonathan, N. Liquid Exfoliation of Layered Materials. *Science* **340**, 1226419, doi:10.1126/science.1226419 (2013).

15 Akinwande, D., Petrone, N. & Hone, J. Two-dimensional flexible nanoelectronics. *Nature communications* **5**, 5678, doi:10.1038/ncomms6678 (2014).

16 Novoselov, K. S. *et al.* Electric Field Effect in Atomically Thin Carbon Films. *Science* **306**, 666-669, doi:10.1126/science.1102896 (2004).

17 Choi, W. *et al.* Recent development of two-dimensional transition metal dichalcogenides and their applications. *Materials Today* **20**, 116-130, doi:https://doi.org/10.1016/j.mattod.2016.10.002 (2017).

18 Dean, C. R. *et al.* Boron nitride substrates for high-quality graphene electronics. *Nature Nanotechnology* **5**, 722-726, doi:10.1038/nnano.2010.172 (2010).

19 Kroto, H. W., Heath, J. R., O'Brien, S. C., Curl, R. F. & Smalley, R. E. C60: Buckminsterfullerene. *Nature* **318**, 162-163, doi:10.1038/318162a0 (1985).

20 Iijima, S. Helical microtubules of graphitic carbon. *Nature* **354**, 56-58, doi:10.1038/354056a0 (1991).

21 Brodie, B. C. On the atomic weight of graphite. *Proc. R. Soc. Lond.*, 11-12, doi:https://doi.org/10.1098/rspl.1859.0007 (1860).

22 Wallace, P. R. The Band Theory of Graphite. *Physical Review* **71**, 622-634, doi:10.1103/PhysRev.71.622 (1947).

23 Gall, N. R., Rut'kov, E. V. & Tontegode, A. Y. Two Dimensional Graphite Films on Metals and Their Intercalation. *Int J Mod Phys B* **11**, 1865-1911, doi:10.1142/S0217979297000976 (1997).

24 Landau, L. D. Zur Theorie der phasenumwandlungen II. *Phys. Z. Sowjetunion* **11**, 26-35 (1937).

25 Peierls, R. Some typical properties of solid bodies. *Annales de l'institut Henri Poincaré* **5**, 177-222 (1935).

26 Fasolino, A., Los, J. H. & Katsnelson, M. I. Intrinsic ripples in graphene. *Nature materials* **6**, 858-861, doi:10.1038/nmat2011 (2007).

27 Wang, L. *et al.* One-Dimensional Electrical Contact to a Two-Dimensional Material. *Science* **342**, 614-617, doi:10.1126/science.1244358 (2013).

28 Meyer, J. C. *et al.* Direct Imaging of Lattice Atoms and Topological Defects in Graphene Membranes. *Nano Letters* **8**, 3582-3586, doi:10.1021/nl801386m (2008).

29 Geim, A. K. & Novoselov, K. S. The rise of graphene. *Nature materials* **6**, 183-191, doi:10.1038/nmat1849 (2007).

30 Castro Neto, A. H., Guinea, F., Peres, N. M. R., Novoselov, K. S. & Geim, A. K. The electronic properties of graphene. *Reviews of Modern Physics* **81**, 109-162, doi:10.1103/RevModPhys.81.109 (2009).

31 Roy, S. *et al.* Structure, Properties and Applications of Two-Dimensional Hexagonal Boron Nitride. *Advanced Materials* **33**, 2101589, doi:https://doi.org/10.1002/adma.202101589 (2021).

32 Li, L. H. & Chen, Y. Atomically Thin Boron Nitride: Unique Properties and Applications. *Advanced Functional Materials* **26**, 2594-2608, doi:https://doi.org/10.1002/adfm.201504606 (2016).

33 Cook, M. W. & Bossom, P. K. Trends and recent developments in the material manufacture and cutting tool application of polycrystalline diamond and polycrystalline cubic boron nitride. *International Journal of Refractory Metals and Hard Materials* **18**, 147-152, doi:https://doi.org/10.1016/S0263-4368(00)00015-9 (2000).

34 Engler, M., Lesniak, C., Damasch, R., Ruisinger, B. & Eichler, J. 12 edn (Göller).

35 Novoselov, K. S. *et al.* Two-dimensional atomic crystals. *Proceedings of the National Academy of Sciences* **102**, 10451-10453, doi:10.1073/pnas.0502848102 (2005).

36 Bhimanapati, G. R., Kozuch, D. & Robinson, J. A. Large-scale synthesis and functionalization of hexagonal boron nitride nanosheets. *Nanoscale* **6**, 11671-11675, doi:10.1039/C4NR01816H (2014).

37 Elias, C. *et al.* Direct band-gap crossover in epitaxial monolayer boron nitride. *Nature communications* **10**, 2639, doi:10.1038/s41467-019-10610-5 (2019).

38 Watanabe, K., Taniguchi, T. & Kanda, H. Direct-bandgap properties and evidence for ultraviolet lasing of hexagonal boron nitride single crystal. *Nature materials* **3**, 404-409, doi:10.1038/nmat1134 (2004).

39 Chen, X. *et al.* High-quality sandwiched black phosphorus heterostructure and its quantum oscillations. *Nature communications* **6**, 7315, doi:10.1038/ncomms8315 (2015).

40 Cao, Y. *et al.* Quality Heterostructures from Two-Dimensional Crystals Unstable in Air by Their Assembly in Inert Atmosphere. *Nano Letters* **15**, 4914-4921, doi:10.1021/acs.nanolett.5b00648 (2015).

41 Lee, G.-H. *et al.* Electron tunneling through atomically flat and ultrathin hexagonal boron nitride. *Applied Physics Letters* **99**, 243114, doi:10.1063/1.3662043 (2011).

42 Liu, Y. *et al.* Promises and prospects of two-dimensional transistors. *Nature* **591**, 43-53, doi:10.1038/s41586-021-03339-z (2021).

43 Huo, N. & Konstantatos, G. Recent Progress and Future Prospects of 2D-Based Photodetectors. *Advanced Materials* **30**, 1801164, doi:https://doi.org/10.1002/adma.201801164 (2018).

44 Dickinson, R. G. & Pauling, L. THE CRYSTAL STRUCTURE OF MOLYBDENITE. *Journal of the American Chemical Society* **45**, 1466-1471, doi:10.1021/ja01659a020 (1923).

45 Chhowalla, M. *et al.* The chemistry of two-dimensional layered transition metal dichalcogenide nanosheets. *Nature Chemistry* **5**, 263-275, doi:10.1038/nchem.1589 (2013).

46 Xu, J., Zhang, J., Zhang, W. & Lee, C.-S. Interlayer Nanoarchitectonics of Two-Dimensional Transition-Metal Dichalcogenides Nanosheets for Energy Storage and Conversion Applications. *Advanced Energy Materials* **7**, 1700571, doi:https://doi.org/10.1002/aenm.201700571 (2017).

47 Mak, K. F., Lee, C., Hone, J., Shan, J. & Heinz, T. F. Atomically Thin MoS2: A New Direct-Gap Semiconductor. *Physical Review Letters* **105**, 136805, doi:10.1103/PhysRevLett.105.136805 (2010).

48 Manzeli, S., Ovchinnikov, D., Pasquier, D., Yazyev, O. V. & Kis, A. 2D transition metal dichalcogenides. *Nature Reviews Materials* **2**, 17033, doi:10.1038/natrevmats.2017.33 (2017).

49 Frindt, R. F., Yoffe, A. D. & Bowden, F. P. Physical properties of layer structures : optical properties and photoconductivity of thin crystals of molybdenum disulphide. *Proceedings of the Royal Society of London. Series A. Mathematical and Physical Sciences* **273**, 69-83, doi:10.1098/rspa.1963.0075 (1963).

50 Joensen, P., Frindt, R. F. & Morrison, S. R. Single-layer MoS2. *Materials Research Bulletin* **21**, 457-461, doi:https://doi.org/10.1016/0025-5408(86)90011-5 (1986).

51 Splendiani, A. *et al.* Emerging Photoluminescence in Monolayer MoS2. *Nano Letters* **10**, 1271-1275, doi:10.1021/nl903868w (2010).

52 Mak, K. F. & Shan, J. Photonics and optoelectronics of 2D semiconductor transition metal dichalcogenides. *Nature Photonics* **10**, 216-226, doi:10.1038/nphoton.2015.282 (2016).

53 Baugher, B. W. H., Churchill, H. O. H., Yang, Y. & Jarillo-Herrero, P. Optoelectronic devices based on electrically tunable p–n diodes in a monolayer dichalcogenide. *Nature Nanotechnology* **9**, 262-267, doi:10.1038/nnano.2014.25 (2014).

54 Schmidt, H., Giustiniano, F. & Eda, G. Electronic transport properties of transition metal dichalcogenide field-effect devices: surface and interface effects. *Chemical Society reviews* **44**, 7715-7736, doi:10.1039/C5CS00275C (2015).

55 Lin, L., Peng, H. & Liu, Z. Synthesis challenges for graphene industry. *Nature materials* **18**, 520-524, doi:10.1038/s41563-019-0341-4 (2019).

56 Wang, X.-Y., Narita, A. & Müllen, K. Precision synthesis versus bulk-scale fabrication of graphenes. *Nature Reviews Chemistry* **2**, 0100, doi:10.1038/s41570-017-0100 (2017).

57 Sun, L. *et al.* Chemical vapour deposition. *Nature Reviews Methods Primers* **1**, 5, doi:10.1038/s43586-020-00005-y (2021).

58 Koh, A. T. T., Foong, Y. M. & Chua, D. H. C. Cooling rate and energy dependence of pulsed laser fabricated graphene on nickel at reduced temperature. *Applied Physics Letters* **97**, 114102, doi:10.1063/1.3489993 (2010).

59 Li, H. *et al.* Mechanical Exfoliation and Characterization of Single- and Few-Layer Nanosheets of WSe2, TaS2, and TaSe2. *Small* **9**, 1974-1981, doi:https://doi.org/10.1002/smll.201202919 (2013).

60 Naguib, M. *et al.* Two-Dimensional Nanocrystals Produced by Exfoliation of Ti3AlC2. *Advanced Materials* **23**, 4248-4253, doi:https://doi.org/10.1002/adma.201102306 (2011).

61 Hernandez, Y. *et al.* High-yield production of graphene by liquid-phase exfoliation of graphite. *Nature Nanotechnology* **3**, 563-568, doi:10.1038/nnano.2008.215 (2008).

62 Zhang, Y., Zhang, L. & Zhou, C. Review of Chemical Vapor Deposition of Graphene and Related Applications. *Accounts of Chemical Research* **46**, 2329-2339, doi:10.1021/ar300203n (2013).

63 Gutiérrez, H. R. *et al.* Extraordinary Room-Temperature Photoluminescence in Triangular WS2 Monolayers. *Nano Letters* **13**, 3447-3454, doi:10.1021/nl3026357 (2013).

64 Liu, B. *et al.* Chemical Vapor Deposition Growth of Monolayer WSe2 with Tunable Device Characteristics and Growth Mechanism Study. *ACS Nano* **9**, 6119-6127, doi:10.1021/acsnano.5b01301 (2015).

65 Karfa, P., Chandra Majhi, K. & Madhuri, R. in *Two-Dimensional Nanostructures for Biomedical Technology* (eds Raju Khan & Shaswat Barua) 35-71 (Elsevier, 2020).

66 Yi, M. & Shen, Z. A review on mechanical exfoliation for the scalable production of graphene. *Journal of Materials Chemistry A* **3**, 11700-11715, doi:10.1039/C5TA00252D (2015).

67 Backes, C. *et al.* Spectroscopic metrics allow in situ measurement of mean size and thickness of liquid-exfoliated few-layer graphene nanosheets. *Nanoscale* **8**, 4311-4323, doi:10.1039/c5nr08047a (2016).

68 Lin, Z. *et al.* Solution-processable 2D semiconductors for high-performance large-area electronics. *Nature* **562**, 254-258, doi:10.1038/s41586-018-0574-4 (2018).

69 Torrisi, F. *et al.* Inkjet-Printed Graphene Electronics. *ACS Nano* **6**, 2992-3006, doi:10.1021/nn2044609 (2012).

70 Carey, T., Jones, C., Le Moal, F., Deganello, D. & Torrisi, F. Spray-Coating Thin Films on Three-Dimensional Surfaces for a Semitransparent Capacitive-Touch Device. *ACS applied materials & interfaces* **10**, 19948-19956, doi:10.1021/acsami.8b02784 (2018).

71 Kim, H., Miura, Y. & Macosko, C. W. Graphene/Polyurethane Nanocomposites for Improved Gas Barrier and Electrical Conductivity. *Chemistry of Materials* **22**, 3441-3450, doi:10.1021/cm100477v (2010).

72 Butler, S. Z. *et al.* Progress, Challenges, and Opportunities in Two-Dimensional Materials Beyond Graphene. *ACS Nano* **7**, 2898-2926, doi:10.1021/nn400280c (2013).

73 Hummers, W. S. & Offeman, R. E. Preparation of Graphitic Oxide. *Journal of the American Chemical Society* **80**, 1339-1339, doi:10.1021/ja01539a017 (1958).

74 Dreyer, D. R., Park, S., Bielawski, C. W. & Ruoff, R. S. The chemistry of graphene oxide. *Chemical Society reviews* **39**, 228-240, doi:10.1039/B917103G (2010).

75 Eda, G. & Chhowalla, M. Chemically Derived Graphene Oxide: Towards Large-Area Thin-Film Electronics and Optoelectronics. *Advanced Materials* **22**, 2392-2415, doi:https://doi.org/10.1002/adma.200903689 (2010).

76 Eng, A. Y. S., Ambrosi, A., Sofer, Z., Šimek, P. & Pumera, M. Electrochemistry of Transition Metal Dichalcogenides: Strong Dependence on the Metal-to-Chalcogen Composition and Exfoliation Method. *ACS Nano* **8**, 12185-12198, doi:10.1021/nn503832j (2014).

77 Ryder, C. R. *et al.* Covalent functionalization and passivation of exfoliated black phosphorus via aryl diazonium chemistry. *Nature Chemistry* **8**, 597-602, doi:10.1038/nchem.2505 (2016).

78 Ida, S., Shiga, D., Koinuma, M. & Matsumoto, Y. Synthesis of Hexagonal Nickel Hydroxide Nanosheets by Exfoliation of Layered Nickel Hydroxide Intercalated with Dodecyl Sulfate Ions. *Journal of the American Chemical Society* **130**, 14038-14039, doi:10.1021/ja804397n (2008).

79 Ding, Z. *et al.* Lithium intercalation and exfoliation of layered bismuth selenide and bismuth telluride. *Journal of Materials Chemistry* **19**, 2588-2592, doi:10.1039/B820226E (2009).

80 Naguib, M., Mochalin, V. N., Barsoum, M. W. & Gogotsi, Y. 25th Anniversary Article: MXenes: A New Family of Two-Dimensional Materials. *Advanced Materials* **26**, 992-1005, doi:https://doi.org/10.1002/adma.201304138 (2014).

81 Zhang, C. *et al.* Transparent, Flexible, and Conductive 2D Titanium Carbide (MXene) Films with High Volumetric Capacitance. *Advanced Materials* **29**, 1702678, doi:https://doi.org/10.1002/adma.201702678 (2017).

82 Coleman, J. N. Liquid Exfoliation of Defect-Free Graphene. *Accounts of Chemical Research* **46**, 14-22, doi:10.1021/ar300009f (2013).

83 Kaur, H. & Coleman, J. N. Liquid-phase Exfoliation of Nonlayered non-van der Waals Crystals into Nanoplatelets. *Advanced Materials* **n/a**, 2202164, doi:https://doi.org/10.1002/adma.202202164 (2022).

84 Wang, Y. *et al.* Directly Exfoliated Ultrathin Silicon Nanosheets for Enhanced Photocatalytic Hydrogen Production. *The Journal of Physical Chemistry Letters* **11**, 8668-8674, doi:10.1021/acs.jpclett.0c02049 (2020).

85 Lotya, M. *et al.* Liquid Phase Production of Graphene by Exfoliation of Graphite in Surfactant/Water Solutions. *Journal of the American Chemical Society* **131**, 3611-3620, doi:10.1021/ja807449u (2009).

86 Smith, R. J. *et al.* Large-Scale Exfoliation of Inorganic Layered Compounds in Aqueous Surfactant Solutions. *Advanced Materials* **23**, 3944-3948, doi:https://doi.org/10.1002/adma.201102584 (2011).

87 Backes, C. *et al.* Edge and confinement effects allow in situ measurement of size and thickness of liquid-exfoliated nanosheets. *Nature communications* **5**, 4576, doi:10.1038/ncomms5576 (2014).

88 Kelly, A. G., O'Suilleabhain, D., Gabbett, C. & Coleman, J. N. The electrical conductivity of solution-processed nanosheet networks. *Nature Reviews Materials*, doi:10.1038/s41578-021-00386-w (2021).

89 Caffrey, E. *et al.* Quantifying the Piezoresistive Mechanism in High-Performance Printed Graphene Strain Sensors. *ACS applied materials & interfaces* **14**, 7141-7151, doi:10.1021/acsami.1c21623 (2022).

90 Kouroupis-Agalou, K. *et al.* Fragmentation and exfoliation of 2-dimensional materials: a statistical approach. *Nanoscale* **6**, 5926-5933, doi:10.1039/C3NR06919B (2014).

91 Li, Z. *et al.* Mechanisms of Liquid-Phase Exfoliation for the Production of Graphene. *ACS Nano* **14**, 10976-10985, doi:10.1021/acsnano.0c03916 (2020).

92 Khan, U., O'Neill, A., Lotya, M., De, S. & Coleman, J. N. High-Concentration Solvent Exfoliation of Graphene. *Small* **6**, 864-871, doi:https://doi.org/10.1002/smll.200902066 (2010).

93 Backes, C. *et al.* Guidelines for Exfoliation, Characterization and Processing of Layered Materials Produced by Liquid Exfoliation. *Chemistry of Materials* **29**, 243-255, doi:10.1021/acs.chemmater.6b03335 (2017).

94 Liu, C.-X. & Choi, J.-W. Improved Dispersion of Carbon Nanotubes in Polymers at High Concentrations. *Nanomaterials* **2**, doi:10.3390/nano2040329 (2012).

95 Cunningham, G. *et al.* Solvent Exfoliation of Transition Metal Dichalcogenides: Dispersibility of Exfoliated Nanosheets Varies Only Weakly between Compounds. *ACS Nano* **6**, 3468-3480, doi:10.1021/nn300503e (2012).

96 May, P., Khan, U., Hughes, J. M. & Coleman, J. N. Role of Solubility Parameters in Understanding the Steric Stabilization of Exfoliated Two-Dimensional Nanosheets by Adsorbed Polymers. *The Journal of Physical Chemistry C* **116**, 11393-11400, doi:10.1021/jp302365w (2012).

97 Hernandez, Y., Lotya, M., Rickard, D., Bergin, S. D. & Coleman, J. N. Measurement of Multicomponent Solubility Parameters for Graphene Facilitates Solvent Discovery. *Langmuir* **26**, 3208-3213, doi:10.1021/la903188a (2010).

98 Coleman, J. N. Liquid-Phase Exfoliation of Nanotubes and Graphene. *Advanced Functional Materials* **19**, 3680-3695, doi:https://doi.org/10.1002/adfm.200901640 (2009).

99 Bergin, S. D. *et al.* Towards Solutions of Single-Walled Carbon Nanotubes in Common Solvents. *Advanced Materials* **20**, 1876-1881, doi:https://doi.org/10.1002/adma.200702451 (2008).

100 Gupta, A. & Vasudevan, S. Understanding Surfactant Stabilization of MoS2 Nanosheets in Aqueous Dispersions from Zeta Potential Measurements and Molecular Dynamics Simulations. *The Journal of Physical Chemistry C* **122**, 19243-19250, doi:10.1021/acs.jpcc.8b05922 (2018).

101 Furtado, C. A. *et al.* Debundling and Dissolution of Single-Walled Carbon Nanotubes in Amide Solvents. *Journal of the American Chemical Society* **126**, 6095-6105, doi:10.1021/ja039588a (2004).

102 Rubinstein, M. & Colby, R. H. *Polymer Physics*. (Oxford University Press, 2003).

103 Hansen, C. M. Hansen Solubility Parameters: A User's Handbook, Second Edition. *CRC Press* (2007).

104 Joel Henry Hildebrand, J. M. P., Robert Lane Scott. *Regular and Related Solutions: The Solubility of Gases, Liquids, and Solids*. (Van Nostrand Reinhold Company, 1970).

105 Derjaguin, B. & Landau, L. Theory of the stability of strongly charged lyophobic sols and of the adhesion of strongly charged particles in solutions of electrolytes. *Progress in Surface Science* **43**, 30-59, doi:https://doi.org/10.1016/0079-6816(93)90013-L (1993).

106 Evert Johannes Willem Verwey, J. T. G. O., K. van Nes. *Theory of the Stability of Lyophobic Colloids: The Interaction of Sol Particles Having an Electric Double Layer*. (Elsevier Publishing Company, 1948).

107 Sargam, Y., Wang, K., Tsyrenova, A., Liu, F. & Jiang, S. Effects of anionic and nonionic surfactants on the dispersion and stability of nanoSiO2 in aqueous and cement pore solutions. *Cement and Concrete Research* **144**, 106417, doi:https://doi.org/10.1016/j.cemconres.2021.106417 (2021).

108 Kang, J. *et al.* Thickness sorting of two-dimensional transition metal dichalcogenides via copolymer-assisted density gradient ultracentrifugation. *Nature communications* **5**, 5478, doi:10.1038/ncomms6478 (2014).

109 Backes, C. *et al.* Production of Highly Monolayer Enriched Dispersions of Liquid-Exfoliated Nanosheets by Liquid Cascade Centrifugation. *ACS Nano* **10**, 1589-1601, doi:10.1021/acsnano.5b07228 (2016).

110 Backes, C. *et al.* Equipartition of Energy Defines the Size–Thickness Relationship in Liquid-Exfoliated Nanosheets. *ACS Nano* **13**, 7050-7061, doi:10.1021/acsnano.9b02234 (2019).

111 Novoselov, K. S., Mishchenko, A., Carvalho, A. & Castro Neto, A. H. 2D materials and van der Waals heterostructures. *Science* **353**, aac9439, doi:10.1126/science.aac9439 (2016).

112 Yan, W. *et al.* Giant gauge factor of Van der Waals material based strain sensors. *Nature communications* **12**, 2018, doi:10.1038/s41467-021-22316-8 (2021).

113 Georgiou, T. *et al.* Vertical field-effect transistor based on graphene–WS2 heterostructures for flexible and transparent electronics. *Nature Nanotechnology* **8**, 100-103, doi:10.1038/nnano.2012.224 (2013).

114 Britnell, L. *et al.* Strong Light-Matter Interactions in Heterostructures of Atomically Thin Films. *Science* **340**, 1311-1314, doi:10.1126/science.1235547 (2013).

115 Walsh, L. A. & Hinkle, C. L. van der Waals epitaxy: 2D materials and topological insulators. *Applied Materials Today* **9**, 504-515, doi:https://doi.org/10.1016/j.apmt.2017.09.010 (2017).

116 Choi, H. K. *et al.* Hierarchical Porous Film with Layer-by-Layer Assembly of 2D Copper Nanosheets for Ultimate Electromagnetic Interference Shielding. *ACS Nano* **15**, 829-839, doi:10.1021/acsnano.0c07352 (2021).

117 Lin, Z., Huang, Y. & Duan, X. Van der Waals thin-film electronics. *Nature Electronics* **2**, 378-388, doi:10.1038/s41928-019-0301-7 (2019).

118 Zhan, C. *et al.* Conductive polymer nanocomposites: a critical review of modern advanced devices. *Journal of Materials Chemistry C* **5**, 1569-1585, doi:10.1039/C6TC04269D (2017).

119 Chee, W. K., Lim, H. N., Huang, N. M. & Harrison, I. Nanocomposites of graphene/polymers: a review. *RSC Advances* **5**, 68014-68051, doi:10.1039/C5RA07989F (2015).

120 Torrisi, F. & Coleman, J. N. Electrifying inks with 2D materials. *Nature Nanotechnology* **9**, 738-739, doi:10.1038/nnano.2014.218 (2014).

121 Yang, Y. *et al.* Size Dependence of Dielectric Constant in a Single Pencil-Like ZnO Nanowire. *Nano Letters* **12**, 1919-1922, doi:10.1021/nl204353t (2012).

122 Marsden, A. J. *et al.* Electrical percolation in graphene–polymer composites. *2D Materials* **5**, 032003, doi:10.1088/2053-1583/aac055 (2018).

123 Bellew, A. T., Manning, H. G., Gomes da Rocha, C., Ferreira, M. S. & Boland, J. J. Resistance of Single Ag Nanowire Junctions and Their Role in the Conductivity of Nanowire Networks. *ACS Nano* **9**, 11422-11429, doi:10.1021/acsnano.5b05469 (2015).

124 Lin, Z. *et al.* Solution Processable Colloidal Nanoplates as Building Blocks for High-Performance Electronic Thin Films on Flexible Substrates. *Nano Letters* **14**, 6547-6553, doi:10.1021/nl503140c (2014).

125 Šuvakov, M. & Tadić, B. Modeling collective charge transport in nanoparticle assemblies. *Journal of Physics: Condensed Matter* **22**, 163201, doi:10.1088/0953-8984/22/16/163201 (2010).

126 Large, M. J. *et al.* Large-Scale Surfactant Exfoliation of Graphene and Conductivity-Optimized Graphite Enabling Wireless Connectivity. *Adv Mater Technol-Us* **5**, 2000284, doi:https://doi.org/10.1002/admt.202000284 (2020).

127 Berryman, J. G. Random close packing of hard spheres and disks. *Physical Review A* **27**, 1053-1061, doi:10.1103/PhysRevA.27.1053 (1983).

128 Chaikin, P. M., Donev, A., Man, W., Stillinger, F. H. & Torquato, S. Some Observations on the Random Packing of Hard Ellipsoids. *Industrial & Engineering Chemistry Research* **45**, 6960-6965, doi:10.1021/ie060032g (2006).

129 Delaney, G. W., Hilton, J. E. & Cleary, P. W. Defining random loose packing for nonspherical grains. *Phys. Rev. E* **83**, 051305, doi:10.1103/PhysRevE.83.051305 (2011).

130 Kelly, A. G. *et al.* Highly Conductive Networks of Silver Nanosheets. *Small* **n/a**, 2105996, doi:https://doi.org/10.1002/smll.202105996 (2022).

131 Cunningham, G. *et al.* Percolation scaling in composites of exfoliated MoS2 filled with nanotubes and graphene. *Nanoscale* **4**, 6260-6264, doi:10.1039/C2NR31782F (2012).

132 Barwich, S. *et al.* On the relationship between morphology and conductivity in nanosheet networks. *Carbon* **171**, 306-319, doi:10.1016/j.carbon.2020.09.015 (2021).

133 White, S. I., DiDonna, B. A., Mu, M. F., Lubensky, T. C. & Winey, K. I. Simulations and electrical conductivity of percolated networks of finite rods with various degrees of axial alignment. *Phys Rev B* **79**, 024301, doi:10.1103/PhysRevB.79.024301 (2009).

134 Du, F., Fischer, J. E. & Winey, K. I. Effect of nanotube alignment on percolation conductivity in carbon nanotube/polymer composites. *Physical Review B - Condensed Matter and Materials Physics* **72**, 121404, doi:10.1103/PhysRevB.72.121404 (2005).

135 Li, C. & Chou, T.-W. Electrical conductivities of composites with aligned carbon nanotubes. *Journal of nanoscience and nanotechnology* **9**, 2518-2524 (2009).

136 Hull, D. & Clyne, T. W. in *An Introduction to Composite Materials Cambridge Solid State Science Series* (eds D. Hull & T. W. Clyne) 9-38 (Cambridge University Press, 1996).

137 Karsli, N. G., Aytac, A. & Deniz, V. Effects of initial fiber length and fiber length distribution on the properties of carbon-fiber-reinforced-polypropylene composites. *Journal of Reinforced Plastics and Composites* **31**, 1053-1060, doi:10.1177/0731684412452678 (2012).

138 Suter, J. L., Groen, D. & Coveney, P. V. Chemically Specific Multiscale Modeling of Clay–Polymer Nanocomposites Reveals Intercalation Dynamics, Tactoid Self-Assembly and Emergent Materials Properties. *Advanced Materials* **27**, 966-984, doi:https://doi.org/10.1002/adma.201403361 (2015).

139 Beaumont, P. 50 Years of Carbon Fibre. *Applied Composite Materials* **24**, 271-275, doi:10.1007/s10443-017-9586-8 (2017).

140 Papageorgiou, D. G., Kinloch, I. A. & Young, R. J. Mechanical properties of graphene and graphene-based nanocomposites. *Progress in Materials Science* **90**, 75-127, doi:https://doi.org/10.1016/j.pmatsci.2017.07.004 (2017).

141 Lee, C., Wei, X., Kysar Jeffrey, W. & Hone, J. Measurement of the Elastic Properties and Intrinsic Strength of Monolayer Graphene. *Science* **321**, 385-388, doi:10.1126/science.1157996 (2008).

142 Stankovich, S. *et al.* Graphene-based composite materials. *Nature* **442**, 282-286, doi:10.1038/nature04969 (2006).

143 Young, R. J. & Lovell, P. A. *Introduction to polymers.* (CRC press, 2011).

144 Biccai, S. *et al.* Negative Gauge Factor Piezoresistive Composites Based on Polymers Filled with MoS2 Nanosheets. *Acs Nano* **13**, 6845-6855, doi:10.1021/acsnano.9b01613 (2019).

145 Young, R. J. *et al.* The mechanics of reinforcement of polymers by graphene nanoplatelets. *Composites Science and Technology* **154**, 110-116, doi:https://doi.org/10.1016/j.compscitech.2017.11.007 (2018).

146 Li, Z. *et al.* Effect of the orientation of graphene-based nanoplatelets upon the Young's modulus of nanocomposites. *Composites Science and Technology* **123**, 125-133, doi:https://doi.org/10.1016/j.compscitech.2015.12.005 (2016).

147 Young, R. J., Kinloch, I. A., Gong, L. & Novoselov, K. S. The mechanics of graphene nanocomposites: A review. *Composites Science and Technology* **72**, 1459-1476, doi:https://doi.org/10.1016/j.compscitech.2012.05.005 (2012).

148 Papageorgiou, D. G., Tzounis, L., Papageorgiou, G. Z., Bikiaris, D. N. & Chrissafis, K. β -nucleated propylene–ethylene random copolymer filled with multi-walled carbon nanotubes: Mechanical, thermal and rheological properties. *Polymer* **55**, 3758-3769, doi:https://doi.org/10.1016/j.polymer.2014.06.012 (2014).

149 Jan, R. *et al.* Flexible, thin films of graphene–polymer composites for EMI shielding. *Materials Research Express* **4**, 035605, doi:10.1088/2053-1591/aa6351 (2017).

150 Peng, S., Yu, Y., Wu, S. & Wang, C.-H. Conductive Polymer Nanocomposites for Stretchable Electronics: Material Selection, Design, and Applications. *ACS applied materials & interfaces* **13**, 43831-43854, doi:10.1021/acsami.1c15014 (2021).

151 Kim, J., Yim, B.-s., Kim, J.-m. & Kim, J. The effects of functionalized graphene nanosheets on the thermal and mechanical properties of epoxy composites for

anisotropic conductive adhesives (ACAs). *Microelectronics Reliability* **52**, 595-602, doi:https://doi.org/10.1016/j.microrel.2011.11.002 (2012).

152 Schopp, S. *et al.* Functionalized Graphene and Carbon Materials as Components of Styrene-Butadiene Rubber Nanocomposites Prepared by Aqueous Dispersion Blending. *Macromolecular Materials and Engineering* **299**, 319-329, doi:https://doi.org/10.1002/mame.201300127 (2014).

153 Kinloch Ian, A., Suhr, J., Lou, J., Young Robert, J. & Ajayan Pulickel, M. Composites with carbon nanotubes and graphene: An outlook. *Science* **362**, 547-553, doi:10.1126/science.aat7439 (2018).

154 Trionfi, A. *et al.* Direct imaging of current paths in multiwalled carbon nanofiber polymer nanocomposites using conducting-tip atomic force microscopy. *J Appl Phys* **104**, 083708, doi:10.1063/1.3000458 (2008).

155 Manta, A., Gresil, M. & Soutis, C. Predictive Model of Graphene Based Polymer Nanocomposites: Electrical Performance. *Applied Composite Materials* **24**, 281-300, doi:10.1007/s10443-016-9557-5 (2017).

156 Hicks, J., Behnam, A. & Ural, A. A computational study of tunneling-percolation electrical transport in graphene-based nanocomposites. *Applied Physics Letters* **95**, 213103, doi:10.1063/1.3267079 (2009).

157 Dong, S., Chen, S., Li, B. & Wang, X. Electrical properties of anisotropic graphene/PDMS composites induced by aligned ferromagnetic particles. *Journal of Intelligent Material Systems and Structures* **32**, 1377-1385, doi:10.1177/1045389X20969864 (2020).

158 Wu, S. *et al.* Aligning multilayer graphene flakes with an external electric field to improve multifunctional properties of epoxy nanocomposites. *Carbon* **94**, 607-618, doi:https://doi.org/10.1016/j.carbon.2015.07.026 (2015).

159 Stauffer, D. Scaling theory of percolation clusters. *Physics Reports* **54**, 1-74, doi:https://doi.org/10.1016/0370-1573(79)90060-7 (1979).

160 Flory, P. J. Molecular Size Distribution in Three Dimensional Polymers. I. Gelation1. *Journal of the American Chemical Society* **63**, 3083-3090, doi:10.1021/ja01856a061 (1941).

161 Stauffer, D. & Aharony, A. *Introduction to percolation theory.* (Taylor & Francis, 1992).

162 Kusy, R. P. & Turner, D. T. Electrical Resistivity of a Polymeric Insulator containing Segregated Metallic Particles. *Nature Physical Science* **229**, 58-59, doi:10.1038/physci229058a0 (1971).

163 Kirkpatrick, S. Percolation and Conduction. *Reviews of Modern Physics* **45**, 574-588, doi:10.1103/RevModPhys.45.574 (1973).

164 Kogut, P. M. & Straley, J. P. Distribution-induced non-universality of the percolation conductivity exponents. *Journal of Physics C: Solid State Physics* **12**, 2151-2159, doi:10.1088/0022-3719/12/11/023 (1979).

165 Straley, J. P. Critical phenomena in resistor networks. *Journal of Physics C: Solid State Physics* **9**, 783-795, doi:10.1088/0022-3719/9/5/017 (1976).

166 Balberg, I., Azulay, D., Goldstein, Y. & Jedrzejewski, J. Possible origin of the smaller-than-universal percolation-conductivity exponent in the continuum. *Phys. Rev. E* **93**, 062132, doi:10.1103/PhysRevE.93.062132 (2016).

167 Johner, N., Grimaldi, C., Balberg, I. & Ryser, P. Transport exponent in a three-dimensional continuum tunneling-percolation model. *Phys Rev B* **77**, 174204, doi:10.1103/PhysRevB.77.174204 (2008).

168 Balberg, I., Azulay, D., Toker, D. & Millo, O. Percolation and tunneling in composite materials. *Int J Mod Phys B* **18**, 2091-2121, doi:Doi 10.1142/S0217979204025336 (2004).

169 Vionnet-Menot, S., Grimaldi, C., Maeder, T., Strassler, S. & Ryser, P. Tunneling-percolation origin of nonuniversality: Theory and experiments. *Phys Rev B* **71**, 064201, doi:10.1103/PhysRevB.71.064201 (2005).

170 Garboczi, E. J., Snyder, K. A., Douglas, J. F. & Thorpe, M. F. Geometrical percolation threshold of overlapping ellipsoids. *Phys. Rev. E* **52**, 819-828, doi:10.1103/PhysRevE.52.819 (1995).

171 Hernandez, Y. R. *et al.* Comparison of carbon nanotubes and nanodisks as percolative fillers in electrically conductive composites. *Scripta Materialia* **58**, 69-72, doi:https://doi.org/10.1016/j.scriptamat.2007.08.025 (2008).

172 Ma, P.-C. *et al.* Enhanced Electrical Conductivity of Nanocomposites Containing Hybrid Fillers of Carbon Nanotubes and Carbon Black. *ACS applied materials & interfaces* **1**, 1090-1096, doi:10.1021/am9000503 (2009).

173 Strelniker, Y. M., Havlin, S. & Bunde, A. in *Encyclopedia of Complexity and Systems Science* (ed Robert A. Meyers) 3847-3858 (Springer New York, 2009).

174 Balberg, I., Binenbaum, N. & Wagner, N. Percolation Thresholds in the Three-Dimensional Sticks System. *Physical Review Letters* **52**, 1465-1468, doi:10.1103/PhysRevLett.52.1465 (1984).

175 Kale, S., Sabet, F. A., Jasiuk, I. & Ostoja-Starzewski, M. Effect of filler alignment on percolation in polymer nanocomposites using tunneling-percolation model. *J Appl Phys* **120**, 045105, doi:10.1063/1.4959610 (2016).

176 O'Suilleabhain, D., Vega-Mayoral, V., Kelly, A. G., Harvey, A. & Coleman, J. N. Percolation Effects in Electrolytically Gated WS2/Graphene Nano:Nano Composites. *ACS applied materials & interfaces* **11**, 8545-8555, doi:10.1021/acsami.8b21416 (2019).

177 O'Driscoll, D. P. *et al.* Printable G-putty for Frequency and Rate Independent, High Performance Strain Sensors *Small* **submitted** (2020).

178 Drozdov, A. D. & de Claville Christiansen, J. Modeling electrical conductivity of polymer nanocomposites with aggregated filler. *Polymer Engineering & Science* **60**, 1556-1565, doi:https://doi.org/10.1002/pen.25401 (2020).

179 Hu, N. *et al.* The electrical properties of polymer nanocomposites with carbon nanotube fillers. *Nanotechnology* **19**, 215701, doi:10.1088/0957-4484/19/21/215701 (2008).

180 Liu, J. *et al.* Visualized simulation for the nanostructure design of flexible strain sensors: from a numerical model to experimental verification. *Materials Horizons* **6**, 1892-1898, doi:10.1039/C9MH00389D (2019).

181 Hu, H., Ma, Y., Yue, J. & Zhang, F. Porous GNP/PDMS composites with significantly reduced percolation threshold of conductive filler for stretchable strain sensors. *Composites Communications* **29**, 101033 (2022).

182 Shi, Z.-c. *et al.* Ultra low percolation threshold and significantly enhanced permittivity in porous metal–ceramic composites. *Journal of Materials Chemistry C* **2**, 6752-6757 (2014).

183 Kelly, A. G., Vega-Mayoral, V., Boland, J. B. & Coleman, J. N. Whiskey-phase exfoliation: exfoliation and printing of nanosheets using Irish whiskey. *2D Materials* **6**, 045036, doi:10.1088/2053-1583/ab3892 (2019).

184 Boland, C. S. *et al.* Sensitive, high-strain, high-rate bodily motion sensors based on graphene-rubber composites. *ACS Nano* **8**, 8819-8830, doi:10.1021/nn503454h (2014).

185 Gou, J., Zhuge, J. & Liang, F. in *Manufacturing Techniques for Polymer Matrix Composites (PMCs)* (eds Suresh G. Advani & Kuang-Ting Hsiao) 95-119 (Woodhead Publishing, 2012).

186 Gao, F. Clay/polymer composites: the story. *Materials Today* **7**, 50-55, doi:https://doi.org/10.1016/S1369-7021(04)00509-7 (2004).

187 Armstrong, G. An introduction to polymer nanocomposites. *European Journal of Physics* **36**, 063001, doi:10.1088/0143-0807/36/6/063001 (2015).

188 Avila-Orta, C. *et al.* (2019).

189 Kim, H. *et al.* Graphene/polyethylene nanocomposites: Effect of polyethylene functionalization and blending methods. *Polymer* **52**, 1837-1846, doi:https://doi.org/10.1016/j.polymer.2011.02.017 (2011).

190 Melly, S. K., Liu, L., Liu, Y. & Leng, J. Active composites based on shape memory polymers: overview, fabrication methods, applications, and future prospects. *Journal of Materials Science* **55**, 10975-11051, doi:10.1007/s10853-020-04761-w (2020).

191 Wang, B., Lee, B. K., Kwak, M. J. & Lee, D. W. Graphene/polydimethylsiloxane nanocomposite strain sensor. *Review of Scientific Instruments* **84**, 105005-105005, doi:10.1063/1.4826496 (2013).

192 Liu, Z. & Zhang, Y. Enhanced mechanical and thermal properties of SBR composites by introducing graphene oxide nanosheets decorated with silica particles. *Composites Part A: Applied Science and Manufacturing* **102**, 236-242, doi:https://doi.org/10.1016/j.compositesa.2017.08.005 (2017).

193 Hu, G. *et al.* Functional inks and printing of two-dimensional materials. *Chemical Society reviews* **47**, 3265-3300, doi:10.1039/C8CS00084K (2018).

194 He, P. *et al.* Screen-Printing of a Highly Conductive Graphene Ink for Flexible Printed Electronics. *ACS applied materials & interfaces* **11**, 32225-32234, doi:10.1021/acsami.9b04589 (2019).

195 Wan, Y.-J. *et al.* Recent advances in polymer-based electronic packaging materials. *Composites Communications* **19**, 154-167, doi:https://doi.org/10.1016/j.coco.2020.03.011 (2020).

196 Sass, R. 153-167 (2013).

197 Quemada, D. Rheology of concentrated disperse systems and minimum energy dissipation principle. *Rheologica Acta* **16**, 82-94 (1977).

198 Batchelor, G. K. The effect of Brownian motion on the bulk stress in a suspension of spherical particles. *Journal of Fluid Mechanics* **83**, 97-117, doi:10.1017/S0022112077001062 (1977).

199 Krieger, I. M. & Dougherty, T. J. A mechanism for non - Newtonian flow in suspensions of rigid spheres. *Transactions of the Society of Rheology* **3**, 137-152 (1959).

200 Choi, G. N. & Krieger, I. M. Rheological studies on sterically stabilized model dispersions of uniform colloidal spheres: II. Steady-shear viscosity. *Journal of Colloid and Interface Science* **113**, 101-113, doi:https://doi.org/10.1016/0021-9797(86)90210-9 (1986).

201 Arapov, K. *et al.* Conductive Screen Printing Inks by Gelation of Graphene Dispersions. *Advanced Functional Materials* **26**, 586-593, doi:https://doi.org/10.1002/adfm.201504030 (2016).

202 Zhang, D. W. *et al.* Graphene-based counter electrode for dye-sensitized solar cells. *Carbon* **49**, 5382-5388, doi:https://doi.org/10.1016/j.carbon.2011.08.005 (2011).

203 Senthil Kumar, K., Chen, P.-Y. & Ren, H. A Review of Printable Flexible and Stretchable Tactile Sensors. *Research* **2019**, 3018568, doi:10.34133/2019/3018568 (2019).

204 Gould, R. F. in *Contact Angle, Wettability, and Adhesion* Vol. 43 *Advances in Chemistry* (ed F. Gould Robert) i-iii (AMERICAN CHEMICAL SOCIETY, 1964).

205 Ye, S., Rathmell, A. R., Chen, Z., Stewart, I. E. & Wiley, B. J. Metal Nanowire Networks: The Next Generation of Transparent Conductors. *Advanced Materials* **26**, 6670-6687, doi:https://doi.org/10.1002/adma.201402710 (2014).

206 Gao, X., Bian, G. & Zhu, J. Electronics from solution-processed 2D semiconductors. *Journal of Materials Chemistry C* **7**, 12835-12861, doi:10.1039/C9TC03935J (2019).

207 Ricciardulli, A. G. & Blom, P. W. M. Solution-Processable 2D Materials Applied in Light-Emitting Diodes and Solar Cells. *Adv Mater Technol-Us* **5**, 1900972, doi:https://doi.org/10.1002/admt.201900972 (2020).

208 Abdolhosseinzadeh, S., Jiang, X., Zhang, H., Qiu, J. & Zhang, C. Perspectives on solution processing of two-dimensional MXenes. *Materials Today* **48**, 214-240, doi:https://doi.org/10.1016/j.mattod.2021.02.010 (2021).

209 Shi, H. & Kleinstreuer, C. Simulation and Analysis of High-Speed Droplet Spray Dynamics. *Journal of Fluids Engineering* **129**, 621-633, doi:10.1115/1.2717621 (2006).

210 Scardaci, V., Coull, R., Lyons, P. E., Rickard, D. & Coleman, J. N. Spray Deposition of Highly Transparent, Low-Resistance Networks of Silver Nanowires over Large Areas. *Small* **7**, 2621-2628, doi:https://doi.org/10.1002/smll.201100647 (2011).

211 Zheng, Y., Li, S., Shi, W. & Yu, J. Spray-coated nanoscale conductive patterns based on in situ sintered silver nanoparticle inks. *Nanoscale Research Letters* **9**, 145, doi:10.1186/1556-276X-9-145 (2014).

212 Secor, E. B. Principles of aerosol jet printing. *Flexible and Printed Electronics* **3**, 035002, doi:10.1088/2058-8585/aace28 (2018).

213 Huang, Q. & Zhu, Y. Printing Conductive Nanomaterials for Flexible and Stretchable Electronics: A Review of Materials, Processes, and Applications. *Adv Mater Technol-Us* **4**, 1800546, doi:https://doi.org/10.1002/admt.201800546 (2019).

214 Rodes, C., Smith, T., Crouse, R. & Ramachandran, G. Measurements of the Size Distribution of Aerosols Produced by Ultrasonic Humidification. *Aerosol Science and Technology* **13**, 220-229, doi:10.1080/02786829008959440 (1990).

215 Mahajan, A., Frisbie, C. D. & Francis, L. F. Optimization of Aerosol Jet Printing for High-Resolution, High-Aspect Ratio Silver Lines. *ACS applied materials & interfaces* **5**, 4856-4864, doi:10.1021/am400606y (2013).

216 Smith, M., Choi, Y. S., Boughey, C. & Kar-Narayan, S. Controlling and assessing the quality of aerosol jet printed features for large area and flexible electronics. *Flexible and Printed Electronics* **2**, 015004, doi:10.1088/2058-8585/aa5af9 (2017).

217 Window, A. L. *Strain gauge technology*. 4 (Springer, 1992).

218 Souri, H. *et al.* Wearable and Stretchable Strain Sensors: Materials, Sensing Mechanisms, and Applications. *Advanced Intelligent Systems* **2**, 2000039, doi:https://doi.org/10.1002/aisy.202000039 (2020).

219 Fiorillo, A. S., Critello, C. D. & Pullano, S. A. Theory, technology and applications of piezoresistive sensors: A review. *Sensor Actuat a-Phys* **281**, 156-175, doi:10.1016/j.sna.2018.07.006 (2018).

220 Gullapalli, H. *et al.* Flexible Piezoelectric ZnO–Paper Nanocomposite Strain Sensor. *Small* **6**, 1641-1646, doi:https://doi.org/10.1002/smll.201000254 (2010).

221 Yao, S. & Zhu, Y. Wearable multifunctional sensors using printed stretchable conductors made of silver nanowires. *Nanoscale* **6**, 2345-2352, doi:10.1039/C3NR05496A (2014).

222 Zhao, H., O'Brien, K., Li, S. & Shepherd, R. F. Optoelectronically innervated soft prosthetic hand via stretchable optical waveguides. *Science Robotics* **1**, eaai7529, doi:10.1126/scirobotics.aai7529 (2016).

223 Wang, Z. L. Triboelectric Nanogenerators as New Energy Technology for Self-Powered Systems and as Active Mechanical and Chemical Sensors. *ACS Nano* **7**, 9533-9557, doi:10.1021/nn404614z (2013).

224 Dong, T., Gu, Y., Liu, T. & Pecht, M. Resistive and capacitive strain sensors based on customized compliant electrode: Comparison and their wearable applications. *Sensors and Actuators A: Physical* **326**, 112720, doi:https://doi.org/10.1016/j.sna.2021.112720 (2021).

225 Deng, C. *et al.* High-performance capacitive strain sensors with highly stretchable vertical graphene electrodes. *Journal of Materials Chemistry C* **8**, 5541-5546, doi:10.1039/D0TC00491J (2020).

226 Shintake, J., Piskarev, E., Jeong, S. H. & Floreano, D. Ultrastretchable Strain Sensors Using Carbon Black-Filled Elastomer Composites and Comparison of Capacitive Versus Resistive Sensors. *Adv Mater Technol-Us* **3**, 1700284, doi:10.1002/admt.201700284 (2018).

227 Nur, R. *et al.* A Highly Sensitive Capacitive-type Strain Sensor Using Wrinkled Ultrathin Gold Films. *Nano Letters* **18**, 5610-5617, doi:10.1021/acs.nanolett.8b02088 (2018).

228 Wang, C. *et al.* Advanced Carbon for Flexible and Wearable Electronics. *Advanced Materials* **31**, 1801072, doi:https://doi.org/10.1002/adma.201801072 (2019).

229 Kim, S.-R., Kim, J.-H. & Park, J.-W. Wearable and Transparent Capacitive Strain Sensor with High Sensitivity Based on Patterned Ag Nanowire Networks. *ACS applied materials & interfaces* **9**, 26407-26416, doi:10.1021/acsami.7b06474 (2017).

230 Jayathilaka, W. A. D. M. *et al.* Significance of Nanomaterials in Wearables: A Review on Wearable Actuators and Sensors. *Advanced Materials* **31**, 1805921, doi:https://doi.org/10.1002/adma.201805921 (2019).

231 Cohen, D. J., Mitra, D., Peterson, K. & Maharbiz, M. M. A Highly Elastic, Capacitive Strain Gauge Based on Percolating Nanotube Networks. *Nano Letters* **12**, 1821-1825, doi:10.1021/nl204052z (2012).

232 Shin, U.-H. *et al.* Highly stretchable conductors and piezocapacitive strain gauges based on simple contact-transfer patterning of carbon nanotube forests. *Carbon* **80**, 396-404, doi:https://doi.org/10.1016/j.carbon.2014.08.079 (2014).

233 Binnig, G., Rohrer, H., Gerber, C. & Weibel, E. Surface Studies by Scanning Tunneling Microscopy. *Physical Review Letters* **49**, 57-61, doi:10.1103/PhysRevLett.49.57 (1982).

234 Binnig, G., Quate, C. F. & Gerber, C. Atomic Force Microscope. *Physical Review Letters* **56**, 930-933, doi:10.1103/PhysRevLett.56.930 (1986).

235 Ueberschlag, P. PVDF piezoelectric polymer. *Sensor Review* **21**, 118-126, doi:10.1108/02602280110388315 (2001).

236 Dagdeviren, C. *et al.* Recent progress in flexible and stretchable piezoelectric devices for mechanical energy harvesting, sensing and actuation. *Extreme Mechanics Letters* **9**, 269-281, doi:https://doi.org/10.1016/j.eml.2016.05.015 (2016).

237 Dagdeviren, C. *et al.* Conformable amplified lead zirconate titanate sensors with enhanced piezoelectric response for cutaneous pressure monitoring. *Nature communications* **5**, 4496, doi:10.1038/ncomms5496 (2014).

238 Ha, M. *et al.* Bioinspired Interlocked and Hierarchical Design of ZnO Nanowire Arrays for Static and Dynamic Pressure-Sensitive Electronic Skins. *Advanced Functional Materials* **25**, 2841-2849, doi:https://doi.org/10.1002/adfm.201500453 (2015).

239 Arnau, A. & Soares, D. in *Piezoelectric Transducers and Applications* (ed Antonio Arnau Vives) 1-38 (Springer Berlin Heidelberg, 2008).

240 William D Van Dyke, P. A. D. Metal foil type strain gauge and method of making same. United States patent (1946).

241 Keil, S. in *Technology and Practical Use of Strain Gages With Particular Consideration of Stress Analysis Using Strain Gages* 1-16 (2017).

242 Ned, A. A. *Selecting Strain Gages Silicon vs Metal Foil*, <https://kulite.com/assets/media/2018/01/SelectingStrainGagesSiliconvsMetalFoil.pdf> (2018).

243 Smith, C. S. Piezoresistance Effect in Germanium and Silicon. *Physical Review* **94**, 42-49, doi:10.1103/PhysRev.94.42 (1954).

244 Blazquez, G., Pons, P. & Boukabache, A. Capabilities and limits of silicon pressure sensors. *Sensors and Actuators* **17**, 387-403, doi:https://doi.org/10.1016/0250-6874(89)80026-5 (1989).

245 Amjadi, M., Kyung, K.-U., Park, I. & Sitti, M. Stretchable, Skin-Mountable, and Wearable Strain Sensors and Their Potential Applications: A Review. *Advanced Functional Materials* **26**, 1678-1698, doi:https://doi.org/10.1002/adfm.201504755 (2016).

246 Billard, A. & Kragic, D. Trends and challenges in robot manipulation. *Science* **364**, eaat8414, doi:10.1126/science.aat8414 (2019).

247 Simmons, J. G. Generalized formula for the electric tunnel effect between similar electrodes separated by a thin insulating film. *J Appl Phys* **34**, 1793-1803 (1963).

248 Hempel, M., Nezich, D., Kong, J. & Hofmann, M. A Novel Class of Strain Gauges Based on Layered Percolative Films of 2D Materials. *Nano Letters* **12**, 5714-5718, doi:10.1021/nl302959a (2012).

249 Cai, Y. *et al.* Extraordinarily Stretchable All-Carbon Collaborative Nanoarchitectures for Epidermal Sensors. *Advanced Materials* **29**, 1606411, doi:https://doi.org/10.1002/adma.201606411 (2017).

250 Tsai, M.-Y. *et al.* Flexible MoS2 Field-Effect Transistors for Gate-Tunable Piezoresistive Strain Sensors. *ACS applied materials & interfaces* **7**, 12850-12855, doi:10.1021/acsami.5b02336 (2015).

251 Manzeli, S., Allain, A., Ghadimi, A. & Kis, A. Piezoresistivity and Strain-induced Band Gap Tuning in Atomically Thin MoS2. *Nano Letters* **15**, 5330-5335, doi:10.1021/acs.nanolett.5b01689 (2015).

252 Li, X. *et al.* Stretchable and highly sensitive graphene-on-polymer strain sensors. *Scientific Reports* **2**, 870, doi:10.1038/srep00870 (2012).

253 Lee, J. *et al.* A stretchable strain sensor based on a metal nanoparticle thin film for human motion detection. *Nanoscale* **6**, 11932-11939, doi:10.1039/C4NR03295K (2014).

254 Wang, S. *et al.* Network cracks-based wearable strain sensors for subtle and large strain detection of human motions. *Journal of Materials Chemistry C* **6**, 5140-5147, doi:10.1039/C8TC00433A (2018).

255 Shi, X., Liu, S., Sun, Y., Liang, J. & Chen, Y. Lowering Internal Friction of 0D–1D–2D Ternary Nanocomposite-Based Strain Sensor by Fullerene to Boost the Sensing Performance. *Advanced Functional Materials* **28**, 1800850, doi:https://doi.org/10.1002/adfm.201800850 (2018).

256 Boland, C. S. Stumbling through the Research Wilderness, Standard Methods To Shine Light on Electrically Conductive Nanocomposites for Future Healthcare Monitoring. *Acs Nano* **13**, 13627-13636, doi:10.1021/acsnano.9b06847 (2019).

257 Lakes, R. *Viscoelastic Materials.* (Cambridge University Press, 2009).

258 Jin, L. *et al.* Microstructural origin of resistance–strain hysteresis in carbon nanotube thin film conductors. *Proceedings of the National Academy of Sciences* **115**, 1986-1991, doi:10.1073/pnas.1717217115 (2018).

259 Busfield, J. J. C., Thomas, A. G. & Yamaguchi, K. Electrical and mechanical behavior of filled rubber. III. Dynamic loading and the rate of recovery. *Journal of Polymer Science Part B: Polymer Physics* **43**, 1649-1661, doi:https://doi.org/10.1002/polb.20452 (2005).

260 Liu, H. *et al.* Electrically conductive thermoplastic elastomer nanocomposites at ultralow graphene loading levels for strain sensor applications. *Journal of Materials Chemistry C* **4**, 157-166, doi:10.1039/C5TC02751A (2016).

261 Zhang, F., Hu, H., Hu, S. & Yue, J. Significant strain-rate dependence of sensing behavior in TiO2@carbon fibre/PDMS composites for flexible strain sensors. *Journal of Advanced Ceramics* **10**, 1350-1359, doi:10.1007/s40145-021-0509-7 (2021).

262 Amjadi, M. & Park, I. in *2015 28th IEEE International Conference on Micro Electro Mechanical Systems (MEMS)*. 744-747.

263 Zhang, H. *et al.* Metallic Sandwiched-Aerogel Hybrids Enabling Flexible and Stretchable Intelligent Sensor. *Nano Letters* **20**, 3449-3458, doi:10.1021/acs.nanolett.0c00372 (2020).

264 Boland, C. S. Quantifying the Contributing Factors toward Signal Fatigue in Nanocomposite Strain Sensors. *ACS Applied Polymer Materials* **2**, 3474-3480, doi:10.1021/acsapm.0c00510 (2020).

265 Kun, F., Carmona, H. A., Andrade, J. S. & Herrmann, H. J. Universality behind Basquin's Law of Fatigue. *Physical Review Letters* **100**, 094301, doi:10.1103/PhysRevLett.100.094301 (2008).

266 Diani, J., Fayolle, B. & Gilormini, P. A review on the Mullins effect. *European Polymer Journal* **45**, 601-612, doi:https://doi.org/10.1016/j.eurpolymj.2008.11.017 (2009).

267 Cantournet, S., Desmorat, R. & Besson, J. Mullins effect and cyclic stress softening of filled elastomers by internal sliding and friction thermodynamics model. *International Journal of Solids and Structures* **46**, 2255-2264, doi:https://doi.org/10.1016/j.ijsolstr.2008.12.025 (2009).

268 Sauer, J. A. & Richardson, G. C. Fatigue of polymers. *International Journal of Fracture* **16**, 499-532, doi:10.1007/BF02265215 (1980).

269 Zhang, C., Gou, X. & Xiao, R. Hysteresis in glass microsphere filled elastomers under cyclic loading. *Polymer Testing* **95**, 107081, doi:https://doi.org/10.1016/j.polymertesting.2021.107081 (2021).

270 Zheng, Q., Lee, J.-h., Shen, X., Chen, X. & Kim, J.-K. Graphene-based wearable piezoresistive physical sensors. *Materials Today* **36**, 158-179, doi:https://doi.org/10.1016/j.mattod.2019.12.004 (2020).

271 O'Driscoll, D. P., Vega-Mayoral, V., Harley, I., Boland, C. S. & Coleman, J. N. Optimising composite viscosity leads to high sensitivity electromechancial sensors. *2D Materials* **5**, 035042, doi:10.1088/2053-1583/aacba6 (2018).

272 Vigolo, B., Coulon, C., Maugey, M., Zakri, C. & Poulin, P. An Experimental Approach to the Percolation of Sticky Nanotubes. *Science* **309**, 920-923, doi:10.1126/science.1112835 (2005).

273 Arif, M. F., Kumar, S., Gupta, T. K. & Varadarajan, K. M. Strong linear-piezoresistive-response of carbon nanostructures reinforced hyperelastic polymer nanocomposites. *Composites Part A: Applied Science and Manufacturing* **113**, 141-149, doi:10.1016/j.compositesa.2018.07.021 (2018).

274 Vudayagiri, S., Junker, M. D. & Skov, A. L. Factors affecting the surface and release properties of thin polydimethylsiloxane films. *Polymer Journal* **45**, 871-878, doi:10.1038/pj.2012.227 (2013).

275 Farivar, F. *et al.* Unlocking thermogravimetric analysis (TGA) in the fight against "Fake graphene" materials. *Carbon* **179**, 505-513, doi:https://doi.org/10.1016/j.carbon.2021.04.064 (2021).

276 Jurewicz, I. *et al.* Locking Carbon Nanotubes in Confined Lattice Geometries – A Route to Low Percolation in Conducting Composites. *The Journal of Physical Chemistry B* **115**, 6395-6400, doi:10.1021/jp111998p (2011).

277 Du, H., Fang, C., Zhang, J., Xia, X. & Weng, G. J. Segregated carbon nanotube networks in CNT-polymer nanocomposites for higher electrical conductivity and dielectric permittivity, and lower percolation threshold. *International Journal of Engineering Science* **173**, 103650, doi:https://doi.org/10.1016/j.ijengsci.2022.103650 (2022).

278 Carcia, P. F., Suna, A. & Childers, W. D. Electrical-Conduction and Strain Sensitivity in Ruo2 Thick-Film Resistors. *J Appl Phys* **54**, 6002-6008, doi:Doi 10.1063/1.331779 (1983).

279 Kang, I., Schulz, M. J., Kim, J. H., Shanov, V. & Shi, D. A carbon nanotube strain sensor for structural health monitoring. *Smart Materials and Structures* **15**, 737, doi:10.1088/0964-1726/15/3/009 (2006).

280 Xu, S. *et al.* Soft Microfluidic Assemblies of Sensors, Circuits, and Radios for the Skin. *Science* **344**, 70-74, doi:10.1126/science.1250169 (2014).

281 Ma, Y. *et al.* Relation between blood pressure and pulse wave velocity for human arteries. *Proceedings of the National Academy of Sciences* **115**, 11144-11149, doi:10.1073/pnas.1814392115 (2018).

282 Baughman, R. H., Zakhidov, A. A. & de Heer, W. A. Carbon Nanotubes--the Route Toward Applications. *Science* **297**, 787-792, doi:10.1126/science.1060928 (2002).

283 Sandler, J. K. W., Kirk, J. E., Kinloch, I. A., Shaffer, M. S. P. & Windle, A. H. Ultra-low electrical percolation threshold in carbon-nanotube-epoxy composites. *Polymer* **44**, 5893-5899, doi:https://doi.org/10.1016/S0032-3861(03)00539-1 (2003).

284 Yousefi, N. *et al.* Highly Aligned Graphene/Polymer Nanocomposites with Excellent Dielectric Properties for High-Performance Electromagnetic Interference Shielding. *Advanced Materials* **26**, 5480-5487, doi:https://doi.org/10.1002/adma.201305293 (2014).

285 Park, M. *et al.* Highly stretchable electric circuits from a composite material of silver nanoparticles and elastomeric fibres. *Nature Nanotechnology* **7**, 803-809, doi:10.1038/nnano.2012.206 (2012).

286 Narongthong, J., Le, H. H., Das, A., Sirisinha, C. & Wießner, S. Ionic liquid enabled electrical-strain tuning capability of carbon black based conductive polymer composites for small-strain sensors and stretchable conductors. *Composites Science and Technology* **174**, 202-211, doi:10.1016/j.compscitech.2019.03.002 (2019).

287 Liu, H. *et al.* Electrically conductive polymer composites for smart flexible strain sensors: a critical review. *Journal of Materials Chemistry C* **6**, 12121-12141, doi:10.1039/C8TC04079F (2018).

288 Levin, Z. S., Robert, C., Feller, J. F., Castro, M. & Grunlan, J. C. Flexible latex—polyaniline segregated network composite coating capable of measuring large strain on epoxy. *Smart Materials and Structures* **22**, 015008, doi:10.1088/0964-1726/22/1/015008 (2013).

289 Liao, H., Guo, X., Wan, P. & Yu, G. Conductive MXene Nanocomposite Organohydrogel for Flexible, Healable, Low-Temperature Tolerant Strain Sensors. *Advanced Functional Materials* **29**, 1904507, doi:https://doi.org/10.1002/adfm.201904507 (2019).

290 Cai, Y. *et al.* Stretchable Ti3C2Tx MXene/Carbon Nanotube Composite Based Strain Sensor with Ultrahigh Sensitivity and Tunable Sensing Range. *ACS Nano* **12**, 56-62, doi:10.1021/acsnano.7b06251 (2018).

291 Bauhofer, W. & Kovacs, J. Z. A review and analysis of electrical percolation in carbon nanotube polymer composites. *Composites Science and Technology* **69**, 1486-1498, doi:10.1016/j.compscitech.2008.06.018 (2009).

292 McLachlan, D. S., Blaszkiewicz, M. & Newnham, R. E. Electrical Resistivity of Composites. *Journal of the American Ceramic Society* **73**, 2187-2203, doi:https://doi.org/10.1111/j.1151-2916.1990.tb07576.x (1990).

293 Lin, L. *et al.* Towards Tunable Sensitivity of Electrical Property to Strain for Conductive Polymer Composites Based on Thermoplastic Elastomer. *ACS applied materials & interfaces* **5**, 5815-5824, doi:10.1021/am401402x (2013).

294 Gang, Y. *et al.* A carbon nanotube/polymer strain sensor with linear and anti-symmetric piezoresistivity. *Journal of Composite Materials* **45**, 1315-1323, doi:10.1177/0021998310393296 (2011).

295 Zhang, R., Baxendale, M. & Peijs, T. Universal resistivity-strain dependence of carbon nanotube/polymer composites. *Physical Review B - Condensed Matter and Materials Physics* **76**, 195433, doi:10.1103/PhysRevB.76.195433 (2007).

296 Yang, H., Yuan, L., Yao, X. & Fang, D. Piezoresistive response of graphene rubber composites considering the tunneling effect. *Journal of the Mechanics*

and Physics of Solids **139**, 103943, doi:https://doi.org/10.1016/j.jmps.2020.103943 (2020).

297 Rahman, R. & Servati, P. Effects of inter-tube distance and alignment on tunnelling resistance and strain sensitivity of nanotube/polymer composite films. *Nanotechnology* **23**, 055703, doi:10.1088/0957-4484/23/5/055703 (2012).

298 Hu, N. *et al.* Investigation on sensitivity of a polymer/carbon nanotube composite strain sensor. *Carbon* **48**, 680-687, doi:10.1016/j.carbon.2009.10.012 (2010).

299 Amjadi, M., Pichitpajongkit, A., Lee, S., Ryu, S. & Park, I. Highly Stretchable and Sensitive Strain Sensor Based on Silver Nanowire–Elastomer Nanocomposite. *ACS Nano* **8**, 5154-5163, doi:10.1021/nn501204t (2014).

300 Chun, S., Choi, Y. & Park, W. All-graphene strain sensor on soft substrate. *Carbon* **116**, 753-759, doi:10.1016/j.carbon.2017.02.058 (2017).

301 Gao, J. *et al.* Ultrastretchable Multilayered Fiber with a Hollow-Monolith Structure for High-Performance Strain Sensor. *ACS Applied Materials and Interfaces* **10**, 34592-34603, doi:10.1021/acsami.8b11527 (2018).

302 Kim, J. H. *et al.* Simple and cost-effective method of highly conductive and elastic carbon nanotube/polydimethylsiloxane composite for wearable electronics. *Scientific Reports* **8**, 1-11, doi:10.1038/s41598-017-18209-w (2018).

303 Kim, J. Y. *et al.* 3D printable composite dough for stretchable, ultrasensitive and body-patchable strain sensors. *Nanoscale* **9**, 11035-11046, doi:10.1039/c7nr01865g (2017).

304 Lee, W. S. *et al.* Multiaxial and Transparent Strain Sensors Based on Synergetically Reinforced and Orthogonally Cracked Hetero-Nanocrystal Solids. *Advanced Functional Materials* **29**, 1806714-1806714, doi:10.1002/adfm.201806714 (2019).

305 Lee, Y. Y. *et al.* A Strain-Insensitive Stretchable Electronic Conductor: PEDOT:PSS/Acrylamide Organogels. *Advanced Materials* **28**, 1636-1643, doi:10.1002/adma.201504606 (2016).

306 Paleo, A. J. *et al.* The piezoresistive effect in polypropylene—carbon nanofibre composites obtained by shear extrusion. *Smart Materials and Structures* **19**, 065013-065013, doi:10.1088/0964-1726/19/6/065013 (2010).

307 Pham, G. T., Park, Y. B., Liang, Z., Zhang, C. & Wang, B. Processing and modeling of conductive thermoplastic/carbon nanotube films for strain sensing. *Composites Part B: Engineering* **39**, 209-216, doi:10.1016/j.compositesb.2007.02.024 (2008).

308 Wang, S., Zhang, X., Wu, X. & Lu, C. Tailoring percolating conductive networks of natural rubber composites for flexible strain sensors via a cellulose nanocrystal templated assembly. *Soft Matter* **12**, 845-852, doi:10.1039/c5sm01958c (2016).

309 Wang, Y. *et al.* Super-elastic graphene ripples for flexible strain sensors. *ACS Nano* **5**, 3645-3650, doi:10.1021/nn103523t (2011).

310 Christ, J. F., Aliheidari, N., Ameli, A. & Pötschke, P. 3D printed highly elastic strain sensors of multiwalled carbon nanotube/thermoplastic polyurethane nanocomposites. *Materials & Design* **131**, 394-401, doi:https://doi.org/10.1016/j.matdes.2017.06.011 (2017).

311 Casiraghi, C. *et al.* Inkjet printed 2D-crystal based strain gauges on paper. *Carbon* **129**, 462-467, doi:https://doi.org/10.1016/j.carbon.2017.12.030 (2018).

312 Foygel, M., Morris, R. D., Anez, D., French, S. & Sobolev, V. L. Theoretical and computational studies of carbon nanotube composites and suspensions: Electrical and thermal conductivity. *Phys Rev B* **71**, 104201, doi:10.1103/PhysRevB.71.104201 (2005).

313 Guyot-Sionnest, P. Electrical Transport in Colloidal Quantum Dot Films. *Journal of Physical Chemistry Letters* **3**, 1169-1175, doi:10.1021/jz300048y (2012).

314 Grillard, F. *et al.* Conductivity and percolation of nanotube based polymer composites in extensional deformations. *Polymer* **53**, 183-187, doi:10.1016/j.polymer.2011.11.020 (2012).

315 Pu, J.-H. *et al.* 2D end-to-end carbon nanotube conductive networks in polymer nanocomposites: a conceptual design to dramatically enhance the sensitivities of strain sensors. *Nanoscale* **10**, 2191-2198, doi:10.1039/C7NR08077H (2018).

316 Xu, H. *et al.* Influence of processing conditions on dispersion, electrical and mechanical properties of graphene-filled-silicone rubber composites.

Composites Part A: Applied Science and Manufacturing **91**, 53-64, doi:https://doi.org/10.1016/j.compositesa.2016.09.011 (2016).

317 Zhao, J. *et al.* Ultra-sensitive strain sensors based on piezoresistive nanographene films. *Applied Physics Letters* **101**, 063112, doi:10.1063/1.4742331 (2012).

318 Chen, Z. *et al.* Enhancing the Sensitivity of Percolative Graphene Films for Flexible and Transparent Pressure Sensor Arrays. *Advanced Functional Materials* **26**, 5061-5067, doi:https://doi.org/10.1002/adfm.201503674 (2016).

319 Takei, K. *et al.* Highly sensitive electronic whiskers based on patterned carbon nanotube and silver nanoparticle composite films. *Proceedings of the National Academy of Sciences* **111**, 1703-1707, doi:10.1073/pnas.1317920111 (2014).

320 Chhetry, A. *et al.* MoS2-Decorated Laser-Induced Graphene for a Highly Sensitive, Hysteresis-free, and Reliable Piezoresistive Strain Sensor. *ACS applied materials & interfaces* **11**, 22531-22542, doi:10.1021/acsami.9b04915 (2019).

321 Chen, S., Wei, Y., Yuan, X., Lin, Y. & Liu, L. A highly stretchable strain sensor based on a graphene/silver nanoparticle synergic conductive network and a sandwich structure. *Journal of Materials Chemistry C* **4**, 4304-4311, doi:10.1039/C6TC00300A (2016).

322 Pan, S. *et al.* A highly stretchable strain sensor based on CNT/graphene/fullerene-SEBS. *RSC Advances* **10**, 11225-11232, doi:10.1039/D0RA00327A (2020).

323 Shi, J. *et al.* Graphene Reinforced Carbon Nanotube Networks for Wearable Strain Sensors. *Advanced Functional Materials* **26**, 2078-2084, doi:https://doi.org/10.1002/adfm.201504804 (2016).

324 Gabbett, C. *et al.* The Effect of Network Formation on the Mechanical Properties of 1D:2D Nano:Nano Composites. *Chemistry of Materials* **30**, 5245-5255, doi:10.1021/acs.chemmater.8b01945 (2018).

325 Griffin, A. *et al.* Spectroscopic Size and Thickness Metrics for Liquid-Exfoliated h-BN. *Chemistry of Materials* **30**, 1998-2005, doi:10.1021/acs.chemmater.7b05188 (2018).

326 Vega-Mayoral, V. *et al.* Exciton and charge carrier dynamics in few-layer WS2. *Nanoscale* **8**, 5428-5434, doi:10.1039/C5NR08384B (2016).

327 Lu, Q. *et al.* Investigation of shape controlled silver nanoplates by a solvothermal process. *Journal of Colloid and Interface Science* **342**, 8-17, doi:https://doi.org/10.1016/j.jcis.2009.09.066 (2010).

328 Wiley, B. J. *et al.* Synthesis and Optical Properties of Silver Nanobars and Nanorice. *Nano Letters* **7**, 1032-1036, doi:10.1021/nl070214f (2007).

329 Callegari, A., Tonti, D. & Chergui, M. Photochemically Grown Silver Nanoparticles with Wavelength-Controlled Size and Shape. *Nano Letters* **3**, 1565-1568, doi:10.1021/nl034757a (2003).

330 Sun, X. M. & Li, Y. D. Cylindrical Silver Nanowires: Preparation, Structure, and Optical Properties. *Advanced Materials* **17**, 2626-2630, doi:https://doi.org/10.1002/adma.200500957 (2005).

331 Berkdemir, A. *et al.* Identification of individual and few layers of WS2 using Raman Spectroscopy. *Scientific Reports* **3**, 1755, doi:10.1038/srep01755 (2013).

332 del Corro, E. *et al.* Excited Excitonic States in 1L, 2L, 3L, and Bulk WSe2 Observed by Resonant Raman Spectroscopy. *ACS Nano* **8**, 9629-9635, doi:10.1021/nn504088g (2014).

333 Kelly Adam, G. *et al.* All-printed thin-film transistors from networks of liquid-exfoliated nanosheets. *Science* **356**, 69-73, doi:10.1126/science.aal4062 (2017).

334 Pan, K. *et al.* Sustainable production of highly conductive multilayer graphene ink for wireless connectivity and IoT applications. *Nature communications* **9**, 5197, doi:10.1038/s41467-018-07632-w (2018).

335 De, S. & Coleman, J. N. Are There Fundamental Limitations on the Sheet Resistance and Transmittance of Thin Graphene Films? *ACS Nano* **4**, 2713-2720, doi:10.1021/nn100343f (2010).

336 Wu, J. & McLachlan, D. S. Percolation exponents and thresholds obtained from the nearly ideal continuum percolation system graphite-boron nitride. *Phys Rev B* **56**, 1236-1248, doi:10.1103/PhysRevB.56.1236 (1997).

337 Liu, S. *et al.* Solution processed, vertically stacked hetero-structured diodes based on liquid-exfoliated WS2 nanosheets: from electrode-limited to bulk-limited behavior. *Nanoscale* **14**, 15679-15690, doi:10.1039/D2NR04196K (2022).

338 Chiteme, C., McLachlan, D. S. & Sauti, G. ac and dc percolative conductivity of magnetite-cellulose acetate composites. *Phys Rev B* **75**, 094202, doi:10.1103/PhysRevB.75.094202 (2007).

339 Kelly, A. G. *et al.* Tuneable photoconductivity and mobility enhancement in printed MoS 2 /graphene composites. *2D Materials* **4**, 041006, doi:10.1088/2053-1583/aa8442 (2017).

340 Garcia, J. R., O'Suilleabhain, D., Kaur, H. & Coleman, J. N. A Simple Model Relating Gauge Factor to Filler Loading in Nanocomposite Strain Sensors. *ACS Applied Nano Materials* **4**, 2876-2886, doi:10.1021/acsanm.1c00040 (2021).

341 Chen, S., Song, Y., Ding, D., Ling, Z. & Xu, F. Flexible and Anisotropic Strain Sensor Based on Carbonized Crepe Paper with Aligned Cellulose Fibers. *Advanced Functional Materials* **28**, 1802547, doi:https://doi.org/10.1002/adfm.201802547 (2018).

342 Araromi, O. A. *et al.* Ultra-sensitive and resilient compliant strain gauges for soft machines. *Nature* **587**, 219-224, doi:10.1038/s41586-020-2892-6 (2020).

343 Yang, H. *et al.* Automatic strain sensor design via active learning and data augmentation for soft machines. *Nature Machine Intelligence* **4**, 84-94, doi:10.1038/s42256-021-00434-8 (2022).

344 Su, Y. *et al.* In-Plane Deformation Mechanics for Highly Stretchable Electronics. *Advanced Materials* **29**, 1604989, doi:https://doi.org/10.1002/adma.201604989 (2017).

345 Zhang, Y. *et al.* Experimental and Theoretical Studies of Serpentine Microstructures Bonded To Prestrained Elastomers for Stretchable Electronics. *Advanced Functional Materials* **24**, 2028-2037, doi:https://doi.org/10.1002/adfm.201302957 (2014).

346 Kim, D.-H. *et al.* Epidermal Electronics. *Science* **333**, 838-843, doi:10.1126/science.1206157 (2011).

347 Lanzara, G., Salowitz, N., Guo, Z. & Chang, F.-K. A Spider-Web-Like Highly Expandable Sensor Network for Multifunctional Materials. *Advanced Materials* **22**, 4643-4648, doi:https://doi.org/10.1002/adma.201000661 (2010).

348 Li, S. *et al.* Contact-Resistance-Free Stretchable Strain Sensors with High Repeatability and Linearity. *ACS Nano* **16**, 541-553, doi:10.1021/acsnano.1c07645 (2022).

349 Agilent. Cary 100/300/4000/5000/6000i/7000 Spectrophotometers User's Guide.

350 Rocha, F. S., Gomes, A. J., Lunardi, C. N., Kaliaguine, S. & Patience, G. S. Experimental methods in chemical engineering: Ultraviolet visible spectroscopy—UV-Vis. *The Canadian Journal of Chemical Engineering* **96**, 2512-2517, doi:https://doi.org/10.1002/cjce.23344 (2018).

351 Woodward, L. A. in *Raman Spectroscopy: Theory and Practice* (ed Herman A. Szymanski) 1-43 (Springer US, 1967).

352 Dietzek, B., Cialla, D., Schmitt, M. & Popp, J. in *Confocal Raman Microscopy* (eds Jan Toporski, Thomas Dieing, & Olaf Hollricher) 47-68 (Springer International Publishing, 2018).

353 Keresztury, G. in *Handbook of Vibrational Spectroscopy* (2001).

354 Ember, K. J. I. *et al.* Raman spectroscopy and regenerative medicine: a review. *npj Regenerative Medicine* **2**, 12, doi:10.1038/s41536-017-0014-3 (2017).

355 Ferrari, A. C. *et al.* Raman spectrum of graphene and graphene layers. *Physical review letters* **97**, 187401 (2006).

356 Wang, W., Li, Z., Marsden, A. J., Bissett, M. A. & Young, R. J. Interlayer and interfacial stress transfer in hBN nanosheets. *2D Materials* **8**, 035058 (2021).

357 Smith, D. J. Ultimate resolution in the electron microscope? *Materials Today* **11**, 30-38, doi:https://doi.org/10.1016/S1369-7021(09)70005-7 (2008).

358 Inkson, B. J. in *Materials Characterization Using Nondestructive Evaluation (NDE) Methods* (eds Gerhard Hübschen, Iris Altpeter, Ralf Tschuncky, & Hans-Georg Herrmann) 17-43 (Woodhead Publishing, 2016).